AURONE-DERIVED TRIAZOLES AS POTENTIAL SCAFFOLDS FOR FLUORESCENT AND ANTI-INFLAMMATORY MOLECULES

By

Daniel L. Bryant

A Dissertation Submitted in Partial Fulfillment
of the Requirements for the Degree of
Doctor of Philosophy in Molecular Biosciences

Middle Tennessee State University
November 2023

Dissertation committee:

Anthony L. Farone, Chair

Scott D. Handy

Paul C. Kline

Justin M. Miller

David E. Nelson

DECLARATION

The works presented throughout this dissertation are my original work. Certain aspects of this work were performed in collaborations with the MTSU Biology and Chemistry departments. I am the main contributor of the works described below. However, the synthesis and purification of each aurone-derived 1,2,3-triazole were performed by Dr. Arjun Kafle and Shrijana Bhattarai under the supervision of Dr. Scott Handy. Eve Technologies performed the multiplex cytokine panels, and Novogene performed the mRNA library preparation and RNA sequencing. Sydney Ferguson, Reece Long, and Desta Kidane assisted in the performance of some assays. All data analyses presented in the text were performed by me. Certain aspects of this dissertation, including certain figures, were utilized in my dissertation proposal. Chapter II is an edited and reformatted version of the paper "Aurone-derived 1,2,3-triazoles as potential fluorescence molecules in vitro" of which I am the primary author[1]. This paper was used in accordance with the rules set by RSC Advances, the journal which it is published in, cited below.

Bryant, D. L., Kafle, A., Handy, S. T., Farone, A. L. & Miller, J. M. Aurone-derived 1,2,3-triazoles as potential fluorescence molecules in vitro. *RSC Advances* **12**, 22639-22649, doi:10.1039/D2RA02578G (2022).

Dedicated to my beautiful wife Sophie who put up with me and kept me sane throughout these past 6+ years, to my puppy Kira who waited so long for her dinner some nights, and to my father who couldn't be bothered to read this.

ACKNOWLEDGEMENTS

I would like to thank my advisor, Dr. Anthony Farone, for his continuing support throughout the entirety of my graduate school career. Without him, I would not have even enrolled at MTSU, much less be getting my Ph. D. He has been a wonderful mentor. Thank you to Dr. Mary Farone for putting up with me running amuck in her lab space, reorganizing it, and failing to label things correctly early in my career. She has also been there for me when I wasn't sure I'd make it through. I will always be grateful to her. I'd also like to thank Dr. Justin Miller for his guidance with many aspects of my life as a doctoral student and Dr. Scott Handy, who helped me to understand how polarity may affect fluorescence, allowed me to be a part of a provisional patent, and synthesized these ATs which are the core component of my dissertation. I'd like to thank Dr. Paul Kline for training me on certain aspects of analytical chemistry, mainly determining monosaccharide composition. The first year and a half after I joined Dr. Farone's laboratory were spent in Dr. Kline's laboratory using his reagents and machinery, of which I couldn't be more grateful. I'd like to thank Dr. David Nelson. He provided me with my initial training and helped me cultivate many skills which I have used throughout my doctoral studies. His investment in my training, guidance on my research, and personal advice have been essential to getting me this far. He also let me use his *Nos2*-mCherry-PEST and p65-EGFP cell lines and, though I did not use the p65 reporter in this dissertation (please forgive me, I swear I tried), I am thankful for that as well. A big thank you to my lab mates, former and current, with an emphasis on Desta, Raj, Sydney, Brock, and Alyssa all who have helped, guided, or trained me. They are all fantastic. Finally, I'd like to thank my parents, Jerry and Kim. They have been a great support all these years.

ABSTRACT

Natural products derived from various plants have been used throughout history for many different purposes. One such naturally occurring compound, flavonoids, are responsible for the pigmentation in most flowering plants. Flavonoids have been demonstrated to have unique properties, both biological and photophysical. Various classes of flavonoids exist including flavones and flavonols, which have been studied for their biological activities. Two flavonoids, Quercetin and Apigenin, are commercially available and have been shown to possess anti-inflammatory properties. One derivative of flavone, the aurone, has been predominantly examined for their photophysical properties as fluorophores and their biological activities in cancer cells. Recently, studies have implicated aurones as anti-inflammatories, though their mechanism has yet to be thoroughly elucidated. Aurones are highly modifiable, and many substitutions can be added to either the benzofuranone or benzylidene groups, or both, thus modulating their biological activities and fluorescent properties. Compounds containing the 1,2,3-triazole moiety have been explored for their use as COX-2 inhibitors and as fluorophores. Therefore, it was thought that the incorporation of a 1,2,3-triazole as a modification of existing aurones may lead to similar, if not more potent fluorescent and biological activities. This dissertation explores the use of novel aurone-derived salicyl-substituted 1,2,3-triazoles (ATs) as fluorescence molecules and anti-inflammatory compounds. It was found that, with the appropriate modifications, certain ATs may exhibit such properties. A single representative AT was utilized for each purpose. AT5 was shown to have unique properties as a fluorophore, yielding an excitation and emission spectra with a large Stokes shift, which increased as polarity of the solvent increased and was maximal in phosphate

buffered saline, while also increased in other aqueous or protic solutions. Another AT, AT111, was demonstrated to have anti-inflammatory properties, limiting the effect of LPS on the induction of an inflammatory response in macrophages. AT111 lowered the production of inflammatory mediators such as IL-6, MCP-1, and iNOS, while not interfering with expression of other inflammatory proteins such as TNF-α and COX-2. It was determined that AT111 did not mitigate the initial TLR4 driven NF-κB response but did increase phosphorylation of ERK2. AT111 was also shown to increase histone, TRAF4, and MKNK2 transcription in both PMA-differentiated U937 human and RAW 264.7 murine macrophage-like cells. Gene expression profiles, along with the modulation of LPS-induced expression of many inflammatory proteins, but not all attributed to LPS, possibly implicates various mechanisms that are different from those observed in many anti-inflammatory compounds. Though the aforementioned effects were only apparent in the higher micromolar range, this dissertation demonstrates the potential for these novel ATs to function as both a fluorescent and anti-inflammatory scaffold that may be modified to augment these effects.

TABLE OF CONTENTS

LIST OF TABLES

LIST OF FIGURES

LIST OF APPENDICES

LIST OF ABBREVIATIONS

5-LOX	5-Lipooxygenase
A.U.	Arbitrary units
ABCG2	ATP-binding cassette sub-family G member 2
Adj.	Adjusted
ALBIA	Addressable-laser bead immunoassay
ANOVA	Analysis of variance
AP-1	Activator protein-1
ATs	Aurone-derived 1,2,3-triazoles
AVL	AT111 vs LPS/vehicle DEGs
AVU	DEGs of AT111 (and LPS) treated cells to the untreated cells
BCA	Bicinchoninic acid
BMDM	bone marrow-derived macrophage
BP	Biological processes
BRD2	Bromodomain containing 2
BSA	Bovine Serum Albumin
C3AR1	Complement C3a receptor 1
CC	Cellular components
CCL	C-C motif ligands
CCR	C-C receptor
CD	Cluster of differentiation
CIDs	Chronic inflammatory diseases
CLEC7A	C-type lectin domain containing 7A
COX	Cyclooxygenase
CTAB	Hexadecyltrimethylammonium bromide
CuAAC	Cu (I)- catalyzed azide-alkyne cycloaddition
CXCL	C-X-C motif ligands
CXCR	C-X-C motif chemokine receptors
Cyto	cytoplasmic
DAB2IP	Disabled adapter protein 2 interacting protein
DAMP	Damage-associated molecular pattern
DAVID	Database for Annotation, Visualization, and Integrated Discovery
DEG	Differentially expressed genes
DI	Deionized
DMEM	Dulbecco's modification of Eagle's Medium
DMF	Dimethylformamide
DMSO	Dimethyl sulfoxide
DNMT3B	DNA (cytosine -5-)-methyltransferase
DUSP	Dual specificity phosphatase
EC_{50}	Half maximal effective concentration
Edn1	Endothelin 1
EDTA	Ethylenediamine tetra-acetic acid
EET	Eosinophil extracellular trap

eIF4E	Eukaryotic translation initiation factor 4E
ELISA	Enzyme-linked immunosorbent assay
eNOS	Endothelial NOS
ERK	Extracellular signal-regulated kinases
ESIPT	Excited state intramolecular proton transfer
ET	Extracellular trap
$E_T(30)$	Molar electronic transition energies of pyridium N-phenolate betaine dye 36
E_T^N	Relative normalized $E_T(30)$ values on a scale between TMS and water
EtOAc	Ethyl acetate
FBS	Fetal bovine serum
FCRLB	Fc receptor like B
FITC	Fluorescein isothiocyanate
FTs	Flavonoid-derived 1,2,3-triazoles
GAP	GTPase-activating protein
GAPDH	Glyceraldehyde 3-phosphate dehydrogenase
GEF	Guanine nucleotide exchange-factors
GI	Gastrointestinal
GM-CSF	Granulocyte-macrophage colony stimulating factor 2
GO	Gene ontology
GPCR	G protein-coupled receptors signaling
HDAC	Histone deacetylase
HRP	Horseradish peroxidase
HSP	Heat-shock protein 70
IC_{50}	Half-maximal inhibitory concentrations
IDB	Irritable bowel disease
IFN	Interferon
IHB	Intermolecular hydrogen bonding
IKK	Inhibitor of κ B (IκB) kinase
IKKβ	Inhibitor of κ B kinase β
IL	Interleukin
iNOS	Inducible nitric oxide synthase
IRAK	IL-1 receptor-associated kinases
IRF	IFN-regulatory factor
IκBα	Inhibitor of κB-α
JNK	c-Jun N-terminal kinases
KDM6B	Lysine demethylase 6B
KEGG	Kyoto encyclopedia of genes and genomes
LBP	LPS-binding protein
LF-PVDF	Low-fluorescence polyvinylidene difluoride
LILRB3	Leukocyte immunoglobulin like receptor B3
lncRNA	Long non-coding RNA
LPS	Lipopolysaccharide
LVC	LPS+DMSO vehicle control
LVU	DEGs in the LVC cells compared to the untreated cells

MAPK	Mitogen-activated protein kinase
MAPKAPK	MAPK-activated protein kinases
MCP-1	Monocyte chemoattractant protein-1
MD	Myeloid differentiation factor
MEK	Mitogen-activated protein kinase kinase
MET	Macrophage extracellular trap
MF	Molecular functions
MFHAS1	Malignant fibrous histiocytoma amplified sequence 1
$MgSO_4$	Magnesium sulfate
MHC	Major histocompatibility complex
MNK	MAPK-interacting kinases
MRSA	Methicillin resistant *S. aureus*
MSK	mitogen- and stress- activated kinases
MSX1	Msh homeobox 1-like protein
MyD88	Myeloid differentiation primary response gene 88
NATs	*N-2*-aryl-1,2,3-triazole derivatives
NEMO	NF-κB essential modulator
NET	Neutrophil extracellular trap
NF-κB	Nuclear factor-kappa light chain enhancer of activated b-cells
NITs	*N-2*-indolyl-1,2,3-triazoles
NMR	Nuclear magnetic resonance
NO	Nitric oxide
NOD2	Nucleotide binding oligomerization domain containing 2
NOS	Nitric oxide synthase
NSAIDs	Non-steroidal anti-inflammatory drugs
ORAI1	ORAI calcium release-activated calcium modulator 1
PAD4	peptidyl arginine deiminase 4
PAGE	Polyacrylamide gel electrophoresis
PAMP	Pathogen associated molecular patterns
PBS	Phosphate-buffered saline
PCA	Principal component analysis
PGE_2	Prostaglandin E_2
P-gp	P-glycoprotein
PIK3R1	PI3K regulatory subunit 1
PKC	Protein kinase C
PMA	Phorbol 12-myristate 13-acetate
PPM	parts per million
PRR	Pattern recognition receptors
PSA	Polar surface area
PTM	Post-translational modifications
RA	Rheumatoid arthritis
RdRp	RNA-dependent RNA-polymerase
RFU	Relative fluorescence units
RIP1	Receptor-interacting serine/threonine-protein kinase 1

RIPA	Radioimmunoprecipitation assay
RNS	Reactive nitrogen species
ROCK	Rhoa and rho-associated protein kinases
ROI	Region of interest
ROS	Reactive oxygen species
RPMI	Roswell Park Memorial Institute 1640 medium
RSK	Ribosomal-S6-kinases
RSV	Respiratory syncytial virus
RT	Room temperature
SAHA	Suberoylanilide hydroxamic acid
SDS	Sodium dodecyl-sulfate
SEM	Standard error of the mean
SEm	Scanning emissions
SES	Scanning emissions spectra
SIRT	Sirtuin
Slc26a9	Solute carrier family 26 member 9
SPRED	Sprouty protein with EVH-1 domain
STRING	Search tool for the retrieval of interacting genes/proteins
TANK	TRAF family member-associated NF-κB activator
TBK1	TANK-binding kinase 1
TBS	Tris-buffered saline
TBS/C	TBS containing 0.1 % casein
TCCs	1,2,3-triazole containing compounds
TGM2	Transglutaminase 2
TICAM1	TIR domain containing adaptor molecule 1
TIR	Toll-interleukin 1 receptor
TIRAP	TIR domain containing adaptor protein
TLC	Thin layer chromatography
TLR	Toll-like receptor
TMS	Tetramethylsilane
TNF-α	Tumor necrosis factor-α
TRAF	TNF receptor associated factor
TRAM	Toll/IL-1R domain-containing adaptor-inducing IFN-β-related adaptor molecule
TREML4	Triggering receptor expressed on myeloid cells like 4
TRIF	TIR domain-containing adaptor inducing interferon-β
TSA	Trichostatin A
UV/Vis	Ultraviolet/ visible light
Zpf36l1	Zinc finger protein 36, C3H type-like 1

Chapter I

Introduction

1.1 Flavonoids: Nature's Jack of All Trades

Flavonoids are a class of naturally occurring small polyphenolic molecules found almost ubiquitously in plants and have been shown to have a versatile set of uses. Flavonoids, and their derivatives, are being heavily explored for their bioactive potential. There are many different types of flavonoids including isoflavonoids, various flavonols, flavones, chalcones, and aurones[2]. Many flavonoids have been shown to have potential as anti-inflammatory, antioxidant, anti-bacterial, anti-viral, and anti-cancer compouds[3-10]. Due to their bioactivities, various flavonoids have been used as the prominent compound in nutraceuticals. For example, the flavonol quercetin is a commercially available antioxidant that has been linked with anti-carcinogenic, anti-microbial, anti-viral, and anti-inflammatory properties[4,11-13]. The commercially available flavone, Apigenin, has also been shown to possess similar qualities[14-21]. In addition to their bioactivities, modified flavonoid derivatives also exhibit fluorescent properties[22,23].

1.2 Bioactivities and Anti-cancer Properties of Aurones

One class of flavonoid, the aurones, have been gaining interest due to their bioactivities and fluorescent properties[24-26]. Aurones are a naturally occurring flavonoid derivative found to give a yellowish pigment in some flowering plants like the yellow-rocket snapdragon[27] and other plants belonging to sub-family *Cyrtandroidea*[28]. Aurones are considered anthochlors and can serve as ultraviolet guides for pollinators on petals[29]. Both naturally occurring and synthetic aurones have been characterized as bioactive molecules with biological effects

similar to other flavonoids. Aurones have been extensively studied for their anti-cancer properties[30], which includes decreasing cancer cell proliferation[31,32], invasion[31], and by modulating the multi-drug resistant transporter proteins ATP-binding cassette sub-family G member 2 (ABCG2), and P-glycoprotein (P-gp) which are associated with increased drug resistance in certain cancers[33-36].

1.3 Anti-microbial Effects of Natural and Synthetic Aurones

Aurones have also been shown to have anti-microbial properties. In the 2010 article "Synthesis and biological evaluation of a novel series of 2,2-bisaminomethylated aurone analogues as anti-inflammatory and antimicrobial agents", Bandgar *et al.* were the first to demonstrate aurones as anti-microbials[37]. Six analogs out of the nine compounds screened were shown to be effective at inhibiting growth of multiple bacteria including *E. coli, S. aureus,* and *K. pnuemoniae*, though only three were deemed as promising[37]. The authors also found that six of the nine screened aurones were able to inhibit growth of multiple fungi, with four of the nine having moderate inhibition[37]. In a more recent study, Olleik *et al.* found that various aurones were able to prevent growth of methicillin resistant *S. aureus* (MRSA) as well as other gram-positive bacteria, though there was no significant effect demonstrated on *P. aeruginosa* and most other gram-negatives tested[38]. The study also showed that certain aurones had antifungal activity at concentrations less than 100 μM though it was only limited to two tested species, *Fusarium graminearum* and *Aspergillus niger*[38]. However, another study in 2019 by Alqahtani *et al.* further demonstrated the anti-fungal potential of aurones using a synthetic aurone dubbed SH1009[39]. In the study, SH1009 reduced the growth of various *Candida* ssp.,

through inhibition of the cell cycle[39]. Aurones, at concentrations in the micromolar range, were also shown to decrease *Candida* ssp. growth[40].

Additionally, aurones have been studied as anti-virals[25,26]. Haudecoeur *et al*. found that certain naturally occurring aurones, including aureusidin, inhibited the NS5B RNA-dependent RNA-polymerase (RdRp) of the hepatitis C virus with a half-maximal inhibitory concentrations (IC_{50}) in the low micromolar range[41]. Later, the same group found that changing the side chain of aureusidin to indoles with various modifications increased the efficacy of aurones, some having an IC_{50} in the single digit micromolar range[42]. Another group demonstrated that aurones decreased the cytopathic effect of the influenza A (H1N1) virus on a monolayer of Madin-Darby canine kidney cells, which they predicted, using computational analyses, could potentially displace sialic acid from neuraminidase (NA), the glycoprotein responsible for cleaving sialic acid on cell surface receptors allowing for the release of mature virions[43,44]. This was supported by Chintakrindi *et al.*, who showed that some methoxy-aurones reduced H1N1 titer and interfered with enzymatic activity of H1N1 NA[45].

1.4 Current Need for Anti-inflammatories

Inflammation is partially due to the response of the innate immune system, the first line of defense activated due to the presence of pathogens. The cells of the innate immune system, including macrophages, become activated releasing pro-inflammatory cytokines, chemokines, reactive oxygen species (ROS), and reactive nitrogen species (RNS), such as nitric oxide (NO), and various prostaglandins[46-50]. Though a normal inflammatory response is necessary for the function of the innate immune system, dysregulation of this response can lead to chronic inflammatory diseases (CIDs), such as rheumatoid arthritis (RA) and inflammatory bowel

diseases (IBD)[51,52]. Currently there are many commercially available anti-inflammatories, including corticosteroids and non-steroidal anti-inflammatory drugs (NSAIDs). Commercial corticosteroids, most often glucocorticoids, are hormonal steroids, known for their anti-inflammatory activity used in the treatment of CIDs and other acute inflammatory responses[53]. Glucocorticoids exhibit anti-inflammatory activity through binding to the glucocorticoid receptor which then translocate to the nucleus[54]. Activated glucocorticoid receptors have been shown to directly interact with the p65 subunit of the transcription factor nuclear factor-kappa light chain enhancer of activated B-cells (NF-κB), reducing the duration of its nuclear occupancy[53-59]. Unfortunately, prolonged use of corticosteroids can lead to skin atrophy and decreased wound healing, eye problems such as glaucoma and cataracts, diabetes mellitus, Cushing's syndrome, hypertension, increased risk of infection including the reactivation of latent viruses, gastrointestinal bleeding, peptic ulcers, pancreatitis, and other severe side effects[60].

NSAIDs, such as ibuprofen, naproxen, and aspirin, act as anti-inflammatories through a different mechanism of action than that of corticosteroid drugs[61]. NSAIDs typically act through inhibition of prostaglandin synthesis by the enzymes cyclooxygenase 1 (COX-1) and cyclooxygenase 2 (COX-2)[61]. Upon inflammatory stimuli, COX-2 is upregulated leading to increased synthesis of prostaglandins through oxidation of arachidonic acid[50,62,63]. Though COX proteins and low levels of prostaglandins are necessary for homeostasis, high levels of prostaglandins, including prostaglandin E_2 (PGE_2), can lead to acute inflammation through interaction with prostaglandin receptors[64-68]. NSAIDS are also linked to side effects, such as ulceration in the gastrointestinal (GI) tract, cardiovascular disease, renal injury, hepatoxicity,

intracerebral hemorrhage, and increased infection and inflammation of the respiratory tract[69]. NSAIDs indiscriminately target both COX enzymes and inhibition of COX-1 was thought to be the cause of their ulcerative affects[70]. However, selective COX-2 inhibitors also have similar side effects[69]. Due to the adverse side effects of current anti-inflammatory drugs, there is a need for new anti-inflammatory compounds, that do not cause these pathologies.

1.5 Aurones as Promising Anti-inflammatory Compounds

Due to this need, preliminary studies are underway to determine the anti-inflammatory activities of synthetic aurones. In 2010, Bandgar *et al.* found that in PMA differentiated human monocytes (THP-1 cells) all six studied 2,2-bisaminomethylated aurones decreased tumor necrosis factor-α (TNF-α) and interleukin (IL)-6 expression 24 h post-treatment with 1 μg/mL lipopolysaccharide (LPS)[37] a well-known inducer of an inflammatory response in differentiated monocytes and in macrophages. Out of those six aurones only one showed promise as an anti-inflammatory, inhibiting the secretion of the pro-inflammatory cytokines TNF-α and IL-6 by 76% and 97%, respectively, with 29% cytotoxicity[37]. Two others, with 21% and 37% cytotoxicity, were shown to decrease secreted IL-6 by 82% and 74%, but had less of an effect on the levels on secreted TNF-α (35% and 28%, respectively)[37]. A later study by Moon *et al.* showed that the naturally occurring aurone, sulfuretin, was a causative agent for the anti-inflammatory effects seen in *Rhus verniciflua* stoke extracts along with a couple of other flavonoids[71]. In this report, 250 ng/mL sulfuretin was able to decrease IL-6 and ROS production in LPS-stimulated RAW 264.7 murine macrophage-like cells[71]. However, sulfuretin did not diminish PGE_2 production nor reduce levels of nitrite, indicating some limit to its anti-inflammatory effect[71]. In 2017, Park *et al.* was able to demonstrate that a synthetic

aurone (aurone 1), with a 2-(5-hydroxymethylfuryl) side chain (R group; Figure 1, blue colored), was able to decrease multiple markers of inflammation in both LPS-stimulated PMA-differentiated THP-1 cells as well as in LPS-stimulated RAW 264.7 macrophage-like cells[72]. This aurone was shown to restrict LPS-induced secretion of the pro-inflammatory cytokines TNF-α, IL-1β, and IL-8 and was able to restrict *Tnf* expression at the RNA level by reducing nuclear accumulation of the transcription factor p65 (RelA), a member of the NF-κB family, and part of the p65/p50 heterodimer involved in the canonical NF-κB pathway[72,73]. The anti-inflammatory activity of aurone 1 was most likely due to its inhibition of inhibitor of κB kinase β (IKKβ)[72]. Another group in the same year described multiple synthetic dihydropyranoaurones that reduced both levels of inducible nitric oxide synthase (iNOS) and nitrite production in LPS-stimulated RAW 264.7 cells[74]. In 2021, it was shown that two naturally occurring aurones isolated from *Coreopsis lanceolata* L. flowers were able to reduce levels of nitrite, TNF-α, IL-1β, and IL-6 in RAW 264.7 cells at a concentration of 100 μM[75]. However, when examining levels of iNOS they found that though both aurones reduced levels of iNOS, aurone F1, which has a methoxy group on carbon 7, lowered iNOS levels far more than aurone F2, which has both a methoxy group on carbon 7and a glucose monomer at carbon 6 (Figure 1)[75]. This was reflected in levels of COX-2 where aurone F2 had no affect[75]. These studies indicate the potential of modified synthetic aurones for modulation of the innate immune system, potentially attenuating an overly stimulated inflammatory response.

1.6 Fluorescent Properties and Uses of Aurones

In addition to their biological activities, aurones have been gaining popularity as a backbone for fluorophores due to their visible range excitation and emissions spectra, small size, large Stokes shift, and modifiable properties[24,76-78]. In 2007, in one of the earliest studies utilizing this application, while staining β-amyloid plaques, an aurone was able to be imaged using fluorescence microscopy with an excitation filter set of 485 nm and an emission of 540-580 nm[79]. In 2011, Shanker *et al*. described the use of amine-substituted aurones (aminoaurones) as fluorescent probes[76]. While the aminoaurones had greater fluorescent intensities in less polar-protic solvents such as dioxane (E_T30 [Molar electronic transition energies of pyridium N-phenolate betaine dye 36 – a measure of relative polarity[80]]: 36.0) compared to more polar-protic solvents such as methanol (E_T30: 55.5) and water (E_T30: 63.1) the Stokes shift was greater in polar-protic solvents[76]. This is supported by the work of Espinosa-Bustos *et al.* observing aurones to have increased fluorescence in less polar solvents and larger Stokes shifts in more polar solvents[77], indicating that having a methoxy group on the 4 position of the benzofuranone subunit was largely responsible for an observed red-shift in emissions[77]. This was further supported by the work of Muñoz-Becerra *et al*., computationally showing that the presence of a polar substitution at the same position caused an observed red-shift in absorbance and emission spectra and an increased Stokes shift[81]. Due to these fluorescent properties, aurones have been gaining use as fluorescent sensors. For example, Chen *et al.* in 2013 synthesized three 4-hydroxy aurones that would have modulated absorbance and fluorescence spectra upon hydrogen bonding with cyanide, thereby acting as a probe[82]. Chen *et al.* in 2014 developed two aurone based cyanide sensors (compounds 1 and

2) both having a dipyridylamine substitution at the 4' carbon, where compound 2 varied from compound 1 by a methoxy group at carbon 6 (Figure 1)[83]. To act as sensors, the fluorescence emissions of compounds 1 and 2 are quenched through interactions with Cu^{2+} ions[83]. When in the presence of cyanide ions the copper disassociates from compounds 1 and 2, allowing for resumed fluorescence[83]. Xu *et al.* in 2016 also utilized a similar 4'-dipyridylamine aurone with an additional dipyridylamine group at carbon 5 (Figure 1) as a chemical sensor for cyanide using copper as before[83,84]. Zhang *et al.* showed that an aurone with a hydroxyl group on carbon 6 (Figure 1) could be used as a specific sensor for mercury[85]. In 2020, Kafle *et al.* used a 4'-azidoaurone with a fluorine substitution at carbon 6 (Figure 1) as a sensor for hydrogen sulfide[86]. Though aurone bioavailability has been shown in a variety of studies, fluorescence is typically quenched in more aqueous environments[76,77,87]. Kafle *et al*. was able to circumvent this by incorporating the detergent hexadecyltrimethylammonium bromide (CTAB)[86]. Most recently, aurones have shown promise as dual-state fluorophores that are fluorescent both in solution and as a solid, allowing for broader applications[88,89].

1.7 Bioactivities of 1,2,3-triazole Containing Compounds

Azoles are defined as a heterocyclic five-membered ring containing a number of nitrogen atoms[90]. Multiple azoles exist and are readily studied as potential pharmacological agents[90]. Of the azoles, those containing three nitrogen atoms, known as the triazoles and more specifically triazoles where the three nitrogens are at locations 1,2, and 3 of the heterocyclic ring (1,2,3-triazoles; Figure 1; purple), have been consistently examined for their potential as therapeutics[90-93]. The 1,2,3-triazole moiety can be easily added as an augmentation of existing compounds using a Cu (I)- catalyzed Huisgen 1,3-dipolar azide-alkyne cycloaddition

(CuAAC), a type of "click" chemistry, and can additionally be used as a linker while also having the potential to interact biologically[94]. 1,2,3-triazole containing compounds (TCCs) gained popularity for their anticancer effects, which have been extensively explored[90,91], potentially due to their low effective concentrations[95-99] and potency against cancerous cell lines[95,96,100-102]. TCCs have also been thoroughly examined for their role as anti-microbial compounds[90,94] showing promise as antibacterial[96,103-111], antifungal[96,103,106-109,111], anti-protozoan[103,112-115], and antiviral agents[103,116-120]. One TCC was shown to have a half maximal effective concentration (EC_{50}) of 1.163 nM against the hepatitis C virus[119], while others had an EC_{50} the nM range against various HIV strains[121]. Additionally, there are commercially available anti-microbials containing the 1,2,3-triazole moiety[122] such as Radezolid[123], Cefatrizine[124], and Tazobactam (usually used in conjunction with Piperacillin)[125].

1.8 Anti-inflammatory Effects of 1,2,3-triazole Containing Compounds

TCCs have also been studied as potential anti-inflammatories[90,92,93]. In 2009, Wuest *et al.* described the COX-2 inhibitory activity of some TCCs[126]. Several of the TCCs screened were able to inhibit COX-2 in the nanomolar range[126]. However, when examined for selective inhibition of COX-2 vs. COX-1, a constitutively expressed enzyme[127] with similar functions to COX-2, that is thought to be responsible for homeostasis of some prostaglandins[128], they found that only one, 10a, was relatively selective for COX-2 over COX-1 with IC_{50} of 150 nM and 20.8 μM, respectively[126]. Moussa *et al.* in 2018 found similar COX-2 and 5-LOX inhibitory activity in 1,2,3-triazole containing quinazolinone derivatives[129]. The same study was also able to show that some TCCs were able to reduce phorbol 12-myristate 13-acetate (PMA) induced differentiation of THP-1 human monocytes into macrophages after 24 h[129],

however, toxicity of the compounds were not determined. Some compounds did not exhibit ulcerative activity demonstrating potential as anti-inflammatory compounds, supported by *in silico* analyses which revealed promising levels of bioavailability and drug-likeness[129]. A study by Zhang *et al*. in 2019 showed that triazole derivatives of baicalein, a naturally occurring compound with anti-inflammatory activities, was able to reduce respiratory syncytial virus (RSV) induced expression of IL-6, IL-8, NO, COX-2, as well as inflammation induced inhibitor of κB-α (IκBα) degradation, potentially through modulation of multiple inflammatory pathways[130].

TCCs have also been shown to reduce the inflammatory response *in vivo.* The study by Zhang *et al.* (2019), in addition to the aforementioned effects on RSV-induced cytokines, was able to return *in vivo* RSV-induced mRNA of IκBα, COX-2, and type one interferons (IFN; IFN-α/β1) at concentration of 1 mg/kg and return to uninfected levels at 2 mg/kg[130]. A 2015 study by Kim *et al.* demonstrated that phenyl-1*H*-1,2,3-triazole derivatives were able to decrease xylene-induced ear edema in mice[131], while a 2022 study by Hammouda *et al.* showed that TCCs can reduce carrageenan-induced ear edema[122]. One phenyl-1H-1,2,3-triazole derivative (named 2c), was able to *increase* levels of COX-2 in response to TNF-α[131]. They claimed that inhibition of COX-2 leads to an increase in NF-κB activity, which in turn increased COX-2, due to an inhibition of the negative feedback mechanism, thus 2c is anti-inflammatory by inhibiting COX-2 activity rather than decreasing its expression levels[131]. In 2016, Angajala *et al.* described the anti-inflammatory and bactericidal effects of ibuprofen-derived TCCs[132], and found that these compounds reduced carrageenan induced edema in the paws of mice from 3-6 hours post-injection, where three 1-(2-hydroxy-4-(prop-2-yn-1-

yloxy)phenyl)-2-(4-isobutylphenyl)-propan-1-one with 1,4-disubstituted 1,2,3-triazoles with different side chains (R-groups), 13g (4-chloro phenyl R-group), 13l (4-nitrophenyl R-group), and 13o (4-nitrobenzyl R-group), had similar reductive effects to ibuprofen[132]. Molecular modeling revealed that the anti-inflammatory activity of 13o and 13l may be most likely due to effective binding of COX-2[132]. Others found that TCCs were able to reduce Carrageenan-induced edema in the paws of rats after four hours, though they were less potent than ibuprofen at lower doses[133]. Another study found that certain TCCs were able to reduce carrageenan induced paw edema and moderate selective COX-2 inhibition with little to no ulcerative side-effects[134]. One TCC showed effect as a potential anti-proliferative as well, reducing activity of 5-lipoxygenase (5-LOX) activity and tubulin polymerization[134]. These studies together indicate that certain compounds containing a 1,2,3-triazole moiety can act as potent inhibitors of various types of inflammation, both *in vitro* and *in vivo*.

1.9 Fluorescent Properties of 1,2,3-triazoles

In addition to their bioactive effects, TCCs have also been examined for photophysical properties. In 2011, Shi and associates developed *N-2*-aryl-1,2,3-triazole derivatives (NATs) as novel, customizable, blue-light emitting fluorophores whose emissions spectra and photophysical characteristics, such as Stokes shift, could be adjusted based on addition of various sidechains[135]. In 2015, the same group described the fluorescent properties and customizable nature of a new set of TCCs, naphthalene-bridged bis-triazoles[136]. Zhang *et al*. expanded on this concept by developing a class of *N-2*-indolyl-1,2,3-triazoles (NITs) similar in structure to the NATs differing by the presence of an indolyl instead of an aryl which had emission maxima ranging from 345-423 nm with relatively large Stokes shifts from 53-125

nm[137]. For reference, the Stokes shift for various Alexa Fluor dyes are typically less than 30 nm according to their manufacturers[138]. In 2013, Huang *et al.* described two triazole containing rhenium complexes, one with a pyridine-triazole moiety and one with a quinoline-triazole moiety, designated 1^+ and 2^+, respectively, due to the replacement of a bromine ligand with H_2O from the solvent that were shown to have fluorescent properties[139]. Both 1^+ and 2^+ were shown to have relatively large Stokes shifts in 5% (v/v) DMSO in PBS of 185 nm and 261 nm while both had peak excitation of 333 nm and 345 nm with a broad emissions spectra centered at 528 nm and 606 nm, respectively[139]. These compounds were synthesized using a CuAAC "click" chemistry reaction to link a triazole moiety to existing compounds[139]. The popularity and ease of "click" chemistry has led to the development of multiple triazole based fluorophores. For example, Szafrański *et al*. synthesized a reverse transcriptase inhibitor-derived 1,2,3-triazole that had fluorescent properties[140], while Ngororabanga *et al.* described multiple fluorescent coumarin-based triazoles[141]. Meisner and associates used "click" reactions to synthesize two triazole-based fluorophores with large Stokes shifts whose excitation and emissions spectra would red or blue shift upon deprotonation depending on the placement of an electron-donating hydroxyphenyl group[142]. "Click"-synthesized TCCs were also reported as fluorescent molecules with large Stokes shifts by Ghasemi *et al*. with fluorescent maximal emissions in the blue light region[143]. Reddivari *et al*. reported using copper (I) catalyzed "click"-reactions with polyethelene-glycol and water in ultrasonic conditions to synthesize a series of TCCs with anti-oxidant and anti-RNS activity with distinct fluorescent capabilities[144]. These TCCs similarly had peak excitation and emissions at higher wavelengths (366-398 nm and 414-450 nm) with much shorter Stokes shifts ranging from 40-79 nm[144]. Another group

synthesized multiple TCCs, which had large Stokes shifts and emissions in the 488 – 556 nm range with minimal cytotoxicity, was fluorescent in aqueous solutions, and could be used to label proteins[145].

TCCs have been shown to be effective probes. Ghosh *et al*. also described a diaryl triazole phenol which was utilized as a fluorescent probe for fluoride anions[146]. Upon edition of fluoride, as opposed to other anions such as bromide, chloride, and iodide, there was a red-shift in both absorbance and emission spectra[146]. Emission intensities increased upon increased concentrations of fluoride anions[146]. The observed red shifts were not exclusive to fluoride however, as they were detected for both dihydrogen phosphate and acetate[146]. Lai *et al*. developed a sensor that would quench in the presence of silver ions, unlike the aforementioned work of Ghosh *et al*.[146,147]. Another group developed TCCs that were able to detect the presence of bovine serum albumin (BSA) in acetonitrile where the presence of protein effectively increased the compound's fluorescent intensity[148]. Interestingly, the presence of the monosaccharide arabinose caused a small but dose-dependent increase in fluorescent intensity of the compounds, with a stronger effect observed for D-(-)-arabinose as opposed to L-(+)-arabinose primarily due to the stronger hydrogen bonding of L-(+)-arabinose and the fluorophore[148]. In 2020 one group developed 1,2,3-triazole containing probes which was used to detect mercury both in a cuvette and in HeLa cells with great specificity[149,150]. Indeed TCCs have been identified as fluorescent molecules which can be used for sensing metals and other ions[146,147,149-154], amino acids[148], toxins[153], and monosaccharides[148].

1.10 Uses of Flavonoid-derived 1,2,3-triazoles

Recently, there has been a rise in interest regarding modification of existing flavonoid systems with 1,2,3-triazoles (flavonoid-derived 1,2,3-triazoles; FTs) synthesized mostly using "click" chemistry[155]. Though most research focuses on their synthesis, these studies found that FTs had some anti-cancer[156-174], anti-oxidant[173-179], anti-bacterial/anti-fungal[175-177,180-185], and anti-viral properties[130,186], as well as other bioactivities similar to those of both flavonoid derivatives and TCCs[155]. However, one study by Bhowmik *et al.*, showed that the addition of the 1,2,3-triazole moiety to Chrysin, a flavone, in some cases reduced its anti-biofilm activity, while other derivatives lacking a 1,2,3-triazole group tended to have increased activity[187]. FTs have even shown potential as fluorophores[173] and as optical probes for mercury and tin[188].

In addition to other bioactivities, FTs have also been explored for the potential to reduce an inflammatory response. In 2020, Boshra *et al*. described a group of 1,2,3-triazole-hydroxychalcone hybrids that showed selective inhibition of COX-2 versus COX-1, inhibition of LOX-1, and reduced carrageenan-induced paw edema in rats[189]. Menghereş *et al*. synthesized a set of 1,2,3-triazole linked isoflavone benzodiazepine hybrids that were able to decrease the amount of NO produced by cells in response to stimulation with LPS[190]. However, as these compounds were relatively cytotoxic at concentrations of 20 μM, it is difficult to claim the reduction in NO was due to anti-inflammatory activity rather than cell death prior to its synthesis[190]. Most recently, Zheng *et al*. showed that a large group of 1,2,3-triazole hesperetin (a flavanone) derivatives reduced LPS induced production of NO and pro-inflammatory cytokines, TNF-α, IL-6, and IL-1β, in RAW264.7 cells at low micromolar concentrations with minimal impact on cell viability[191]. One compound, d5, was able to reduce levels of iNOS and

COX-2, potentially through interruption of LPS-activated NF-κB signaling[191]. This compound also had effects *in vivo* decreasing signs of acute C-C Motif Chemokine Ligand (CCL) 4-induced liver injury in mice including serum levels of TNF-α, IL-6, and IL-1β[191].

1.11 Aurone-derived 1,2,3-triazoles

Despite this interest there are relatively few studies focusing on *aurone-derived 1,2,3-triazoles* (ATs). In 2022, Saroha *et al.* developed 1,2,3-triazole-aurone hybrids using "click" chemistry[192]. These hybrids were found to be moderate inhibitors of human gastric adenocarcinoma (AGS) cell proliferation with IC_{50} values as low as 11 μM[192]. Molecular docking experiments revealed that these compounds have the potential to be potent inhibitors of cathepsin B, a multifunctional peptidase sometimes associated with inflammation and metastasis, causing predicted inhibition upwards of 87.16%, much higher than that of aspirin and curcumin[192]. The same group also synthesized another set of 1,2,3-triazole-aurone hybrids using microwave catalyzed-"click" chemistry, which inhibited cathepsin B activity up to 85% at concentrations of 1 μM[193]. The same compounds were able to prevent AGS cell proliferation with IC_{50} concentrations as low as 24 μM[193]. The compound with the highest degree of cathepsin B inhibition, 3p, had an IC_{50} value of 41 μM, while the compounds with the lowest IC_{50} values, 3d and 3i, only caused 42.14 % and 61.13 % inhibition, respectively[193]. While these reports represent the first analyses of ATs synthesized using "click" chemistry, another group was able to synthesize a whole new class of AT, using sodium azide and an existing aurone system, where instead of the 1,2,3-triazole group being linked as a side-chain on the benzofuranone core, it was incorporated into the backbone itself, providing an uninvestigated scaffold, which can be easily modified, for potential numerous bioactivities[194].

1.12 Research Aims

Though there are many bioactivities that can be explored with these novel ATs, the primary goal of this dissertation is to explore their potential as both anti-inflammatories and as fluorescence molecules. Novel ATs, some described in "An Unusual Triazole Synthesis from Aurones" from Kafle *et al*. in 2020[194] and some unpublished, are utilized as the key molecules in the exploration. The first aim of this dissertation is to explore the fluorescence application and photophysical properties of representatives of these ATs, which is explored in Chapter II and III. The second aim focuses on the anti-inflammatory potential of representative ATs. The goal of this aim is to determine if this scaffold has the potential to be modified into anti-inflammatory molecules. The effect of these ATs on the production of anti-inflammatory markers and their potential mechanisms is discussed in Chapter III.

CHAPTER II

Aurone-derived 1,2,3-triazoles as potential fluorescence molecules *in vitro*

By Daniel L. Bryant, Arjun Kafle, Scott T. Handy, Anthony L Farone, and Justin M. Miller

Reproduced from Bryant *et al*. 2022[1] with permission from the Royal Society of Chemistry.

Published in RSC Advances

August 2022

DOI: 10.1039/d2ra02578g

Formatted and modified for dissertation.

Graphical abstract, additional information, and complete Table 1 are in Appendix I

2.1 Abstract

Aurones are a class of well-studied natural compounds primarily responsible for the yellow pigment in flowering plants and have been shown to have fluorescent properties as well as beneficial biological effects. Traditionally, aurones can be easily synthesized through a Knoevenagel condensation of benzofuranones with arylaldehydes. Recently, Kafle et al. unexpectedly synthesized a new aurone derivative containing a 1,2,3-triazole within its backbone. Since, 1,2,3-triazole containing structures have been shown to be useful as fluorophores with large Stokes shifts, we hypothesized that these new aurone-derived triazole compounds (Ats) could be utilized as potential fluorophores. Here we describe a newly-synthesized fluorescent compound which has potential for use as a live-cell probe, having a large Stokes shift of 118.3 ±1.01 nm in phosphate-buffered saline with the benefit of increased fluorescence in protic environments, which is uncommon in aurone-derived fluorophores.

2.2 Introduction

Aurones (2-Benzylidene-1-benzofuran-3(2H)-one) are a class of naturally occurring flavonoid derivatives responsible for the pigments in some flowering plants, such as the yellow rocket snapdragon[27]. There has been a recent increase in the study of aurones due to their bioactivities[26]; including anti-inflammatory[37,72,195,196], anti-microbial[37,39,197], and anticancer[32,198,199] properties. In addition, there has been an interest in aurones as fluorescent markers due to their visible range excitation and emission spectra, tunable fluorescence properties, and their potential bioavailability[76-78]. Most notably, in 2011, Shanker and Dilek described four different aurones with a 4' amine substitution on the benzylidene group (aminoaurones)[76]. These aurones had increased Stokes shifts in more polar-protic solvents[76].

Two of the aminoaurones were shown to have increased emissions intensities in nonpolar solvents[76]. Other studies, both computational and experimental, have determined that the fluorescence spectra and Stokes shift of aurones are also dependent on side chain and solvent polarity[77,78]. For example, Espinosa-Bustos *et al.* observed increased emissions intensities in less polar solvents and that location of the sidechains on the benzylidene group of the aurone modulated the absorbance and emissions spectra, which supported the observations by Shanker and Dilek[76,77]. Xue *et al.* computationally examined the aurones presented by Shanker and Dilek, and found that the increased Stokes shifts and red-shifted emissions were due primarily to intramolecular charge transfer[78]. Muñoz-Becerra *et al.* in 2019 described computationally how the addition of a polar side chain on the 4 carbon of the benzofuranone backbone led to an Increased Stokes shifts as well as red-shifted absorbance and emissions spectra[81].

Aurones have also been examined for potential as fluorescent sensors. Starting in 2013, Chen and associates synthesized multiple aurone-based sensors for cyanide[82-84]. In 2018, Zhang *et al.* described a membrane permeable aurone based sensor for Hg^{2+} [85]. Most recently, Kafle *et al.* in 2020 developed an aurone-derived sensor for hydrogen sulfide[86]. Though the potential for aurones as bioavailable fluorescent molecules has been reported, aurones traditionally only fluoresce in non-polar solvents and are quenched in aqueous environments[76,77,86]. Kafle *et al.* were able to bypass the quenching effect of aqueous environments through the use of hexadecyltrimethylammonium bromide (CTAB)[86].

Finding new methods of aurone synthesis has been an area of active research for many years. Two common methods of aurone synthesis were described by Geissman and Harborne in 1955 where they used a condensation reaction between a coumaranone and various

aldehydes[200], and by Varma and Varma in 1992 in which they used an alumina catalyzed reaction of benzofuranones with arylaldehydes[201]. Alternatively, others have utilized palladium and formic acid[202], silver nitrate[203], gold[204], or choline chloride and urea[205] in various condensation and cyclization approaches to the aurone skeleton. In the course of an effort to install an azido group on an intact aurone system, Kafle *et al.* noted instead the synthesis of a new class of aurone-derived salicyl substituted 1,2,3-triazole (AT) (Figure 1)[194].

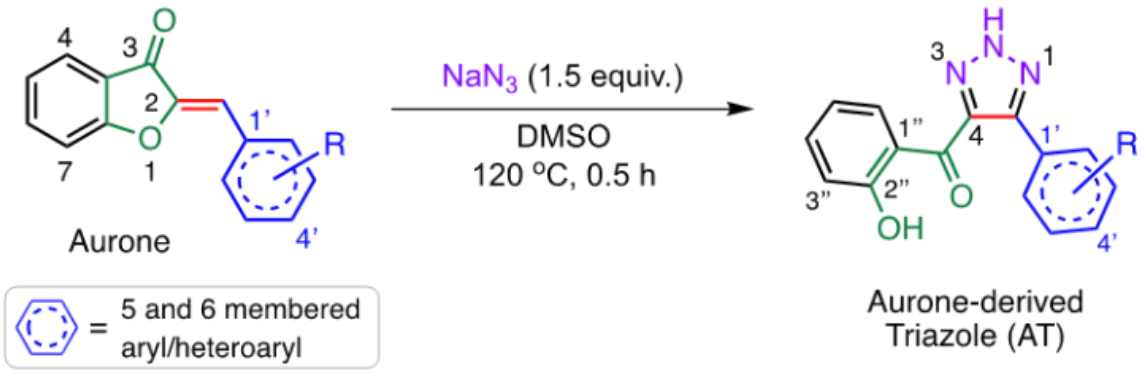

Figure 1. Synthesis of aurone-derived triazoles

1,2,3-triazoles have also been shown to possess fluorescent properties[137,142,146]. In 2015, Ghosh *et al*. described a "click" synthesized 1,2,3-triazole which showed fluorescence in the presence of a fluoride ion[146]. In 2018, Meisner *et al.* established that 1,2,3-triazole containing compounds have larger Stokes shifts with their fluorescent properties affected by the triazole substitution and the ability to form intramolecular hydrogen bonds[142]. Unlike the other 1,2,3-

triazoles, the aurone-derived ATs incorporate a salicylic group substituted at C4 on the triazole ring (Figure 1). With this in mind, it was thought that ATs would have potential as fluorescent compounds. It was hypothesized that 1,2,3-triazoles derived from aurones would have fluorescent properties similar to both triazoles and aurones. Here, we describe ATs with increased fluorescence in polar protic aqueous environments, allowing for increased fluorescence in cellular environments with marked potential as a biologically relevant fluorescent probe.

2.3 Materials and methods

All the reactions and handling of the chemicals were done under an air atmosphere using ACS-grade reagents. Organic solvents were directly employed without further purification. ^{1}H and ^{13}C NMR of all the compounds were recorded on JEOL AS (500 and 125 MHz, respectively), using $CDCl_3$, DMSO-D_6, or acetone-D_6 as a standard reference (Appendix I; Figure S1).[206] Chemical shifts and the coupling constants (J) for ^{1}H and ^{13}C NMR are reported in parts per million (ppm) and in hertz (Hz), respectively. The following conventions are used for multiplicities: s, singlet; d, doublet; t, triplet; m, multiplet; dd, doublet of doublet; tt, triplet of triplet; dt, doublet of triplet; ddd, doublet of doublets of doublets; br, broad. All high-resolution mass spectra were acquired on a Waters Synapt HDMS qToF with Ion Mobility. Reactions were monitored by Thin Layer Chromatography (TLC) on silica-coated plates using short-wavelength (254 nm) UV light. All extracts were concentrated under reduced pressure using Buchi Rotary Evaporator. The compounds were purified by flash silica gel (32-64 μ) column chromatography.

General procedure for the synthesis of aurone-derived triazoles (AT1-AT5)

The aurones and the corresponding triazoles, **AT1-AT5** (structures in Appendix I; Figure S2) were synthesized and characterized based on the literature.[194,200] The characterization data for **AT2** and **AT5** are provided below. Following preparation of the aurone[200], 0.50 mmol of aurone was mixed with 0.75 mmol (1.5 equiv.) of sodium azide (NaN_3) using 1.5 mL DMSO in a 3-dram glass vial and heated at 120 °C for 30 min (unless otherwise specified) in a sand bath. The progress of the reaction was monitored by TLC. After the completion of the reaction, the reaction mixture was cooled to room temperature and transferred to a 50 mL centrifuge tube. It was then diluted with DI water and extracted several times with ethyl acetate (150 mL). Next, the obtained organic fraction was washed with DI water followed by brine. Finally, the organic fraction was dried over anhydrous $MgSO_4$ and concentrated *in vacuo* to obtain the crude product, which was purified by flash column chromatography using mixtures of hexane and ethyl acetate (20-50 % EtOAc/ hexane) to afford the desired triazole.

(5-(5'-bromothiophen-2'-yl)-2H-1,2,3-triazol-4-yl)(2"-hydroxyphenyl)methanone (AT2). Reaction scale: 0.325 mmol (99.8 mg); purified by column chromatography (20 % EtOAc/hexane); yield: 31.6 % (36 mg); orange solid, mp: 159.5-162 °C; ^{1}H NMR (500 MHz, Chloroform-D_6) δ 12.04 (s, 1H), 11.82 (s, 1H), 8.21 (dd, J = 8.1, 1.4 Hz, 1H), 7.61 (d, J = 3.9 Hz 1H), 7.59 – 7.51 (m, 1H), 7.11 – 7.04 (m, 2H), 6.94 (t, J = 7.7 Hz, 1H). ^{13}C NMR (125 MHz, Chloroform-D_6) δ 191.3, 163.9, 137.4, 133.7, 130.7, 129.7, 119.5, 119.3, 118.58, 115.9, 110.5, 109.9. IR (neat) 3177, 2954, 1721, 1628, 1603, 1482, 1257, 909, 747 cm^{-1}. HRMS: calcd for $C_{13}H_8BrN_3O_2S$ 348.9520, observed 348.9518

(5-(4'-Acetamidophenyl)-2H-1,2,3-triazol-4-yl)(2"-hydroxyphenyl)methanone (AT5). Reaction scale: 0.716 mmol (200 mg); reaction time= 2 h; purified by column chromatography (70 % EtOAc/hexane); yield: 40 % (92 mg); yellow solid, mp = 216-220 °C. ^{1}H NMR (300 MHz, DMSO-D_6) δ 11.07 (s, 1H), 10.13 (s, 1H), 7.89 – 7.82 (m, 1H (br), 7.68 (s, 4H), 7.50 (t, *J* = 7.7 Hz, 1H), 6.98-6.91 (m, 2H), 2.07 (s, 3H). ^{13}C NMR (125 MHz, DMSO-D_6) δ 190.9, 168.5, 159.9, 140.2, 135.2, 132.2, 128.9, 122.7, 118.9, 118.6, 117.2, 24.0. IR (neat) 3330, 1655, 1581, 1462, 1317, 1251, 1158, 989, 922, 750 cm^{-1}. HRMS: calcd for $C_{17}H_{14}N_4O_3$ 322.1069, observed 322.1973.

General protocols

All ATs were reconstituted from a purified powder at 100 mM in 100 % dimethyl sulfoxide (DMSO; Fisher Scientific, MA; Cat#: D128-500/ MP Biomedicals; Cat#: 196055). In all experiments the ATs were diluted to 100 μM in the indicated solution with 0.1 % (v/v) DMSO as a cosolvent. To account for DMSO as a cosolvent, all experiments were carried out with 0.1 % (v/v) DMSO as a vehicle control. For experiments measuring fluorescence spectra, the absorbance and emissions of the vehicle control were subtracted as a background.

Cell culture

RAW 264.7 murine macrophage-like cells (ATCC Cat#: TIB-71) and HeLa cells (ATCC Cat#: CCL-2) were cultured in either Dulbecco's modification of Eagle's Medium (DMEM; Corning, NY; Cat#: 10-013-CV) or Roswell Park Memorial Institute 1640 medium (RPMI; Fisher Scientific, MA; Cat#: 11875093), respectively. Both media were supplemented with 10 % heat-inactivated fetal bovine serum and 100 Units/mL penicillin/ streptomycin cocktail (Fisher Scientific, MA; Cat#: 15-140-122). The cells were grown in a humidified

incubator at 37°C with 5 % CO_2 and passaged prior to reaching 90 % confluency every 3-5 days. All cell culture experiments were incubated in this manner unless otherwise stated.

Cytotoxicity assay

Cytotoxicity of each AT was determined using the PrestoBlue cell viability assay (Invitrogen, CA; Cat# A13262). RAW 264.7 cells, or HeLa cells, were seeded at a density of 5 x 10^4 cells/well, or 1 X 10^4 cells/well, respectively, in a sterile 96-well plate and allowed to attach overnight. The cells were washed with 1X phosphate-buffered saline (PBS; Gibco – ThermoFisher Scientific, MA; Cat#: 10010-023), then treated with 100 μM of each AT, or 0.1 % (v/v) DMSO as a vehicle control, for 24 h. Immediately following the treatment, the cells were washed with PBS, and medium containing 1X PrestoBlue was added to the cells for one hour. The absorbance at 570 nm was recorded, and the absorbance at 600 nm was subtracted according to the manufacturer's protocol. The data is presented as a percentage to the average absorbance of the untreated wells for each plate ± SD.

Confocal microscopy

Live cell imaging: RAW 264.7 cells or HeLa cells were seeded at 1 X 10^6 cells/well and 6 x 10^5 cells/well, respectively in 35 mm culture dishes with a glass coverslip inlay c and allowed to attach overnight. The cells were washed 16-18 h post seeding and treated with 100 μM of the indicated AT for an additional 24 h. The cells were imaged post 24 h on a Zeiss LSM 700 confocal microscope. In experiments comparing the different fluorescent properties of each, the ATs were excited with a 405 nm and 555 nm lasers (gain = 650; pinhole 0.92 AU) simultaneously, with detection wavelengths of 300-483 nm and 560-800 nm, respectively, then excited with a 455 nm laser (gain = 650; pinhole = 0.9 AU) with a detection wavelength of

300-598 nm. For experiments where **AT5** was imaged alone, it was excited with a 405 nm laser (gain = 650) with a detection wavelength of 300-598 nm. For time-course experiments, RAW 264.7 cells were washed with PBS 16 h post seeding and 1 mL of medium was added. Cells were then transferred to a Zeiss LSM 700 confocal microscope with a 37 °C, 5 % CO_2 life support chamber for at least 30 min prior to imaging. The cells were treated with 1 mL of 200 μM **AT5** for a final concentration of 100 μM, and immediately imaged. The cells were then imaged immediately as well as every 15 min post treatment for 23 h and 45 min using a 405 nm laser (gain = 600; pinhole = 1.05 AU) with a detection wavelength of 300-584 nm. The cells analyzed were chosen due to survival and tracking until the end of the experiment. Brightness of each image was increased equally in each figure post analysis for clarity.

Fixed cell imaging: RAW 264.7 cells were seeded as described. 16 – 24 h later the cells were washed with PBS and fixed in 1 mL of 4.0 % (v/v) formaldehyde (Fisher Scientific, MA; Cat#: F75P-4) for 10 min. The cells were washed, and the membranes of the cells were permeabilized with 1 mL of 0.1 % (v/v) Triton X-100 (Sigma Aldrich, MO; Cat#: T8787) in PBS for 5 min. Excess Triton was removed, and the cells were then stained with 500 μM **AT5** or 0.5 % (v/v) DMSO as a vehicle control for 30 min. The cells were then washed two more times with PBS to remove excess **AT5** and imaged on the Zeiss LSM 700 confocal microscope using a 405 nm laser (gain 650; pinhole = 1.27 AU) with a detection wavelength of 300-584 nm. The raw fluorescence intensity of each cell was determined by measuring the intensity of the signal in the .CZI file using FIJI[207]. The data is presented as a background corrected mean signal intensity for unit area (pixel) of each cell.

Absorbance and emissions microplate procedure

Absorbance and emissions spectra for **AT5** at varying concentrations were determined by mixing 400 μM of **AT5** or 0.4 % (v/v) DMSO in PBS (Growcells, CA; Cat#: MRFG-6235) in a 96 -deepwell plate (ThermoFisher Scientific, MA; Cat#: 260251). **AT5**, or vehicle, was then diluted serially to 6.25 μM in PBS. 100 μL of each concentration was transferred to a UV/Vis 96-well microplates (Fisher Scientific, MA; Cat#: 21-377-832) in triplicate for three, independent replicates ($n = 9$). Both absorbance and emissions spectra were measured using a CLARIOstar microplate reader (BMG-Labtech, Germany). Absorbance was measured at each wavelength from 220 -1000 nm using the average of 5 flashes per well. The emissions spectra from 350-621 nm (emission bandwidth of 14 nm) were measured using an excitation wavelength of 320 nm (excitation bandwidth of 12 nm) at a gain of 857 and a focal length height of 5 mm using the top optic. Absorbance and emissions spectra for the vehicle at each concentration were subtracted as background.

Solvent polarity

To determine the effect of solvent polarity, 100 mM **AT5** in DMSO was mixed with 1mL of each indicated solvent to a final concentration of 100 μM. Peak excitation was determined by screening emissions of **AT5** at 330 nm on a Hitachi F-4500 fluorescence spectrophotometer. Optimal excitation wavelength was determined for each compound by systematically varying excitation wavelength in 0.1 nm increments until the emissions maximum was observed. Emissions spectra were then recorded using the peak excitation for each solvent. Emissions data for 0.1 % (v/v) DMSO was gathered for each solvent and subtracted as a baseline.

pH sensitivity

The effect of changes in pH of 1X PBS was determined by using 10X PBS (Growcells CA, Cat#: MRFG-6235) diluted with either hydrochloric acid or sodium hydroxide and water to 1X PBS. The acidic or basic 1X PBS was then used to change the pH of 1X PBS to either 5.0, 6.0, 7.0, 7.4, 8.0, 9.0, or 10.0. **AT5** was then diluted to 100 μM in the PBS at each pH. Each well was mixed in a 96-deep-well plate and 100 μL of each was loaded into UV/Vis 96-well microplates (Fisher Scientific, MA; Cat#: 21-377-832) in triplicate for three, independent replicates. Emissions were measured using a CLARIOstar microplate reader as previously described. Emissions spectra for 0.1 % (v/v) DMSO at each pH was subtracted as background.

Detergent Interactions

To determine the effect of different detergents on **AT5**, 100 mM of **AT5** was diluted to 100 μM in the indicated concentrations of either CTAB (Sigma Aldrich, MO; Cat#: H 6269; CMC = 0.9mM[208]), SDS (Fisher Scientific, MA; Cat#: 166-100; CMC ≈ 8mM[209,210]), Triton X-100 (Fisher Scientific, MA; Cat#: BP151-500 ; CMC = 0.18–- 0.24 mM[211-214]), or Tween 20 (Fisher Scientific, MA; Cat#: BP337-100; CMC ≈ 0.050–- 0.057 mM[212,215]), as well as PBS pH 7.4 (Growcells, CA; Cat#: MRFG-6235) and 18 mΩ H_2O. To determine the correct order of mixing, 100 mM **AT5** was diluted to 100 μM in PBS and H_2O either 30 min before or after the addition of Triton X-100 at a final indicated concentration and mixed via pipetting. To create a broad range of emissions for **AT5**, 100 μM of **AT5** in PBS was mixed with the indicated ratios of both Triton X-100 and SDS to a final detergent concentration of 100 mM. Absorbance and emissions spectra were measured for each well using a CLARIOstar microplate reader as previously mentioned.

2.4 Results and discussion

Five ATs; **AT1**, **AT2**, **AT3**, **AT4**, and **AT5** were initially screened for potential fluorescence *in vitro* using confocal microscopy (Figure 2). RAW 264.7 cells were treated with the various ATs for 24 h prior to imaging. These results demonstrated that cells treated with 100 μM of either **AT2** or **AT5** showed notable amounts of fluorescence (Figure 2A and 2B). **AT5** exhibited emissions when excited by the 405 nm (blue) laser while **AT2** did so when excited using both the 488 nm (green) and 555 nm (red) lasers, but not the 405 nm laser (Figure 2A, 2B, and S2)**.** In addition to their differences in fluorescence, both ATs seemed to localize to different areas within the cell; although, from the data collected it is difficult to determine the exact locations of each fluorophore (Figure 2C). Of these ATs only **AT5** showed no statistically significant cytotoxic effect on RAW 264.7 murine macrophage-like cells after 24 h, with an average of 90.7 ± 11.3 % cell viability (Figure 3A). It should be noted that all examined ATs were cytotoxic to HeLa cells after 24 h (Figure 3B). **AT5** was the least cytotoxic with an average of 73.5 ± 16.3 % cell viability (Figure 3B). This apparent lower cytotoxicity may be due to the large methyl acetamide side chain of **AT5** compared to the side chains of **AT1-4** (Figure 2 and S2). Although **AT2** showed potential as a fluorescent probe, the cytotoxicity prohibited its use in live-cell imaging experiments. Additionally, preliminary characterization of **AT2** showed little fluorescence in PBS, DMSO, and cyclohexane (data not shown). Though this may imply **AT2** is interacting with something within the cell to increase its fluorescence. Further research outside the scope of this paper is needed to fully understand this phenomenon. Due to the observed fluorescence and lack of cytotoxicity, **AT5** was further pursued for additional characterization.

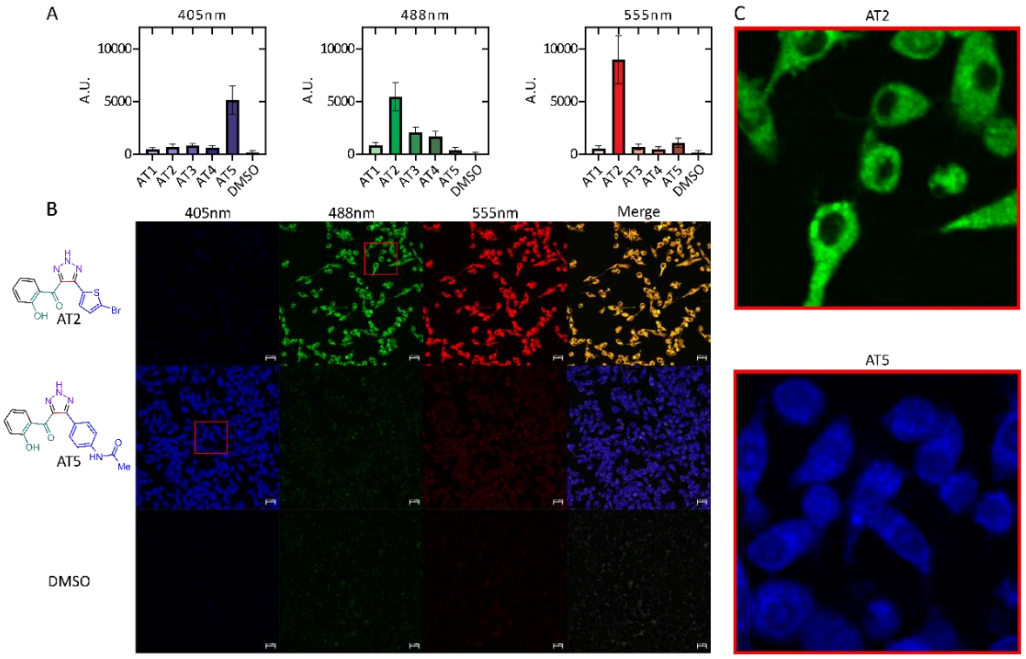

Figure 2. Fluorescence intensity of ATs *in vitro*. RAW 264.7 murine macrophages were incubated for 24h with 100µM of the indicated compound. Cells were imaged using a Zeiss LSM 700 confocal microscope. Signal intensity for cells for each laser were measured using FIJI and standardized to the unit area of each cell. Background in each image was subtracted from each measurement. Values where the fluorescence intensity of the cell was less than the background (negative values) were set to zero. **A.** Mean emission intensity ± SD *n = 150* for each compound. Cells were sampled at random from various fields using the transmitted light image to avoid bias (not shown) across three, independent biological replicates. Emission intensities were determined as a quantification of **B (**and Appendix I; Figure S2**)** showing the fluorescence of each compound *in vitro* for each specific laser. Scale bars are 20 µm. **C.** Enlarged regions of each photo showing distribution of ATs *in vitro*. Brightness across all images was adjusted equally post analysis.

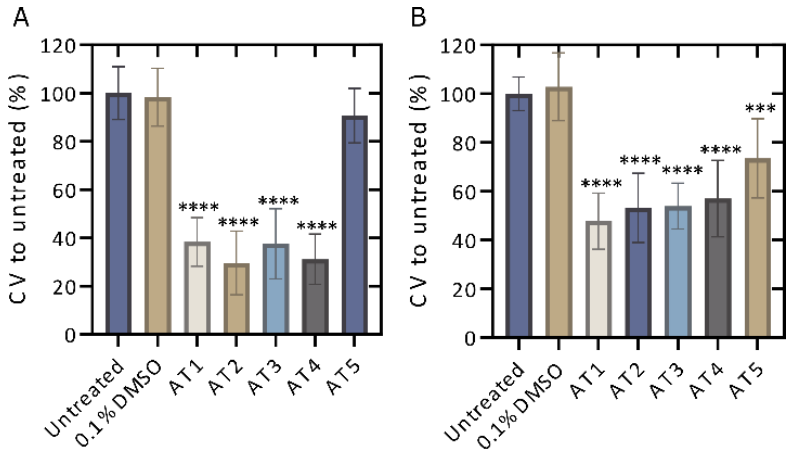

Figure 3. Cell viability of A. RAW 264.7 cells and B. HeLa cells after 24 h treatment with each compound. PrestoBlue and media (1:1 ratio) were added to either RAW 264.7 cells or HeLa cells for 1 hr. post treatment and incubated at 37 °C. Values are shown as the ratio of the difference of absorbance at 570 nm signal and the 600 nm background for each sample to the difference in absorbances for the average of the untreated means ± SD. Each assay was performed in triplicate for three, independent biological replicates, $n = 12$. Statistical significance was determined using a Brown-Forsythe and Welch's ANOVA. *** $p < 0.001$, **** $p < 0.0001$.

To determine whether the fluorescence activity of **AT5** was only visible in RAW 264.7 cells, both RAW 264.7 cells and HeLa cells were incubated with 100 µM **AT5** for 24 h at 37 °C in a 5 % CO_2 incubator and imaged using the Zeiss LSM 700 confocal microscope. We found that although there is a slight difference in the fluorescent intensity of **AT5** in HeLa and RAW 264.7 cells (comparison not shown), **AT5** could indeed be used as a live-cell probe in

different cell lines (Figure 4A and B). To determine the timeframe required for use with live cells, RAW 264.7 cells were treated with 100 μM **AT5** at 37 °C in 5 % CO_2 and imaged every 15 min for approximately 24 hours (Figure 4C). Though fluorescence consistently increased, changes in fluorescence increased approximately 4h post-treatment, at which point the fluorescence intensity seemed to increase at a greater rate for the remainder of the experiment (Figure 4C). Additionally, fluorescence intensity of **AT5** in RAW 264.7 cells never plateaued indicating the potential for increased fluorescence at time points of 24 h or later (Figure 4C). There was observable cell death at time points approaching 24 h, which is potentially due to prolonged exposure to the 405 nm laser because in fields adjacent to the final images of this experiment, there was little to no observable cell death (images not shown). This is supported by the previously mentioned cell viability experiments (Figure 3).

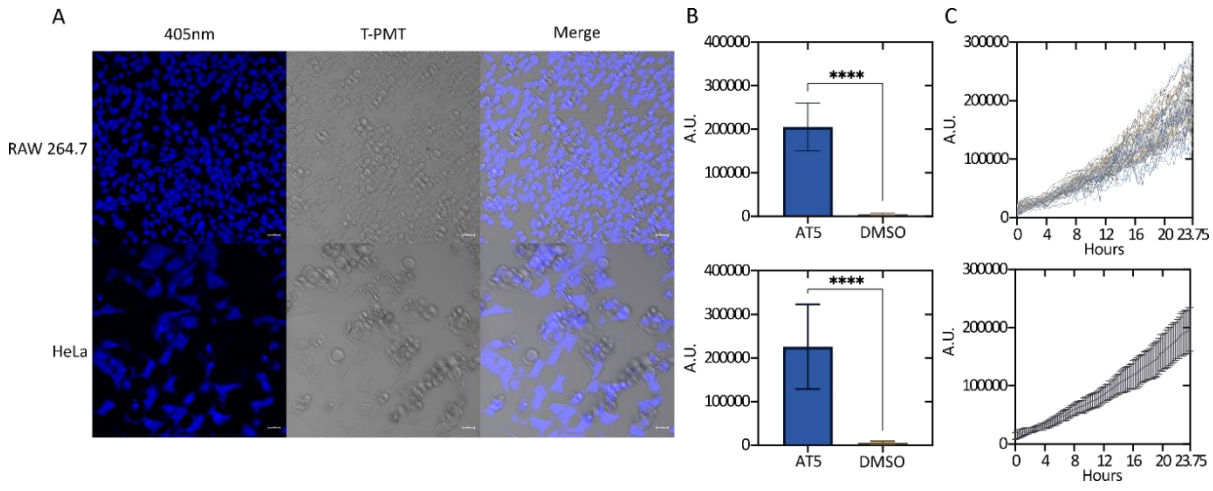

Figure 4. Fluorescence in RAW 264.7 cells and HeLa cells (A). Brightness across all images was adjusted equally post data analysis. **B.** Quantification of **A**. shown as the mean fluorescent signal per unit area ± SD in RAW cells (top) and in HeLa cells (bottom) treated with 100 µM AT5 or 0.1 % (v/v) DMSO for 24 h, *n = 300* cells over 3 independent replicates. Statistical analyses were done using a using a two-tailed t-test with a Welch's correction, ****$p < 0.0001$. Values where the fluorescence intensity of the cell was less than the background (negative values) were set to zero. **C.** Fluorescence signal per unit area in RAW 264.7 cells over time. Images were taken every 15 min for 23.75 h. Data for each individual cell is shown (top) along with the mean ± SD (bottom). *n = 60* cells across three, independent biological replicates.

In addition to acting as fluorophore in live cells, **AT5** was able to stain fixed and permeabilized RAW 264.7 cells (Appendix I; Figure S3) further indicating its applicability. In many images, **AT5** can be seen inside both RAW 264.7 cells and HeLa cells, though it does not seem to be ubiquitous throughout the cell (Figure 2B, 2C, 4A, and S2). It is possible that **AT5** is not simply sequestered, but rather interacting with cellular components. Further research is necessary to validate this idea. Our initial results indicate that pH may also play a role in fluorescence since we observed a slight reduction in emissions of **AT5** in PBS with a pH $\leq$ 6 (Appendix I; Figure S4).

2.4.1 Changes in AT5 fluorescence due to solvent polarity

Solvent polarity has been previously reported to affect the emissions of aurones and their derivatives, showing a trend for increased emissions as polarity decreased[76,77]. It was hypothesized that polarity may influence the fluorescent properties of **AT5** as well. To test this, **AT5** was dissolved to a concentration of 100 μM in various solvents. Each solvent was ranked according to the relative normalized molar electronic transition energies of pyridium *N*-phenolate betaine dye 36 ($E_T(30)$) values (E_T^N) on a scale between tetramethylsilane (TMS; 0.00) and water (1.00)[80,216]. Surprisingly, it was found that the fluorescence of **AT5** increased in polar-protic environments, with the greatest fluorescence occurring in PBS (Figure 5A). Indeed, even the weakest fluorescence in a polar-protic solvent (isopropanol, 889.1 ± 10.96 [SD] RFU) exhibited more than 35-fold stronger emissions ($p < 0.0001$; Unpaired two-tailed t-test with a Welch's correction) compared to chloroform (25.3 ± 0.86[SD] RFU) which had the strongest emissions of both the polar-aprotic and non-polar solvents (Figure 5A). Given that the $E_T(30)$ scale is well known to be highly sensitive to hydrogen-bonding, these results

were also examined in the context of the pi^* scale, which reflects more general solvent polarity[80,217,218]. There was effectively no correlation of fluorescence results with the pi^* scale indicating that hydrogen-bonding is indeed the dominant feature influencing fluorescence intensity, although it should be noted that no attempt was made to ensure anhydrous conditions during fluorescence measurements, so the influence of residual water in the solvents or on the cuvettes cannot be ruled out.

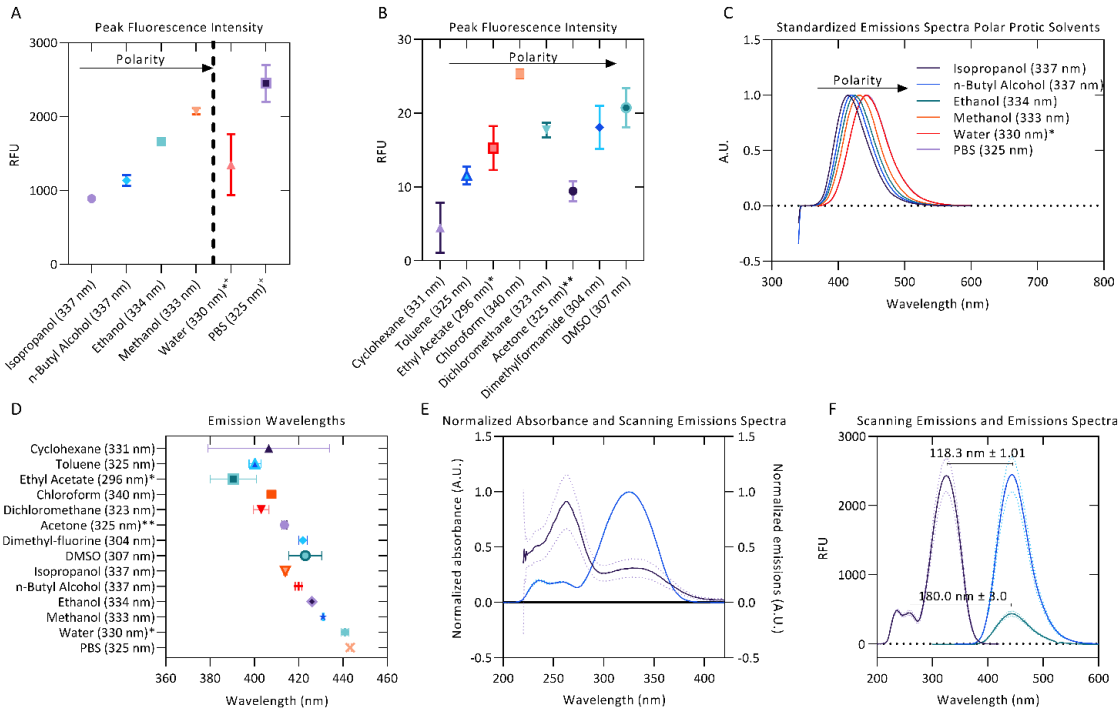

Figure 5. Fluorescent properties of 100 mM AT5 in different solvents. A. Emission intensities of **AT5** in various protic solvents organized by increasing polarity. Excitation wavelengths (in parenthesis) were determined using the scanning emissions spectra. **B.** Emission intensities of **AT5** in various aprotic solvents organized by increasing polarity. Excitation wavelengths (in parenthesis) were determined using the scanning emissions spectra. **C.** Red-shift in emission spectra for protic solvents. The mean emissions spectra for each solvent were standardized, 1 being the highest emission intensity and 0 set to 0 emissions. Excitation wavelengths (in parenthesis) were determined using the scanning emissions spectra. **D.** Peak emission wavelengths for **AT5** in various solvents. Excitation wavelengths (in parenthesis) were determined using the scanning emissions spectra. **E.** Normalized absorbance

and normalized scanning emission spectra ± SD, *n = 9* across three, independent replicates measured using a CLARIOstar microplate reader. Absorbance and scanning emissions spectra for wavelengths > 420 nm not shown. **F.** Scanning emissions spectra and emission spectra of PBS ± SD measured using the spectrophotometer, *n = 3*. Excitation wavelengths (in parenthesis) were determined using the scanning emissions spectra. For all panels (**A-F**), each emission spectra for the various solvents were measured and blank corrected using 0.1 % (v/v) DMSO as a vehicle background. Peak emissions and peak emission wavelengths were determined as *n = 3* independent replicates for the indicated excitation wavelength (in parenthesis) with mean values represented. Vertical lines represented standard deviation calculated for each set of measurements. *Low solubility. **Negative values for one replicate led to only using an *n = 2*. [+]Aqueous solvents not statistically different due to high variability. [0]Polarity data not known for PBS. [1]Polarity based on the relative normalized $E_T(30)$ [E_T^N] polarity[216].

Water is the most polar-protic solvent on this scale, so it was expected that water would cause **AT5** to have the highest fluorescence emissions, but due to the low solubility of **AT5** in water, it was unable to go fully into solution potentially limiting its detectable fluorescence. The data also suggests that polarity in aprotic solvents has little to no effect on the fluorescence emissions of **AT5**, but rather is dependent on the protic nature of the solvent (Figure 5A and B; Table 1). This suggests a potential use of **AT5** in selective fluorescence visualization experiments based on solvent environment. This is supported by the similar, but not equivalent, findings of Meisner *et al*. which noted that the emissions of 1,2,3-triazoles were quenched in the polar-aprotic solvent dichloromethane compared to DMSO, which was attributed to the interruption of intramolecular hydrogen bonds[142]. The authors described that the triazoles were acting as the hydrogen bond donor[142]. Conversely, the higher fluorescence (RFU > 800) in **AT5** in polar protic solvents (Isopropanol, n-butyl alcohol, ethanol, methanol, PBS, and water), compared with very slight fluorescence (RFU < 30) in either polar aprotic solvents (DCM, toluene, ethyl-acetate, DMF, and DMSO) or aprotic solvents (acetone, chloroform, and cyclohexane) indicate that **AT5** has increased fluorescence in solvents favoring **AT5** behaving as a hydrogen bond acceptor (Figure 5A and B; Table 1).

Table 1. Stokes shift and peak emissions of AT5 in various solvents. Emission spectra for **AT5** in various solvents was measured and blank corrected using 0.1 % (v/v) DMSO as a vehicle background. Peak emissions and peak emission wavelengths were determined as *n = 3* independent replicates for the indicated excitation wavelength. Stokes shift was determined as the difference between the excitation wavelength and the peak emissions wavelength, *n = 3*
*Low solubility. $^{+}$Aqueous solvents not statistically different due to high variability. ^{0}Polarity data not known for PBS. [1]Polarity based on the relative normalized $E_T(30)$ [E_T^N] polarity[216].

Solvent (excitation)	Relative polarity[1]	Stokes shift (nm)	Std dev.	Peak emission (RFU)	Std dev
Isopropanol (337 nm)	0.546	77.1	0.6	889.1	10.9
n-Butyl Alcohol (337 nm)	0.586	82.9	1.2	1135.3	57.5
Ethanol (334 nm)	0.654	92.1	0.2	1660.3	26.0
Methanol (333 nm)	0.762	98.1	0.3	2072.7	36.8
Water (330 nm)*$^{+}$	1.000	110.9	1.4	1349.0	337.8
PBS (325 nm)$^{+0}$	--	118.3	0.5	2451.0	204.3

In support of this as solvent polarity increases in protic solvents, there is a slight red-shift in emissions spectra ranging from 414.1 ± 0.702nm (isopropanol) to 443.267 ± 0.643 nm (PBS) (Figure 5C and D), though there is a less uniform red-shift as polarity increases in aprotic solvents as well (Figure 5D). It is possible that the hydroxyl group present on C2" could potentially form an intramolecular hydrogen bond with the ketone-group. Both the ketone-group and the amide group on C4' can act as hydrogen bond acceptors, while the hydrogen ion on N2 of the triazole could potentially act as a hydrogen bond donor.

The strongest emissions of **AT5** were observed in PBS, therefore subsequent experiments and characterization were performed in PBS. The absorbance spectra showed two major peaks, with the largest peak absorbance occurs between 262 and 263 nm (Figure 5E).

There was an additional smaller absorbance peak with a maximum occurring between 328 and 330 nm (Figure 5E). The absorbance and emission intensity of both peaks was linked to concentration of **AT5** (Appendix I; Figure S5). Excitation at 262nm yielded slight emissions of 443.4 ± 40.99 RFU with a mean peak emission wavelength of 442 ± 2.8 nm (Figure 5F). To determine which wavelength of excitation was ideal, the scanning excitation spectra (SES) for emissions at 442nm, which systematically records the intensity of emissions at a given wavelength for each excitation wavelength, was recorded. Though excitation occurs at 262 nm, peak excitation for emissions at 442 nm most likely occurs at 324.7 ± 0.3 nm (Figure 5F). This was confirmed by measuring emissions from **AT5** excited at 325 nm and found peak emissions at 443.3 ± 0.64 nm with peak emissions of 2451 ± 250.1 RFU (Figure 5F). Due to the fact that the highest absorbance peak did not correspond with peak fluorescence, the SES was used to determine peak excitation in all solvents. Using the peak SES and peak emissions (SE) to determine Stokes shift, a large Stokes shift of 118.3 ± 1.01 nm (n = 3) was observed for **AT5** in PBS (Figure 5F). Large Stokes shifts are a common feature of other triazoles[137,142]. Unlike emissions, the SE Stokes shift of **AT5** in various solvents (calculated as the difference in peak emissions, n = 3, compared to the peak excitation wavelength initially determined through SES) was not solely dependent on whether the solvent was protic or aprotic (Table 1). The SE Stokes shift of **AT5** in cyclohexane was determined to be 75.53 ± 22 nm, though the large standard deviation is most likely due to a lack of signal intensity with emissions of only 6.07 ± 3.68 RFU. Though the SE Stokes shift of DMSO and DMF were 116.1 ± 6.1 nm and 117.9 ± 1.6 nm, respectively, the emissions for each were weak (approximately 20.7 ± 3.7 RFU and 18.1 ± 4.1 RFU). The SE Stokes shift of **AT5** in methanol was measured as 98.1 ± 0.3 nm

while the SE Stokes shift in water was around 110.9 ± 1.4 nm indicating the greatest SE Stokes shifts with the strongest emissions occur in aqueous solvents (Table 1). As previously stated, **AT5** was relatively insoluble in water, but was soluble in PBS and cell culture medium, indicating a possible interaction with components of those solutions. The large SE Stokes shift of **AT5** in PBS further indicates its potential as a useful biological probe.

2.4.2 Detergent Micelle Models

Since ionic detergents such as CTAB and sodium dodecyl-sulfate (SDS) have been shown to modulate the strength of fluorescent probes[86,219,220] and since detergent micelles have been used as membrane mimics for the study of membrane proteins[221,222], it was decided that the interactions of **AT5** with both ionic and neutral detergents should be characterized. To do this, various concentrations flanking the critical micelle concentration of CTAB, Triton X-100 (Triton), SDS, or Tween 20 (Tween) were separately mixed with 100 µM **AT5** in PBS. For all detergents, the lowest concentration seemed to increase the fluorescent intensity of **AT5** (Figure 6). As the concentration of both neutral detergents (Triton and Tween) increased, the emissions of **AT5** had an average percent decrease of 90.10 ± 0.73 % and 54.72 ± 3.28 %, respectively, demonstrating that neutral detergents had a strong quenching effect at concentrations above the CMC (Figure 6A and B). Additionally, it was found that in 10 mM Triton X-100, addition of **AT5** prior to detergent addition slightly increased fluorescence (Appendix I; Figure S6). Based on this, for all subsequent experiments, **AT5** was added prior to detergent. Unlike both neutral detergents, in the cationic detergent, CTAB, the emission of **AT5** was quenched at concentrations greater than 0.125 mM. For this condition, the average percent decrease was 80.8 ± 0.7 % (of peak fluorescence at 0.03125 mM) with midpoint

occurring at 0.25 mM CTAB (Figure 6C). In SDS, the intensity of **AT5** was quenched at 1.25 mM to approximately 14.7 ± 1.1 % lower than its initial peak fluorescence (at 0.3125 mM, Figure 6D). In all detergents as concentrations increased, there was a slight but noticeable blue-shift in peak emissions wavelength, with the most drastic change occurring in CTAB shifting from a peak emission wavelength around 443 nm (all concentrations < 0.25 mM) to a peak emissions wavelength around 430 nm (all concentrations > 4 mM) (Figure 6C).

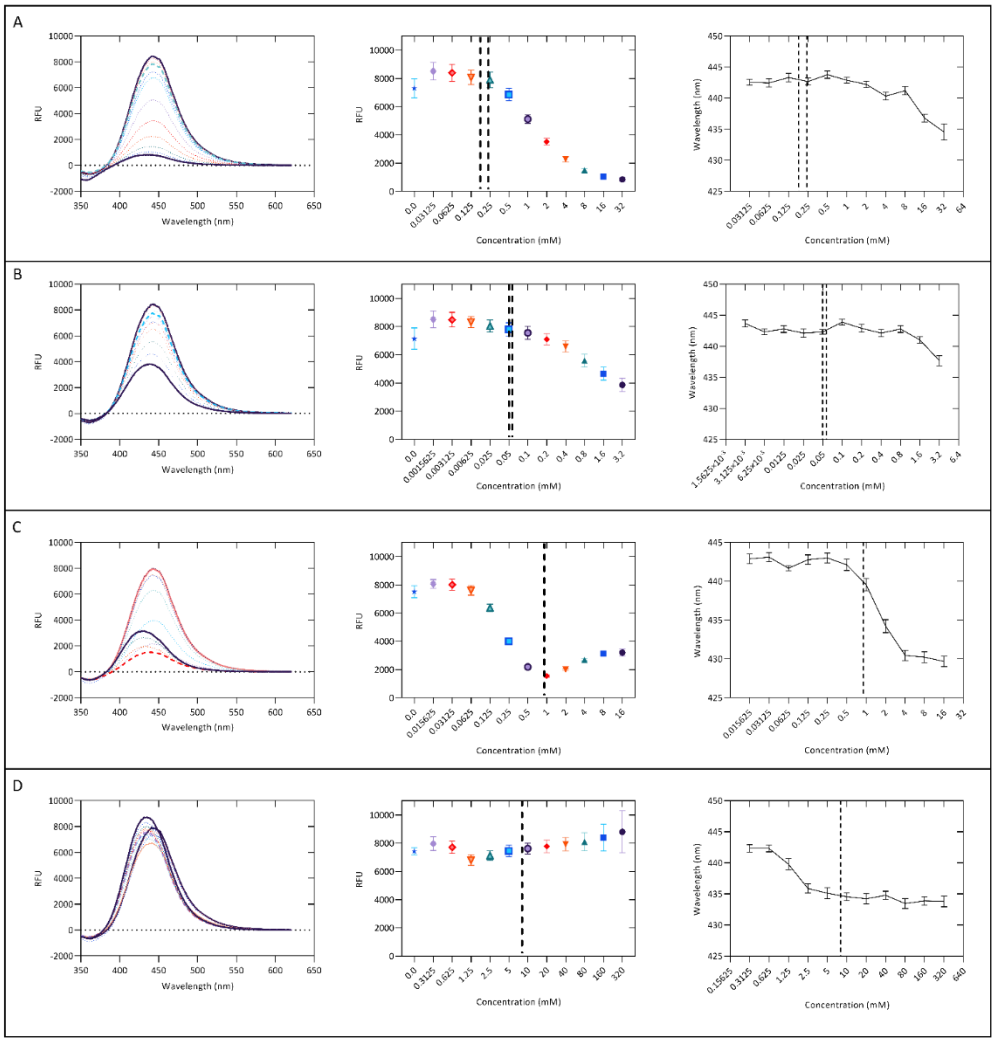

Figure 6. Fluorescent properties of AT5 in various detergents and PBS. Mean emissions spectra, mean peak emissions, and peak emissions wavelength of AT5 in various concentrations of: **A.** Triton X-100, **B.** Tween 20, **C.** CTAB, and **D.** SDS. Dashed lines represent the CMC while two dashed lines represent the reported ranges of CMCs for each detergent. Column three displays the change in wavelength for each concentration at $\log_2$ intervals (Data at 0 mM not able to be shown). Each data is shown as the average of 9 wells from three, independent replicates ± SD (spectral standard deviation not shown).

Due to the quenching effect of Triton and the lack of quenching observed with higher concentrations of SDS, we decided to use these detergents to mimic a mixed lipid composition environment. We hypothesized that, as the molar ratio shifted from a large Triton concentration to a large SDS concentration, we would observe increasing emission intensities. Indeed, a broad range of emission intensities from 100 μM **AT5** from 753.4 ± 49.5 RFUs (100 mM Triton: 0 mM SDS) to 8705 ± 872 RFUs (0 mM Triton: 100 mM SDS) (Figure 7A and B). This implies that in regions of anionic lipids (as opposed to neutral lipids), **AT5** would have increased fluorescence. Peak emission wavelengths were also shown to slightly shift as the detergent concentration shifted from Triton to SDS (Figure 7C), matching those observed in high concentrations of Triton and SDS (Figure 6A, 6D, 7C). Ionic detergents such as CTAB and SDS can affect fluorescence through their ability to form, or disrupt, hydrogen bonds[223,224]. These data potentially indicate a possible interruption of the hydrogen bonding of water to **AT5**. It is also possible for ionic interactions between the anionic head group of SDS with the amide nitrogen of **AT5** on its side chain leading to an effect the fluorescent properties of **AT5**, while the blue-shift observed in all detergents may be due to increasing hydrophobic interactions[225].

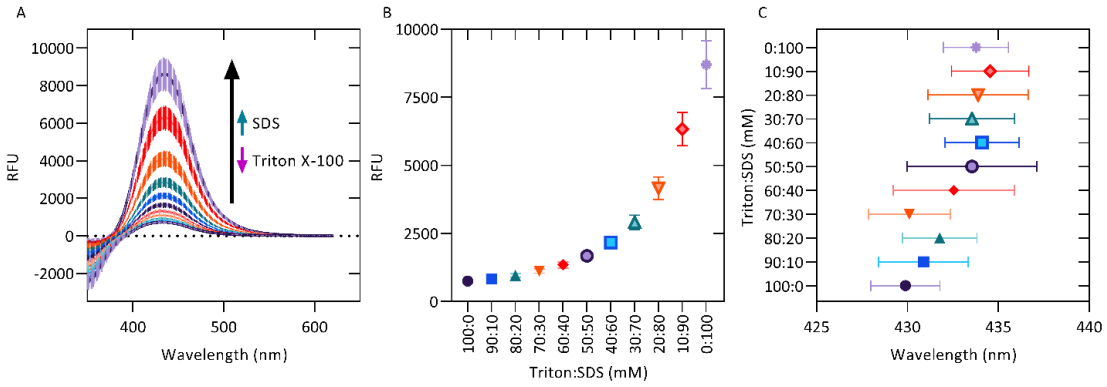

Figure 7. **Mixed micelles of varying concentrations of Triton X-100 and SDS**. **A.** Mean emissions spectra ± SD of 100 µM AT5 in 100 mM of varying ratios of Triton X-100 to SDS in 1X PBS. The black arrow designates increase in SDS and a decrease in Triton. This is further illustrated by **B.** the peak emission intensity ± SD for each ratio of detergent. The ratio shifts from 100mM Triton X-100 and 0mM SDS (left) to 0mM Triton X-100 and 100mM SDS (right). **C.** Peak emission wavelength ± SD for each ratio of Triton X-100: SDS. Emissions were recorded using the CLARIOstar microplate reader on a 96-well UV : VIS microplate in triplicate for three, independent replicates ($n = 9$).

2.5 Conclusions

Aurones are a widely researched class of flavonoid with many bioactivities. Recently there has been increased interest in their use as fluorescent probes. “Click” 1,2,3-triazole structures have also been shown to have potential use as fluorophores as well. Recently, our group has synthesized and characterized aurone-derived triazoles. Five of these aurone-derived triazoles (**AT1-5**) were examined for their potential use as live-cell fluorescent probes. Of these five, **AT2** and **AT5** fluoresced in cells, but **AT5** was the only compound which was not substantially cytotoxic, potentially due to its R’ group. **AT5** was shown to have high fluorescence intensity in polar protic solvents, potentially implying the need for **AT5** to act as a hydrogen bond acceptor, though further study is warranted. In micellular models, emissions of **AT5** were quenched in detergents at most concentrations below the CMC, though the fluorescence recovery observed in ionic detergents indicates the potential for ionic interactions with **AT5**, and their potential effect on the fluorescent properties of **AT5**. Here **AT5** was shown to have potential as a fluorophore in live-cell microscopy.

Author Contributions

Daniel L. Bryant: Conceptualization, data curation, formal analysis, investigation, project administration, validation, visualization, and writing–- original draft. Arjun Kafle: Conceptualization, data curation, formal analysis, methodology, resources, and writing – original draft. Anthony L. Farone: Funding acquisition, supervision, and writing – review & editing. Scott T. Handy: Conceptualization, funding acquisition, supervision, and writing – review & editing. Justin M. Miller: Conceptualization, funding acquisition, project administration, supervision, visualization, and Writing – review and editing.

Conflicts of interest

There are no conflicts to declare.

Acknowledgements

The authors would all like to acknowledge the Molecular Biosciences program at Middle Tennessee State University for financial support as well as David Nelson PhD. for insight and training. The authors would also like to acknowledge Shrijana Bhattarai for her contributions and support.

CHAPTER III

Fluorescent Properties of AT111

3.1 Background

1,2,3-triazole-containing compounds have shown promise as compounds of interest due to their bioactivities, ranging from anti-inflammatory[90,92,93,122,126,129-134] to anti-microbial effects[90,94,96,103-111,116-121], and fluorescent characteristics[135-137,139-154]. Many TCCs are characterized by a large Stokes shift and tunable fluorescent spectra[135-137,139,142,143,145]. Some aurones are also known to have fluorescent properties, possessing large Stokes shifts in polar-protic solvents while having more fluorescence in polar-aprotic and less polar solvents[76,77]. Aurones have also been shown to be rather tunable as fluorophores and certain structures can cause shifts in emissions spectra[77]. Both aurones and TCCs have also been increasingly seen in applications as fluorescent probes or sensors[82-86,145-154] indicating the fluorescent potential of compounds that incorporate the two moieties into a singular compound. In 2020, Kafle *et al.* was able to serendipitously synthesize a novel class of ATs[194] that place a 1,2,3-triazole moiety inside the backbone of an aurone. In this article, they describe a relatively simple way to synthesize salicyl-substituted ATs using a heat catalyzed reaction of sodium azide and an existing aurone system in DMSO or other polar-aprotic solvents[194]. Though studies involving triazole-aurones exist[192,193], there has been little study on the use of these ATs as fluorescent molecules. In a previous publication, which has been re-formatted for chapter II, an AT, AT5, was described having increased emissions and large Stokes shifts in polar-protic environments[1]. AT5 was also shown to stain live and fixed cells proving its potential as a useful fluorescent probe[1]. Though only AT5 was shown to have strong fluorescence in various

solvents, another AT, AT2, was shown to have potential as a fluorophore *in vitro* although this could not be reproduced in a cuvette, indicating other factors which may affect its fluorescence[1]. Additionally, all other ATs showed fluorescence, albeit minimally, *in vitro* compared to the vehicle control, further strengthening the potential of ATs as fluorescent molecules[1]. Due to these findings presented in chapter II, it was decided to examine the fluorescent potential of AT111, an AT that has shown to have anti-inflammatory properties discussed in later chapters.

3.2 Materials and Methods

General experimentation

(2-hydroxyphenyl)(5-(3,4,5-trimethoxyphenyl)-2*H*-1,2,3-triazol-4-yl)methanone (AT111) was synthesized and characterized as described previously as **12** in the 2020 work; *An unusual Triazole Synthesis from Aurones* by Kafle *et al.*[194]. AT5 was synthesized and characterized in the 2022 publication; *Aurone-derived 1,2,3-triazoles as potential fluorescence molecules in vitro* by Bryant *et al.* reformatted in chapter II[1]. Briefly, ATs were synthesized from a previously prepared aurone[200]. The aurone (0.05 mmol) was mixed with NaN_3 (0.75 mmol; 1.5 equivalents) in 1.5mL of 100% DMSO in a glass vial. The mixture was heated for 30 min at 120 ℃. After 30 min, the reaction was brought to RT and then diluted with DI water. Following this, the reaction was extracted with ethyl acetate, then washed in DI water and brine. The organic fraction was dried on $MgSO_4$ and concentrated in a vacuum to obtain a crude product. This product was then purified using 20-50 % EtOAc/hexane in conjunction with flash column chromatography. Following purification, ATs were reconstituted in 100 % DMSO (MP Biomedicals; Cat#: 196055) at a concentration of 100 mM. For all experiments,

the ATs were diluted to 100 μM in various solution with 0.1 % (v/v) DMSO as a cosolvent. A solution of 0.1 % (v/v) DMSO in the various solvents, without the presence of an AT, was used either as a blank/ background or as a vehicle control. All statistical analyses were done using GraphPad Prism version 10.0.0-10.0.1 for Windows, GraphPad Software, Boston, Massachusetts USA, www.graphpad.com.

Fluorescence cuvette procedure

To determine the fluorescence properties of AT111, 100mM AT111 in 100 % DMSO was diluted in either cyclohexane, DMSO, 18 mΩ water, or PBS for a final concentration of 100 μM in the specified solvent with 0.1% (v/v) DMSO as a cosolvent. 1 mL of the mixture was added to a quartz cuvette. Excitation and emissions spectra were determined using a Duetta Fluorescence and Absorbance Spectrometer (Horiba Scientific; Kyoto, Japan). Emission intensities for wavelengths 250 – 1100 nm were measured for excitation wavelengths from 250 – 1000 nm in 10 nm increments and were measured in 0.5 s intervals. Excitation spectra were determined by plotting the inverse of the emissions spectra, where the fluorescence intensities at each excitation wavelength was plotted for the specific emissions wavelengths. Peak spectra were chosen for the excitation and emission wavelengths with the highest intensities. The data is presented as the average of the fluorescence intensity (counts/μA; arbitrary units [A.U.]) of the compound minus the fluorescence intensity of the blank (0.1% [v/v] DMSO) across three, independent experiments for each solvent.

Cell culture

RAW 264.7 murine macrophage-like cells (RAW 264.7 cells; ATCC Cat#: TIP-71) were cultured at 37 ℃ in a humidified incubator with an atmosphere of 5 % CO_2 in air. The cells were grown in Dulbecco's modification of Eagle's medium (DMEM; Corning, NY; Cat#: 10-013-CV) supplemented with 10 % (v/v) heat-inactivated fetal bovine serum (FBS) and 100 Units/mL of a penicillin and streptomycin cocktail (Fisher Scientific, MA; Cat#: 15-140-122) and passaged every 3-7 days prior to reaching 90 % confluency.

Confocal microscopy

All live cell imaging was performed as previously described in Bryant *et al*. and in chapter II[1] and Appendix I. Briefly, RAW 264.7 cells were seeded at a density of 1 x 10^6 cells per dish in a 35 mm glass bottom cell culture dish (Cellvis, CA; Cat#: D35-14-1.5-N). The cells were allowed to attach and grow over night for 16-18 h. The following day, the cells were washed with pre-warmed 1x PBS and treated 100 μM of the specified AT or the vehicle (0.1 % [v/v] DMSO) for 24 h. Following this incubation, the cells were imaged on a Zeiss LSM 700 confocal microscope following the exact specifications for experiments comparing the different fluorescent properties of each AT previously described and listed in chapter II[1]. The fluorescence intensities of each cell for each treatment/ excitation wavelength were determined using FIJI[207]. The data is displayed as the mean background-corrected signal/ unit area (px) ± one standard deviation for 150 cells across multiple fields of view for three, independent biological replicates. All negative values, where the background had a higher signal than the cell, were set to zero. The brightness across all images (except for the brightfield, [T-PMT]) was raised equally post-analysis for visualization.

3.3 Results and Discussion

Due to the fluorescent properties of AT5 and AT2 in chapter II, it was thought that there may be other ATs that may exhibit similar characteristics[1]. Though AT1, AT3, and AT4 had minimal fluorescence *in vitro*, they still had more signal than the vehicle control indicating that there is minute, but measurable fluorescence from these ATs[1]. AT111 (Figure 8) is another AT which has three methoxy groups on the 3', 4', and 5' carbons on the arylI) group (generic structure of ATs in chapter II, Figure 1).

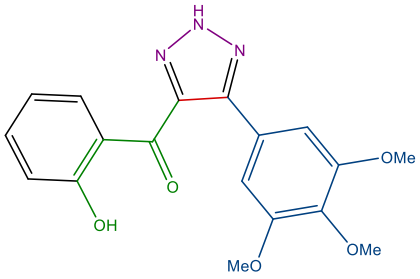

Figure 8. Structure of AT111.

AT111 is shown to have anti-inflammatory effects at concentrations > 25 μM and is used to demonstrate the potential of ATs as anti-inflammatory molecules, described later in chapter IV. Due to the fluorescent nature of other ATs and its demonstrated bioactivities, it was decided to examine AT111 as a fluorescence molecule. An initial screen of AT 111 *in vitro* revealed that though AT111 was far less fluorescent than AT5, it was still slightly more fluorescent than the vehicle control (Figure 9). Live cell imaging revealed that AT111 emitted less fluorescence than AT5 across three excitation wavelengths (405 nm, 488 nm, and 555 nm; $p<0.0001$ for all three wavelengths). The fluorescent intensity of AT111 excited by the 405 nm laser was approximately 11.9 times weaker than that of AT5 (Figure 9A). Conversely,

emissions from AT111 were over 1.5 and 3-fold weaker than AT5 when excited by the 488 nm and 555 nm lasers, respectively (Figure 9B and C). These findings are similar to the intensities determined for AT1, 2, and 4 (Figure 2)[1] where all three of those ATs had less fluorescence than AT5 for both the 405 nm and 555 nm excitation. However, the findings for AT111 differ than the others since it was shown that AT111 had statistically less fluorescence intensity than AT5 when excited by the 488 nm laser (346.7 ± 150.5 A.U. compared to 528.8 ± 189.4 A.U., respectively; $p<0.0001$; Figure 9B). AT111 having minimal fluorescence was predicted as it was hypothesized that the increased fluorescence exhibited by AT5 was potentially due to hydrogen bonding of the amide nitrogen or ketone on the 4' position[1]. Although AT2 and AT5 had fluorescence *in vitro*, AT111, AT1, AT3, and AT4 produced minimal signal[1]. This could potentially be due to the rotation of the aryl side chain, or lack of charge displacement as could occur with AT5's amide nitrogen, leading to comparatively decreased emissions.

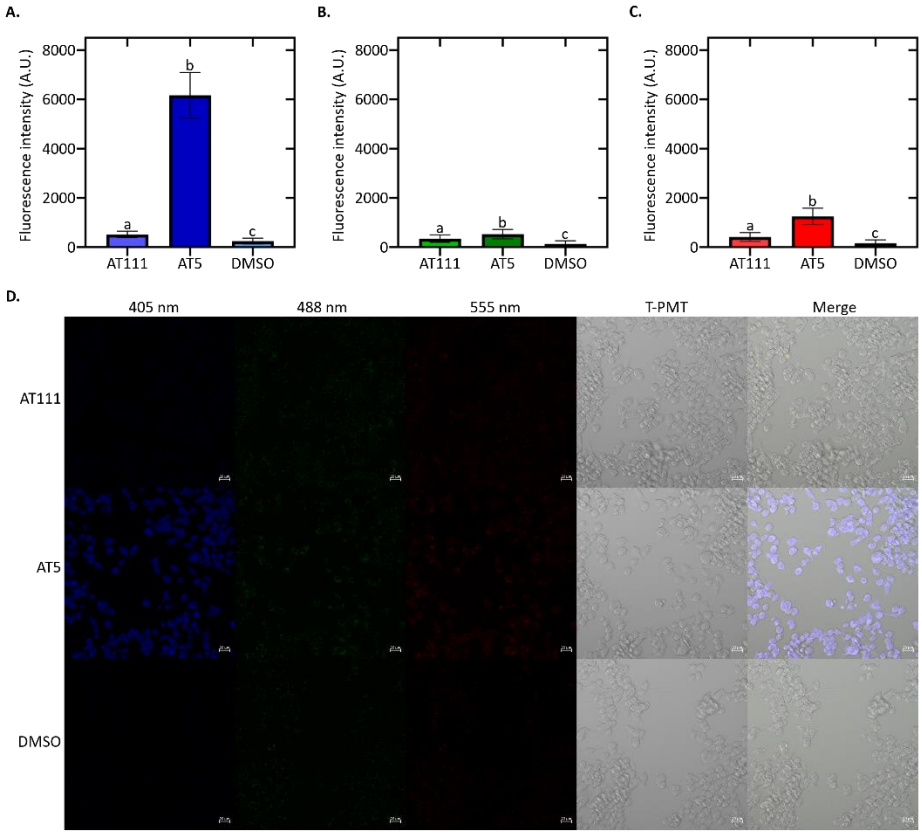

Figure 9. Fluorescence of AT111 *in vitro*. Quantification of fluorescent signals of AT111 and AT5 in RAW 264.7 cells excited by A. 405 nm, B. 488 nm, and C. 555 nm lasers. The values are displayed as the mean fluorescence intensity ± SD for 150 cells sampled randomly across three biological replicates using confocal microscopy, *n = 150*. Fluorescence intensity values were determined as a quantification of the background corrected signal for 150 cells using FIJI[207]. Statistical significance between each group was determined using an ordinary one-way ANOVA with a Tukey's post-hoc analysis. D. Representative confocal images of AT111, AT5, and the vehicle *in vitro*. Brightness of each image was uniformly adjusted post-analysis for visualization.

To understand the fluorescence characteristics of AT111, the excitation and emissions spectra and intensities for AT111 was obtained in four different solvents, including cyclohexane (less polar-aprotic), DMSO (polar-aprotic), water (polar-protic), and PBS (aqueous/saline; polar-protic). It was found that, contrary to AT5[1] (Chapter II, Figure 5a and b, Table 1), AT111 had increased emissions in a polar-aprotic solvent compared to less polar-aprotic and polar-protic solvents (Figure 10A, Table 2). In DMSO (a polar-aprotic solvent) AT111 had an average peak emission intensity of 996.97 ± 71.37 A.U. while in water (a polar-protic solvent) it had a peak intensity of 576.4 ± 194.15 A.U. (Figure 10A and Table 2; $p<0.01$). In cyclohexane (a less-polar-aprotic solvent) AT111 had stronger emissions than water with an average of 736.76 ± 132.14 A.U. ($p>0.05$). In congruence with these opposite observations of AT111 compared to AT5, emissions in PBS were the weakest (414.11 ± 54.63 A.U.) and statistically less than in DMSO and cyclohexane ($p<0.0001$ and <0.005, respectively).

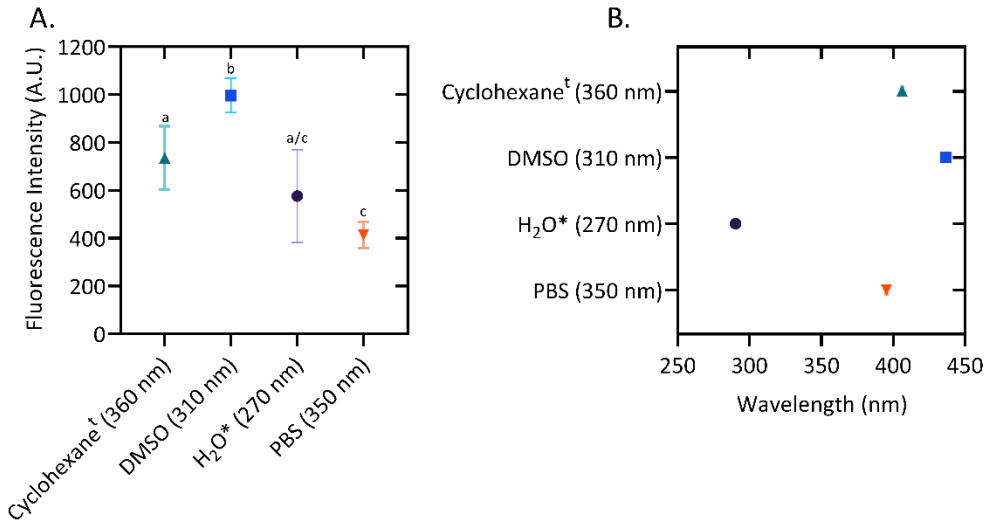

Figure 10. Fluorescent properties of AT111 in different solvents. A. Average emission intensities of 100 µM AT111 in various solvents. Peak excitation wavelengths (in parenthesis) were determined using the scanning emissions spectra (SES) for the **B.** average peak emissions wavelength for each solvent. Peak emission intensities and wavelengths are displayed as the mean ± SD of at least 4 independent replicates. [t]Formation of emulsions. *Potentially low solubility. Statistical differences were determined using an ordinary one-way ANOVA with a Tukey's post-hoc analysis, $p<0.05$ between the indicated groups.

Table 2: Peak emissions and Stokes shift of AT111 in different solvents. Emission spectra for AT111 in various solvents was measured and blank corrected using 0.1 % (v/v) DMSO as a vehicle background. Peak emissions and peak emission wavelengths were determined as at least four independent replicates for the indicated excitation wavelength. Stokes shift was determined as the difference between the excitation wavelength and the peak emissions wavelength. [1]Polarity based on the relative normalized $E_T(30)$ [E_T^N] polarity scale[216]. [t]Formation of emulsions. *Potential low solubility.

Solvent (excitation)	Relative polarity[1]	Stokes shift (nm)	Peak emission wavelength (nm)	Std dev.	Peak emission (A.U.)	Std dev.
APROTIC						
Cyclohexane (360 nm)[t]	0.006	46.3	406.3	0.28	736.76	132.14
DMSO (310 nm)	0.444	126.6	436.6	0.70	996.97	71.37
PROTIC						
H_2O (270 nm)*	1.000	20.5	290.5	0.26	576.40	194.15
PBS (350 nm)	--	45.4	395.4	0.66	414.11	54.63

It should be noted that AT111 is largely insoluble in water. Even with 0.1 % (v/v) DMSO as a cosolvent, there may still be some solubility issues. A similar issue is observed for cyclohexane where 0.1% (v/v) DMSO forms an emulsion which contains AT111. While vortexing the sample would not disaggregate this emulsion, it did allow for reproducible measurements of fluorescent properties. For both water and cyclohexane, the larger variance in peak intensity could potentially be due to variance in solubilized AT111 from sample to sample. Though these caveats exist and may be responsible for the fluctuations of the peak emissions intensities, the peak excitation and emissions wavelengths were consistent for each replicate.

To determine the Stokes shift of AT111, the peak emission wavelength was determined for each individual replicate, the indicated excitation wavelength was subtracted, and the difference was averaged yielding a mean and standard deviation (SD; Table 2). This value slightly varies from the peak emissions wavelength determined for the average spectra as the peak wavelength's emission intensities may be lower in some replicates versus others. For example, AT111 in PBS has an average peak emission wavelength of 395.4 ± 0.66 nm, however the peak emissions wavelength based on the average emissions intensities of all five replicates is determined to be 396.011 nm which is within one standard deviation. For the purpose of evaluating the Stokes shift, the former method is used. AT111 is shown to have the largest Stokes shift in DMSO (126.6 ± 0.70 nm) and the smallest in H_2O (20.54 ± 0.26 nm) compared to the other solvents (Table 2). This is consistent with the large Stokes shifts observed in both aurones[76,77] and triazoles[137,139,142,143,145], however it is more similar to other 1,2,3-triazoles whose large Stokes shifts may be observed in more polar-aprotic solvents[137,142,145]. Interestingly, this was a deviation from the findings for AT 5 which had both the strongest emission intensities and largest Stokes shifts in the aqueous solvents (Chapter II; Table 1).

There was also a significant red shift in the peak emissions wavelength for AT111 in DMSO compared to other solvents (Figure 10B, Table 2). The average peak emissions of AT111 in DMSO differed by 30.35 nm compared to cyclohexane (Figure 10B). There was also a larger red shift when compared to PBS (41.23 nm) and H_2O (146.14 nm) indicating that while the protic nature of the solvent is also possibly a factor (Figure 10B). The noticeable difference in spectra for AT111 in H_2O compared to PBS (Figure 11A and D) is possibly due to the presence of phosphates or salt ions within the solution, as solvents can influence the

characteristics of fluorophores. An example of this is described by Baraldi *et al.* showing that solvent polarity had a profound effect on the absorbance and emissions spectra of fluorophore M2; shifting the peak absorption from 16310 cm^{-1} (613 nm) in cyclohexane to 22570 cm^{-1} (443 nm) in water[226].

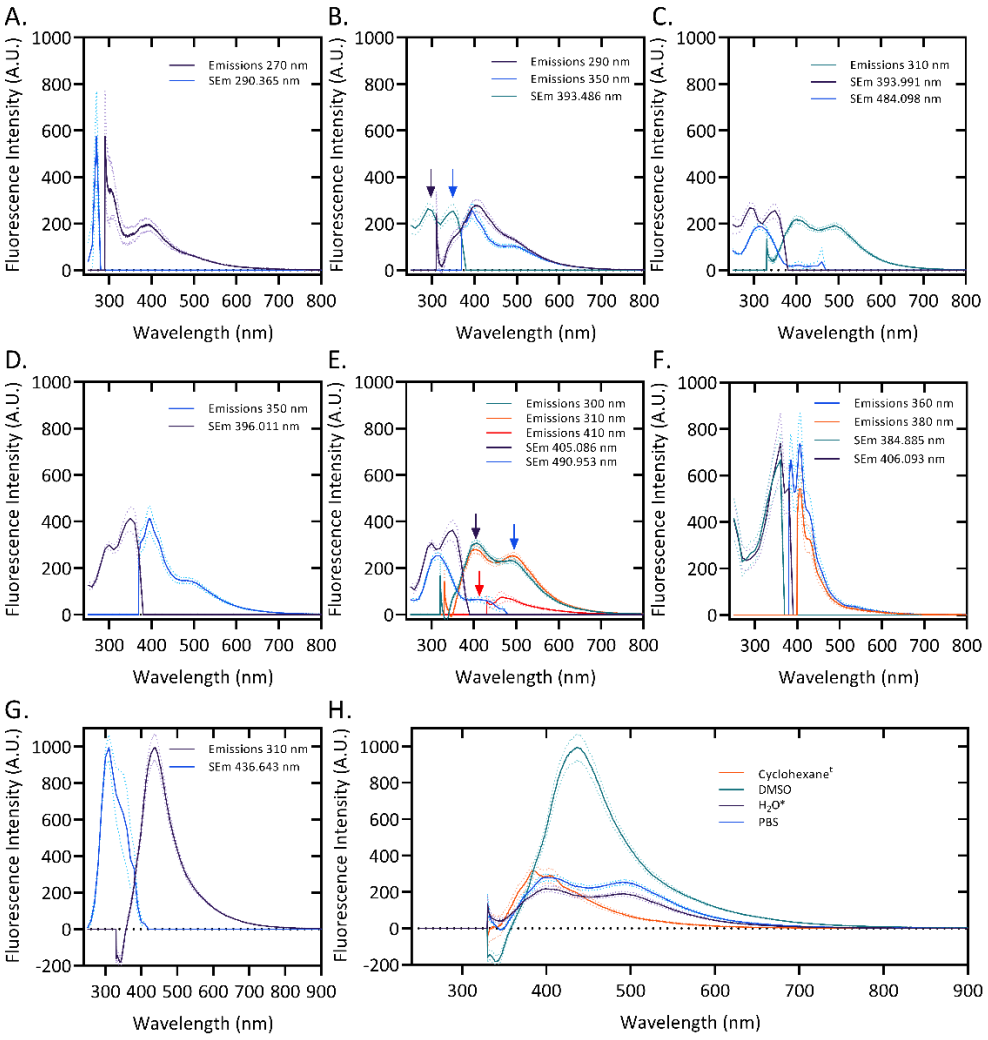

Figure 11: Emissions spectra of AT111 in various solvents. Average excitation (scanning emissions; SEm) and emissions spectra of 100 µM AT111 in **A. B. C.** water*, **D. E.** PBS, **F.** cyclohexane[t], and **G.** DMSO. Color-coded arrows indicate the respective excitation or emissions peaks correlated with that wavelength. **H.** Emissions spectra of AT111 in each solvent excited at 310 nm. Spectra are displayed as the mean emission/ SEm intensities for each indicated wavelength ± S.D. (dotted lines). *Possible low solubility. [t]Formation of emulsions. SEm spectra overlap for all solvents is found in Appendix II; Figure S1.

Investigation of the average excitation and emissions spectra for each solvent revealed certain interesting features. For example, AT111 in water revealed a maximum emissions peak at 290.365 nm and a second, lower peak occurring around 393.486 nm, when excited at 270 nm (Figure 11A). SES for 290.365 nm showed only the excitation peak at 270 nm, however SEm for 393.486 nm revealed two peaks, the highest peak occurring at 290 nm while the second peak occurred at 350 nm (Figure 11B). Excitation at 290 nm led to a peak emission wavelength of 406.596 nm while excitation at 350 nm showed one at 393.991 nm with a shoulder peaking at 484.098 nm (Figure 11B). SEm for 393.991 nm showed both excitations peak at 290 nm and 350 nm, while SEm for 484.098 nm had only one peak at 310 nm (Figure 11C). Emissions spectra for 310 nm excitation had two peaks at 489.486 nm and 398.535 nm (Figure 11C). SES for 398.535 nm again revealed peaks at 290 nm and 350 nm. This is expected as emissions from excitation at both wavelengths were higher at 398.535 nm than emissions at 310 nm. However, it is curious that there was a larger peak at 489.486 nm when excited at 310 nm as larger blue-shifted emissions occur at both 290 nm and 350 nm (Figure 11C).

In PBS, AT111 had an average peak excitation and emissions wavelengths at 350 nm and 396.011 nm, respectively, while also having shoulders for both the excitation and emissions spectra (Figure 11D). The shoulder in the emissions spectra extended from 470.830 nm to 489.975 nm while the scanning emissions shoulder occurred at 300 nm (Figure 11D). Excitation at 300 nm leads to a doublet of peaks at 405.086 nm and 490.953 nm (Figure 11E). Scanning emissions spectra for 405.086 nm revealed the original peaks at 300 nm and 350nm while scanning emissions for 490.953 nm revealed a spectra with a peak at 310 nm (Figure

11E). Excitation at 310 nm led to an emissions spectrum similar to 300 nm however the 405.086 nm peak was shifted to 399.039 nm with slightly lower emissions while the 490.953 nm peak shifted to 491.443 nm with slightly higher emissions (Figure 11E). Scanning emissions for both 490.953 nm and 491.443 nm showed an expected large signal at 310 nm, but no peak at 350 nm while revealing a slight shoulder peaking at 410 nm (Figure 11E). This spectrum is very similar to the one in water (Figure 11C) with the exception of the 410 nm shoulder (Figure 11E). Excitation at 410 nm only revealed a slight peak at 467.380 nm (Figure 11E).

The multiple observed peaks in emissions spectra for both water and PBS may be due to excited state intramolecular proton transfer (ESIPT) which can cause the formation of a tautomer (Figure 12). When there is strong intramolecular hydrogen bonding, ESIPT occurs more easily leading to emissions with a large Stokes shift[227]. When there is a weaker or no intramolecular hydrogen bonding, ESIPT happens less readily or not at all leading to an emissions spectrum with a small Stokes shift[227].

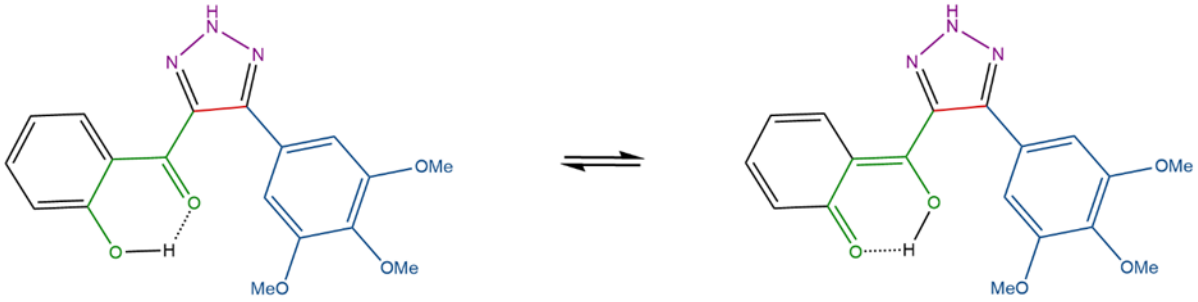

Gibbs Energy: 100.41 [kJ/mol]
pKa: 7.369

Gibbs Energy: 141.12 [kJ/mol]
pKa: 8.072

Figure 12. Proposed tautomerization caused by ESIPT.

ESIPT is known to occur in methyl salicylate derivatives and 2-hydroxybenzophenone derivatives[227-229], which are structurally similar to the hydroxyphenol and methanone portions of AT111, where excitation of the molecule from a high-energy wavelength can lead to tautomerization from the enol-form to the ketol-form of the molecule. ESIPT is complex and the nature of the solvent can have a strong effect[230] which varies from molecule to molecule. For example, Tang *et al.* determined computationally that ESIPT of alizarin was most favorable in polar protic and polar aprotic solvents compared to less polar aprotic solvents[231] and Qin *et al.* demonstrated one fluorophore which had increased ESIPT in all aprotic solvents (decreasing with an increase in polarity) which was possibly inhibited by intermolecular hydrogen bonding of protic solvents[232], though this was not the focus of their study. Others have shown that ESIPT can theoretically occur more readily in less polar aprotic solvents[233] though the protic nature of the solvents seemed to have a larger effect. The work of Chen *et* al. demonstrated that increases in solvent polarity can interfere with ESIPT in another fluorophore, as well[234]. While Joshi *et al.* demonstrated that the addition of diethyl ether as a hydrogen-bond acceptor increased ESIPT of salicylic acid in cyclohexane[235]

Since intermolecular hydrogen bonds have been suggested to interfere with ESIPT[236-238], it is possible that both tautomers of AT111 may exist simultaneously in protic solvents, leading to multiple peaks with differing spectra due to this interference. For AT111, in both PBS and in water, excitation at 310 nm led to dual emissions peaks occurring at similar wavelengths (398.535 nm/ 489.486 nm for water and 399.039 nm/ 491.443 nm in PBS) (Figure 11H). The presence of a red-shifted peak can also be observed in the emissions spectra excited at the peak SEm wavelengths for both PBS and water (Figure 11A and D). The idea that ESIPT

in this molecule is modulated by the presence of a protic solvent is further supported by the spectra of cyclohexane and DMSO. In cyclohexane, peak excitation occurs at 360 nm while peak emission occurs at 406.093 nm (Figure 11F). Excitation of the smaller, peak at 380 nm leads to a symmetrical emissions peak at 406.596 nm while scanning emissions for the more blue-shifted emissions peak at 384.885 nm revealed another symmetrical excitation peak at 360 nm (Figure 11F). Both peak excitation and emission spectra possess a doublet of peaks as well, however, due to the small Stokes shift in cyclohexane, it is unlikely that ESIPT is occurring in this solvent. In DMSO, there is only one excitation and emission peak occurring at 310 nm and 436.643 nm, respectively (Figure 11G). This similar excitation of 310 nm having a red-shifted peak accompanied by a large Stokes shift could potentially indicate ESIPT. A comparison of the emissions spectra for all solvents excited at 310 nm shows that in both protic solvents there is the presence of a second red-shifted peak compared to that of cyclohexane. The lack of a large Stokes shift in cyclohexane, coupled with the red-shifted peaks in PBS, DMSO, and to an extent water, may imply that ESIPT for this molecule seems to occur primarily in polar solvents. Though the occurrence of ESIPT is normally marked by a singular lower energy peak coupled with a large Stokes shift, the presence of a higher energy peak could indicate interference. This interference has been shown to possibly be caused by *inter*molecular hydrogen bonding (IHB) in protic/aqueous solvents[236-238], a phenomenon that has been shown theoretically before in methyl salicylate[239,240]. This suggests that ESIPT for AT111 may occur in polar solvents but is hindered by intermolecular hydrogen bonds from protic solvents. This is not unprecedented as Seo *et al* and Kenfac *et al* had similar findings, though Kenfac *et al*. did not explore this in less polar solvents such as cyclohexane or toluene[236,238]. The presence

of a large higher-energy emissions peak with a small Stokes shift and a red-shifted peak with a large Stokes shift in both aqueous solvents (Figure 11A-E and H) support this hypothesis. This is further validated by the aforementioned excitation and emissions spectra of AT111 in DMSO, which is singular with a large Stokes shift (Figure 11G). It is worth noting that AT111 in DMSO is more fluorescent compared to the other three solvents (Table 2, Figure 11G and H), and this increase in emission intensities could make it slightly difficult to discern the impact of this solvent on ESIPT induced tautomerization. Though ESIPT is a possible explanation of the solvatochromic behavior of AT111, extensive research and computational analysis is required to elucidate a definitive answer.

These findings demonstrate that AT111 has a slight potential to act as a fluorescent molecule, which can possibly undergo ESIPT in polar aprotic solvents. This work also further solidifies the fluorescent potential of ATs in general. However, AT111 has minimal fluorescence compared to AT5. This is most likely due to the amido-group on the 4' carbon present on AT5 while the lack of fluorescent intensity for AT111 may be due to its rotational potential between the triazole group and the aryl R-group. AT111 has similar fluorescent intensities *in vitro* as AT1, AT3, and AT4 which also all have symmetrical R-groups (Figure 8 and Appendix I; Figure S2).

Chapter IV

Anti-inflammatory Effects of AT5 and AT111

4.1 Background

In response to a foreign stimulus or pathogen, the cells of the innate immune system, particularly macrophages, become activated, releasing multiple pro-inflammatory cytokines, chemokines, ROS, RNS, and prostaglandins[46-50,241]. Usually, these inflammatory mediators are beneficial, leading to the eradication of the invading micro-organism. For example, the pro-inflammatory cytokine TNF-α stimulates the production of pro-inflammatory cytokines in various tissues[242]. Cytokines and chemokines such as IL-1β, IL-6, and monocyte chemoattractant protein-1 (MCP-1) have essential roles to play in the inflammatory response of innate immune cells. IL-1β is important for activating an acute inflammatory response[243] while promoting angiogenesis[244] and stimulating immune cell recruitment through the increase of adhesion molecules on various tissue types[245]. IL-6 is a key inflammatory mediator and, along with IL-1β and TNF-α, increases naive $CD4^+$ T cell differentiation into T-helper (Th) 17 cells, an adaptive immune cell type associated with the production of the pro-inflammatory cytokine, IL-17[246,247]. MCP-1 is a chemokine involved in the recruitment of monocytic cells, memory T-cells, and natural killer cells, to the site of inflammation[248].

Though these mediators are necessary in regulated amounts, their over-production can lead to detrimental effects. Prolonged or heightened expression of TNF-α, IL-1α/β (IL-1), IL-6, and MCP-1 have all been connected to CIDs such as RA[243,246,248,249] and IBD[52,250]. IL-1β has also been associated with progression and drug resistance of certain cancers[244] and has been linked to diabetes myelitis[245].

Pro-inflammatory signaling occurs when foreign antigens and cytokines bind to their respective receptors. These receptors then activate a signaling cascade which leads to the activation of response genes[241,245,251]. Certain receptors, known as pattern recognition receptors (PRRs), recognize pathogen associated molecular patterns (PAMPS) from bacteria, viruses, or fungi, as well as some cellular signals, and lead to an inflammatory response[251]. One PRR, Toll-like receptor (TLR) 4, recognizes bacterial LPS, as well as other PAMPS, and leads to the activation of highly characterized signal transduction pathways, which upregulate the expression of pro-inflammatory cytokines, chemokines, NO, ROS, and prostaglandins, as well as increasing cell proliferation[73,252-257]. Though receptors for cytokines and PAMPs are different, they often activate common pathways. For example, TNF receptors, the IL-1 receptor, and TLR4 all lead to the activation of the NF-κB pathway and mitogen-activated protein kinases (MAPKs)[245,252,258-260].

TLRs and IL-1 also share a homologous Toll-interleukin 1 receptor (TIR) intracellular domain[261,262]. As such, the LPS/TLR4 pathway has been utilized by researchers as one model for inflammation in aurone research[37,71,72,75] and is a known model for systemic inflammation[263]. To activate the LPS/TLR4 signaling cascade, LPS binds to both cluster of differentiation (CD)14 and LPS-binding protein (LBP), which is then translocated to TLR4 where it binds to myeloid differentiation factor (MD)-2[252]. For the canonical pathway, the LPS-CD14-LBP-MD2 complex binds to homodimers of TLR4[252]. This causes a conformational change that leads to the recruitment of TIR domain containing adaptor protein (TIRAP)[252]. TIRAP then recruits myeloid differentiation primary response gene 88 (MyD88), which allows for the phosphorylation of IL-1 receptor-associated kinases (IRAK)[73,264]. This then leads to the

phosphorylation of both the inhibitor of κ B (IκB) kinase (IKK) complex, consisting of IKKα, IKKβ, and NF-κB essential modulator (NEMO), and activation of MAPKs[252,259,265,266]. The IKK complex phosphorylates p65 (RelA) at Ser 536 and IκBα, which is then ubiquitinated and degraded, releasing the p65 (RelA)-containing NF-κB transcription factors leading to their subsequent nuclear translocation[73,259,266,267].

Following the initial MyD88-dependent pathway, TLR4 is endocytosed and a MyD88-independent pathway is activated via TIR domain-containing adaptor inducing interferon-β (TRIF; also known as TIR domain containing adaptor molecule 1 [TICAM1]) through Toll/IL-1R domain-containing adaptor-inducing IFN-β-related adaptor molecule (TRAM)[268]. This may lead to the activation of both TNF receptor associated factor (TRAF) 6 and receptor-interacting serine/threonine-protein kinase 1 (RIP1/RIPK1)[73,260,261,269], both leading to NF-κB activation (Figure 13). TRIF also activates TRAF3, which eventually leads to nuclear localization of IFN-regulatory factor (IRF) 3[270,271] through activation of TRAF family member-associated NF-κB activator (TANK)-binding kinase 1 (TBK1) and IKKi/ε, which leads to the subsequent production of type-1 interferons[252,268] (Figure 13).

TLR4 activation by LPS leads to the phosphorylation of various MAPKs including p38 MAPK (p38), c-Jun N-terminal kinases (JNK), and extracellular signal-regulated kinases (ERK) 1 and 2, which eventually leads to the activation of the transcription factor activator protein 1 (AP-1) through regulation of its subunits, c-Jun and c-Fos[272-274]. Both p38 and JNK have been associated with an inflammatory response[275-281]. p38 and JNK have been linked to the upregulation of ATF2, a subunit of AP-1, which is linked to the LPS-induced transcription of IL-6, TNF-α, and IL-1β[278,279]. ERK1/2 has also been linked to the inflammatory response

through p38γ/δ[282] and regulation of IL-10[283,284] and TNF-α[285,286]. ERK1/2 phosphorylates numerous cytoplasmic and nuclear proteins including transcription factors, other kinases, phosphatases, receptors, and others to modulate different cellular functions[274]. One such group of kinases are the MAPK-activated protein kinases (MAPKAPKs) including ribosomal-S6-kinases (RSKs), mitogen- and stress- activated kinases (MSKs) and MAPK-interacting kinases (MNK). Typically, both ERK1 (p44) and ERK2 (p42) are studied together as both are seemingly controlled by mitogen-activated protein kinase kinase 1 and 2 (MEK1/2) while also sharing an 83 % similar amino acid sequence[287]. However, this concept is an area of debate with some groups demonstrating alternative roles for the two proteins[288]. Though most of these kinases are phosphorylated by both p38 and ERK1/2, MNK2 interacts solely with ERK1/2[274,289]. MNK1/2 are involved in phosphorylation the eukaryotic translation initiation factor 4E (eIF4E) subunit involved in cap-dependent translation[290]. This modulation of eIF4E by MNK2 has been implicated as a key point in the promotion of the anti-inflammatory phenotype in tumor-associated macrophages and suppression of MNK2 led to a pro-inflammatory polarized state[291]. This demonstrates a potential role of ERK1/2 in inflammation.

Since both aurones and TCCs have been shown to have potential as anti-inflammatory compounds[37,71,72,74,75,90,92,93,122,126,129-134], it is reasonable that ATs could have similar biological activities. In this chapter, the anti-inflammatory effects of AT5 and AT111 are explored in detail, examining their dose-dependent effect on cell viability and the expression of RNS, iNOS, COX-2, as well as pro-inflammatory cytokines and chemokines in LPS-stimulated macrophages. Certain aspects of the LPS/TLR4 signal transduction pathways are also examined.

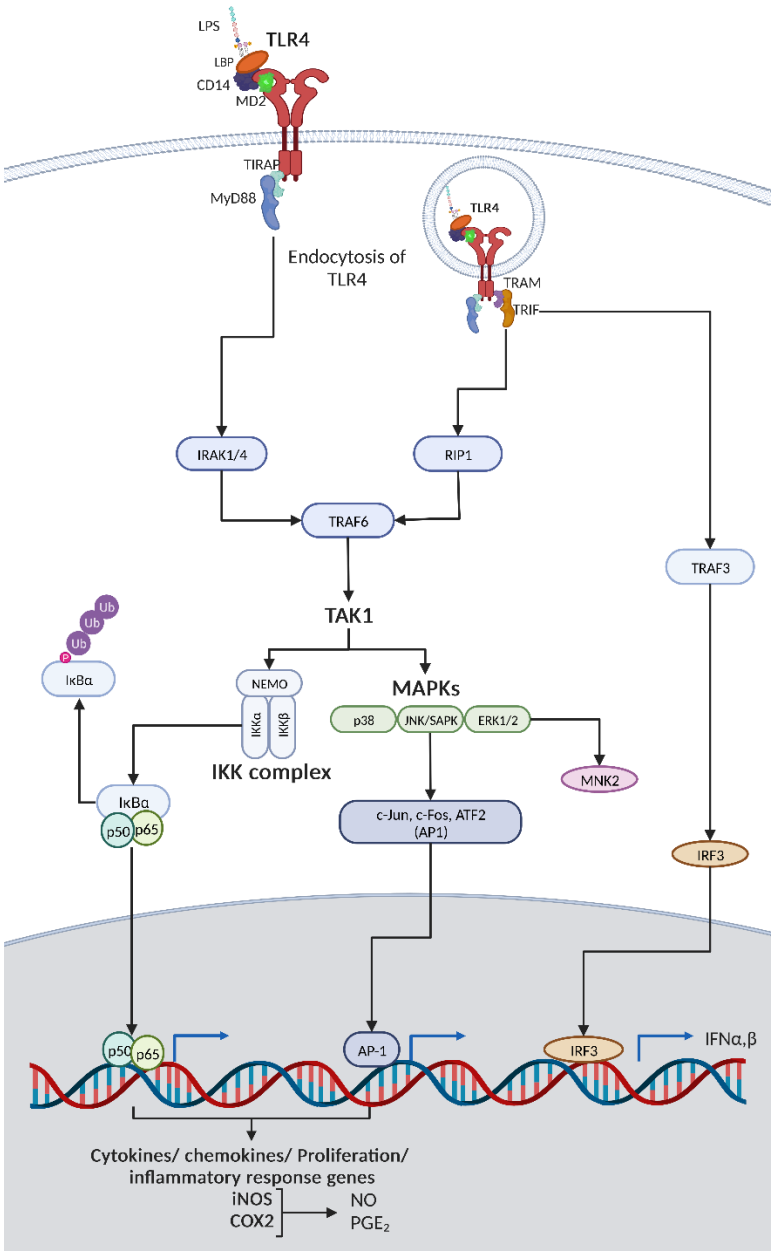

Figure 13. LPS/TLR4 signal transduction pathway. Created with BioRender.com.

4.2 Materials and Methods

Reagents and antibodies

The primary antibodies iNOS (13120S), COX-2 (12282S), p65 (6956s), p-p65 (Ser536; 3033s), ERK1/2 (p44/p42; 9107S), p-ERK1/2 (p-p44/p-p42; Thr202/Tyr204; 4370S), SAPK/JNK (9252S), p-SAPK/p-JNK (Thr183/Tyr185; 9255S), p38 MAPK (8690S), and p-p38 (Thr180/Tyr182; 9216S), were purchased from Cell Signaling Technology (Danvers, MA). Both StarBright Blue 700 Goat Anti-Mouse IgG (#12004159) and hFAB™ Rhodamine Anti-Tubulin Primary Antibody (#12004165) were purchased from Bio-Rad (Hercules, CA). Invitrogen Goat anti-Rabbit IgG (H+L) Cross-Adsorbed Secondary Antibody, DyLight™ 800 (SA5-10036/PISA510036) was purchased from Fisher Scientific (Waltham, MA). All DuoSet ELISAs; IL-6 (DY406-05), IL-10 (DY417-05), MCP-1 (DY479-05), TNF-α (DY410-05), GM-CSF (DY415-05), and accessory reagents (DY995/DY999) were purchased from Bio-techne/R&D Systems (Minneapolis, MN). DMSO was purchased from ATCC (4-x; Manassas, VA), Laemmli SDS sample buffer, reducing (6X) (AAJ61337AD), Molecular Probes™ PrestoBlue™ Cell Viability Reagent (A13262), MP Biomedicals™ AlbumiNZ™ Protease-reduced BSA (ICN989850), PBS Tablets (BP2944100), PBS (10-010-049), 0.4 % Trypan Blue Solution (15-250-061), 10X TBS (MT-46012CM), Triton x-100 (AAA16046AP), Tween20 (Polysorbate 20; BP337-100), Halt™ Protease and Phosphatase Inhibitor Cocktail (100X; PI78440), Invitrogen™ NucBlue™ Live ReadyProbes™ Reagent (Hoechst 33342; R37605), and Puromycin (A1113803) were purchased from Fisher Scientific (Waltham, MA). Bay 11-7082 (B5556-10MG), LPS from *Salmonella enterica s*erovar Typhirium (L6143-1MG),

Dexamethasone (D4902-25) and Griess reagent (modified; G4410-10G) were purchased from Millipore-Sigma (Burlington, MA). All other reagents and kits are listed below.

Cell culture and maintenance.

RAW 264.7 murine macrophage (RAW 264.7) cells (ATCC; TIB-71) were cultured in Dulbecco's modification of Eagle's Medium (DMEM, Fisher Scientific; MT10013CV) supplemented with 100 U/mL Penicillin/ Streptomycin cocktail (Fisher Scientific; 15-140-148) and 10 % (v/v) fetal bovine serum (FBS; DMEM complete medium) in a 37 ℃ humidified incubator with an atmosphere of 5 % CO_2, unless otherwise indicated. Cells were passed using trypsin-EDTA (Fisher Scientific; 25-200-056) every 3-5 days and kept below 90 % confluency. U937 human-monocytic (U937) cells (ATCC; CRL-1593.2) were cultured in Roswell-Park Memorial Institute medium (RPMI) similarly supplemented with 1000 U/mL Penicillin/ streptomycin cocktail and 10 % (v/v) FBS (RPMI complete medium) in identical atmospheric conditions. U937 cells were differentiated into macrophages using 100 nM phorbol 12-myristate-13-acetate (PMA) for 72 h. For most cell-based experiments, RAW 264.7 cells were seeded at a density of $5x10^5$ cells/ mL in a 96-well, or 6-well, tissue culture treated flat-bottom microplate and allowed to attach overnight (16-18 h) in the previously described conditions. For experiments involving a 24 h pretreatment with ATs or controls, RAW 264.7 cells were seeded at a concentration of $2.5x10^5$ cells/ mL. Post-incubation, the cells were washed with 1X phosphate-buffered saline, then treated, or pretreated then cotreated, for the indicated times with either LPS, various ATs, both LPS and ATs, or DMSO at the indicated concentrations for each experiment. The cells and supernatants were collected separately and either immediately assayed or stored at -80 ℃ for later use. Bioavailability of both AT5 and AT111 was predicted

using values calculated by the Molinspiration Cheminformatics free web services and compared to known criteria following the four rules of five for compound solubility/permeability described by Lipinski *et al.* as well as having a lower polar surface area (PSA) and a limited number of rotatable bonds (Appendix III; Table S1)[292-295]. In some experiments, the supernatants were diluted 20-fold in complete medium and sent to Eve Technologies (Alberta, Canada) for Mouse Cytokine Pro-inflammatory Focused 10-Plex Discovery Assay Array (MDF10) using an addressable-laser bead immunoassay (ALBIA).

Nitric oxide assay.

To measure the effect of ATs on the amount of LPS-induced NO production, RAW cells were either pretreated with the indicated concentrations of ATs for 0, 4, 24 h, then cotreated with 100 ng/mL LPS for 24 h. 50 µL of the collected supernatants were incubated with an equivalent amount of Modified Griess Reagent (Millipore-Sigma; G4410) for 15 min at 37ºC in air. Absorbance at 570 nm for each well was measured using a CLARIOstar microplate reader (BMG-Labtech, Germany). Nitrite, a biological stable byproduct of NO oxidation, concentrations for each well were determined by a comparison of the blank corrected absorbances to the absorbance values of a standard curve of known nitrite concentrations, using the standard and dilution protocol described in the Promega Griess Reagent System (Promega, WI; G2930). Each experiment was carried out in triplicate with a minimum of three, independent biological replicates for a total of at least nine replicate values (n = 9) unless otherwise indicated. The values are displayed as the mean standardized nitrite concentration as a ratio compared to the vehicle (0.1 % [v/v] DMSO) for each biological replicate ± S.D. Statistical differences were determined using a Brown-Forsythe and Welch ANOVA with a

Dunnett T3 multiple comparisons test for each treatment compared to the vehicle control. For the dose response curves, a 50 % inhibitory concentration (IC_{50}) was calculated by plotting a non-linear fit to the standardized nitrite ratio along the $\log_{10}$ of each concentration.

Presto Blue cell viability assay.

To determine the potential cytotoxicity of the various ATs, cells were incubated with a 1:10 dilution of Molecular Probe's Presto Blue (Fisher Scientific; A13261) in DMEM for one hour in the previously described atmospheric conditions according to the manufacturer's protocol. Following the incubation, absorbance at 560 nm was measured and absorbance at 600 nm was subtracted as a reference wavelength. $Absorbance_{560\text{-}600\ nm}$ of a no-cell control well was subtracted from each value as a background. Each experiment was carried out in triplicate with a minimum of three, independent biological replicates for a total of at least nine replicate values (n = 9) unless otherwise indicated. The values are displayed as the mean standardized cell viability as a ratio compared to the untreated control for each biological replicate ± S.D. Statistical differences were determined using a Brown-Forsythe and Welch ANOVA with a Dunnett T3 multiple comparisons test for each treatment compared untreated sample.

Cytokine Enzyme-linked Immunosorbent Assay

The effect of ATs on cytokine secretion was determined using the DuoSet enzyme-linked immunosorbent assay (ELISA) kit for each indicated cytokine according to the manufacturer's protocol. Briefly, the capture antibody for each protein was allowed to incubate on a High-bind 96-well microplate for 16-18 h then washed 3 times with 0.05 % (v/v) Tween 20 in PBS using a BioTek plate-washer ELx50. Non-specific protein binding to the plate was blocked using reagent diluent (1 % [w/v] bovine serum albumin [BSA] in PBS) for one hour

at room temperature (RT), washing again. The previously harvested supernatants were diluted to a working concentration for each cytokine/chemokine (1:100 for TNF-α, 1:500 for MCP-1, 1:200 for IL-6) in DMEM. Then, 100 µL of each diluted sample, or standard, was added to the ELISA plate and incubated at RT for two hours. The plate was washed again, and the detection antibody was added for an additional two hours. To allow for a colorimetric quantification, streptavidin conjugated to horseradish peroxidase (HRP) was added to each well and incubated for 20 min protected from light. The plate was washed a final time and 100 µL of substrate solution (1:1 mixture of H_2O_2 and Tetramethylbenzidine) was added for 20 min. The enzymatic reaction was then stopped by the addition of 50 µL 2 N H_2SO_4. The $absorbance_{450\ nm}$ (with a correction wavelength of 540 nm) for each well was measured. The $absorbance_{450\text{-}540\ nm}$ of the blank was also subtracted from the raw data for each well. Cytokine/chemokine levels in each sample were determined through comparison of the blank corrected raw data to the values of a standard of known concentrations. Concentrations of each well were standardized to the vehicle control (0.1 % [v/v] DMSO) for each biological replicate. Data is represented as the mean standardized amounts of each cytokine/chemokine compared to the vehicle control ± standard deviation (S.D.) in triplicate for at least three biological replicates. Values below the limit of detection were set to zero and values above the limit of detection were excluded. Statistical differences were determined using a Brown-Forsythe and Welch ANOVA with a Dunnett T3 multiple comparisons test for each treatment compared untreated sample.

Protein extraction

Cells were seeded and pretreated/ cotreated with the ATs or indicated controls for 15 min or 24 h, as described earlier. Post-treatment, the supernatants were removed, and the cells were lysed using 200 µL of ice-cold radioimmunoprecipitation assay (RIPA) buffer containing 1x Halt protease and phosphatase inhibitor cocktail and 1x Halt EDTA ($RIPA^+$) coupled with manual dislocation. Cell lysates in $RIPA^+$ were collected in 1.5 mL microcentrifuge tubes, placed on ice, then vortexed for 30 seconds every 5 min for 15 min to expedite lysis. Cell debris was pelleted via centrifugation at 21.1k x g for 15 min at 4 ℃. The supernatants containing the proteins were transferred to a fresh microcentrifuge tube and the pellet discarded. Proteins were stored at -80 ℃ for later use.

SDS-PAGE and western Blotting

Total protein concentration of each extract was determined using the Pierce Bicinchoninic Acid (BCA) assay according to the manufacturer's protocol using the microplate procedure with no modifications. Equivalent amounts of protein, ranging–from 10 - 15 µg depending on the assay, from each sample were brought to an equal volume using $RIPA^+$, then mixed with 6x Laemmli buffer. The proteins were denatured by boiling the samples at >95 ℃ for 10 min. The proteins were then loaded into 4-12 % Tris-glycine sodium dodecyl sulfate polyacrylamide gel electrophoresis (SDS-PAGE; Fisher Scientific; XP04125BOX) gels and separated at 100 V for 1.5 h in 1 X tris-glycine running buffer (Fisher Scientific; LC2675). During this step, the low-fluorescence polyvinylidene difluoride (LF-PVDF) membranes were activated in 100 % methanol for 30 s then washed in 18 mΩ water for two min. The LF-PVDF membranes, blotting paper, and reservoir pads were soaked in 1 X Towbin transfer buffer

containing 20 % (v/v) methanol (transfer buffer). After separating, the proteins were transferred onto the pre-soaked LF-PVDF membranes at 25 V for 2.5 h at RT in transfer buffer using the Xcell II Blot Module transfer system.

The membranes were washed in 1X tris-buffered saline solution (TBS) containing 0.1 % (v/v) tween 20 (TBS/T; wash buffer) for 15 min changing the wash buffer every 5 min. The membranes were then blocked in 5 % (v/v) BSA in TBS for 1 h at RT, rocking gently. The membranes were washed again and then incubated with 10 mL of the primary antibody solution containing the indicated primary antibodies (either a mouse monoclonal antibody, a rabbit monoclonal antibody, or both) in 5 % (v/v) BSA in TBS/T for 16-18 h at 4ºC on an orbital shaker. The primary antibody cocktail was removed, the membranes washed as before, and 10 mLs of the secondary antibodies conjugated to Starbright Blue 520, Starbright Blue 700, or Dylight800, and the hFab-rhodamine primary antibody were added at a 1:10,000 dilution in TBS with 0.1 % (w/v) casein (TBS/C; Bio-Rad; CA1610782) and 0.02% SDS for 1 h at RT, rocking gently. Next, the secondary antibody cocktail was removed, and the membranes were washed again as before.

The membranes were imaged using the Bio-Rad ChemiDoc MP system. Protein levels for each sample were quantified using the Bio-Rad Image Lab software and standardized to the β-tubulin signal for each sample, which had been standardized to the β-tubulin signal for the untreated control. The data for iNOS or COX-2 is presented as a ratio of standardized protein in each sample compared to the vehicle control ± S.D. The data for the pathway analysis is shown as the average reduction of the ratio of phosphorylated: non-phosphorylated protein

standardized using β-tubulin for each sample compared to the vehicle control for each biological replicate ± SD with the vehicle control set to 1.

***Nos2* Reporter cell imaging**

Nos2 reporter RAW 264.7 cells were obtained as a generous gift from the laboratory of Dr. David Nelson, generated as described in Ghosh *et al.* 2019[296] and were used to measure transactivation of the *Nos2* promoter. The promoter sequence contained both the proximal (−48 to −209 bp) and distal (−913 to −1029 bp) core promoter regulatory sites known to allow for NF-κB binding (+1 to -1200 bp) positioned immediately upstream of DNA coding for mCherryPEST[296]. The *Nos2* reporter cells were cultured in DMEM complete medium supplemented with 10 μg/mL puromycin for continued selection ($DMEM^+$), as the reporter also carried the puromycin resistance gene. The cells were grown at 37 ℃ in a humidified incubator with 5 % CO_2. Expression of mCherryPEST from the *Nos2* promoter was measured using confocal microscopy. For the assay, the cells were seeded as earlier described in a 35 mm tissue culture petri dish containing a #1.5 glass coverslip inlay (Cellvis, Mountain View, CA; D35-14-1.5-N) and allowed to attach for 16-18 h. The cells were then pretreated for 4 h with either 100 μM ATs, 10 μM dexamethasone (dex), 0.1 % (v/v) DMSO, or not in $DMEM^+$. The cells were washed in 1 X PBS then cotreated with 1 μg/mL LPS and incubated for 24 h. Following this incubation, the cells were imaged using a Zeiss LSM 700 confocal microscope (Zeiss, Oberkochen, Baden-Württemberg, Germany) equipped with a stage top incubator, XL-incubator, CO_2 control, and a Zeiss Plan-Apochromat 20x/0.8 m27 objective. mCherry fluorescence was excited using a 555 nm laser. The mCherry fluorescence signal of each cell was quantified using FIJI[207]. Briefly, the signal (RFU/A.U.) in each cell was measured and

divided by the measurement area of the whole cell (pixels; px) to get a value for signal/unit area. The RFU/px for an area with no cells in each image was subtracted from the signal as a background. For values where the background signal was higher than the measured cellular signal, the value was set to zero, as it is impossible to measure a negative fluorescent signal. The values shown are the average of 150 cells per treatment across three, independent biological replicates (*n = 150*). Outliers from each sample were detected using the ROUT method with a Q = 1 % using GraphPad Prism version 10.0.0-10.0.1 for Windows (GraphPad Software, Boston, Massachusetts USA, www.graphpad.com) then removed, yielding an n of 114 – 148 cells. The white point for each image was adjusted equally post-analysis for visualization.

Nuclear translocation of p65

Approximately $2x10^5$ RAW 264.7 cells were seeded in a 35 mm tissue culture petri dish containing a #1.5 glass coverslip inlay (Cellvis; D35-14-1.5-N). cells were allowed to attach overnight (16-18 h) then washed in 1 X PBS. The cells were then pretreated for 4 h with either 100 μM ATs or various controls, then cotreated with, or without, 100 ng/mL LPS for 15 min. The cells were washed twice with ice cold PBS and fixed in 3.7 % (v/v) formaldehyde for 10 min at RT. The cells were washed three times with chilled PBS. The fixed cells were then permeabilized and non-specific binding was blocked in a single step using PBS with 0.3 M glycine, 10 % (v/v) goat serum, and 0.5 % (v/v) Tween 20 for 1 h at RT. The cells were washed three times for 5 min and incubated overnight at 4°C in a 1:1000 dilution of rabbit anti-mouse p65 antibody in 5 % (v/v) goat serum in PBS with 0.1 % (v/v) Tween 20. Next, the primary antibody was removed, and the cells were washed three more times with PBS for 5 min each

Next, 200 µL of 1:200 dilution of goat anti-mouse IgG (H+L) cross-adsorbed secondary antibody conjugated to fluorescein isothiocyanate (FITC) (Invitrogen, MA; F-2761) in 10 % normal goat serum (ThermoFisher Scientific; 50062Z) was added to the center of the coverslip inlay and incubated at RT for 1 h. The secondary antibody was removed, and the cells were washed again three times for 5 min each, then 1 mL of PBS was added to the cells. To stain the nucleus with Hoechst33342, two drops of NucBlue Ready Probes were added and the cells were incubated for 15 min at RT. The PBS/NucBlue was removed, and the cells were washed once with PBS, and 200 µL PBS was added to the center well to prevent drying. The stained cells were then imaged using a Zeiss LSM 700 confocal microscope using 405 nm and 488 nm lasers to excite Hoechst33342 and FITC, respectively. The ratio of nuclear to cytoplasmic p65 was determined by measuring the blank corrected signal/ unit area for a small region of interest (ROI) for both the nucleus, excluding the nucleolus, and the cytoplasm as described earlier using FIJI[207]. Using the ratio of the signal divided by the unit area accounted for differences in the size of each ROI. Data is represented as the mean ratio–for 150 - 152 cells across three, independent biological replicates ± S.D., n = 150. Outliers from each sample were detected using the ROUT method with a Q = 1 % using GraphPad Prism version 10.0.0-10.0.1 then removed, yielding an – of 144 - 150 cells.

RNA extraction

RAW 264.7 cells or PMA-differentiated U937 cells were pretreated with 100 µM AT111, AT5, or various controls in duplicate for 4 h then cotreated with 1 µg/mL LPS, or not, for another 4 h. After treatment, cells from the duplicate wells for each treatment were harvested, pooled, and pelleted in ice-cold PBS at 300 x g for 5 min. The RNA was either

extracted immediately, or the cells were stored at -80 ℃ in RNAlater. The PBS was removed, and the RNA was extracted using the Maxwell® 16 LEV simplyRNA cells kit (Promega; AS1270) according to the manufacturer's protocol with no deviations using the Maxwell® 16 instrument by Promega. The quantity and purity of the RNA was determined using a NanoDrop Lite (ThermoFisher Scientific, MA). The quality of the extracted RNA was determined using a 1 % (v/v) Clorox® bleach agarose (1 % [w/v]) denaturing gel as described by Aranda *et al.*[297].

cDNA synthesis and qRT-PCR

cDNA was synthesized using the VERSO cDNA synthesis kit (ThermoFisher Scientific; AB1453A) according to the manufacturer's protocol using random hexamers and 1 ng of RNA. Assuming equal synthesis of cDNA across all samples, 1 µL of cDNA was amplified and quantified using the Maxima SYBR Green qPCR Master Mix (2X), with separate ROX vial (ThermoFisher Scientific; K0253) according to the manufacturer's protocol. Volumes of each solution were adjusted to a 10 µL final volume. The primers used are listed in Table 3. Thermocycling was performed using a Bio-Rad C1000 Touch thermocycler with a CFX96™ Real-Time System (Bio-Rad, CA)**.** Following the Maxima protocol, the initial denaturation was carried out at 95 ℃ for 10 min, then cDNA levels were amplified using 40 cycles of a denaturation step at 95 ℃ for 15 s followed by an annealing step at 60 ℃ for 30 s then finished with a 30 s extension at 72 ℃. Immediately after, a melt curve analysis, verifying the production of a single amplicon, was performed for each well by denaturing the DNA at 95 ℃ then the temperature was lowered to 53 ℃ and gradually increased by 0.5 ℃ every 5 s until 95 ℃ was reached.

Table 3. Primes for qPCR.

Gene	Direction	Sequence
TNF-α[298]	F	5' – AGCAAACCACCAAGTGGAGGA – 3'
Tnf	R	5' – GCTGGCACCACTAGTTGGTTGT – 3'
iNOS[299]	F	5' – CCCTTCCGAAGTTTCTGGCAGCAGC – 3'
Nos2	R	5' – GGCTGTCAGAGCCTCGTGGCTTTGG – 3'
IL-1β[299]	F	5' – TGCTTCCAAACCTTTGACCTGGGC – 3'
Il1b	R	5' – CAGGGTGGGTGTGCCGTCTTTC – 3'
IL-6[299]	F	5' – GTACTCCAGAAGACCAGAGG – 3'
Il6	R	5' – TGCTGGTGACAACCACGGCC – 3'
MCP-1[300]	F	5' – GCAGGTCCCTGTCATGCTTC – 3'
Ccl2	R	5' – ACAGCTTCTTTGGGACACCT – 3'
GM-CSF[299]	F	5' – ACTCTGCTCACGAAGGAACTCAGC – 3'
Csf2	R	5' – CACAGCTCGGAAGAGCATCGCA – 3'
COX-2[301]	F	5' – GGAGAGACTATCAAGATAGT – 3'
Ptgs2	R	5' – ATGGTCAGTAGACTTTTACA – 3'
GAPDH[299]	F	5' – CACTCACGGCAAATTCAACGGC – 3'
Gapdh	R	5' – CCTTGGCAGCACCAGTGGATGCAGG – 3'

Statistical analyses.

All statistical analyses were done using GraphPad Prism version 10.0.0-10.0.1 for Windows. The specific analysis for each experiment is indicated in the figure legend. All means were ± S.D.

RNA sequencing

Extracted RNA was sent to Novogene (Beijing, China/ Sacramento, CA) for next generation sequencing using the NovaSeq sequencing platform (Illumina, CA). RNA quality was determined by Novogene using an Agilent Bioanalyzer while sample quantification and purity was determined by nanodrop. QC results are shown in Appendix IV. Samples passing the quality control step were then processed by Novogene using a non-stranded/ non-directional protocol. To do this, mRNA was isolated from total RNA using poly-T

oligonucleotides immobilized on magnetic beads. The RNA was then fragmented, and first strand cDNA synthesis was performed using random hexamer primers. A second strand was synthesized in the same manner. The cDNA library was prepared by Novogene for use on Illumina systems using a NEBNext Ultra II RNA Library Prep kit for Illumina (New England BioLabs, MA; E7770S/L). The library was checked for quantity and size distribution using Qubit/real-time PCR and bioanalyzer, respectively. Libraries were pooled and sequenced, with a sequencing length of 150 paired end reads and 9 G per sample, on a NovaSeq 6000 sequencer (Illumina, CA). Data quality control, including checking for distribution of sequencing quality, error rate distribution, nucleotide distribution, and raw data quality composition was performed by Novogene. All samples had a Q30 score above 92 %.

RNA sequencing (RNAseq) analysis was done using the usegalaxy.org public server on the Galaxy web platform[302]. The resulting Fastq files containing the raw read data was uploaded to the server and quality of each file was checked using FastQC (Galaxy Version 0.73+galaxy0)[303].The FastQC files were then compiled in to a single report using the MultiQC tool (Galaxy Version 1.11)[304]. Due to the presence of adapter sequences, the reads were trimmed using Trimmomatic (Galaxy Version 0.38.0)[305] using a sliding window of 5 bases with an average quality of 20 and a minimum quality of 3. An initial "ILLUMINACLIP" step was performed to remove the adapter sequences:

5' adapter:
5' – AGATCGGAAGAGCGTCGTGTAGGGAAAGAGTGTAGATCTCGGTGGTCGCCGTATCATT – 3'
3' adapter:
5' – GATCGGAAGAGCACACGTCTGAACTCCAGTCACGGATGACTATCTCGTATGCCGTCTTCTGCTTG – 3'

An additional FastQC[303]/MultiQC[304] analysis was carried out on the trimmed paired output reads. The trimmed reads were aligned to either the Genome Reference Consortium Human

Build 38 patch release 14 (hb38; downloaded from National Center for Biotechnology Information) for human RNA or the Genome Reference Consortium Mouse Build 39 (mm39; downloaded from Ensembl.org) for murine RNA using HISAT2 (Galaxy Version 2.2.1+galaxy0)[306] leading to a binary alignment/map (BAM) file. Quality and statistics of the alignments were determined using SAMtools (Galaxy Version 2.0.3)[307-309] and MultiQC[304] for each of the BAM files. The reads were then assembled to the reference genomes using StringTie (Galaxy Version 2.1.7+galaxy1)[310,311] set to output a file for differential expression then merged using the StringTie merge tool (Galaxy Version 2.1.7+galaxy1)[310,311]. The number of each reads for each gene were counted, and pre-processed for differential expression analysis, using the htseq-count tool (Galaxy Version 0.9.1), using the HISAT2 BAM files with the merged StringTie output[312]. The transcript counts were analyzed for clustering and differential expression across the treatment groups using DESeq2 (Galaxy Version 2.11.40.7+galaxy1)[313]. One replicate from the untreated, the vehicle, and AT111 samples were not used in the mouse differential gene analysis due to the lack of clustering revealed by principal component analysis (PCA) using DESeq2[313]. Differentially expressed genes (DEGs) were annotated using the Annotate DESeq2/DEXSeq tool referencing the StringTie merge output. Volcano plots were created with the Volcano plot tool on the Galaxy web platform (Galaxy Version 0.0.5) using annotated DESeq2 files with a significance threshold of 0.05 and a log2FC of ± 1. DEGs were considered biologically relevant with an adjusted (adj.) p-value of 0.05 or less and an absolute fold change ≥ 2 (absolute $\log_2$FC ≥ 1). Genes that had a normalized count average of 0.5 counts per million or less (average normalized count ≤ 15) across *all* samples were excluded from analysis. For example, if all samples had 15 counts or

less on average the gene would be excluded. If all samples had an average count of ≤ 15 but one, the gene would be retained. Additionally, all genes where an adj. p-value could not be determined either by instances of no counts or low counts, were excluded. Gene enrichment analysis was carried out using Database for Annotation, Visualization, and Integrated Discovery (DAVID; v2023q2)[314-316]. DEGs were examined for enrichment compared to a background of the total genes probed which passed the count requirement stated earlier[317]. Some genes, mainly consisting of predicted genes and non-coding RNAs (GM [mouse], LOC [human]), could not be identified by DAVID. Other genes, including named genes, long non-coding RNAs (lncRNA), and pseudo-genes, that could not be initially identified by DAVID were examined for aliases using the GeneCards Suite for human genes[318,319] and the Mouse Genome Index for murine genes[320-322]. Successful identifications of these genes were added to the DAVID list of both DEGs and background genes. Gene ontology (GO) and annotations were done using the GOTERM_BP_Direct, GOTERM_CC_DIRECT, GOTERM_MF_DIRECT, and INTERPRO categories. Terms passing an EASE score (p-value) and FDR[323] ≤ 0.05, with a minimum pathway size = 2, were selected as significant. Using the ShinyGO (v0.77) platform[324], DEGs were mapped to various pathways via the Kyoto Encyclopedia of Genes and Genomes (KEGG)[325] and subsequent figures were rendered using Pathview[326]. Venn diagrams comparing upregulated and downregulated DEGs of different treatments made using Venny (v2.1)[327]. Heatmaps and cluster diagrams were constructed using the heatmap2 function of gplots[328] and GO graphs were constructed using the ggplot2 (3.4.3)[329] library in RStudio[330,331]. Search Tool for Retrieval of Interacting Genes/Proteins (STRING) network clusters and visualization were done using the STRING network[332] app within

Cytoscape[333]. To do this, annotated genes were first converted into corresponding ensemble IDs through DAVID and uploaded into the Cytoscape application. Genes without corresponding ensemble IDs, i.e., most non-protein coding genes, were excluded. The network was then "STRINGified" using medium confidence (0.4) and genes with multiple ensemble IDs were curated to the ones included in the STRING network, and annotated gene names were assigned to the remaining genes along with other attributes from the Annotate DESeq2 output files, including fold change and adj. p-value.

4.3 Results and discussion:

To examine the anti-inflammatory effect of ATs on LPS-stimulated RAW 264.7 macrophages, 47 ATs were screened for their ability to reduce levels of nitrite, an end product of NO metabolism[334], used as an indirect measurement of NO production and therefor the inflammatory response. To do this, RAW 264.7 cells were initially treated with 100 ng/mL LPS alone for 24 h, washed with PBS, then treated with 100 µM ATs in 1.0 % (v/v) DMSO, or various controls, without LPS for an additional 24 h. Out of the 47 ATs screened, 26 ATs caused a significant reduction in nitrite compared to the LPS-medium control. However, none showed any significant reduction compared to the vehicle control (1.0 % [v/v] DMSO; Figure 14 A). The reason for this is two-fold. First, this experimental design was incidentally a demonstration of the ability of ATs to reduce inflammation after the removal of inflammatory stimuli. Upon removal of LPS after 24 h there was no additional LPS-induced inflammatory response. Although there could have been more stimuli from secreted cytokines. Secondly, 1.0 % (v/v) DMSO is biologically active and has been shown to have anti-inflammatory activities, as well[335]. Additionally, for unknown reasons, the amount of nitrite secreted from the RAW 264.7

cells in response to LPS stimulation varied from biological replicate to biological replicate. However, the trends in biological activity from each AT or control remained rather consistent when compared to the average positive or vehicle control from respective plates. Because the focus of this chapter is to explore the effect of ATs on the inflammatory response induced by LPS, it is reasonable to examine the trends in biological activity rather than focus on the actual concentration of RNS, cytokine, or chemokine produced. As such, for this experiment, the levels of nitrite in each well were standardized as a ratio to the *average* value of the LPS-medium control for each plate. Though there was no statistical difference between the vehicle control and the ATs; AT1, AT3, AT5, AT100, and AT141 did slightly reduce levels of secreted nitrite compared to the vehicle alone, with AT5 having the most effect at a ratio of 0.30 ± 0.2 A.U. compared to the vehicle's 0.52 ± 0.19 A.U. (Figure 14 A and B). In addition to determining the background effect of 1.0 % (v/v) DMSO, this experiment also provided insight into the bioactivity of various ATs. Though none of the ATs were able to cause a stronger anti-inflammatory response than the vehicle, there were 12 ATs which decreased cell viability. Both AT2 and AT4 caused significantly more cell death than the vehicle control, with only 27.1 ± 10.9 % and 42.7 ± 14 % ($p<0.001$ and $p<0.05$, respectively) compared to 66.4 ± 23.2% cell viability (Figure 14 C and D). Notably, AT124 and AT132 were the most potent with cell viabilities of only 17.9 ± 7.4 % and 21.5 ± 7.3 % (Figure 14 C and D).

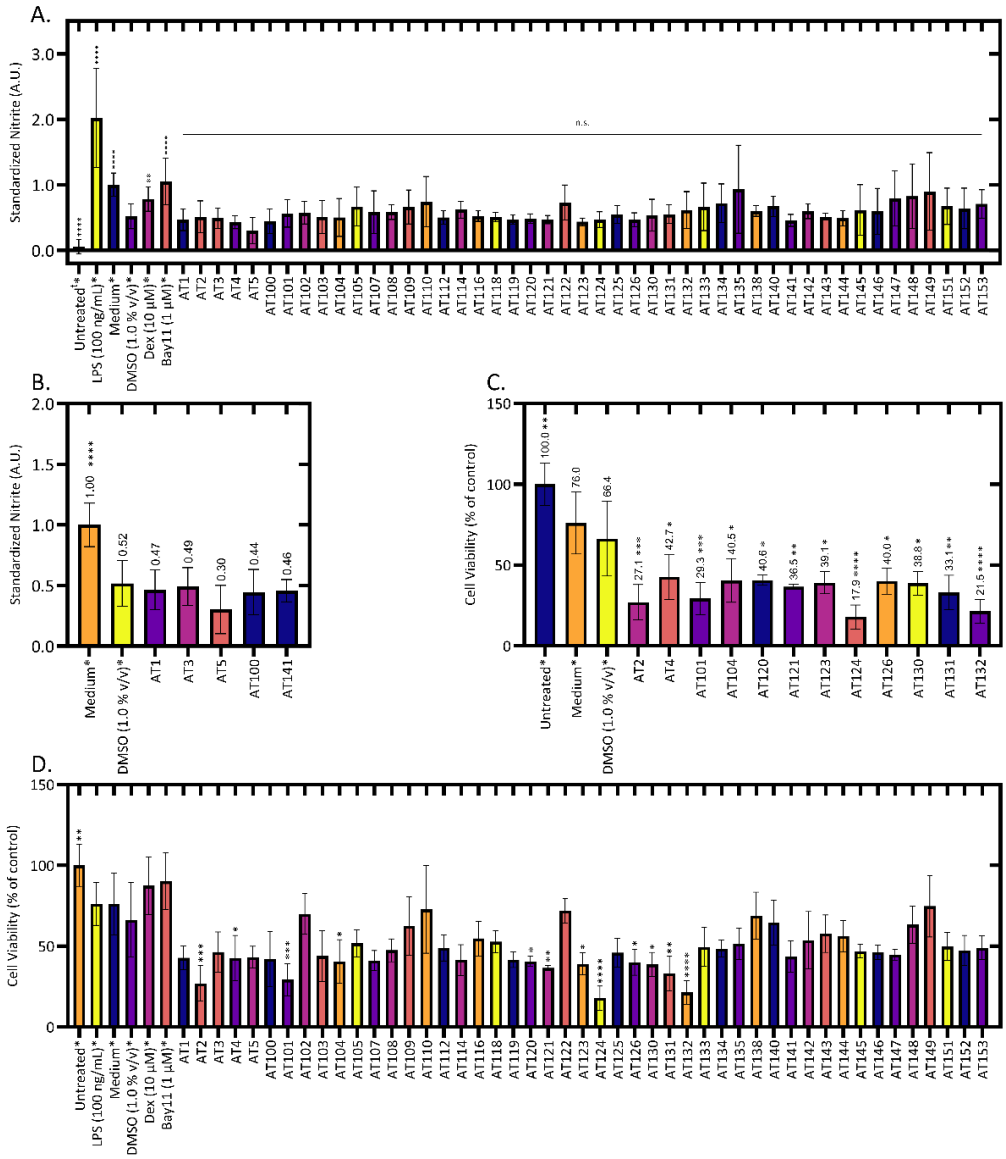

Figure 14. Screen of ATs in 1.0 % (v/v) DMSO. RAW 264.7 cells were stimulated with LPS for 24 h then treated with the indicated ATs (100 µM) or controls for another 24 h without LPS. A and B. Relative secreted nitrite levels for all ATs (A) and ATs which had the most effect on nitrite production (B). C and D. Percent cell viability for ATs with statistically significant effects (C) and all ATs (D). Data for each *plate* was compared to the average appropriate control (Medium*; A and B, and untreated; C and D) for that plate to account for plate-to-plate

variation. Data is represented as the mean ratio or percent of each control ± S.D. [t]Negative values, where the signal was less than the blank, were set to zero. The data was measured for each AT in triplicate across 3-4 biological replicates for an n of at least 9. *Controls were measured in triplicate across 10 plates over 4 days for a total n = 30. Statistical significance for each treatment compared to the respective control was measured using a Brown-Forsythe and Welch ANOVA with a Dunnett T3 multiple comparisons test to the vehicle control. *p<0.05, **p<0.01, ***p<0.001, ****p<0.0001.

To determine the effect of the vehicle as well as to examine the bioactivity of ATs at various concentrations, a dose response analyses was performed using certain ATs which may have some effect either on cell viability or nitrite secretion from the initial screen (Figure 14). Additionally, the anti-inflammatory compound Aurone 9067, describe by Park *et al.*(2017)[72], was used as a benchmark compound. All treatments, except for 0.5 % (v/v) DMSO, were able to lower levels of secreted nitrite when compared to cells treated with LPS for 24 h followed by medium for 24 h (Figure 15 A). However, when compared to the respective vehicles, there were few significant effects. Compared to the 1.0 % (v/v) DMSO vehicle, no compounds statistically lowered nitrite levels, while 9067 and dexamethasone seemed to have higher nitrite levels (Figure 15 B). The apparent lack of effect of 9067 was unexpected and differed from the originally published findings. The comparative effects of dexamethasone at 10 μM may be due to the fact that, though it is anti-inflammatory, it is not resuspended in 1.0 % (v/v) DMSO, and thus the vehicle (0.016% [v/v] DMSO) for that compound may be below a concentration where it exerts a biologically noticeable effect. This discrepancy has no real effect on the assay, as

the dexamethasone was used as an anti-inflammatory control, thus demonstrating that DMSO itself reduces the levels of nitrite produced in response to LPS greater than that of a known anti-inflammatory. This observed anti-inflammatory effect of DMSO at this concentration is in agreement with the findings of Elisia *et al.* where 1.0 % (v/v) DMSO had a significant impact on levels of nitrite within the supernatant of LPS treated murine macrophages[335]. As concentrations of DMSO were reduced along with dosage, certain ATs were seen to lower nitrite more than their respective vehicle (Figure 15 C and D). For example, at 75 μM AT3, AT124, and AT132 all led to a significantly greater reduction in levels of nitrite than 0.75 % DMSO, reducing relative levels of nitrite to .42 ± 0.10 A.U., 0.38 ± 0.06 A.U., and 0.46 ± 0.09 A.U. compared to 0.71 ± 0.25 A.U., respectively (Figure 15 C). At 50 μM, only AT124 showed a statistical effect limiting nitrite production to 0.44 ± 0.06 A.U. of the positive control compared to 0.5 % (v/v) DMSO (0.78 ± 0.28 A.U.; Figure 15 D). Although there was an observed effect of AT3, AT124, and AT132 that was greater than the vehicle, this can be attributed to a cytotoxic effect caused by these aurones at the various concentration (Figure 15 E-H). All ATs, excluding AT5 at both 75 μM and 50 μM lowered cell viability compared to the positive control. When compared to their respective vehicle controls, all ATs with the exception of AT5, at all concentrations, showed a reduction in cell viability (Figure 15 F-H). This suggests that the nitrite reduction observed may be augmented by a decreased number of cells present to produce NO, with the exception of AT5. Though it was not statistically significant, AT5 at 100 μM led to the reduction of nitrite levels to 0.38 ± 0.18 A.U. compared to its corresponding vehicle control (0.71 ± 0.25 A.U.) while at 75 μM and 50 μM it led to 0.46 ± 0.15 A.U. and 0.55 ± 0.10 A.U. (Figure 15 B-D).

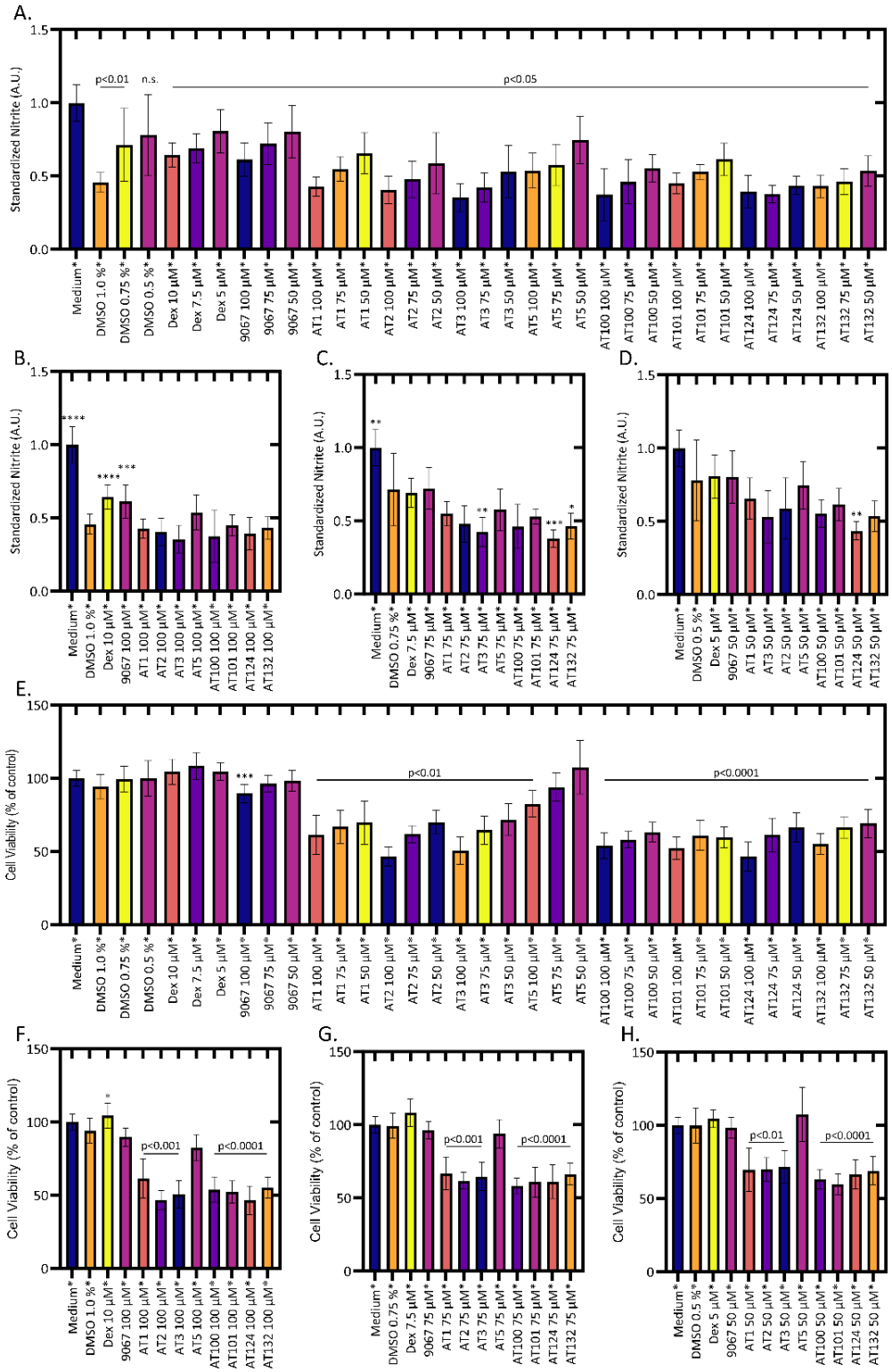
A.
Standardized Nitrite (A.U.)
p<0.01
n.s.
p<0.05
B.
C.
D.
E.
Cell Viability (% of control)
p<0.01
p<0.0001
F.
G.
H.
p<0.001
p<0.0001

Figure 15 Dose-dependent response to various ATs. RAW 264.7 cells were pretreated with 100 ng/mL LPS for 24 h then cotreated, or not, with the indicated controls or ATs at the indicated doses. A. Relative nitrite production for ATs at all concentrations (plate-standardized to the positive [medium*] control), subdivided into 100 μM (B), 75 μM (C), and 50 μM (D). E. Percent cell viability for ATs at all concentrations (plate-standardized to the positive [medium*] control), subdivided into 100 μM (F), 75 μM (G), and 50 μM (H). Statistical analysis for A and E was done using a Brown-Forsythe and Welch ANOVA with a Dunnett T3 multiple comparisons test compared to the positive (Medium*) control, while B, C, D, F, G, and H were compared to their relative vehicle (DMSO*) controls. Controls were done in triplicate across 5 biological replicates (n = 15) encompassing three biological replicates for the diluted ATs (n = 9). *P < 0.05, **P < 0.01, ***P< 0.001, and ****P < 0.0001.

Since there was an observed cytotoxic effect of most ATs, it was decided to examine the effect of each of the compounds on the cell viability of RAW 264.7 cells after 24 h. Similarly to the observations in LPS, all examined ATs led to a statistical decrease in cell viability compared to the untreated control except for AT5 (Figure 16). Additionally, both AT5 and AT145 were not statistically different from the 1.0 % (v/v) DMSO control. The lack of statistical significance for AT145 is potentially due to the high variability of the vehicle, as AT145 reduced cell viability to 53.6 ± 8.7 % of the untreated cells whereas the vehicle only reduced cell viability to 86.9 ± 30 % (Figure 16).

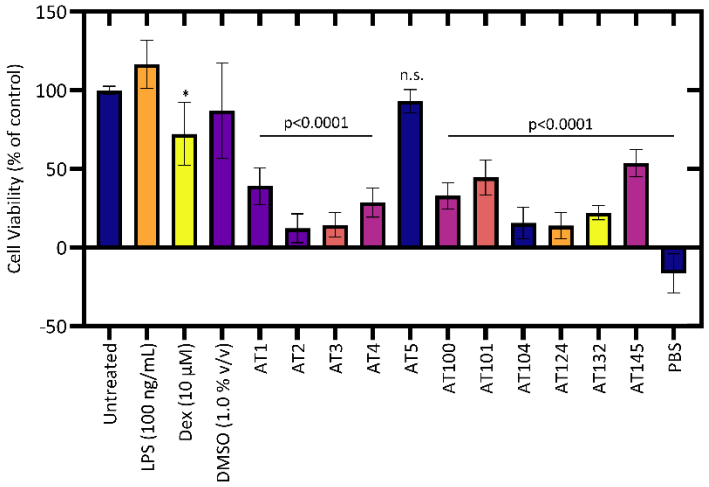

Figure 16. The effect of ATs on cell viability after 24 h. RAW 264.7 cells were treated with 100 µM ATs in 1.0% DMSO or the various controls, without LPS, for 24 hours. The data is displayed as the percent viability compared to the untreated control. This was done in three separate wells across three biological replicates $n = 9$. One biological replicate of the untreated control was used in Figure 3A and previously published in Bryant *et al.* 2022[1]. Statistical significance for each treatment was determined using a Brown-Forsythe and Welch ANOVA with a Dunnett's T3 multiple comparisons test, compared to the untreated control; *p<0.05.

To reduce the effect of DMSO, each AT was resuspended at a concentration of 100 mM in 100 % DMSO, so that the AT's final concentration of 100 µM contains only 0.1 % (v/v) DMSO as a cosolvent, which has been previously shown to have a weaker biological effect[335]. Though 0.1 % (v/v) DMSO may still affect various cellular processes that may impact certain biological assays, including the detection of NO using a Griess reagent system, the effect is weak enough to still calculate significance[335]. The experiment was then repeated where RAW

264.7 cells were treated with LPS for 24 h then treated with 100 μM ATs in 0.1 % (v/v) DMSO, or various controls, without LPS, for 24 additional hours (Figure 17). Compared to the DMSO (vehicle) control, all ATs except for AT5 seemed to have caused a statistical reduction in nitrite (Figure 17 A). The positive LPS-medium control had more nitrite produced than the vehicle (1.28 ± .19 A.U.), demonstrating the still present, but not statistically significant, effect of 0.1 % (v/v) DMSO (Figure 17 A) for this experiment. Interestingly, AT5 had only a slight, but not statistically significant effect on relative nitrite levels, reducing them to 83.7 ± 8.9 % of the vehicle (Figure 17 A). All ATs also reduced cell viability to below 75 % of the vehicle, with AT5 having the least effect (71.3 ± 5.9 %), AT2 having the second least effect (59.9 ± 7.0 %), and AT3 having the strongest effect, reducing cell viability to 54.4 ± 3.2 % of the vehicle (Figure 17 B).

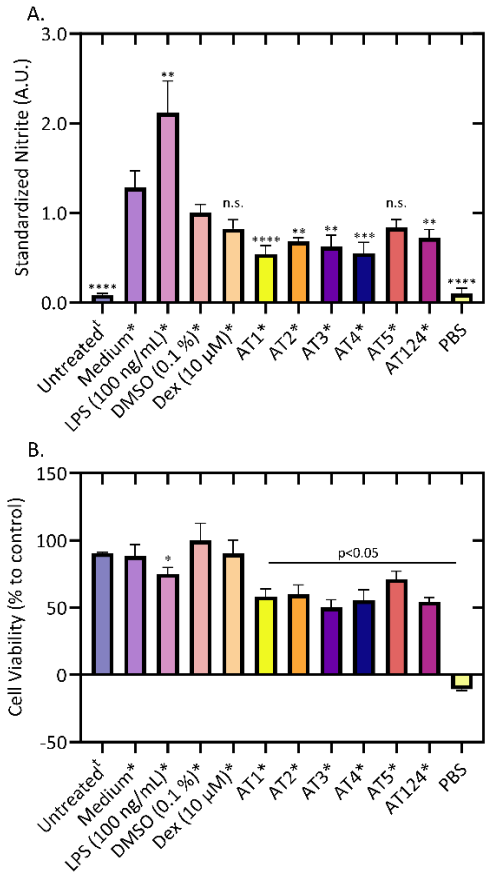

Figure 17. Effect of ATs in 0.1 % DMSO. RAW 264.7 cells were pretreated with 100 ng/mL LPS for 24 h, then *treated with the various ATs or controls for an additional 24 h. Relative levels of nitrite in the supernatant (A) and percent cell viability (B) were measured. The data is represented as a ratio or percentage of the vehicle (0.1% [v/v] DMSO). The data was measured in triplicate for 2 biological replicates, n = 6. †n = 3 from one biological replicate. Statistical significance for each treatment compared to the respective control was determined using a Brown-Forsythe and Welch ANOVA with a Dunnett's T3 multiple comparisons test, compared to the vehicle control. *p<0.05, **p<0.01, ***p<0.001, ****p<0.0001.

Though these experiments shed some light on the ability of ATs to possibly decrease the levels of NO produced after the stimuli has been removed, this did not reveal the effect of ATs on NO production during continuous exposure to LPS, nor whether pre-incubation with ATs could inhibit the macrophage response to LPS. In order to study the effect of the ATs during the inflammatory response, it was initially determined that RAW 264.7 cells should be pretreated with LPS for 12 h then cotreated with the ATs or controls for an additional 12 h with LPS. This showed that all ATs had a potent effect on NO production (< 61% of the vehicle control, $p<0.001$; Appendix III; Figure S1), and that only AT2 lowered cell viability compared to the vehicle.

4.3.1 Cotreatment with ATs for 24 h.

To see the effect of the ATs from the onset of inflammation, it was decided that RAW 264.7 cells should be treated with both LPS and ATs, or controls, simultaneously. RAW 264.7 cells were cotreated with AT1, AT2, AT3, AT4, AT5, AT124, or various controls, with 100 ng/mL LPS for 24 h. All ATs were able to significantly reduce nitrite levels in the supernatant compared to the vehicle control (Figure 18 A) while being more of an effect than both dexamethasone (10 μM) and Bay 11-7082 (1 μM). However, all ATs, except for AT5, reduced cell viability to < 65 % of the untreated cells (Figure 18 B).

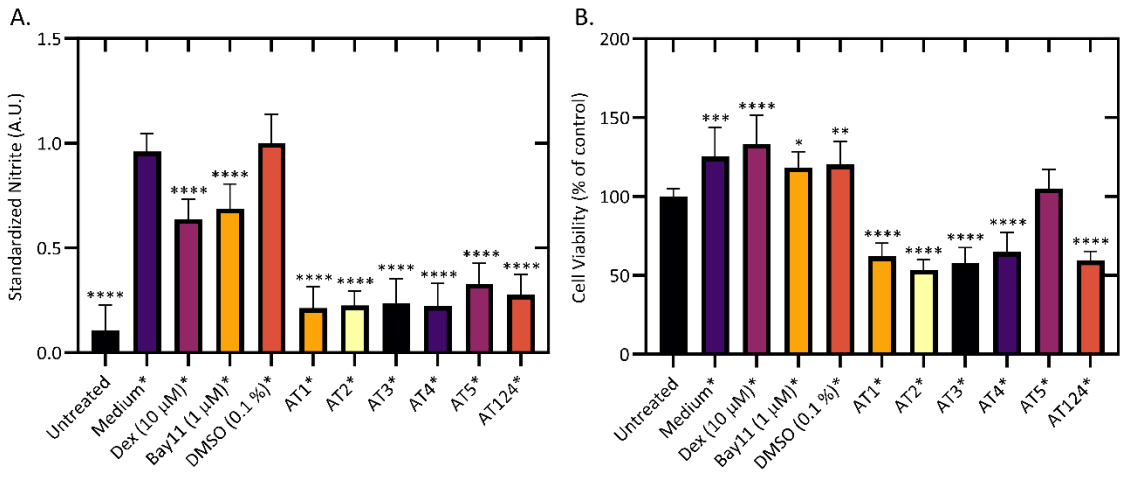

Figure 18. Effect of ATs on both nitrite production and cell viability. RAW 264.7 cells were cotreated with LPS and 100 μM ATs or various controls for 24 h and relative levels of nitrite in the supernatant (A) and percent cell viability (B) were determined. Each treatment was run in triplicate wells for three biological replicates for an n = 9. The data is presented as either a ratio or percentage of the average signal of the vehicle (A) or untreated (negative; B) control from each biological replicate. Statistical significance was determined for each treatment compared to the respective control using a one-way ANOVA with Dunnett's multiple comparisons test. *p<0.05, **p<0.01, ***p<0.001, ****p<0.0001.

All controls also showed a statistical *increase* in cell viability compared to the untreated cells (Figure 18 B). This is perplexing as LPS-induced cytotoxicity in RAW 264.7 cells has been shown at concentrations above 2 μg/mL[336] while another study showed that LPS-induced toxicity occurred at concentrations as low as 1 ng/mL, though only at 48 h, not 24 h[337]. Incidentally, only AT5 did not have a statistical difference between the cell viability of the

vehicle control cells and the untreated cells (Figure 19 B). Since AT5 seemed to reduce nitrite effectively with minimal effect on cell viability, it was selected for further analyses.

In addition to stimulating NO production, LPS also leads to the induction of pro-inflammatory cytokines and chemokines such as TNF-α, MCP-1, GM-CSF, or IL-6. To determine the effect of AT5 on the relative cytokine production, the levels of secreted cytokines from the cells used for Figure 18 were measured using an addressable LASER-bead immuno-assay (ALBIA) performed by Eve Technologies (Alberta, Canada). As with the previous experiments, when examining the concentration of each cytokine/ chemokine for each well, it is apparent that the RAW 264.7 cells responded more strongly to LPS stimulation for some biological replicates vs. others, leading to the inconsistent production of the indicated proteins (Figure 19 A).

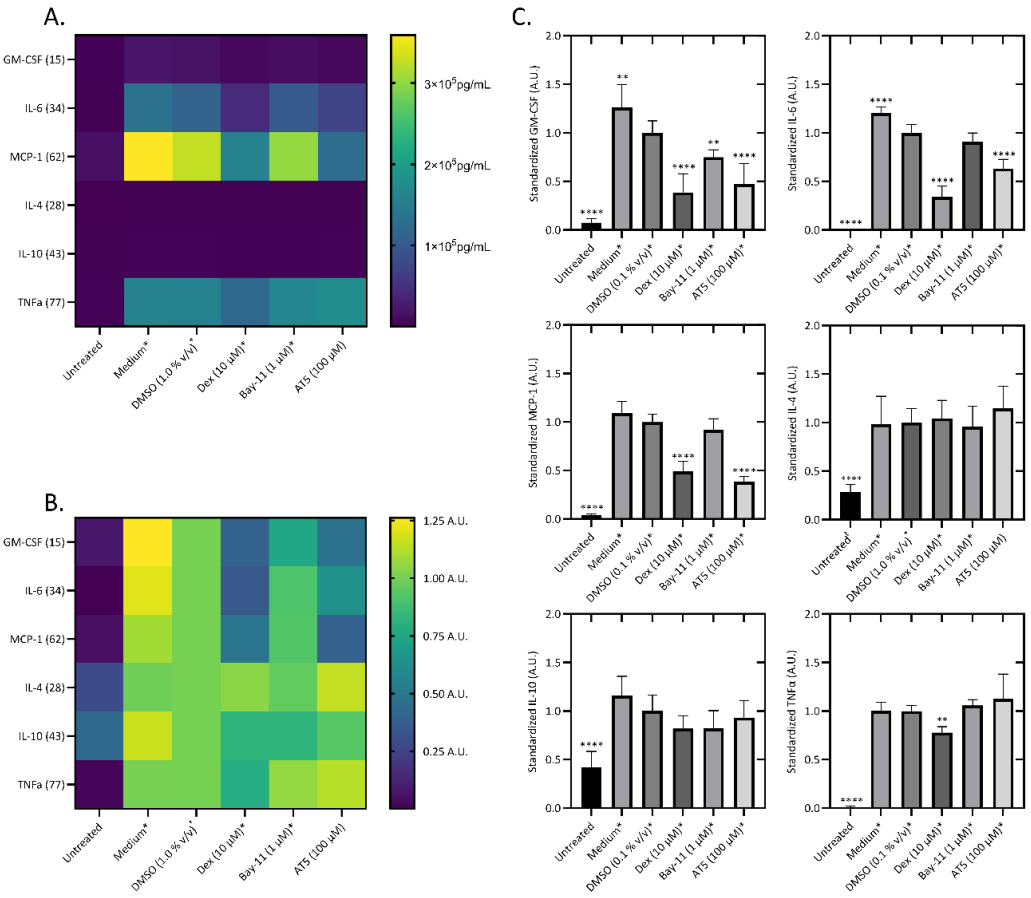

Figure 19. Effect of AT5 on inflammatory cytokine and chemokine production. RAW 264.7 cells were cotreated with 100 μM AT5 or various controls for 24 h. A. Average concentration of the indicated cytokines/chemokines determined by ALBIA. B. Relative levels of each indicated cytokine/chemokine compared to the vehicle control. C. Graphical representation of B. Supernatants previously collected for Figure 19 A were diluted 1:20 and sent to Eve Technologies. The concentrations of each indicated protein were measured in a multiplexed system for each replicate. Supernatants were collected from triplicate wells for three biological replicates, n = 9. [t]Some values were below the limit of detection and omitted. Statistical analysis was performed using a one-way ANOVA with Dunnett's multiple comparisons test compared to the vehicle control. **p<0.01, ****p<0.0001.

When examining the trends as a ratio to the vehicle control for each biological replicate the inter-plate effect is removed, allowing for better visualization of the effect of AT5 on the LPS-induced cellular response (Figure 19 B and C). When analyzed this way, treatment with 100 μM AT5 led to a significant decrease in the levels of pro-inflammatory proteins GM-CSF (0.47 ± 0.21 A.U.), MCP-1 (0.38 ± 0.06 A.U.), and IL-6 (0.63 ± 0.09) compared to the 0.1 % (v/v) DMSO (vehicle) control (Figure 20 A-C). Though AT5 reduced GM-CSF, MCP-1, and IL-6, it had little effect on TNF-α production (Figure 19). Additionally, AT5 had minimal effect on the relative levels of IL-4 and IL-10 (Figure 19). Both IL-4 and IL-10 are upregulated by an inflammatory stimuli and act as part of a negative feedback mechanism, which switches macrophages from a pro-inflammatory M1 state to a wound healing M2 state[338].

Since there was a measurable decrease in the relative levels of some pro-inflammatory cytokines, the effect of AT5 on their transcription was examined. To do this RNA was extracted from RAW 264.7 cells cotreated with AT5 and 100 ng/mL LPS, LPS only, or medium only, for 18 h. The quantity and quality of the extracted RNA was determined using a nanodrop and a 1.0% (w/v) agarose gel containing 1.0% (v/v) Clorox® bleach as described by Aranda *et al.*[297]. Since there was no apparent degradation in either the 28S or 18S subunits of the ribosomal RNA (Appendix III; Figure S2), 1 ng of the extracted RNA was converted into cDNA using the Verso cDNA synthesis kit (ThermoFisher Scientific; AB1453B). Quantity of cDNA for the pro-inflammatory genes, iNOS (*Nos2*), IL-6 (*Il6*), IL-1β (*Il1b*), GM-CSF (*Csf2*), MCP-1 (*ccl2*), TNF-α (*Tnf*), and COX-2 (*Ptgs2*) were measured using qPCR.

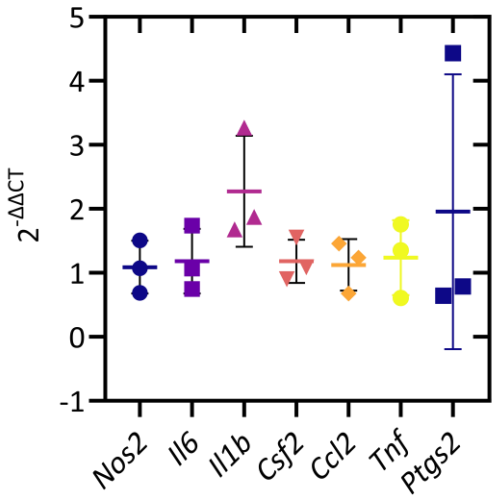

Figure 20. Relative changes in levels of inflammatory response genes. RNA was extracted from RAW 264.7 cells cotreated with AT5 (100 µM) and 1 µg/mL LPS, LPS only, or medium only for 18 h. Equivalent amounts of RNA were converted into cDNA for each sample. The difference in relative levels of gene expression was determined using the ΔΔCT method, for AT5 + LPS compared to LPS only, using GAPDH as the standardization control. The data is represented as the relative fold-change for three, independent biological replicates. Each biological replicate consists of two technical replicates averaged together, n = 3. Technical replicates with no amplification were excluded from the analyses.

In contrast to the levels of cytokines and chemokines present in the supernatant, AT5 had little effect on their transcription 18 h-post treatment (Figure 20). However, AT5 increased levels of IL-1β to a fold change of 2.33 ± 0.82 A.U. higher than the LPS only control (Figure 20). *Il1b*, the gene encoding IL-1β, is transcribed in cells post-interaction with an inflammatory

stimuli such as LPS[339]. *Il1b* is then translated into pro-IL-1β where it is present in the cytosol[339]. Typically, pro-IL-1β is cleaved into mature IL-1β by the inflammasome, allowing for its export from the cell. However, RAW 264.7 cells lack the ASC protein subunit required for NLRP3 inflammasome formation, thus IL-1β is not released from the cell[340]. The upregulation of *Il1b* after 18 h in AT5 treated cells needs further study as it seems that AT5 diminished the levels of other pro-inflammatory cytokines. Further research is warranted to examine the down-stream levels of pro-IL-1β.

Preliminary western blot analysis of protein levels for COX-2 showed that AT5 had minimal effect (Appendix III; Figure S3A), while iNOS seemed to be decreased slightly in one replicate (Appendix III; Figure S3B). Both iNOS levels and COX-2 levels seemed to be in agreement with the relative levels of mRNA.

The discrepancy between mRNA after 18 h and protein levels after 24 h for the inflammatory cytokines is possibly due to the time point examined. 18 h is relatively late with regard to the LPS-induction of cytokine RNAs. For example, Das *et al*. (2015) found that *Tnf Il1b,* and *Nos2* RNA levels peaked between 2 and 6 h post-LPS treatment in BV-2 murine microglial cells[341]. Xie *et al*. (2018) showed that RNA levels *IL1B*, *IL6*, and *IL8* as well as multiple chemokines peaked between 4 and 6 h post-LPS treatment in human gingival fibroblasts[342]. However, another study showed that *Il6* RNA levels were at their peak 18 h post-LPS treatment in RAW 264.7 cells, but that *Il10, Tnf,* and *Il1b* RNA levels peaked between 2 and 6 h[343]. A large variety of studies seem to examine RNA levels from 1-6 h post-LPS treatment[341-346], though Ye *et al.* (2019) chose to measure RNA levels 24 h post-treatment[347]. With the majority of recent articles showing peak RNA levels for most cytokines prior to 18 h,

it is plausible that AT5 has an effect on RNA levels at earlier time points but has minimal effect on RNA levels at 18 h, with the exception of *Il1b*. As such, future analysis of the affect ATs have on RNA levels of pro-inflammatory response genes will be investigated at 4 h post-LPS treatment.

To determine if AT5 has a dose-dependent effect on LPS-induced NO production in macrophages, RAW 264.7 cells were cotreated with various concentrations of AT5, or controls, and 100 ng/mL LPS for 24 hours and nitrite levels in the supernatant was measured as before. Similar to earlier findings at 100 μM, cells treated with AT5 at concentrations above 50 μM had significantly reduced levels of nitrite compared to the vehicle control (Figure 21 A) with a half inhibitory concentration (IC_{50}) of 178.4 μM (Figure 21 B). Cell viability for each dose was statistically similar to the untreated control (Appendix III; Figure S4), indicating no cytotoxicity at 24 h.

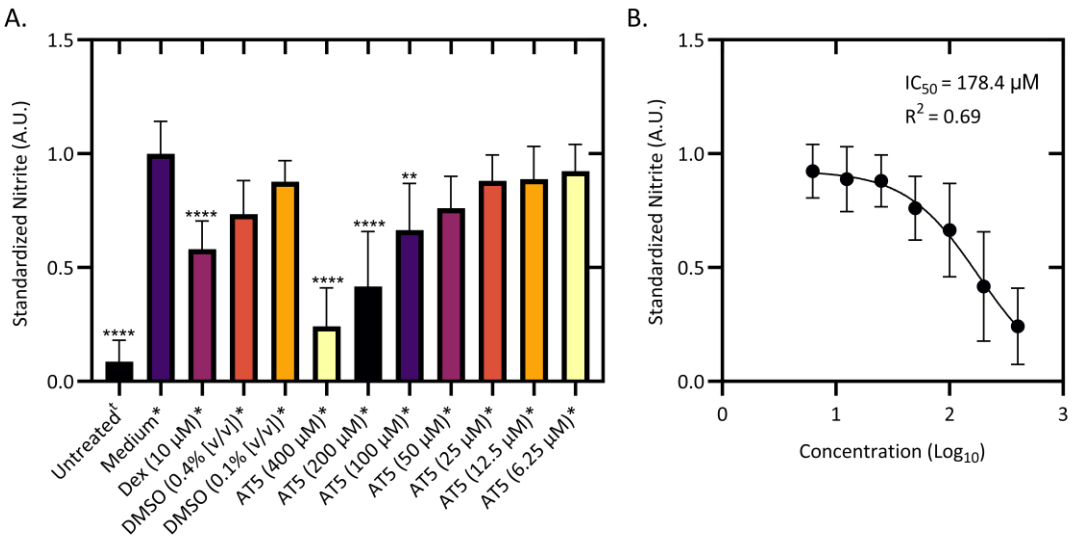

Figure 21. Dose dependent effect of AT5 on LPS-induced NO production. RAW 264.7 cells were cotreated with different concentrations of AT5, or control, and LPS for 24 h. A. Relative levels of nitrite standardized as a ratio to the positive control (0.1% [v/v] DMSO) for each biological replicate. B. IC_{50} value determined by plotting a non-linear fit to the ratio over the log_{10} concentration of AT5. Each data point is represented as the mean ratio of the positive control performed in triplicate for five independent biological replicates, n = 15. Statistical significance for A. was determined using a one-way ANOVA with a Dunnett's multiple comparisons test compared to the vehicle control. Negative values, where the signal for the treatment was less than the blank, were set to zero. *$p<0.05$, ***$p<0.001$, ****$p<0.0001$.

AT5 was not as potent at 100 μM as previously shown in Figure 18. In this experiment, at 100 μM only lowered nitrite to 75.0 ± 20.6 % of the vehicle control and only 66.4 ± 20.5 % of the positive control (Figure 21). AT5 used in the initial two biological replicates had more of an effect on nitrite levels in the supernatant compared to the last three replicates (Appendix III; Figure S5 A). Between the first two replicates and the subsequent three replicates, a new vial of RAW 264.7 cells were ordered from ATCC. These RAW 264.7 cells had a lower passage number. These new cells were also validated to be free of mycoplasma contamination (Appendix III; Figure S6). Alternatively, after the first two experiments, a new preparation of AT5 was acquired and thought to have been different from the other preparations. Comparing the fluorescent spectra of the new batch of AT5 to another later batch which had been confirmed to be AT5 using NMR, showed distinct differences (data not shown). These differences may have been due to either variation in dilution or structure. In subsequent experiments, AT5 was validated rigorously to avoid this issue. Comparing relative NO production between the biological replicates of the old and new cells, AT5 had a lesser effect in the lower passage cells (Appendix III; Figure S5 A). AT5 at 400 μM with the previous cells was able to cause a reduction of nitrite in the supernatant to 0.062 ± 0.029 A.U. compared to only 0.363 ± 0.089 A.U. in the lower passage cells ($p<0.0001$, Appendix III; Figure S5 A). Although this may indicate differences in AT5, dexamethasone (10 μM) also had less of an effect with the low passage RAW 264.7 cells, originally reducing relative NO levels to 0.460 ± 0.084 A.U. of the control with the higher passage cells, compared to only 0.660 ± 0.068 A.U. in the lower passage cells ($p<0.01$, Appendix III; Figure S5 A). Additionally, ELISAs of GM-CSF and MCP-1 from the first two biological replicates revealed strong bioactivity of AT5 (Appendix III; Figure S5

B and C) where in later experiments, though with different treatment times, AT5 had minimal activity. (Figures 27 and 30). Due to the different RAW 264.7 cells or batch to batch differences in ATs, or both, AT5 had less bioactivity from this point onward.

The initial inflammatory response of macrophages to LPS is due to the TLR4-MyD88 dependent signaling pathway, which leads to the phosphorylation, and subsequent nuclear localization, of p65 (RelA)-containing NF-κB transcription factors, and the phosphorylation of MAPKs, including p38[73,259,266,267]. To determine if the effect of AT5 on the expression of pro-inflammatory cytokines was due to modulation of the LPS-TLR4-MyD88 pathway, RAW 264.7 cells were stimulated with LPS and AT5, LPS and DMSO, or medium only for 15 min, and levels of phosphorylated p65 (Ser538) and p38 (Thr180/Tyr182) were normalized to levels of non-phosphorylated p65 and p38 as a ratio then relative levels were determined compared to the DMSO control. After 15 min, cells treated with AT5 showed no difference in phosphorylated p65 and p38 compared to the vehicle control (Figure 22).

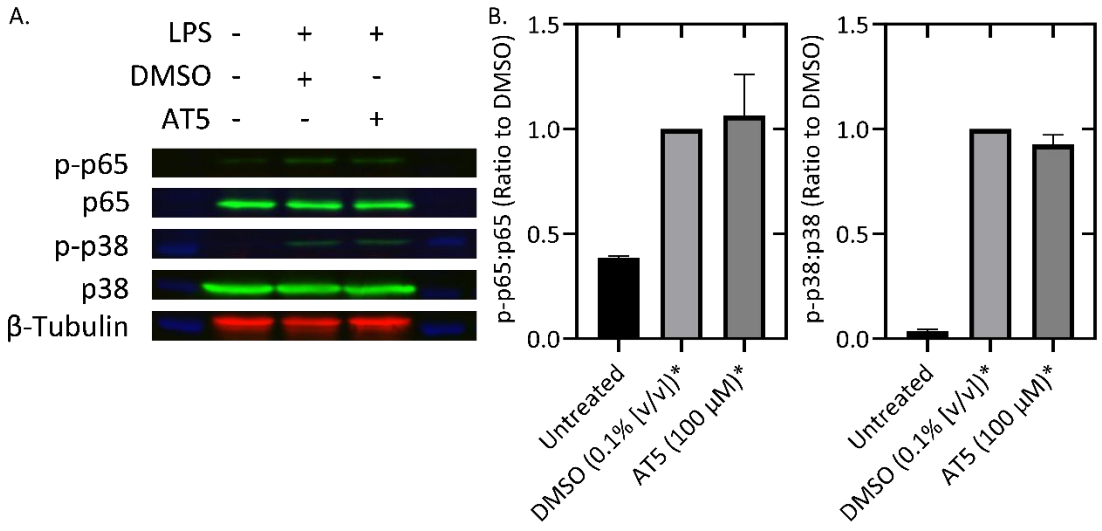

Figure 22. The effect of AT5 on LPS-induced phosphorylation of p65 and p38. Total protein from RAW 264.7 cells stimulated with either LPS (100 ng/mL) with 0.1 % (v/v) DMSO, LPS with 100 µM AT5, or not treated, for 15 min were extracted. Levels of phosphorylated p65 (Ser536) and p38 (Thr180/Tyr182) versus total p65 and p38 were determined using A. western blotting for each protein standardized to the loading control (β-tubulin). B. Quantification of A. Data is represented as the relative amounts of the indicated phosphorylated protein to the same total protein standardized to the signal of β-tubulin compared to the DMSO control. Blots were flipped along the horizontal axis for visualization. Full analyzed blots are displayed in Appendix III; Figure S7, n = 2 biological replicates.

The minimal effect of AT5 on p65 and p38 phosphorylation may have been due to the apparent change in biological activity of AT5. However, it is more likely that after only 15 min, AT5 was unable to pass into the cells and accumulate to a high enough concentration to interfere with the initial LPS signal transduction pathway. Indeed, examination of the time-course fluorescent data (Figure 4C) reveals that although there is a slight increase in fluorescence between t = 0 and 4 h post treatment. Cellular fluorescence starts to increase at a faster rate after 4 h, increasing throughout the course of the experiment. The sudden shift in potency of AT5 in conjunction with the need to modify the experimentation to allow for the compound to enter the cell in detectable amounts led to the conclusion that a different AT should be examined for biological activity, and that various pretreatment times should be examined. For the ability to compare results, a new group of ATs (110, 111, and 141) were examined for anti-inflammatory potential after a 24 h cotreatment with 100 ng/mL LPS. AT110 and AT141 had been initially screened with the other ATs examining their potential to modulate the inflammatory response (Figure 14). AT111 was excluded from that initial screen due to insufficient replicates. Of these new ATs, all were able to reduce relative levels of nitrite by at least 36 % compared to the control (Figure 23 A).

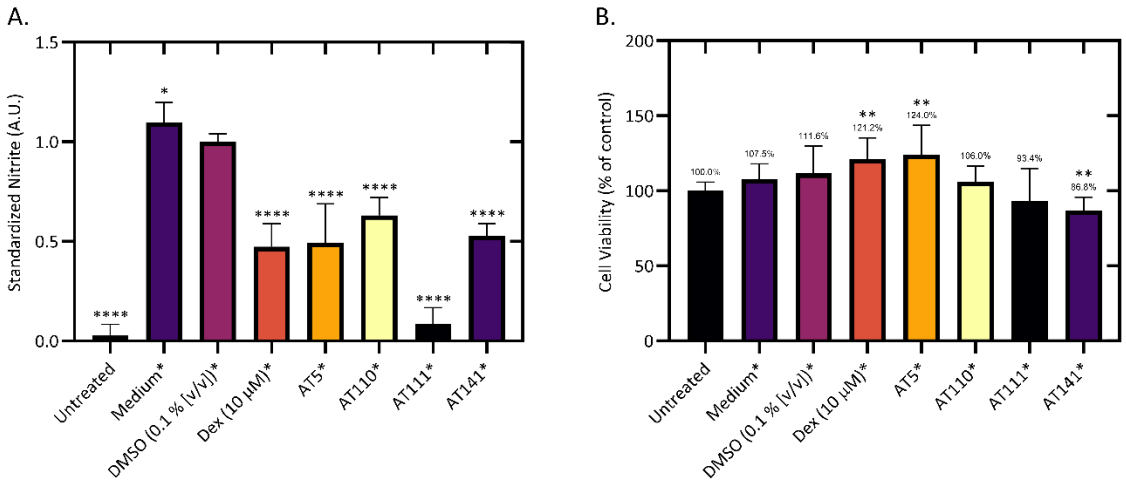

Figure 23. Screen of a second group of ATs for anti-inflammatory activity. A. nitrite production and B. cell viability of RAW 264.7 cells cotreated with LPS and 100 µM ATs or various controls for 24 h. Each treatment was conducted in triplicate wells for four biological replicates (n = 12). The data is presented as either a ratio or percentage of the average signal of the vehicle (A.) or untreated (negative; B.) control from each biological replicate. Negative values were set to zero. Statistical significance was determined for each treatment compared to the respective control using a Brown-Forsythe and Welch ANOVA with a Dunnett T3 multiple comparisons test compared to the vehicle control. *p<0.05, **p<0.01, ***p<0.001, ****p<0.0001.

Of those screened, treatment with AT111 attenuated the LPS-induced nitrite production close to baseline levels (0.085 ± 0.081 A.U.) while AT5 diminished nitrite to 0.492 ± 0.196 A.U. (Figure 23 A). While the other ATs had a similar effect as AT5, AT111 was much more potent, reducing relative levels of secreted nitrite by .407 A.U. more than AT5 (Figure 23 A). As expected, AT5 did not diminish cell viability, however it led to a 24.0 ± 19.5 % increase in cell viability compared to the untreated control (Figure 23 B). In this experiment, LPS treatment with medium alone caused an increase in cell viability of 7.5 ± 10.4 % and the vehicle control had an increase in viability of 11.6 ± 18.1 %, so it is possible that though AT5 inhibited the LPS induction of NO production, it did not mitigate the increase in cell viability (Figure 23). Dexamethasone also caused an increase in cell viability by 21.2 ± 14.0 % further supporting this possibility. AT111 and AT141 decreased cell viability by 6.57 ± 21.42 % and 13.19 ± 8.96 %, respectively (Figure 23 B). Although AT111 had a minimal, and variable, effect on cell viability, the effect on secreted nitrite levels from LPS-stimulated RAW 264.7 cells was considered sufficient to merit further study. Further analysis showed that AT111 reduced nitrite in a dose-dependent manner with a statistically significant effect at concentrations of 50 μM or greater (Figure 24 A) with an IC_{50} of 60.8 μM (R^2 = 0.88; Figure 24 B).

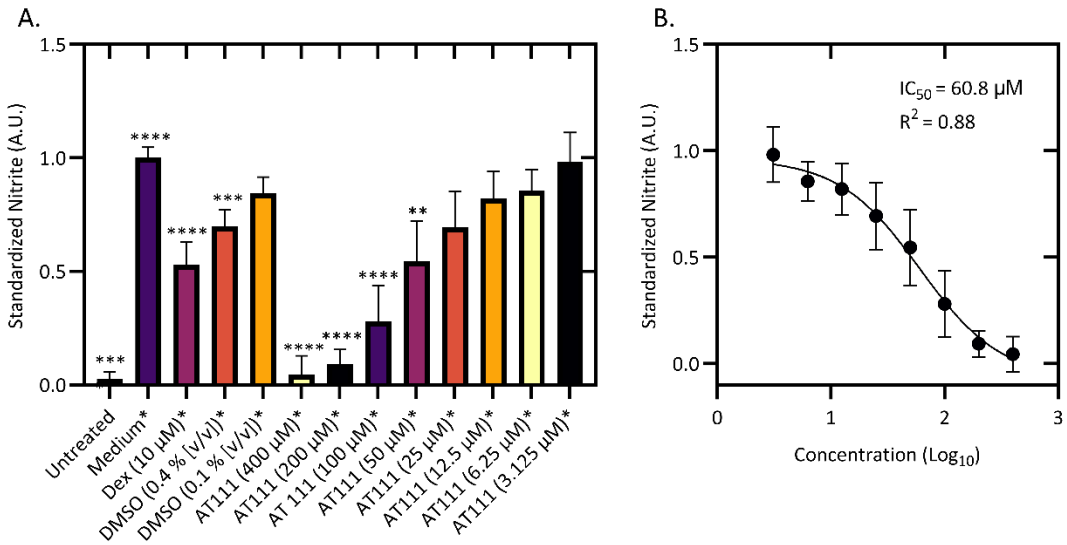

Figure 24. Dose dependent effect of AT111 on LPS-induced NO production. RAW 264.7 cells were stimulated with different concentrations of AT111, or control, and LPS for 24 h. A. Relative levels of nitrite standardized as a ratio to the vehicle control (0.1% [v/v] DMSO) for each biological replicate. B. IC_{50} value determined by plotting a non-linear fit to the ratio over the log_{10} concentration of AT111. Each data point is represented as the mean ratio of the positive control performed in triplicate for four, independent biological replicates, n = 12. Statistical significance for A. was determined using a Brown-Forsythe and Welch ANOVA with a Dunnett T3 multiple comparisons test compared to the vehicle control. Negative values, where the signal for the treatment was less than the blank, were set to zero. *$p<0.05$, ***$p<0.001$, ****$p<0.0001$.

Cell viability was only reduced by AT111 at 400 μM (78.03 ± 26.54 %, $p<0.05$). AT111 also reduced to 92.33 ± 17.38 % at 200 μM, however, this was not statistically significant (Appendix III; Figure S8). At all concentrations less than or equal to 100 μM AT111 failed to decrease cell viability, but rather led to a slight, but not significant, increase ranging from 6.9 ± 9.1 % (12.5 μM) to 14.9 ± 9.6 % (3.125 μM) greater than the untreated control (Appendix III; Figure S8). Since the IC_{50} for AT111 was determined to be approximately 60.8 μM, to be consistent, a 100 μM concentration of AT111 was used for any experiments where a dose-dependent effect was not measured.

4.3.2 Pretreatment with ATs for 24 h.

As previously stated, it had been determined that to analyze the effect of the ATs on the early stages of the LPS-TLR4 signal transduction pathway, the ATs should be allowed to enter the cell for 4 to 24 h based on the findings for AT5 in Chapter II; Figure 4C. Therefore, it was indicated that AT5 and AT111 should be added to the cells 24 h prior to treatment with LPS. Cells pretreated with various doses of either AT5 or AT111 or controls showed similar results to the 24 h cotreated cells. However, there was a larger amount of variation for each treatment. Again, AT111 had a stronger effect than AT5, statistically reducing levels of nitrite at 50 μM (0.577 ± 0.260 A.U.; Figure 25 A).

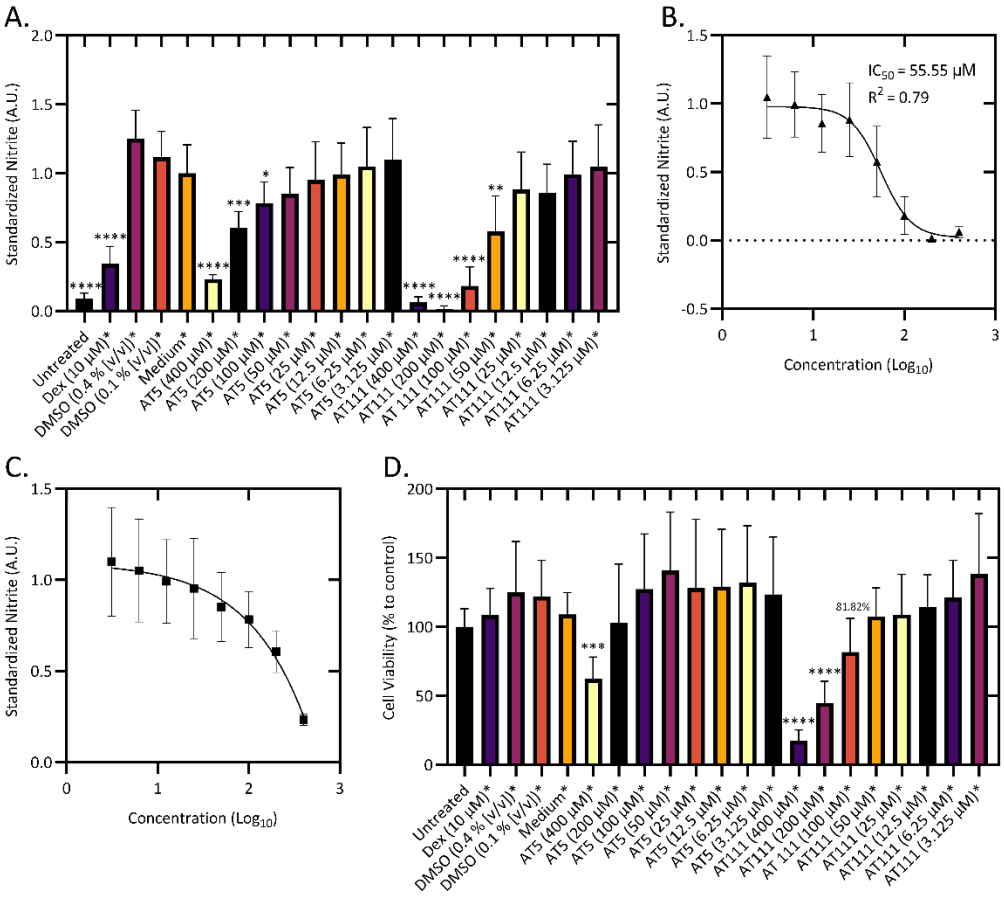

Figure 25. Dose dependent effect of AT5 and AT111 on A. LPS-induced NO production and D. cell viability. RAW 264.7 cells were stimulated with different concentrations of AT5, AT111, or control for 24 h then cotreated with 100 ng/mL LPS for an additional 24 h. A. The data is presented as either a ratio or percentage of the average signal of the positive (medium*) (A-C.) or untreated (negative; D.) control from each biological replicate. The experiment was performed in triplicate across three, independent biological replicates, n = 9. IC_{50} values were determined by plotting a non-linear fit to the ratio over the $\log_{10}$ concentration of B. AT111 or C. AT5. Statistical significance for A. and D. were determined using a Brown-Forsythe and

Welch ANOVA with a Dunnett T3 multiple comparisons test compared to the relevant control. Negative values, where the signal for the treatment was less than the blank, were set to zero. *p<0.05, ***p<0.001, ****p<0.0001.

AT5 at 100 μM was able to reduce relative nitrite to 0.784 ± 0.154 A.U. while at 50 μM levels were reduced to 0.852 ± 0.190 A.U. (Figure 25 A). AT111 was also determined to have an IC_{50} of 55.55 μM (r^2 = 0.79) while no IC_{50} value could be determined for AT5 at the given concentrations (Figure 25 B and C). AT111 at 100 μM had more bioactivity than AT5 at 400 μM reducing levels of nitrite to 0.182 ± 0.139 A.U. and 0.233 ± 0.031 A.U., respectively. While the effective concentrations of AT5 and AT111 on nitrite production stayed relatively similar, the influence on cell viability seemed to increase. Both ATs at 400 μM caused significant reductions in cell viability compared to the untreated control (Figure 25 D). For concentrations of 200 μM and lower, AT5 led to a slight increase in cell viability, ranging from 3.1 % (200 μM) to upwards of 40.9 % (50 μM). However, this large increase observed at some concentrations was not statistically significant due to the large range of values and standard deviation. Using AT5 as an example, at 50 μM the standard deviation was 42.23 % with values ranging from 100.9 % to 210.7 % and an average of 140.9 % (Figure 25 D). Although there was a large variation of cell viability, certain conclusions can still be drawn. Treatment with AT111 at concentrations of 200 μM and 400 μM led to a decline in cell viability, with only 44.88 ± 15.70 % (p<0.0001) and 17.63 ± 7.60 % (p<0.0001), respectively (Figure 25 D). At 100 μM AT111 did decrease cell viability to 81.82 ± 24.41 %, though this was not statistically significant. At concentrations of 50 μM and lower, AT111 had no effect on cell viability.

However, with each dilution of AT111, cell viability did increase, reaching 138.2 ± 43.79 % (3.125 μM; Figure 25 D), though it was not statistically significant.

Macrophage stimulation with LPS leads to the upregulation of iNOS, the protein responsible for cleaving L-arginine into NO and citrulline, as well as COX-2, which leads to PGE_2 synthesis from arachidonic acid[348-350]. Since both AT5 and AT111 were able to interfere in NO production, it is possible that these compounds may be interfering upstream, decreasing synthesis of iNOS and possibly COX-2. To test this, RAW 264.7 cells were pretreated for 24 h with 100 μM of AT5, AT111, or controls at the indicated concentrations, then cotreated, or not, with 1 μg/mL LPS for an additional 12, 16, 18, or 24 h. At 12, 16, and 18 h post-LPS treatment, AT111, but not AT5, diminished levels of iNOS production down to baseline levels (Figure 26 A, B, and C).

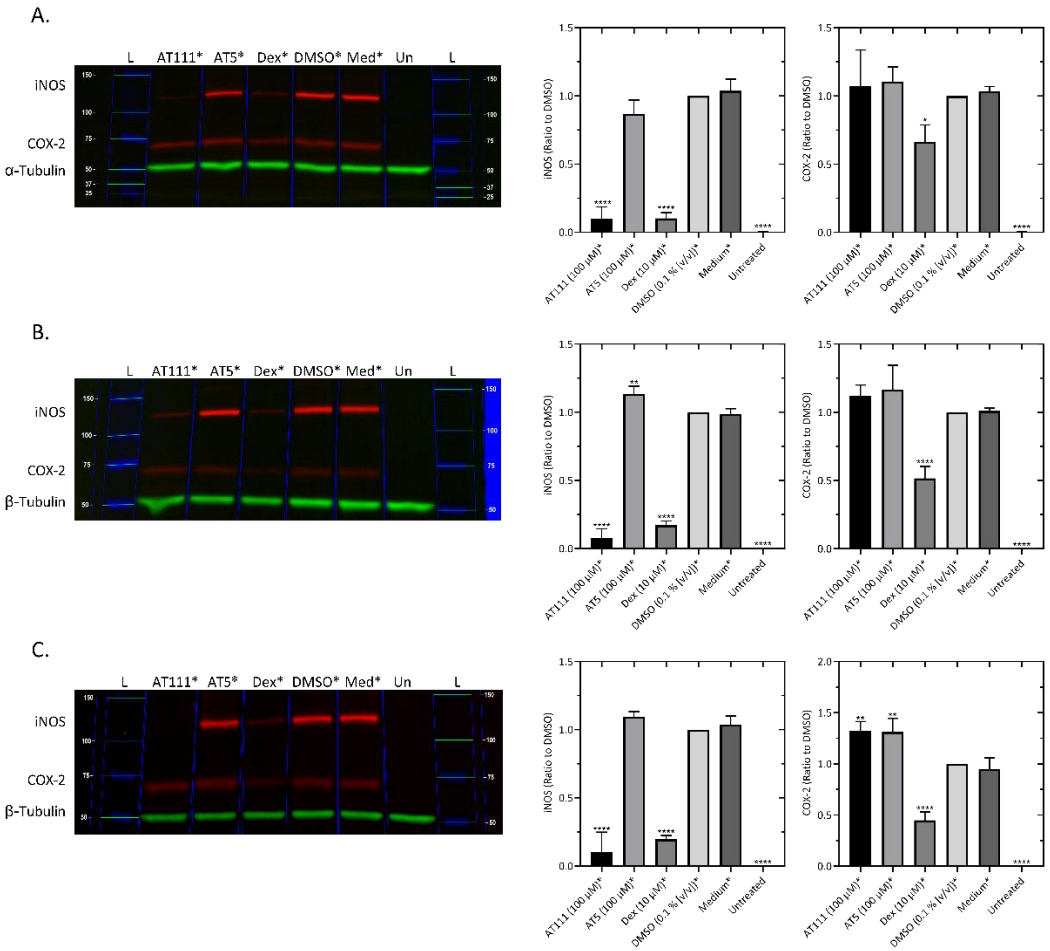

Figure 26. AT111, not AT5, reduces levels of iNOS, but not COX-2. Levels of iNOS and COX-2 were determined using western blotting. RAW 264.7 cells were pretreated for 24 hours with 100 μM of AT111, AT5, or indicated control, then *cotreated with 1 μg/mL LPS for either 12 (A), 16 (B), or 18 (C) h. Protein (15 μg) was loaded into each lane determined by BCA assay. Representative western blots are displayed for each timepoint (left). Quantification (right) of the average levels of either iNOS or COX-2 normalized to the level of β-tubulin (left) relative to the DMSO (0.1 % [v/v])/ vehicle control, determined using densitometry with ImageLab (Bio-Rad, CA). The experiment was performed across three biological replicates, n = 3. Statistical analysis was done using an ordinary one-way ANOVA with a Dunnett's multiple

comparisons test compared to the vehicle (DMSO) control (*p<0.05, **p<0.01, ****p<0.0001). White and dark points were adjusted post analysis for visualization. Full blots are displayed in Appendix III; Figure S9.

At 18 h, both AT5 and AT111 increased the relative amount of COX-2 of 1.312 ± 0.133 and 1.320 ± 0.094 A.U. compared to the DMSO control (Figure 26 C). At 24 h post-LPS addition, the amounts of iNOS across all treatment types varied greatly for each biological replicate (Appendix III; Figure S10). In one replicate, the levels of iNOS for the dexamethasone control were far greater than that of the DMSO control. In other replicates the amount of iNOS for AT111 was similar to the vehicle control as well (Appendix III; Figure S10). This was initially thought to be a technical error, however the protein levels of COX-2 seemed to vary little across biological replicates. Indeed, the levels of COX-2 for the dexamethasone, though not quantified, seemed to be reduced in the same manner as the levels at 12, 16, and 18 h post-LPS addition (Appendix III; Figure S10 and Figure 26). This variation in iNOS levels for the treatments at 24 h post-LPS addition is unusual. However, it may be due to over-confluency which has been shown to influence metabolism and gene expression in various epithelial cell lines[351,352].

The effect of AT5 and AT111 on relative levels of secreted IL-6, TNF-α, and MCP-1, was also examined. Diluted supernatants from the cells used in Figure 25 were assayed for the indicated protein using an ELISA. In this experiment, AT5 was only able to reduce levels of IL-6 and TNF-α at concentrations of 200 μM and 400 μM, while only reducing MCP-1 at 400 μM (Figure 27). This is in stark contrast to the earlier findings that showed cells cotreated with

AT5 for 24 h had reduced levels of MCP-1 at concentrations as low as 25 μM (Appendix III; Figure S6 D). AT5 was able to reduce levels of IL-6 with an IC_{50} of 202.6 μM ($R^2 = 0.65$) and TNF-α with an IC_{50} of 166.8 μM ($R^2 = 0.73$; Figure 27 A and B). These may not be the most accurate IC_{50} values as there was not a high enough dosage to measure the bottom of the curve. For MCP-1, the calculated IC_{50} of AT5 had an R^2 of 0.15 indicating that this value is not an accurate representation; more data is needed to accurately determine this value (Figure 27 C). AT111 was able to reduce levels of IL-6, TNF-α, and MCP-1 much more effectively with an IC_{50} between 41 and 47 μM (Figure 27). Treatment with AT111 at 6.25 μM decreased relative concentrations of IL-6 to 78.02 ± 24.25 % of the positive control (medium + LPS); Figure 27 A). 12.5 μM of AT111 led to a reduction in MCP-1 by an average of 39 % (0.602 ± 0.281 A.U.; Figure 27 C). Though AT111 had an effective dose at low concentrations for IL-6 and MCP-1, it was less effective against TNF-α secretion, decreasing cytokine levels to 0.590 ± 0.217 A.U. of the positive control at 50 μM while havening little effect at 25 μM (Figure 27 B). Cells treated with 0.4 % (v/v) DMSO (the vehicle control for AT concentrations at 400 μM) showed a large statistical increase in both IL-6 and MCP-1 compared to cells treated with 0.1 % (v/v) DMSO but had little effect on TNF-α (Figure 27). Cells pretreated with medium only for 24 h prior to LPS stimulation had significantly less IL-6 in the supernatant than the vehicle control. Though not statistically significant, there is a similar difference in the relative amount of MCP-1 in the supernatants and in the levels of relative nitrite production (Figures 25 A and 27 A and C). The data may suggest that the prolonged application of DMSO at concentrations of 0.4 or 0.1 % (v/v) potentially increases the pro-inflammatory effect of LPS on RAW 264.7 macrophages.

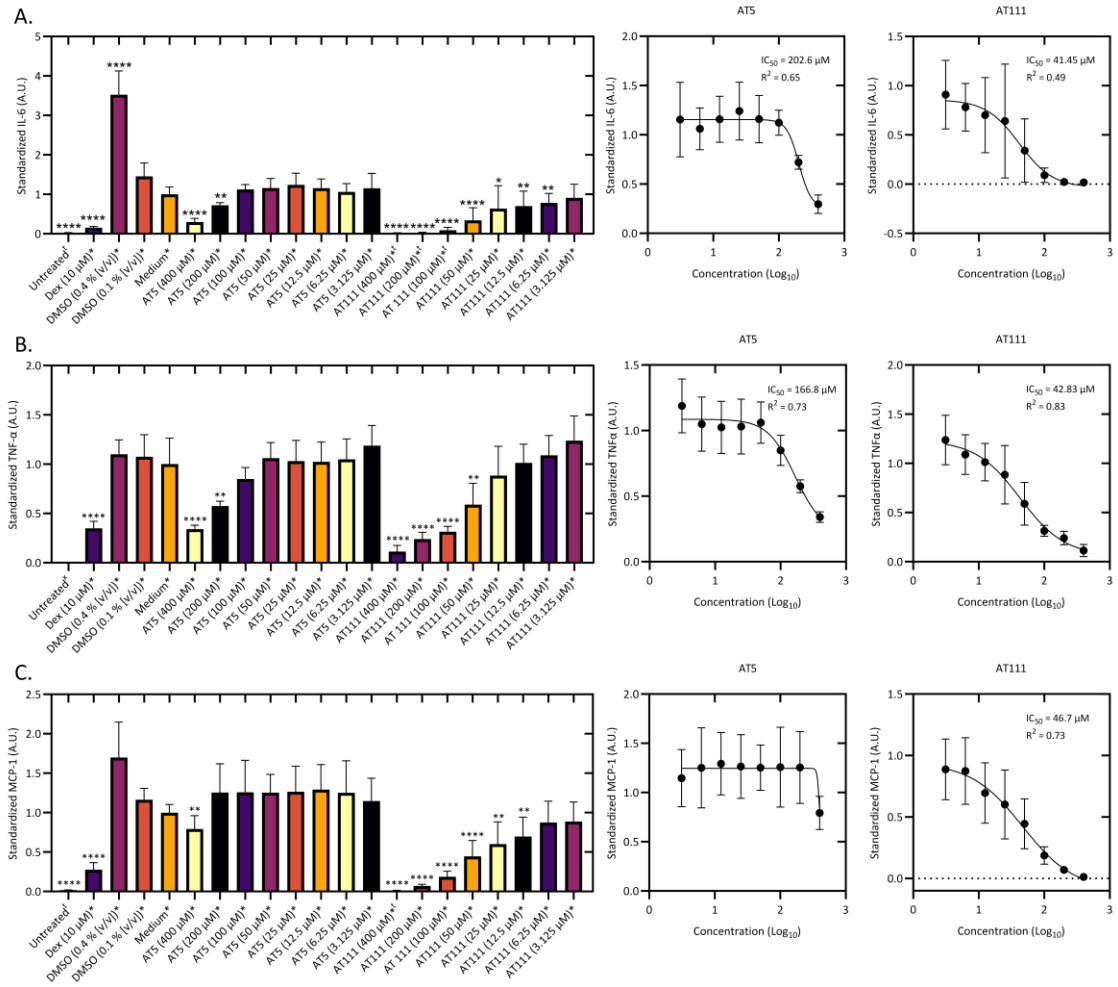

Figure 27. Dose dependent effect of AT5 and AT111 on LPS-induced pro-inflammatory cytokine expression. Supernatants from the Figure 25 experiment were examined for the presence of A. IL-6, B. TNF-α, or C. MCP-1 by ELISA. The data is presented as either a ratio or percentage of the average signal of the positive control from each biological replicate. The experiment was performed in triplicate across three, independent biological replicates, n = 9. IC_{50} values were determined by plotting a non-linear fit to the ratio over the $\log_{10}$ concentration of AT5 (middle) or AT111 (right). Statistical significance was determined using a Brown-

Forsythe and Welch ANOVA with a Dunnett T3 multiple comparisons test compared to the vehicle control. Negative values, where the signal for the treatment was less than the blank, were set to zero. [t]Some values were below the limit of detection. *p<0.05, ***p<0.001, ****p<0.0001.

This is supported by Elisia *et al.* 2016 who found that 0.25 % (v/v) DMSO augmented the *E. coli*-induced production of IL-6 in human whole blood[335]. Their findings suggest that concentrations as low as 0.08% DMSO (v/v) was enough to reduce levels of NO after 24 h[335], which is similar to the findings described here for the same time point (Figures 21, 23, and 24). However, their study focused on the cotreatment of cells with various concentrations of DMSO and did not measure the effect of various pretreatment times. Further analysis beyond the scope of this project is required to elucidate this effect.

The large variation observed for this treatment time is most likely due to the individual wells from one biological replicate. Exclusion of the triplicate wells from this replicate reduced the large standard deviation to a more moderate amount. For example, exclusion of this replicate led the cell viability of AT5 at 50 μM to be 114.0 ± 12.30 %. Exclusion of these replicate wells from the NO IC_{50} calculation for AT111 revealed a much more predictive model, with an $R^2 = 0.88$ as opposed to 0.79 (Data not shown; Figure 25 B). Interestingly, when testing levels of secreted cytokines and chemokines using the supernatants harvested from the cells used in Figure 25, the standard deviation was much smaller and more consistent. Although the number of cells per well was reduced by half from the previous experiments, it is possible that this variation between the independent, biological replicates could be due to confluency since

at 48 h after the initial treatment, 62 h post seeding, allowed for the cells to divide far more than the previous experiments, leading to over-confluency. This may have caused the cells to react differently, not only across each independent biological replicate, but also across triplicate wells. This is further supported by the consistency of iNOS expression in the 24 h western blot (Appendix III; Figure S10). Due to the variation in reactivity among biological replicates at this time point, potentially due to confluency issues, coupled with the time-course data from chapter II (Figure 4C) it was decided to pretreat RAW 264.7 cells for 4 h with AT5, AT111, or controls, then cotreat the cells with 100 ng/mL LPS.

4.3.3 Pretreatment with ATs for 4h.

A dose response curve of the effect on NO production for both AT5 and AT111 at this time point revealed a dose dependent effect for both AT5 and AT111 with AT111 having an IC_{50} of 18.00 μM (Figure 28 A and B). The IC_{50} for AT5 was unable to be accurately calculated (Figure 28C). Additionally, at a concentration of 3.125 μM both AT5 and AT111 increased NO levels in the supernatant. Some drugs have been shown to have the opposite effect at concentrations beyond the minimum effective doses, where instead of a repressor, they may be an activator[353]. This effect may affect the calculated IC_{50} for the compound as it may shift the outcome to a lower concentration. Compared to the vehicle (0.1 % [v/v] DMSO) control, AT5 was able to cause a statistically significant decrease NO levels at concentrations of 100 μM and above while AT111 had a significant effect at 50 μM and above (Figure 28 A). However, AT5 at both 50 μM and 25 μM reduced levels of nitrite to 0.778 ± 0.146 and 0.767 ± 0.124 A.U. of the positive (medium plus 100 ng/mL LPS) control, respectively. Compared to the positive control, AT5 had a statistically significant effect at concentrations as low as 25 μM

(Figure 28 A). Similarly, when compared to the positive control, AT111 had a statistically significant effect at concentrations as low as 25 μM reducing nitrite levels to 0.727 ± 0.174 A.U. (Figure 28 A). At 100 μM AT5 had a much weaker effect than AT111 lowering nitrite levels to only 0.652 ± 0.147 A.U. compared to 0.319 ± 0.117 A.U., respectively (Figure 28 A). When examining whether each compound influenced cell viability, the anti-inflammatory (dexamethasone) control induced a statistical increase of 25.5 ± 19.9 % compared to the untreated control (Figure 28 D). Additionally, though not statistically significant, AT5 at concentrations of 100 μM, 50 μM, and 3.125 μM also led to a 24.1 ± 21.6 %, 22.9 ± 21.0 %, and 22.1 ± 24.88 % increase in cell viability, respectively (Figure 28 D). AT111 only had a similar increase of 20.8 ± 27.2 % at 3.125 μM but led to a non-significant decrease at concentrations of 400 μM and 200 μM to 82.7 ± 25.6 % and 83.8 ± 14.7 %, respectively (Figure 28 D). All other concentrations of AT111 had a slight but not statistical increase in cell viability within 10-14 % of the untreated control while falling within 1-6 % of the vehicle (Figure 28 D). AT5 at most concentrations seemed to slightly increase cell viability to 8-18% higher than the untreated control and only 0.3-9.4 % higher than the vehicle, except for 400 μM (Figure 28 D). This dose-dependent effect, while not low enough to warrant use as a pharmaceutical, suggests the usefulness of these compounds as bioactive scaffolds for further modifications.

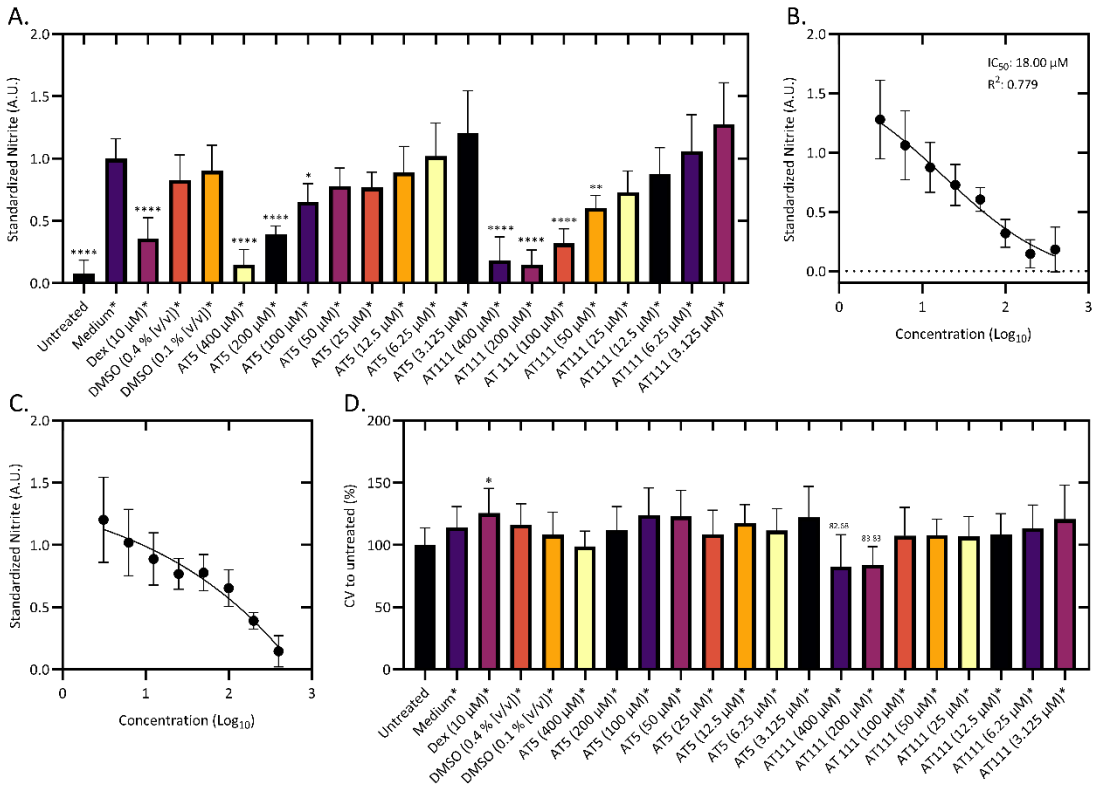

Figure 28. Dose dependent effect of a 4 h pre-treatment of AT5 and AT111 on LPS-induced NO production and cell viability. RAW 264.7 cells were stimulated with different concentrations of AT5, AT111, or control for 4 h then cotreated with 100 ng/mL LPS for an additional 24 h. A. Average relative levels of NO. IC_{50} values were determined by plotting a non-linear fit to the ratio over the $\log_{10}$ concentration of B. AT111 or C. AT5. D. Percent cell viability of RAW 264.7 cells for each treatment. The data is presented as either a ratio or percentage of the average signal of the positive (A-C.) or untreated (negative; D.) control from each biological replicate. The experiment was performed in triplicate across four, independent, biological replicates, n = 12. Statistical significance for A. and D. were determined using a

Brown-Forsythe and Welch ANOVA with a Dunnett T3 multiple comparisons test compared to the relevant control. Negative values, where the signal for the treatment was less than the blank, were set to zero. *$p<0.05$, ***$p<0.001$, ****$p<0.0001$.

As before, due to the effect of AT5 and AT111 on NO production and to begin to elucidate a potential mechanism of action, it was decided to determine if each compound had an effect upstream of NO production looking at the protein expression of both iNOS and COX-2. Using western blot analysis, it was shown that only AT111 decreased levels of iNOS whereas AT5 had no effect (Figure 29 A and B). AT111-treated cells showed a strong decrease in iNOS to 0.0031 ± 0.0029 A.U. of the vehicle control, while AT5 had no effect on iNOS with an average of 1.081 ± 0.452 A.U. (Figure 29 B). However, two of the three replicates seemed to increase iNOS while one caused a decrease. This decrease may be due to the third replicate where the iNOS band seemed to be condensed for AT5 (Appendix III; Figure S11 C). AT5 also seemed to increase relative levels of COX-2 by 38.0 ± 11.0 % while AT111 did not (3.3 ± 5.1 %; Figure 29 C). These findings are similar to the 24 h pretreated experiment, which showed that AT111, but not AT5, lowered iNOS expression (Figure 26). This suggests that AT111, but not AT5, may interrupt the inflammatory response upstream of iNOS without greatly affecting COX-2 expression.

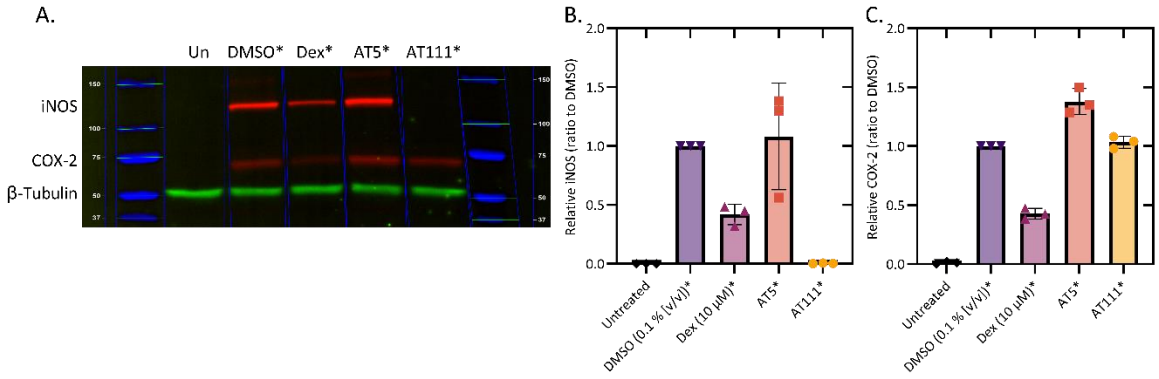

Figure 29. Effect of AT5 and AT111 on iNOS and COX-2 production. RAW 264.7 cells were treated with 100 µM AT111, 100 µM AT5, or the indicated controls for 4 h. The cells were then cotreated with 100 ng/mL LPS for an additional 24 h. 15 µg of protein were loaded into each lane and detected as described in the methods. A. Representative blot depicting iNOS, COX-2, and β-tubulin. Blot flipped and brightened post analysis for visualization. Densitometric analysis of A. for B. iNOS and C. COX-2 is shown, and data was normalized to the vehicle (DMSO) control for each of three biological replicates, n = 3. Full blots for all replicates are shown in Appendix III; Figure S11.

The reason that there is not a 1:1 correlation between measured iNOS levels and levels of nitrite within the supernatant is possibly two-fold. Both time points were measured at 24 h post-addition of LPS. It could be that AT111 decreased levels of iNOS at earlier time points, while also leading to a quicker resolution/ degradation of iNOS. This is supported by the findings in Figure 26, which showed detectable levels of iNOS at time 12, 16, and 18 h time points. Additionally, while western blots are helpful in determining expressed protein levels, the ELISA or other quantifiable techniques, including the NO assay, are more sensitive and

useful in determining the presence of proteins or the relative amount of post-translational modifications of certain proteins. As such, it is plausible that there are levels of iNOS expressed in the AT111 treated samples that are difficult to detect with a western blot and therefore actively cleaving L-arginine into citrulline and NO.

We sought to further understand the anti-inflammatory role of AT111 and AT5, with an increased focus on AT111. The effect of each AT was determined for the secreted levels of inflammatory cytokines MCP-1, IL-6, TNF-α, and IL-10. While IL-10 is technically an anti-inflammatory cytokine, its expression is triggered by LPS, limiting the production of other cytokines[354]. AT111 had an inhibitory effect on the levels of each cytokine apart from TNF-α. (Figure 30). For all other cytokines tested, AT111 reduced each one in a dose-dependent manner with an IC_{50} of 42.72 μM for MCP-1, 47.83 μM for IL-6, and 13.80 μM for IL-10 (Figure 30). By comparison, following the AT5 treatment, the IC_{50} for only IL-6 (206.6 μM) could be calculated (Figure 30 B). Treatment with AT111 caused a statistically significant decrease in the levels of all cytokines at concentrations of 50 μM and above, while AT111 only caused a statistically significant decrease in TNF-α at 400 μM (Figure 30). When cells were pretreated for 24 h prior to the addition of LPS, AT111 lead to a significant reduction in TNF-α at concentrations as low as 50 μM with an IC_{50} value of 42.83 μM (Figure 27 B). This implies a change in the efficiency of AT111 based on time allowed to permeate the cell prior to the addition of LPS. Delivery at 24 h prior may allow AT111 to be at a much higher concentration within the cell at the time of LPS treatment, limiting the induction of the inflammatory response at earlier time points. This is supported by the time course fluorescent analysis of AT5 where intracellular fluorescence increased rapidly from 4 h post-treatment to 24 h post-treatment

(Figure 4 C). This would allow for a greater effect on the production of pro-inflammatory cytokines as there would be a greater inhibition of cytokine production at earlier time points. This same effect is observed for AT5 which caused a statistical reduction in TNF-α at 200 µM and 400 µM (Figure 27 B).

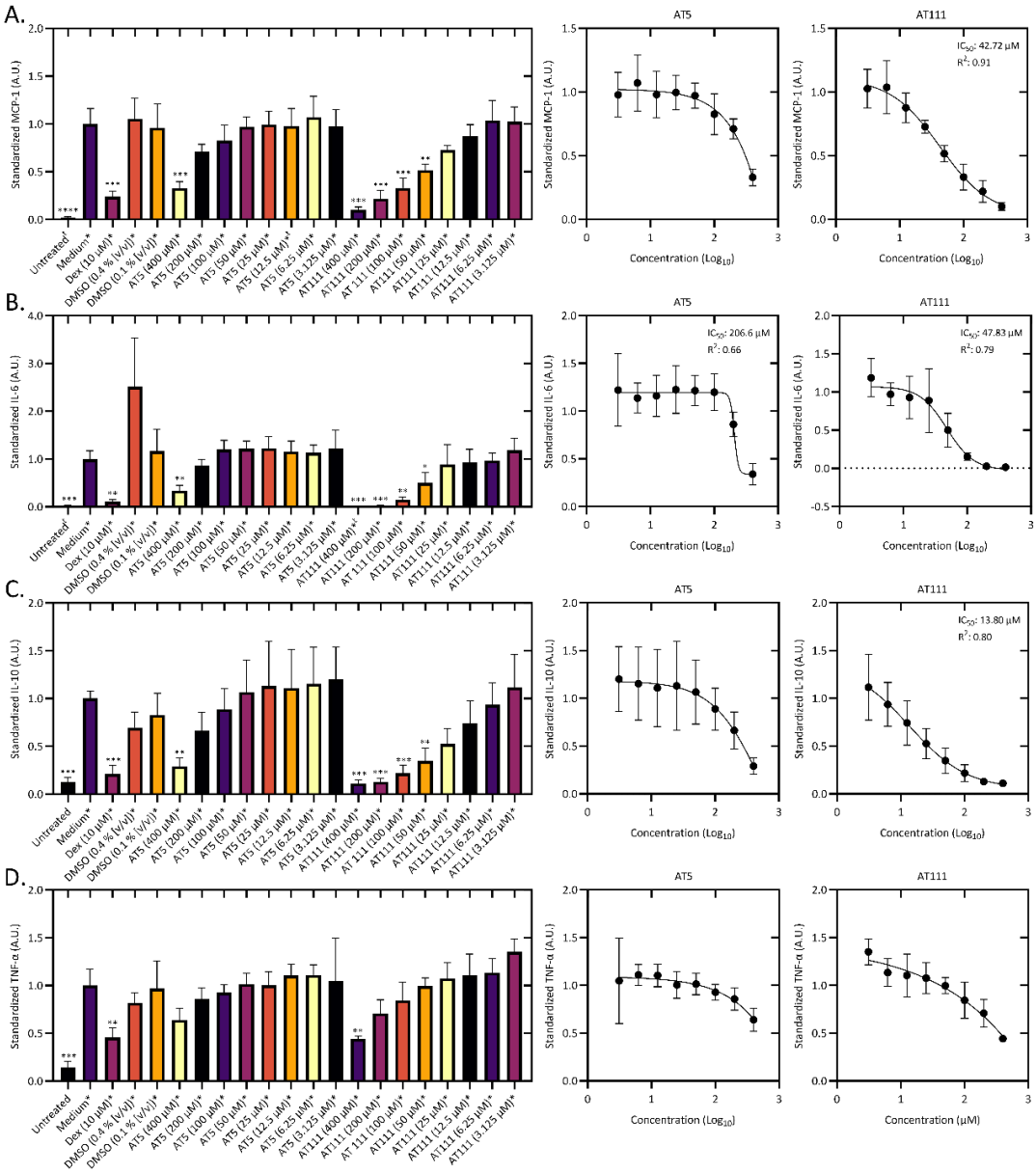

Figure 30. Dose dependent effect of AT5 and AT111 on LPS-induced cytokines. Supernatants from the first three biological replicates from Figure 28 were examined for the presence of A. MCP-1, B. IL-6, C. IL-10, and D. TNF-α by ELISA. The data is presented as either a ratio or percentage of the average signal of the positive control from each biological replicate. The experiment was performed in triplicate across three, independent, biological replicates, n = 9. IC_{50} values were determined by plotting a non-linear fit to the ratio over the log_{10} concentration of AT5 (middle) or AT111 (right). Statistical significance was determined using a Brown-Forsythe and Welch ANOVA with a Dunnett T3 multiple comparisons test compared to the vehicle control. Negative values, where the signal for the treatment was less than the blank, were set to zero. [t]Some values were below the limit of detection, while others were [o]above the limit of detection and excluded. *p<0.05, ***p<0.001, ****p<0.0001.

Since there was a large variability shown by the vehicle controls, the effects of each AT on cytokine secretion were also compared to the positive control. When compared to the positive control, AT111 statistically reduced levels of MCP-1 at 25 μM (0.727 ± 0.049 A.U.; Figure 30 A). AT5 was also able to statistically lower levels of MCP-1 at 200 μM (0.711 ± 0.077 A.U.; Figure 30 A). When compared to the positive control, AT111 was able to statistically reduce levels of IL-6 at a concentration of 25 μM (0.526 ± 0.159 A.U.; p<0.0001; Figure 30 C). AT5, when compared to the positive control, statistically reduced levels of IL-10 at a concentration of 200 μM (0.664 ± 0.194 A.U.; p=0.0112) but had no discernable effect at 100 μM (0.889 ± 0.219 A.U. p=0.9155; Figure 30 C). Additionally, when compared to the positive control, AT111 had a statistical effect on TNF-α at 200 μM (0.707 ± 0.143 A.U.).

Since treatment with AT111 lead decreased levels of inflammatory cytokines and iNOS, the levels of mRNA in each sample were measured. RAW 264.7 cells were treated for 4 h prior to the addition of LPS with 100 μM of each AT or the controls at the indicated concentrations. The cells were then cotreated with each compound and LPS for an additional four hours. Levels of MCP-1 at various time points in RAW 264.7 cells treated with LPS (with 0.1 % [v/v] DMSO) along with the findings in the literature were utilized to determine 4 h as an optimal time point for RNA analysis (Appendix III; Figure S12)[341-346]. RNA quality was then determined for each sample using the bleach gel method described earlier (Appendix III; Figure S13)[297] then converted to cDNA. Relative amounts of cDNA were compared by calculating the $2^{-\Delta\Delta Ct}$ for each sample compared to the vehicle/ positive control as there was no amplification of some genes in the untreated control. Also, the focus of this experiment was to determine the fold change of each gene compared to the vehicle control. It was found that AT111 was able to reduce RNA levels for all genes measured by a fold change of -1.5 or greater except for *Csf2* (Figure 31). Fold changes in RNA levels for *Il10* were not determined as this assay was examining the effect of AT111 on pro-inflammatory mediators' RNA levels. Additionally, COX-2 was not assessed due to a lack of RNA at this time point. For both AT111 and AT5 the calculated differences in mRNA corresponded to the measured cytokine data in Figure 30 except for TNF-α. AT111 was able to reduce protein levels of MCP-1 and IL-6 to 33.1 ± 10.2% and 15.3 ± 5.04% of the positive control (36.7 ± 14.6 % and 13.4 ± 15.6 % of the vehicle) and also reduce mRNA levels to a relative expression level of 0.201 ± 0.016 A.U. and 0.017 ± 0.006 A.U., respectively (Figure 30 A and B, Figure 31 A and B). AT5 was also able to lower relative expression levels of *Ccl2* (the gene encoding MCP-1) to 0.595 ± 0.257

A.U. (Figure 31 A). Differing from the detected protein levels of TNF-α, treatment with AT111 reduced levels of *Tnf* mRNA to 0.398 ± 0.055 A.U. (Figure 31 C). This discrepancy may again be attributed to timing and further experimentation is warranted. AT111 also lowered the relative expression of *Il-1b* to 0.072 ± 0.006 A.U. (Figure 31 D). Relative protein levels of IL-1β in the supernatant could not be determined as RAW 264.7 cells lack the ability to cleave pro-IL-1β into mature IL-1β leaving it sequestered in the cytoplasm of the cell[340].

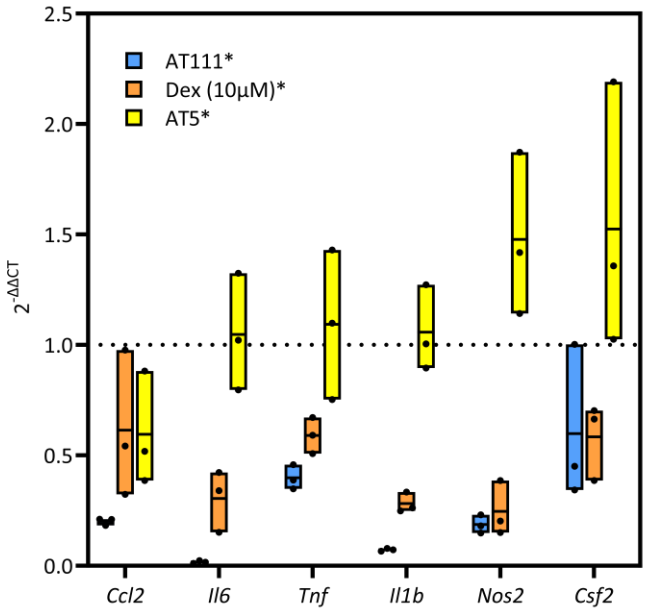

Figure 31. Relative changes in RNA levels of inflammatory response genes. RNA was extracted from RAW 264.7 cells pretreated with 100 µM AT111, 100 µM AT5, or 10 µM dexamethasone for 4 h, then cotreated with 1 µg/mL LPS for 4 h. Equivalent amounts of RNA were converted into cDNA for each sample. The difference in relative levels of gene expression was determined using the ΔΔCT method compared to the vehicle (LPS + 0.1 % [v/v] DMSO), using GAPDH from each sample as the standardization control. The data is represented as the relative fold-change for three, independent biological replicates. Each biological replicate consists of two technical replicates averaged together, n = 3. One technical replicate for *Csf2* was aberrant, occurring around 11 cycles later than the average and was excluded.

AT111 also lowered relative mRNA levels of both *Nos2* and *Csf2*, the genes encoding iNOS and GM-CSF, to similar levels as the dexamethasone-treated control (Figure 31 E and F). In order to observe potential statistical significance, an unpaired two-tailed t-test comparing AT111 with the vehicle was performed on the $2^{-\Delta CT}$ for each gene showing standardized expression of each gene compared to the levels of a house-keeping gene (*Gapdh*) (Appendix III; Figure S14). AT111 showed a statistically significant reduction of *Il1b*, *Il6*, *and iNOS* ($p = 0.0018$, $p = 0.023$, and $p = 0.025$). However, there was no statistical significance determined for *Ccl2*, *Csf2*, and *Tnf* (Statistical data not represented on graph). The lack of significance for *Ccl2* and *Tnf* is most likely due to the variation of standardized mRNA levels for the vehicle control (Appendix III; Figure S14 A, C, and F). However, the ΔCT method does not account for the variance of each biological replicate in response to LPS, therefore the ΔΔCT method, comparing standardized relative expression levels, is a more accurate representation of what may be occurring biologically. By comparison to AT111, AT5 caused a slight increase in the average relative expression levels for *Nos2* and *Csf2* (1.478 ± 0.369 A.U. and 1.524 ± 0.601 A.U.; Figure 31 E and F). Though protein levels of GM-CSF in the supernatants of the 4 h pretreatment could not be determined, this increase in relative levels of iNOS is observed for cells treated for two of the three replicates of AT5 (Figure 29 B). This relative increase for iNOS on the mRNA level and the protein level while decreasing the levels of NO at 100 µM may indicate that AT5 interacts with either iNOS or NO, though further research is required to exactly determine the mechanism of AT5 within the cell. However, at concentrations of 50 µM and lower it is apparent that AT5 has a minimal biological affect. Therefore, the remainder of

the study will emphasize the role of AT111 while still testing the effects of AT5 since it was the focus of Chapter II.

Since treatment with AT111 attenuated levels of NO, iNOS, and *Nos2* it was hypothesized that treatment AT111 may affect the NF-κB transcriptional regulation of *Nos2*. To test this, a reporter RAW 264.7 cell line expressing mCherry under the control of the *Nos2* promoter with both regulatory regions containing NF-κB binding sites, a generous gift from the laboratory of Dr. David Nelson, was utilized[296]. *Nos2*-reporter cells co-treated with LPS and 0.01 % (v/v) DMSO (vehicle control) showed an increase in mCherry fluorescence indicating transactivation of the *Nos2* promoter. This signal was slightly, but not statistically, decreased by dexamethasone (Figure 32).

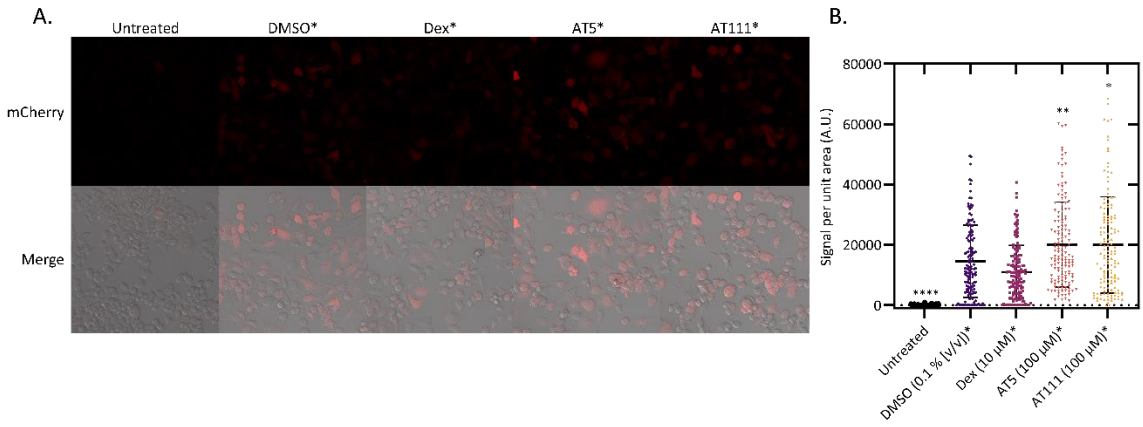

Figure 32. Effect of ATs on NF-κB-dependent transcription of *Nos2*. RAW 264.7 cells lentiviral-transduced to express mCherry under the control of the *Nos2* promoter with both proximal and distal promoter elements containing κB cis-regulatory sites were pretreated with 100 µM AT5, 100 µM AT111, or the indicated controls for 4 h then *cotreated with 1 µg/mL LPS for an additional 24 h. A. Representative images depicting mCherry induction for each treatment. B. Mean fluorescence ± S.D. of A. depicting 114 - 148 cells measured randomly across three biological replicates. Each datum point represents the background-subtracted mean signal/ unit area for one cell. Negative values, where the fluorescence within the cell was lower than the background, were set to zero. Outliers from 150 cells were determined using the ROUT method in Outliers from each sample were detected using the ROUT method with a Q = 1 % using GraphPad Prism version 10.0.0-10.0.1 then removed, n = 114 – 148 cells. Significance was determined using a Kruskal-Wallis with a Dunn's correction compared to the vehicle (DMSO) control. *p<0.05, **p<0.01, ****p<0.0001.

Cells treated with AT5 showed a slight increase in fluorescence compared to the vehicle control indicating a small increase in transcriptional activity on *Nos2* (Figure 32, $p<0.01$). This is congruent with the trends observed in both the qRT-PCR and western blot data (Figure 31 and 29). However, treatment with AT111 also increased fluorescence compared to the vehicle control (Figure 32, $p<0.05$). Since this is contrary to the observed effect that AT111 has on the levels of LPS-induced *Nos2* RNA and iNOS, it was hypothesized that AT111 and AT5 alone may be attributing to the observed fluorescence. To test this *Nos2*-reporter RAW 264.7 cells were treated with 100 μM AT111, AT5, or medium only (untreated) for 24 h, and average cellular fluorescence was measured as before. Treatment with AT111 and AT5 both lead to increased fluorescence, potentially indicating increased transactivation of the *Nos2*-promoter ($p<0.0001$, Appendix III; Figure S15). However, it should be noted that both AT111 and AT5 had detectable fluorescence in RAW 264.7 cells excited by a 555 nm laser (Figure 9C). Therefore, it is plausible that the increased fluorescence observed by both AT111 and AT5 was due to the ATs photophysical properties. The lower levels of *Nos2* RNA and iNOS expression, together with the lack of observed interference on levels of p65-driven mCherry expression, indicate that AT111 may not be interacting with the LPS-NF-κB signal transduction pathway.

4.3.4 ATs and TLR4 signaling.

During LPS-TLR4 signaling, in addition to NF-κB, kinases, including p38 MAPK, ERK1/2, and PAK/JNK are activated[265-267,272-274], contributing to an inflammatory response. To investigate this, the LPS-TLR4 pathway was analyzed by western blotting. Phosphorylation of the kinases or transcription factors downstream of the initial signaling pathway were examined as those post-translational phosphorylation events would be altered by any upstream

effects. Levels of phosphorylated p65 (RelA; Ser536), p38 (MAPK; Thr180/Tyr182), SAPK/JNK (p54/p46; Thr183/Tyr185), and ERK1/2 (Thr202/Tyr204), were measured and compared to levels of the vehicle control. RAW 264.7 cells were treated with AT111, AT5, various controls, or medium only for 4 h then cotreated with 100 ng/mL LPS and each treatment, or with medium only, for 15 min. Lysates for each treatment were harvested and probed for the indicated proteins, both phosphorylated or not. Bay 11-7082 was used as a control as a known inhibitor of IκBα degradation, and p65 nuclear translocation, preventing some downstream effects of NF-κB[355].

Initially, treatment with Bay 11 caused a decrease in phosphorylation of all proteins except ERK2 (Appendix III; Figure S16). For this protein, Bay 11 caused approximately a four-fold increase in ERK2 phosphorylation (Thr202/Tyr204; Appendix III; Figure S16 B). Treatment with AT5 and AT111 caused a similar increase in p-ERK2 (Thr202/Tyr204; Appendix III; Figure S16 B). This increase in ERK2 phosphorylation (Thr202/Tyr204) by Bay 11-7082 has not been previously reported, however Bay 11-7085 *does* stimulate a large increase in p-ERK2 (Tyr204)[356-358]. Additionally, LPS should cause substantial phosphorylation of ERK2 (Thr202/Tyr204)[286,359,360] but did not have this effect (Appendix III; Figure S16 B). Due to these discrepancies, it was thought that some effect which seemed to only influence ERK2 phosphorylation (Thr202/Tyr204) was occurring. Previously, the same experiment was performed to determine the effects of AT111 on the LPS-TLR4 signaling pathway, however, these lysates were initially abandoned due to a lack of observed p65 phosphorylation (Ser536) inhibition (Figure 33). However, treatment with Bay 11-7082 was also able to reduce LPS-stimulated phosphorylation of all other proteins explored, except for

p38 (Thr180/Tyr182), demonstrating its effect. Therefore, these previous lysates were utilized as being more representative of the actual ERK2 biological response to LPS. Indeed, except for ERK2 and p65, which was only slightly reduced by treatment with Bay 11-7082 in the second experiment (Appendix III; Figure S16), both experiments yielded similar results (Appendix III; Figure S17).

As in Figure S16 (Appendix III) both AT5 and AT111 had no effect on phosphorylation of all proteins except for ERK2 (Thr202/Tyr204; Figure 33). Treatment with AT5 led to a slight increase in relative levels of ERK2 phosphorylation (Thr202/Tyr204; 1.251 ± 0.203 A.U.), while treatment with AT111 caused a statistically significant increase (1.478 ± 0.223 A.U.; $p=0.0187$) compared to the DMSO control (Figure 33 B). These data imply that AT111 increases of ERK2 phosphorylation possibly leading to an anti-inflammatory response, or a faster resolution of the inflammatory response.

While AT111 and AT5 did not inhibit p65 phosphorylation (Ser536), it is possible that the nuclear localization of p65 may be affected. To assess the potential of AT111 to reduce the inflammatory response by interfering with the nuclear translocation of p65, similarly to Bay 11-7082[355], relative amounts of nuclear p65 was compared to cytoplasmic p65 using confocal microscopy in cells treated with the various compounds or controls for 4 h then cotreated with LPS for 15 min. RAW264.7 cells treated with LPS and 0.1 % (v/v) DMSO (vehicle control) had an average nuclear to cytoplasmic (nuc:cyto) ratio of 5.721 ± 2.344 A.U. (Figure 34). Cells treated with only medium had a nuc:cyto ratio of 0.664 ± 0.300 A.U. (Figure 34). Cells treated with Bay 11-7082 had a decrease in nuclear p65 compared to the vehicle control with a nuc:cyto ratio of 1.921 ± 1.067 (Figure 34; $p<0.0001$). It was found that both AT111 and AT5

had minimal impact on the levels of nuclear p65 with nuc:cyto ratios of 5.515 ± 2.625 A.U. and 6.234 ± 2.873 A.U. respectively (Figure 34; p>0.9999 for both).

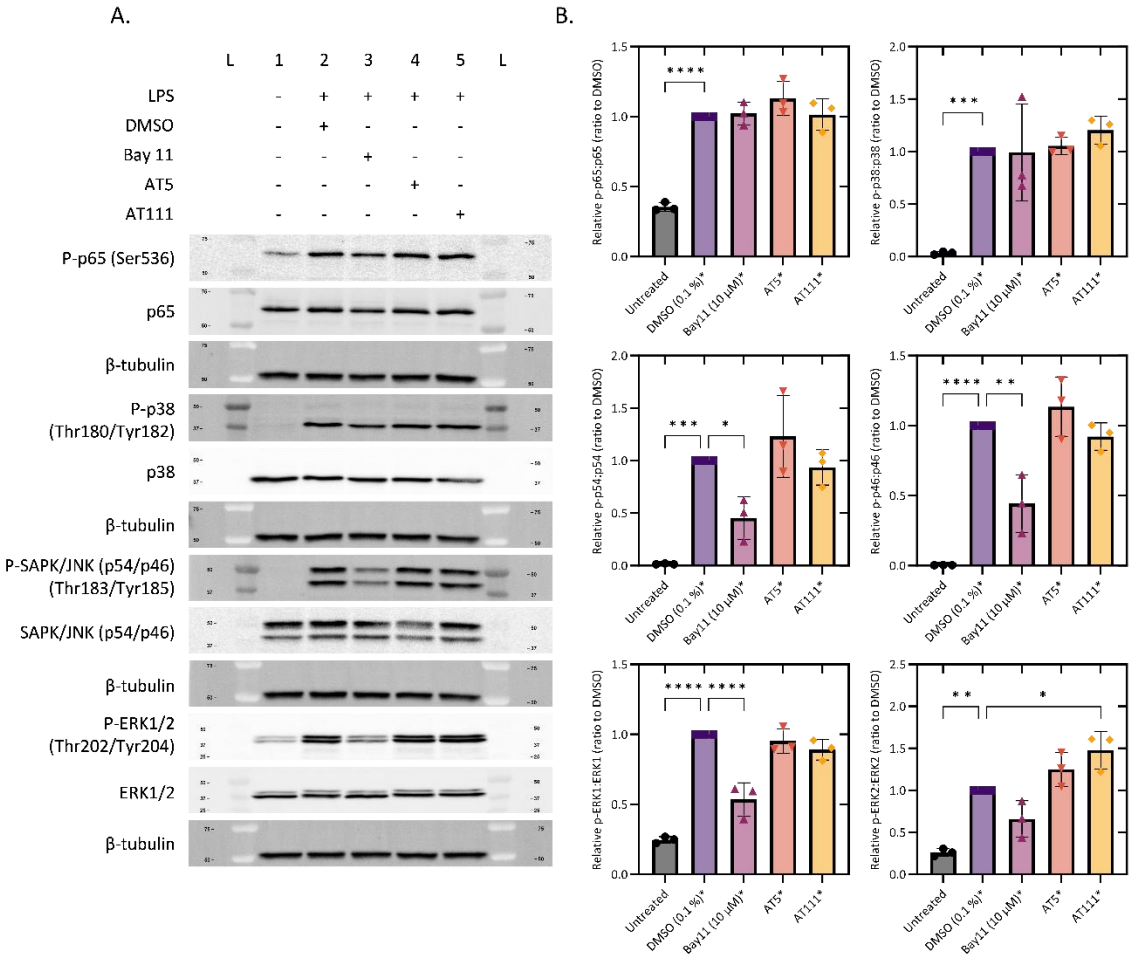

Figure 33. Effect of AT5 and AT111 on the MyD88-dependent, TLR4 signal transduction pathway. RAW 264.7 cells were treated with 100 µM AT111, 100 µM AT5, or the indicated controls for 4 h. The cells were then cotreated with 100 ng/mL LPS for an additional 15 min. 10 µg of total protein were loaded into each lane and detected as described in the methods. A. Representative blot depicting the indicated proteins, and respective β-tubulin from each blot from the same cell lysates. Blot was inverted and the brightness auto-adjusted post analysis for visualization. B. Densitometric analysis of A. for each indicated protein. Data was normalized first to the level of β-tubulin, then the ratio of phosphorylated:total protein for each indicated protein was determined. The resultant ratio is standardized to the vehicle (DMSO) control for each of three, biological replicates. Statistical analysis was done using an ordinary one-way ANOVA with a Dunnet's correction, n = 3. Full blots for all replicates are shown in Appendix III; Figure S18.

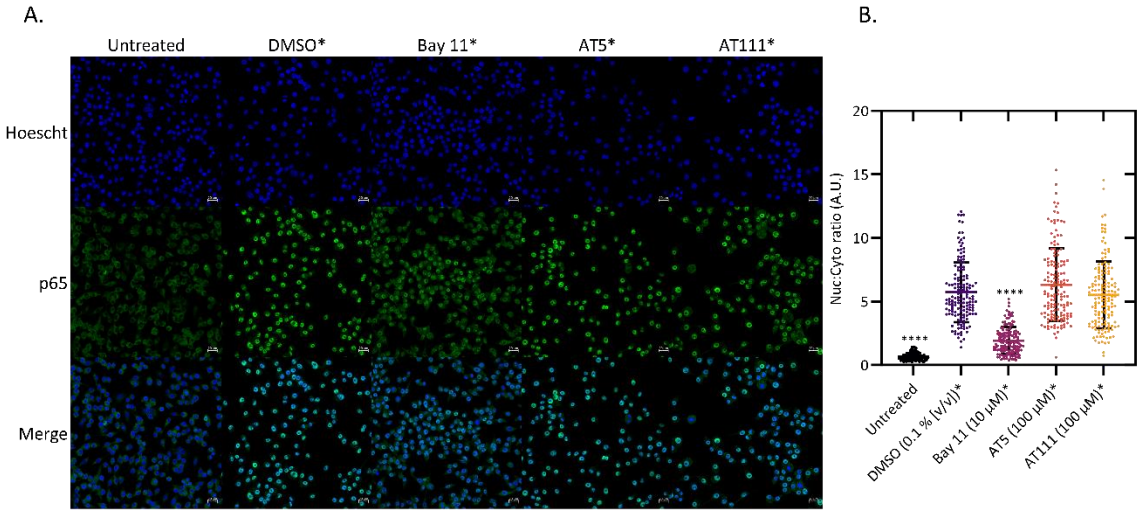

Figure 34. Effect of AT5 and AT111 on the nuclear translocation of p65. RAW 264.7 cells were pretreated with 100 μM AT5, AT111, or the indicated concentration of each control for 4 h, then cotreated with 100 ng/mL LPS for 15 min. Cells were fixed and probed with a p65 specific antibody as described in the methods. A. Representative image of the distribution of p65 in RAW 264.7 cells. B. Mean quantification of A. ± S.D. Levels of p65 in the nucleus and cytoplasm were measured as the signal per unit area of a representative region in each using FIJI[207]. Nuclear regions were distinguished using Hoechst 33342 and regions collected did not include the nucleolus. Images of cells were taken from at least six random fields of view for each biological replicate. The background signal per unit area for each field of view was subtracted. The data is presented as the ratio of nuclear (nuc) to cytoplasmic (cyto) p65. 150 cells were measured for each across three biological replicates. Outliers were determined, and then removed, using the ROUT test on Outliers from each sample were detected using the ROUT method with a Q = 1 % using GraphPad Prism version 10.0.0-10.0.1 then removed. The resultin n = 142 - 150 cells. Statistical significance was determined using a Kruskal-Wallis test with Dunn's multiple comparisons test.

This data implies that AT111 reduces the inflammatory response of LPS-stimulated RAW 264.7 macrophages through a pathway potentially independent of the initial MyD88 signaling pathway. It should be noted that nuclear localization of p65 pulses over time with a large initial pulse and a weaker second pulse in cells stimulated with TNF-α with varying periods of about 100 min[361]. This oscillation varies in LPS-stimulated RAW 264.7 cells expressing an EGFP-RelA (p65) fusion protein and is concentration dependent[362]. Other

studies using this reporter cell line have observed this dose-dependent response in oscillatory activity. Park *et al.* showed minimal oscillations in p65 nuclear localization with a broad peak occurring 30 min post-stimulation with 20 ng/mL LPS extending to 60 min[72], while Hayes *et al.* observed a large peak in nuclear p65 at 30 min post-stimulation with 100 ng/mL LPS and a smaller peak occurring at 120 min post-stimulation[363]. It is possible that the observed anti-inflammatory activity of AT111 is due to an inhibition of the second peak of p65. However, since the cells are treated with each AT or control 4 h prior to LPS addition, it is unlikely that AT111 would affect this second peak without affecting the initial nuclear translocation, though the second peak may be due to the Myd88-independent pathway. Cell signaling is complex and these oscillations have been linked to cytokine expression levels[364] so it is plausible that AT111 inhibits oscillations of NF-κB contributing to its anti-inflammatory activity. However, oscillations in NF-κB signaling are uncommon in TLR-stimulated cells, and most cells stimulated by LPS exhibit a single long-lasting translocation event due to the implementation of a positive feedback mechanism[259,362]. AT111 may also interfere with p50 either by blocking its phosphorylation or DNA binding. However, there is evidence suggesting that interference with p50, through knock-out mutation, or mutations in one of its phosphorylation sites (Ser80) actually leads to an increase in inflammatory activity, including the expression of TNF-α, CXCL2, IL8, CXCL2, CXCL1, RELB, IL-12, and CXCL10 along with the reduction of IL-10[365,366]. Since an explanation of the nature of the anti-inflammatory activity for AT111 has yet to be elucidated, a comparison of the transcriptional profile between cells treated with DMSO, AT111, AT5, or not treated was performed.

4.3.5 RNA sequencing.

Transcriptome profiles for RAW 264.7 macrophages treated with each compound for 4 h then cotreated with LPS (1 μg/mL) for an additional 4 h were determined using RNA sequencing. PMA-differentiated human U937 monocytes (now macrophages) were also examined to begin comparisons between mouse and human model systems. Each sample was examined in triplicate. PCA analysis for the RAW 264.7 cells revealed one replicate from each the vehicle, AT111, and untreated cells failed to cluster and were excluded. The three samples excluded seemed to shift the group of samples they were clustered with. For example, the errant untreated sample clustered with the vehicle group, the vehicle clustered with the AT111 group, and the AT111 sample clustered with the untreated group (Appendix IV; Figure S10). It is highly unlikely that a biological error in which the cells treated with medium reacted identically to cells treated with LPS and DMSO and the cells treated with LPS and AT111 reacted as treated with medium. Unfortunately, it seems more likely that the samples were acquired incorrectly during sequencing. As such samples RA1 (untreated replicate 1), RA2 (vehicle replicate 1), and RA5 (AT111 replicate 1) were excluded. The resulting PCA analysis showed strong clustering of the remaining samples (Figure 35 A). This is congruent with the PCA analysis of U937 cells, which revealed clustering of all treatment types (Figure 35 B). R3 and U3 (A, B, and C) samples (not shown) represent dexamethasone treated cells. It was determined after sequencing that the dexamethasone used in this experiment had expired and thus had a much weaker effect. Since RNA sequencing is expensive and time consuming, coupled with the fact that the dexamethasone treatment is not required for comparison of

transcriptome profiles of the vehicle and AT111, it was decided to not repeat this experiment and exclude dexamethasone from the analysis.

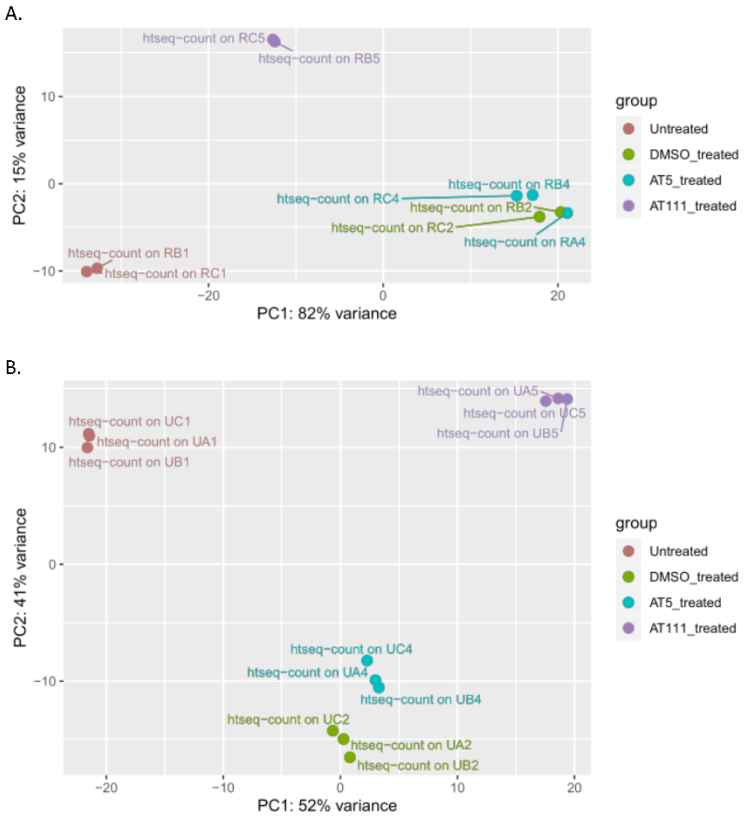

Figure 35. Clustering of transcriptional profiles. PCA analysis showing the variance and grouping of each replicate in A. RAW 264.7 cells and B. PMA-differentiated U937 cells. PCA analysis was done using the DESeq2 tool on the Galaxy web server.

A comparison of the differentially expressed genes (DEGs) in AT111 treated cells compared to the vehicle control revealed dramatic differences in transcriptome profiles (Figure 36). Treatment of AT5 led to minor changes in the expression profiles of both RAW 264.7 cells and U937s, though it had a greater effect in U937 cells. As apparent from the heatmaps in Figure 36 C and D, Expression profiles for AT5-treated cells were more aligned with the LPS+DMSO vehicle control (LVC) than with the untreated control or AT111-treated cells. AT5 led to a significant differential expression of only six genes in RAW 264.7 cells (*Gpi-ps, Gm29216, Serpinb2, Gm9824, Rsph3a, and Morc4*), where only *Gpi-ps*, *Gm29216*, *Serpinb2* were down regulated and *Gm9824*, *Rsph3a*, and *Morc4* were upregulated. In RAW 264.7 cells and in U937 cells, treatment with AT111 led to the significant differential expression of 1854 and 2859 genes, respectively (Figure 36 A and B).

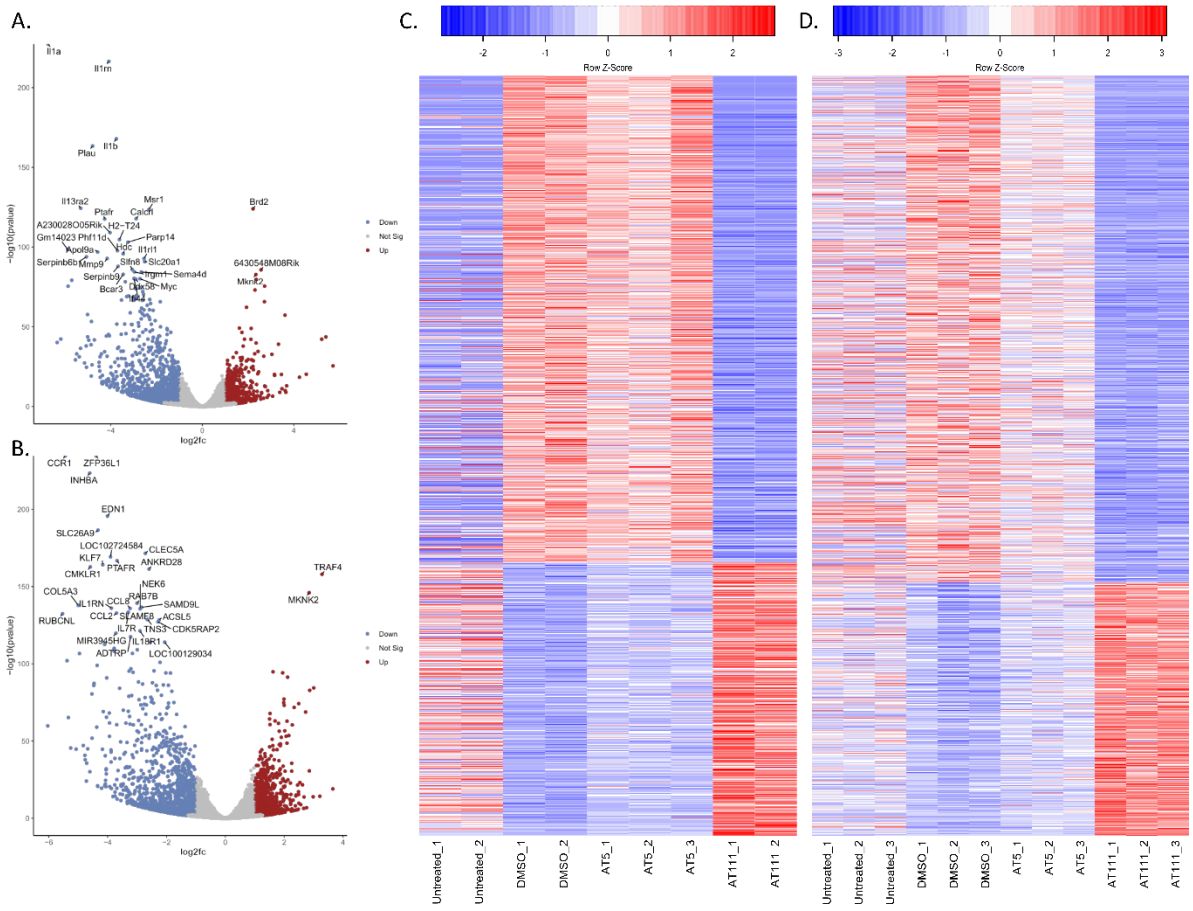

Figure 36. Differential expression profiles in transcripts from RAW 264.7 cells or U937 cells. Cells were pretreated with 100 µM AT111, or indicated control, for 4 h, then cotreated with 1 µg/mL LPS for an additional 4 h. Volcano plots depicting distribution of transcripts for AT111-treated A. RAW 264.7 cells or B. U937 cells. The significance cutoff was set to a $\log_2$FC ≥ 1 and an adj. p-value ≤ 0.05. Blue depicts downregulated significant genes while red depicts upregulated significant genes. The top 30 most significant genes are labeled. Significance values for *Il1a*, C-C motif chemokine receptor (CCR) 1 (*CCR1*), and *ZFP36L1* were beyond

the axis limit. Heatmaps comparing relative expression profiles of AT111 DEGs for all treatments in C. RAW 264.7 cells and D. U937 cells. The relative z-score was determined by subtracting the mean standardized count from the individual standardized count for each gene then divided by the standard deviation. Samples with positive z-scores, indicating counts above the average, are in red, while genes with negative z-scores are in blue. Heatmaps were made using the standardized count output file from DESeq2 and created using heatmap2 from the Gplots library in RStudio.

Genes which passed the cutoff but had less than 0.5 counts per million for all samples were removed, and the resulting 1822 (RAW 264.7) and 2730 (U937) were used for further analysis. DEG profiles in cells treated with AT111 appeared to mimic those of the untreated in RAW 264.7 cells but appeared to be different than the untreated control in U937s. Because the genes shown in the heatmap are of the differentially expressed genes for AT111 compared to the LPS (with 0.1 % DMSO [v/v]) control, it follows that the expression profiles would be the inverse of one another (Figure 36 C and D). However, the difference between the AT111-treated U937 cells and the untreated U937 cells (Figure 36 D) may be that the U937s were first differentiated into macrophages using PMA. The PMA-driven differentiation of U937s has been shown to be the result of protein kinase C (PKC) activation[367] partly due to increased activity of the transcription factors NF-κB and PU.1[368] possibly through Rhoa and rho-associated protein kinases (ROCK)[369]. In this experiment, U937s were differentiated for 72 h with PMA then washed and immediately the indicated treatments were added. In some studies, PMA-differentiation can be followed by a rest period allowing for the resultant macrophages

to recover[370-373] though studies did not have a rest period[374]. Many studies state that this rest period is important for optimization and response profiles[372,375,376], but do not explore the transcriptional profiles as a whole. However, one study showed that this rest period allowed for the PMA-induced expression of pro-IL-1β, to diminish[377]. Since the cells were not allowed to recover, it is possible that AT111 was able to interfere with some of the PMA-induced transcription in addition to that caused by LPS. It is also possible that some genes downregulated by AT111 are genes that may be responsible for or activated after the differentiation of U937 monocytic cells into macrophages.

In RAW 264.7 cells, the expression profiles of AT111 treated cells and the untreated cells are similar, but not identical. Indeed, treatment with AT111 (and LPS) led to the differential expression of 1989 genes compared to the untreated cells. Of those genes, only 1941 were annotated with a gene symbol, and 845 were upregulated and 1144 genes were downregulated. While this difference could be entirely because of AT111 on the RAW 264.7 cells, it is more likely that the LPS present had some role in increasing the levels of certain genes, even if the expression of the genes was inhibited by AT111. When comparing the DEGs (annotated with an official gene symbol, duplicate gene annotations removed) of AT111 (and LPS)-treated cells to the LVC cells (AT111 vs LPS/vehicle DEGs; AVL genes) and the DEGs of AT111 (and LPS)-treated cells to the untreated cells (AVU genes), it was found that 178 of the upregulated AVU genes were also downregulated AVL genes, including many pro-inflammatory cytokines such as *Il6*, *Tnf*, and *Il1b*, as well as *Nos2* (Figure 37 A).

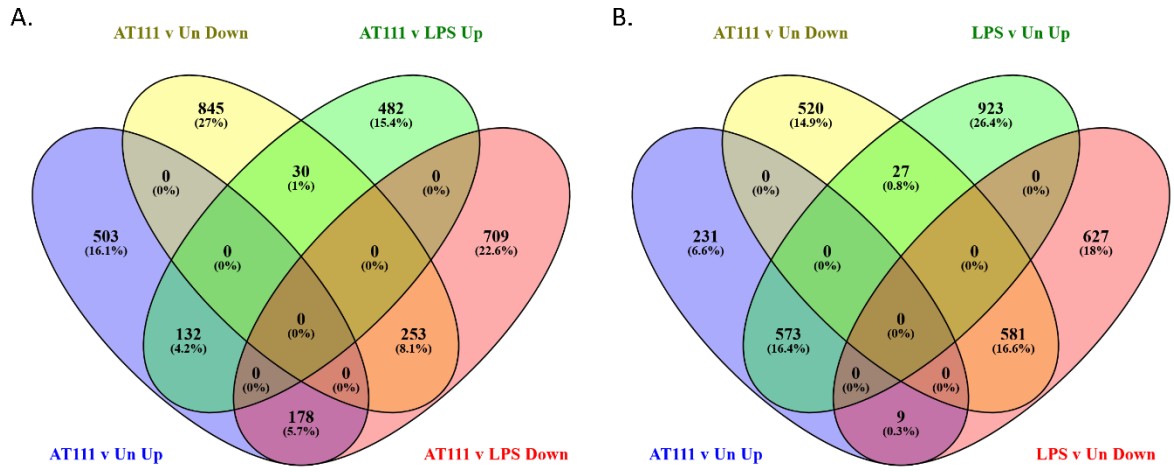

Figure 37. Overlap of DEGs in RAW 264.7 cells. Venn diagrams depicting the overlap of DEGs from A. the comparison of AT111+LPS treated cells compared to the untreated control (AT111 v Un) and AT111+LPS treated cells compared to the vehicle (LPS+DMSO) control (AT111 v LPS) or B. AT111 v Un and cells treated with the vehicle compared to the untreated cells (LPS v Un). DEGs were considered as previously stated and divided into upregulated ($log_2FC \geq 1$) or downregulated ($log_2FC \leq 1$). Venn diagrams were created using Venny.

It should be noted that ",191'AVL genes (66.8% of all AVL genes) were not listed as AVU genes. This implies that the expression levels of these genes in LPS-stimulated cells treated with AT111 are similar to that of the untreated cells (Figure 37 A). Conversely, 1,348 AVU genes (69.4% of all AVU genes) were not listed as AVL genes implying that the expression levels of these genes in LPS-stimulated AT111 treated cells and LVC cells were potentially similar (Figure 37 A). Together this indicates that LPS may be the biggest driving

force behind some of the differential gene expression observed between the AT111-treated cells and the untreated cells. In a comparison between AVU genes and DEGs in the LVC cells compared to the untreated cells (LVU genes) it was found that 573 and 581 AVU genes were similarly upregulated or downregulated LVU genes, respectively (Figure 37 B). As such this indicates that 59.5% of the AVU genes were either upregulated or downregulated due to the addition of LPS and not AT111 (Figure 37 B). Of the remaining genes, 751 AVU genes had no overlap with LVU genes, while 27 genes were conversely upregulated LVU genes and upregulated AVU genes, and 9 other genes following the latter (Figure 37 B). These data further suggest that the discrepancies in expression profiles of certain genes between AT111 and the untreated are possibly due to instances where AT111 had little-impact on their LPS-induced transcription.

To further elucidate the effect AT111 had on LPS-treated cells, and to determine if the expression levels of cytokines observed in the qRT-PCR experiment matched the findings of the RNAseq experiment, it was decided to investigate the differential expression of certain pro-inflammatory response genes. In accordance with the findings of the qRT-PCR experiment in RAW 264.7 cells, the genes for *Il1b, Il6, Tnf, Nos2, Ccl2,* and *Csf2* were all down regulated by AT111 compared to the vehicle control (Table 4; highlighted in green). In addition to those, mRNA levels of 31 other cytokines and chemokines, including many interleukins, CCLs, and C-X-C motif ligands (CXCL), were reduced (Table 4). Though slightly in contrast to the qRT-PCR data (Figure 31), but more in line with the ELISA data (Figure 30 D), AT111 led to a slight reduction in *Tnf,* the gene coding for TNF-α ($Log_2FC = -1.03329$) by approximately 51 % (Table 4).

Table 4. Representative differentially expressed cytokines in LPS-stimulated RAW 264.7 cells treated with AT111 compared to the vehicle control.

Gene	Log_2FC	Adj p-value
Il1a	-6.74407	0.00E+00
Cxcl3	-5.37415	6.45E-30
Il6	-5.00949	2.97E-42
Tnfsf15	-4.71666	2.46E-40
Il36a	-4.39025	8.53E-14
Tnfsf10	-4.35882	2.06E-13
Il1b	-3.75331	7.61E-165
Csf1	-3.39469	4.59E-50
Il15	-3.05075	8.39E-31
Cxcl11	-2.68352	4.16E-11
Cx3cl1	-2.64122	6.76E-12
Il36g	-2.5109	4.85E-06
Tnfsf8	-2.34974	4.24E-04
Csf2	-2.3465	5.19E-04
Il18	-2.32269	9.14E-06
Ccl22	-2.22682	5.26E-50
Ccl6	-2.18755	7.33E-07
Csf3	-1.95278	8.14E-05
Il27	-1.86297	6.02E-08
Il33	-1.79194	2.37E-03
Nos2	-1.78631	9.34E-03
Ccl17	-1.78002	8.17E-03
Cxcl2	-1.7793	2.30E-05
Ccl12	-1.77721	1.40E-02
Ccl7	-1.74555	8.83E-07
Cxcl10	-1.65284	9.29E-05
Bmp10	-1.65199	1.91E-02
Ebi3	-1.53519	4.50E-09
Lta	-1.50773	3.69E-04
Ccl9	-1.40603	5.26E-34
Ccl2	-1.38722	2.88E-06
Osm	-1.30204	1.19E-02
Ltb	-1.23867	3.22E-07
Cxcl14	-1.12449	3.61E-03
Tnf	-1.03329	4.02E-14
Ifnb1	-3.99099	8.34E-20
Il10	-2.80683	4.00E-15

Table 5. Representative differentially expressed cytokines in LPS-stimulated U937 cells treated with AT111 compared to the vehicle control.

Gene	Log_2FC	Adj p-value
CXCL11	-4.47129	3.90E-84
CXCL9	-4.06058	1.24E-19
IL6	-3.77653	6.99E-108
CCL2	-3.69965	1.66E-130
IL1A	-3.44473	2.53E-40
IL36G	-3.39993	2.14E-41
CXCL6	-3.33144	6.22E-18
IL37	-3.32567	4.62E-13
CCL8	-3.23611	1.64E-133
TNFSF10	-2.93229	5.42E-75
CXCL10	-2.87001	8.70E-26
TNFSF13B	-2.8109	5.76E-85
IL24	-2.78646	8.95E-28
CCL7	-2.75386	4.45E-72
EBI3	-2.51906	1.57E-25
CXCL5	-2.20481	2.96E-10
TNFSF15	-2.09548	5.45E-15
IL10	-2.05882	2.27E-45
IL33	-1.99056	7.63E-04
LTA	-1.82961	1.66E-06
CCL13	-1.62195	1.40E-12
CSF1	-1.42783	1.64E-03
CCL1	-1.40579	9.05E-08
IFNL1	-1.25397	3.12E-02
NOS3	-1.15149	4.05E-02
IL16	-1.05331	9.70E-08
CCL3	1.023637	6.61E-14
TNF	1.11184	6.60E-12

However, in PMA-differentiated human U937 cells, of the listed cytokines, only *IL6* and *CCL2* were down regulated (Table 5). Indeed, when comparing the differentially expressed genes for both the vehicle and AT111 compared to the untreated samples, both had similar levels of expression of *IL1B* (Log_2FC = 3.10 and 3.60, respectively) and *CSF2* (Log_2FC = 4.35 and 3.65, respectively). Though the relative level of *CSF2* was slightly less, it did not make the fold change cut-off to be considered biologically relevant. In contrast to *Tnf* in RAW 264.7 cells, in the human U937 cells *TNF* was increased (Log_2FC = 1.11; adj p = $6.60E^{-20}$) in AT111

treated cells compared to the vehicle (Table 5). *NOS2* expression was not induced to high enough levels to meet the cut-off criteria. This lack of inducible *NOS2* expression in human macrophages is well known, and the role of iNOS in human macrophages has been widely debated[378-381]. Alternatively to *NOS2*, *NOS3*, the gene encoding endothelial NOS (eNOS), has been implicated in contributing to NO production in human macrophages, though at a normal housekeeping level[382]. Though eNOS is not normally inducible by LPS, it has been shown to play an important role in activation of NF-κB using eNOS deficient mice[383]. AT111 was able to reduce levels of *NOS3*, in U937 cells, by a $Log_2FC = -1.15$ (Adj. $p = 0.045$), potentially contributing to its anti-inflammatory potential. However, in RAW 264.7 cells, AT111 did not reduce levels of phosphorylated p65, inhibit its nuclear translocation, nor its perceived transcriptional activity (Figures 33, 34, and 32). Though there may be a difference in the human and mouse mechanisms, it seems that lowered levels of eNOS may not be the only contributing factor to the mechanisms behind the anti-inflammatory effects of AT111. Indeed, AT111 had no effect on levels of eNOS in RAW 264.7 murine macrophages, specifically having a $Log_2FC = 0$ and an adj. p-value = 1.0.

Gene ontology and enrichment analysis revealed that AT111 downregulated genes enriched for many immunological processes, including those involved in the innate immunity, response to LPS, and the inflammatory response in both RAW 264.7 and U937 cells (Figure 38). This is to be expected as AT111 seems to interfere with LPS-induced transcription of pro-inflammatory genes. AT111 also downregulated genes linked to G protein-coupled receptors signaling (GPCR). When examining the enriched biological processes (BP), cellular components (CC), molecular functions (MF), and protein domains from the InterPro database

(through DAVID), it appears that AT111 down-regulates transcription of many genes associated with the cell surface and extracellular space including GPCRs, and their signaling, as well as genes for many secreted proteins (extracellular space), including many interleukins, chemokines such as C-X-C chemokine ligands, and cytokines. Additionally, genes related to the plasma membrane are also enriched. This is not surprising because GPCRs make up the largest group of receptors and regulate a broad range of signal transduction pathways[384]. Furthermore, it has already been shown that AT111 leads to the down-regulation of many LPS-induced cytokines and chemokines, therefore reducing genes associated with the GO term "extracellular space". Nevertheless, the reduction in GPCRs and GPCR signaling may provide insight into the possible mechanism of AT111. For example, treatment with AT111 leads to the decrease in many chemokine and cytokine receptors including C-X-C receptors, CC receptors, olfactory receptors, and others. Many of these receptors are either involved in LPS/TLR4-induced inflammatory response, transcriptionally upregulated by LPS treatment, or both[385-388]. It makes sense that if AT111 is interfering with the LPS-induced transcription that it would lead to a significant decrease in their transcription. AT111 also reduces the expression of many receptors with immunoglobulin-like domains, including interleukin receptors, receptor tyrosine kinases, signaling lymphocyte activation molecule family receptors, major histocompatibility complex (MHC) related proteins (8 RAW 264.7, 1 U937), and other types of CDs.

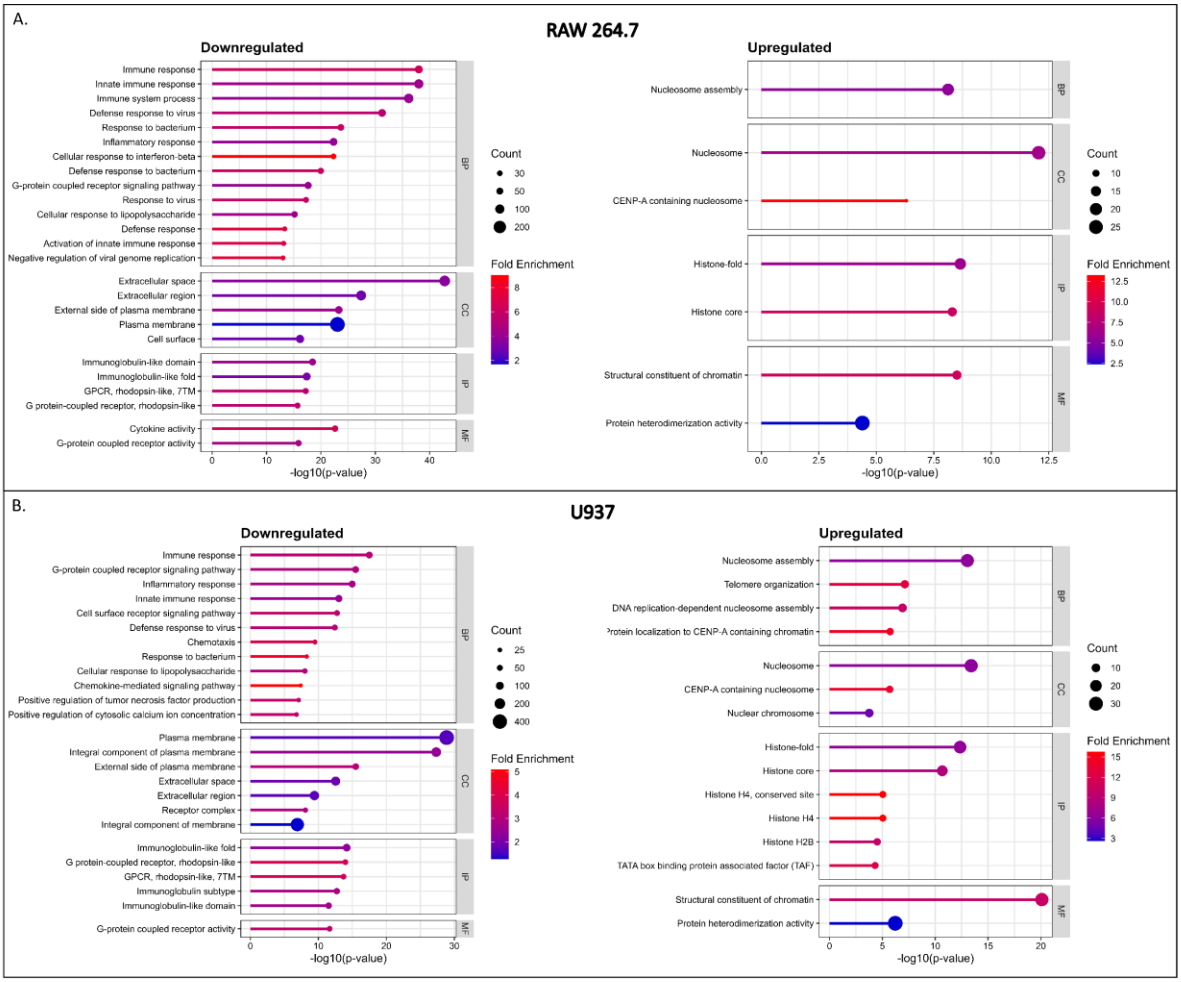

Figure 38. Functional enrichment analysis of differentially expressed genes. Enriched terms for A. RAW 264.7 cells or B. U937 cells treated with AT111 compared to the LVC cells are shown. Functional enrichment was determined with DAVID using the GOTERM_BP/CC/MF_Direct and InterPro categories with an EASE value set to 0.05. Terms with an FDR ≤ 0.05 were considered as significant. The top 25 enriched terms are ranked by their significance. The background used for DAVID was generated from all measured genes with at least one treatment having an average count greater than 15 (0.5 counts/ million). Genes that could not be recognized by DAVID were excluded.

A comparison of the downregulated genes for both cell lines to the Kyoto Encyclopedia of Genes and Genomes (KEGG)[325] database, through DAVID[314,316] (visualized using ShinyGO[324]/Pathview[326]) was done to determine if AT111 may be interfering with any cellular pathways. The most significantly enriched pathway for both cell lines was the pathway related to cytokine-cytokine receptor interaction (mmu04060 Iuse] / hsa04060 [human]; Figure 39).

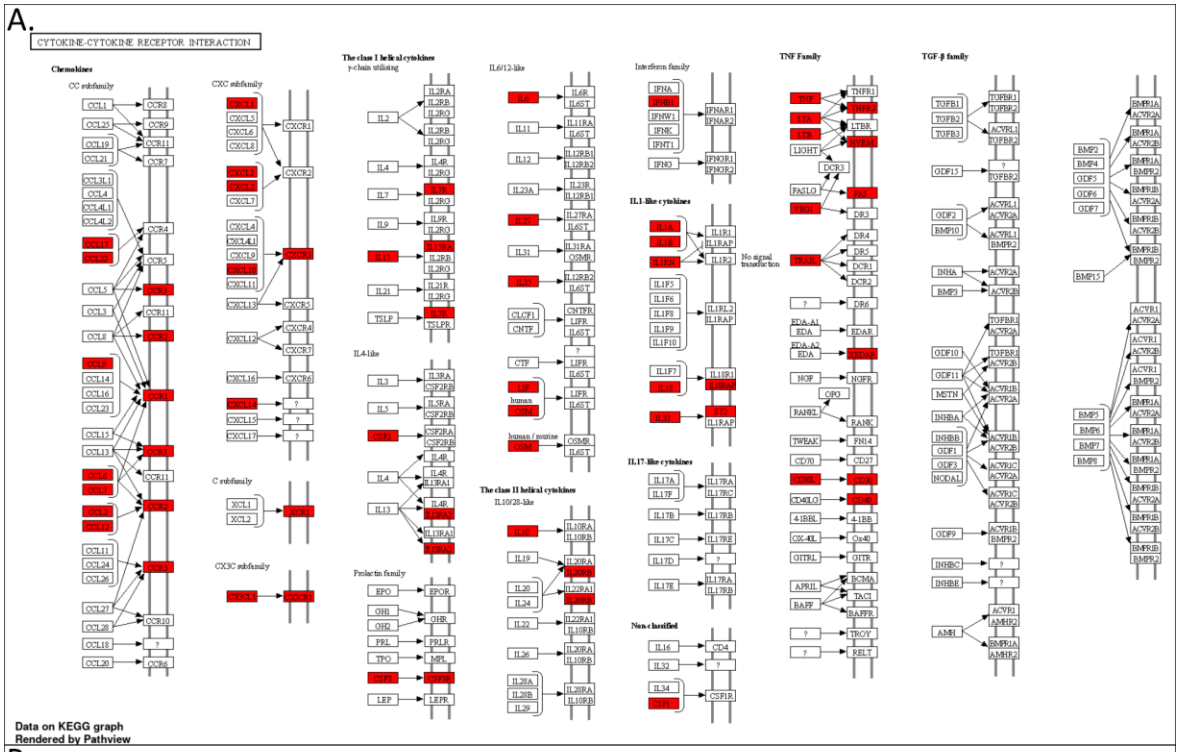
A.
CYTOKINE-CYTOKINE RECEPTOR INTERACTION
Chemokines
CC subfamily
CXC subfamily
C subfamily
CX3C subfamily
The class I helical cytokines
γ-chain utilizing
IL6/12-like
IL4-like
Prolactin family
The class II helical cytokines
IL10/28-like
Interferon family
IL1-like cytokines
No signal transduction
IL17-like cytokines
Non-classified
TNF Family
TGF-β family
Data on KEGG graph
Rendered by Pathview
B.
CYTOKINE-CYTOKINE RECEPTOR INTERACTION
Chemokines
CC subfamily
CXC subfamily
C subfamily
CX3C subfamily
The class I helical cytokines
γ-chain utilizing
IL6/12-like
IL4-like
Prolactin family
The class II helical cytokines
IL10/28-like
Interferon family
IL1-like cytokines
No signal transduction
IL17-like cytokines
Non-classified
TNF Family
TGF-β family
Data on KEGG graph
Rendered by Pathview

Figure 39. AT111 affects the same cytokine-cytokine receptor pathway differently in RAW 264.7 cells and U937 cells. DEGs were compared to the KEGG using DAVID. The top enriched pathway by FDR is shown (cytokine-cytokine receptor pathway, mmu04060/hsa04060) for both A. RAW 264.7 cells and B. U937 cells. Genes belonging to the list of DEGs are shown in red. The entire gene list, including those not differentially expressed, was used as a background. Genes that were not recognized by DAVID were omitted. The image was rendered using Pathview through ShinyGO.

Is it apparent in both cell lines that AT111 leads to the reduction of many genes that encode either cytokines, or their receptors. However, there are important differences in the cytokines and receptors that are downregulated. For example, examining the C-X-C motif chemokine ligands (CXCL) and receptors (CXCR), AT111 downregulated *Cxcl1,2,3,10, 14* and *Cxcr3* in RAW 264.7 cells (Figure 39 A) while down-regulating *CXCL5,6,9,10,11* and *CXCR5* in U937s (Figure 39 B). The most notable difference is the variation in which interleukin-receptors are down regulated. In both RAW 264.7 and U937 cells, AT111 decreased expression of multiple interleukin receptor genes including the murine *Il13ra2* and *Il1rl1* and the human *IL7R* and *IL18R1*. In U937s, AT111 also influenced expression of other interleukin receptors including *IL1R1* (log_2FC = -4.36; adj. p-value = $5.88E^{-97}$), *IL1R2* (log_2FC = -1.65; adj. p-value = $1.12E^{-5}$) *IL18RAP* (log_2FC = -4.04; adj. p-value = $8.64E^{-64}$), which are located in a similar region of chromosome 2 to *IL18R1* (log_2FC = -2.901; adj p-value = $4.19E^{-}119$ in human cells[389] (Table 6). However, in RAW 264.7 cells, AT111 failed to lower many of the same interleukin receptors (Table 6). Only lowering *Il13ra2*, *Il15ra2*, *Il18rap*, *Il1rl1* (ST2 in

Figure 39 A), *Il20rb*, and *Il7r*. This variation may be due to the inherent regulatory differences between murine cells and human cells for these genes, either through response to stimuli or through transcription factor binding motifs[390]. Additionally, intra-species variations in the cellular response to LPS have been recorded for both murine[391] and human[344] cells. However, there are very few reports that make a direct comparison between the two cell lines. Though these differences are great, the overall outcome is comparable as can be seen in the similarity of the enriched terms (Figure 38).

Table 6. Interleukin receptors downregulated by AT111 in either U937 or RAW264.7 cells compared to the vehicle control. Genes that were not present or did not pass the minimum count requirement are labeled with a (-). Genes that were counted but not differentially expressed are indicated in *red*.

	U937		RAW 264.7	
Gene (U937/*Raw 264.7*)	**log_2FC**	**Adj. p-value**	**log_2FC**	**Adj. p-value**
(IL11RA/*Il11ra*)	1.87	1.84E-15	*0.09*	*8.21E-01*
(IL13RA2/*Il13ra2*)	-	-	-5.31	1.51E-121
(IL15RA/*Il15ra*)	-1.10	8.90E-14	-3.15	5.01E-57
(IL17RC/*Il17rc*)	1.12	4.48E-09	*-0.24*	*4.59E-01*
(IL17RE/*Il17re*)	-1.56	2.92E-19	-	-
(IL17REL/*Il17rel*)	-1.29	1.05E-02	-	-
(IL18R1/*Il18r1*)	-2.90	4.19E-119	-	-
(IL18RAP/*Il18rap*)	-4.04	8.64E-64	-2.51	1.67E-27
(IL1R1/*Il1r1*)	-4.36	5.88E-97	-	-
(IL1R2/*Il1r2*)	-1.65	1.12E-05	-	-
(IL1RL1/*Il1rl1*)	-	-	-2.55	1.53E-90
(IL20RB/*Il20rb*)	1.14	4.24E-02	-1.15	6.10E-04
(IL21R/*Il21r*)	-1.33	2.06E-04	-	-
(IL2RA/*Il2ra*)	-5.25	4.14E-44	-	-
(IL2RB/*Il2rb*)	-1.11	1.30E-07	-	-
(IL31RA/*Il31ra*)	-2.05	2.90E-19	*-0.57*	*5.19E-01*
(IL7R/*Il7r*)	-3.30	4.10E-131	-3.22	5.26E-21
(IL9RP3/*Il9rp3*)	1.23	2.06E-03	-	-

The top enriched upregulated GO (and InterPro) terms in both RAW 264.7 cells (Figure 38 A) and U937 cells (Figure 38 B) were all related to the nucleosome, both core subunits and linkers, as well as protein heterodimerization. Histones are made up of 8 subunits, consisting of two copies of each: histone 2A (H2A), histone 2B (H2B), histone 3 (H3) and histone 4 (H4) subunits. About 146 base pairs (bp) of DNA becomes tightly wrapped around each octet of histones to form the nucleosome[392,393]. The H1 histone subunit binds the surrounding linker DNA, stabilizing the nucleosome and allowing for further compaction of the DNA into chromatin[394,395]. Nucleosomes, and subsequently histones, have been extensively studied, and heavily reviewed, due to their prevalence and role in transcriptional regulation[392,394,396-401]. When the nucleosome is intact, and the DNA is tightly wound, transcription is impeded[402]. Access of RNA polymerases to the DNA can be granted or denied by various post-translation modifications (PTMs)[398]. These PTMs include acetylation (where an acetyl group is added to the histone, neutralizing its negative charge allowing for increased transcription), phosphorylation, which also can disrupt histones and lead to acetylation, crotonylation, an indicator of increased transcription and sometimes transcription inhibition, methylation, which has been linked with a decrease in transcription, as well as other PTMs such as succinylation and glutarylation, which can both destabilize the histone-DNA interactions[398,403]. Histone function can also be controlled by the addition of either replication-dependent or replication-independent histone variants[392,398]. Histone variants, such as H3-3A (H3.3), have mutations that lead to changes in their role, thus leading to the destabilization of the nucleosome complex resulting in resumed transcriptional activity[392,398]. Since histones play an important, and dynamic, role in transcriptional regulation, the observed upregulation of genes observed in

cells treated with AT111 may play a part in the observed differential decrease in transcription. However, it is also possible that this observed increase in histone and histone assembly related genes may be a result of the real mechanism of action for AT111, as opposed to the cause.

To examine this possibility, DEGs in AT111-treated LPS-stimulated cells versus the LVC cells (denoted as AT111) were compared to DEGS from LVC cells versus the untreated control (denoted as LPS). There was a distinct overlap between the two groups in both RAW 264.7 cells (Figure 40 A) and U937 cells (Figure 40 B). In both cell types, treatment with AT111 led to the downregulation of a significant portion of LPS upregulated genes (736 for RAW 264.7 and 508 for U937) and resulted in the upregulation of a smaller portion of LPS downregulated genes (307 for RAW 264.7 and 154 for U937; Figure 40). In contrast to their similarities, there is an important difference in the number of genes in both synergistic groups and solo groups. In RAW 264.7 cells, AT111 and LPS shared 18 upregulated genes and 30 downregulated genes, while in U937 cells, 46 and 116 genes were shared, respectively (Figure 40). In RAW 264.7 cells, AT111 also led to the differential expression of 693 genes which were not present in the LPS DEGS (Figure 40 A). This is quite different than the 1906 AT111 DEGs which were not included in the LPS DEGs in U937 cells (Figure 40 B). The large number of DEGs for AT111 in U937s could be due to the lack of a recovery period after the initial differentiation of U937 cells into macrophages using PMA as previously noted. The increased number of LVC to untreated DEGs in RAW 264.7 cells (2,740) compared to that in U937 cells (2,122) may indicate that the expression levels of many LVC DEGs in U937s may be closer to the untreated cells than that in RAW 264.7 cells. In RAW cells, the minimum and maximum $\log_2$FC for LVC DEGs are -5.698 (*S1pr1*) and 12.131 (*Il1b*), while in U937 cells they are -

3.132 (*SNAI3*) and 7.237 (*SLC12A7*), respectively. Regardless, examination of the genes not listed as LVC DEGs may shed some light on the potential mechanisms of AT111.

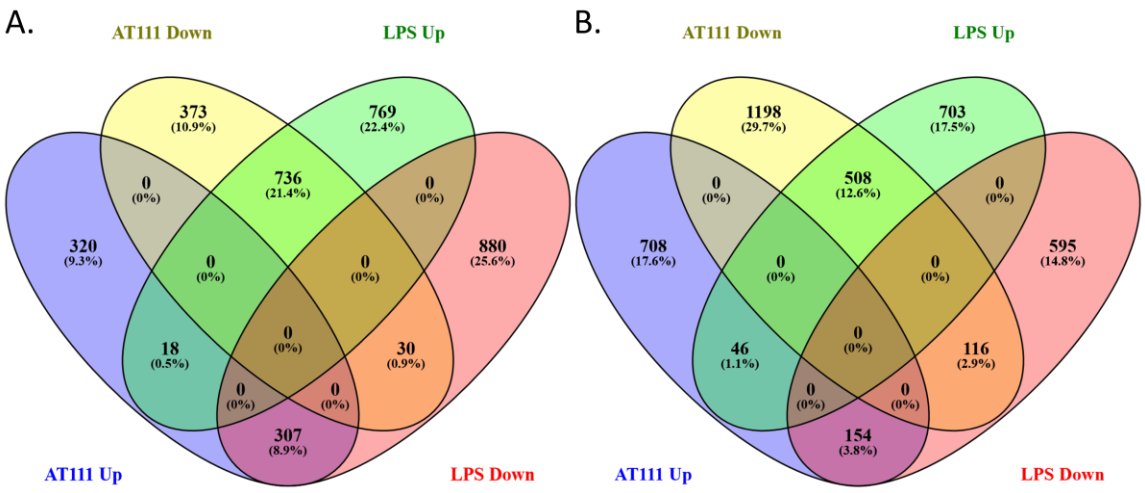

Figure 40. Overlap of DEGs in RAW 264.7 cells and U937 cells. Venn diagrams depicting the overlap of DEGs from the DEGs for AT111 vs. the vehicle control (AT111) compared to the DEGs from the vehicle control vs. the untreated control (LPS) in A. RAW 264.7 cells and B. U937 cells. DEGs were considered as previously stated and divided into upregulated ($log_2FC \geq 1$; up) or downregulated ($log_2FC \leq 1$; down). Venn diagrams were created using Venny[327].

GO analysis of the 393 (RAW 264.7) and 1906 (U937) genes not found in the LVC DEGs showed similar trends in enrichment with each other and with the terms enriched in the total gene set. For example, terms for the immune response (GO:0006955), inflammatory response (GO:0006954), and GPCR signaling pathway (GO:007186) were among the top 25 enriched downregulated biological processes for both cell types (Figure 41). Though not in the top 25 terms for RAW 264.7 cells, the term for the innate immune response (GO:0045087) is also enriched in both. Additionally, terms for protein domains such as immunoglobulin-like domain (IPR007110), immunoglobulin-like fold (IPR013783), and immunoglobulin subtype (IPR003599), were downregulated among both cell types (Figure 41). Though both these terms were enriched across both cell lines, only four genes were conserved between them; Fc Receptor Like B (*FCRLB*), Triggering Receptor Expressed on Myeloid Cells Like 4 (*TREML4*), Transglutaminase 2 (*TGM2*), and Leukocyte Immunoglobulin Like Receptor B3 (*LILRB3*/*Pirb*). *FCRLB*, *TREML4*, and *LILRB3* are all receptor proteins related to roles in the immune response. TGM2, a protein belonging to the transglutaminase family with cross-linking activities, has been associated with many biological processes[404,405], and has been implicated to have a regulatory effect on the innate immune response to cytosolic DNA[406]. The terms for RAW 264.7 cells had a far lower number of genes associated with them. For example, in the immunoglobulin-like fold term (IPR013783) U937 cells had 61 genes associated with this term while RAW 264.7s had 21. Although there was little overlap of the DEGs for both cell lines, the resulting terms were still relatively the same. In terms relating to the immune/inflammatory response (GO:0006955/GO:0006954) the same trend can be observed. RAW 264.7 and U937 cells similarly decreased *CCR1*, *CCR3*, *CD36*, C-type lectin domain

containing 7A (*CLEC7A*) and complement C3a receptor 1 (*C3AR1*) gene transcripts. Though these genes are all receptors, there is still the same observed variance described earlier. In both cell types, AT111 led to the downregulation of other innate immune receptors including many TLRs. In RAW 264.7 cells, both *Tlr7* and *Tlr8* were downregulated, while in U937s *TLR1*, *TLR4*, and *TLR6* were decreased. As stated earlier, this difference, while important, may be due to the differences between mouse and human cell lines.

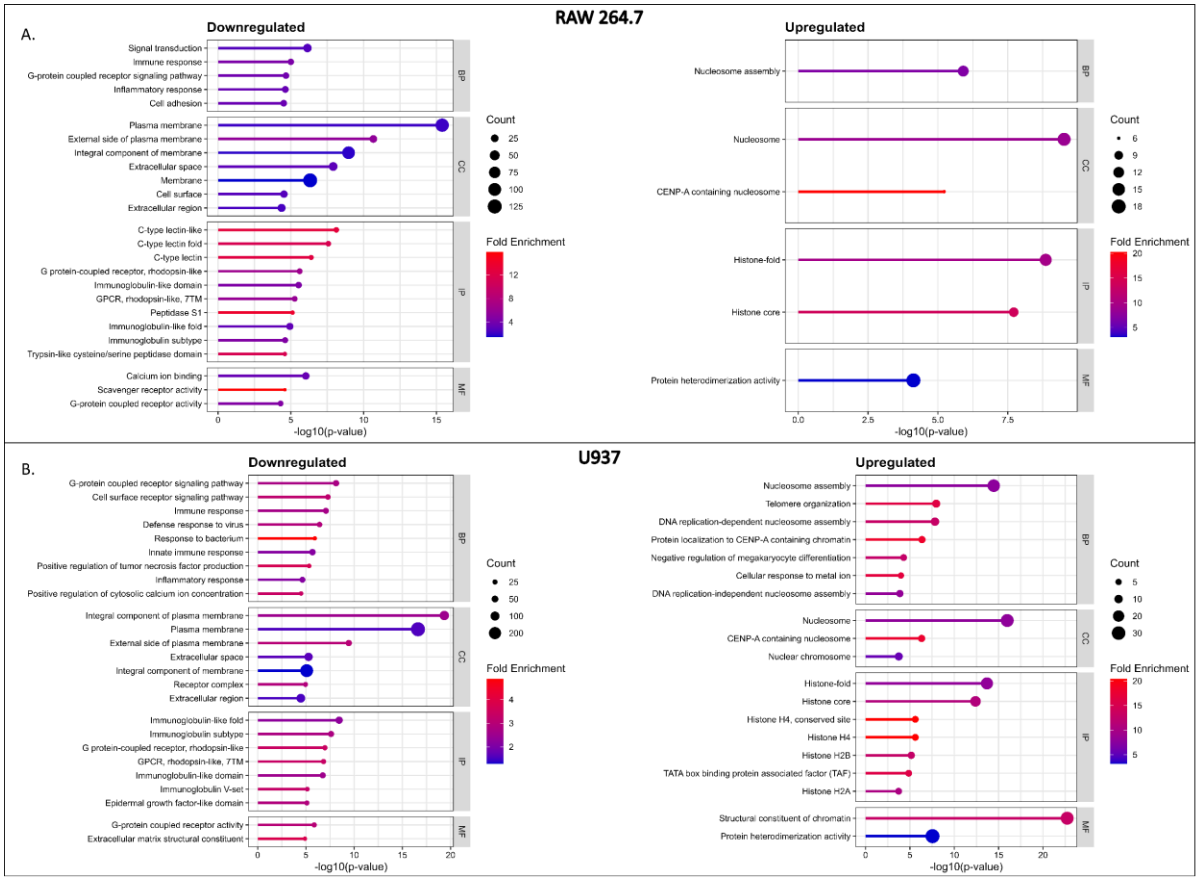

Figure 41. Functional enrichment analysis of AT111 DEGs in RAW 264.7 cells or U937 cells which were not present as LVC DEGs. Functional enrichment for AT111 DEGs compared to the vehicle for both A. RAW 264.7 cells and U937 cells were determined using DAVID using the GOTERM_BP/CC/MF_Direct and InterPro categories with an EASE value set to 0.05. Terms with an FDR ≤ 0.05 were considered as significant. The top 25 enriched terms are ranked by their significance. The background used for DAVID was generated from all measured genes with at least one treatment having an average count greater than 15 (0.5 counts/ million). Genes which could not be recognized by DAVID were excluded.

Although there is variation in the number and specific genes upregulated by AT111 in both U937 cells and RAW 264.7 cells, there are still similarities in the functions of those genes. As a result, AT111 induced the upregulation and downregulation of similar enrichment terms (Figure 41). In both cell types, as before, AT111 treatment led to the upregulation of genes enriched for the nucleosome (GO:0000786), nucleosome assembly (GO:0006334), histone core/fold domains (IPR007125/IPR009072), and protein heterodimerization activity (GO:0046982). Functional annotation clustering of terms with an FDR below 0.05 was done to reveal conserved genes across multiple terms. Indeed, there was significant overlap in genes for each enriched term for both RAW 264.7 cells and U937 cells, many with similar related functions. In RAW 264.7 cells the second cluster (enrichment score = 6.48) grouped three terms related to c-type lectin receptors with carbohydrate binding (Figure 42 D). Nine of the 13 genes represented were found in all groups. This clustering of terms allows the user to group together like terms and determine possible functional overlap. C-type lectins, which included

secreted and transmembrane proteins/receptors, have been implicated in a variety of cellular roles relating to the immune system by binding to polysaccharides/glycans[296,407]. Binding of the transmembrane c-type lectins can trigger activation of various signal transduction pathways leading to inflammation and other antimicrobial responses[407]. Certain genes, such as *Clec4d* and *Cd93* are involved in the inflammatory response of macrophages, while *Stab1* and *Clec1a* seem to be involved in its resolution[408-411]. To examine whether these functional annotation clusters aligned with protein-protein interactions, proteins from either RAW 264.7 cells (Figure 42) or U937 cells (Figure 43) were uploaded into Cytoscape and analyzed using the STRING network app[332,333]. Multiple annotated genes could not be added due to lacking a corresponding ensemble ID and others were excluded from each subsequent step for lacking involvement in the largest protein-protein interaction subnetwork, so the purpose of this is to visualize gene clusters from DAVID while also looking at the local string clusters annotations for similarities and key representative features and distributed trends. In both cell lines used, genes which were differentially expressed only in AT111 treated cells and not LVC cells (Figure 40; Figures 42 B, 43 B) were isolated from the overall DEGs for AT111 treated cells (Figures 42 A, 43 A).

The largest subnetwork of interacting proteins was then divided based on being downregulated or upregulated (Figures 42 C and E, 43 C and E) and the resulting clusters from various terms were analyzed. In RAW 264.7 cells the functional annotation cluster with the highest annotation score for the downregulated genes contained only broad terms such as “plasma membrane” (GO:0005886), “integral component of membrane” (GO:0016021), and “membrane” (GO:0016020) and was therefore skipped for visualization. Cluster 2 for the downregulated (Figure 42 D) and cluster 1 for the upregulated (Figure 42 E) were chosen to

be visualized. For the downregulated genes, the terms associated with c-type lectin receptors and carbohydrate binding (purple) seemed to be isolated to the top-most corner of the cluster and thus relatively clustered together, as expected since these are genes related to the same type of receptor (Figure 42 C and D). Genes from enriched terms relating to the immune system, including "immune response" (GO:0006955) and "inflammatory response" (GO:0006954), and others (GO:0061760, GO:0045087, GO:0032729, GO:0002376) that were not part of cluster 1 (Figure 42 D) also were localized together (Figure 42 C; green), though these only had four overlapping genes (Figure 42 C; red ring). Examination of the local STRING clusters, as determined through STRING functional enrichment of the genes compared to the genome, revealed a similar cluster of terms (CL374, CL376, CL610, CL684, CL202, CL2021, CL2022, CL2099) related to various immune responses (Figure 42 D; yellow ring). All three groupings had only three overlapping genes including *Clec4a2*, *Clec4n*, and *Clec4d* while some genes only had overlap between two of the three groups. Taken together, treatment with AT111 downregulated certain genes associated with some immune functions, which were not differentially expressed in the LVC cells. Many of these genes in the immune/inflammatory enriched terms (GO:0006955, GO:0006954, GO:0061760, GO:0045087, GO:0032729, GO:0002376) are different types of receptors, including CXCRs, c-type lectins, CCRs, and various TLRs. Though these genes are not related to TLR4 in general, downregulation of these genes by AT111 may allow a decreased inflammatory response to chemokines and cytokine expressed *after* the initial signal transduction pathway via LPS/TLR4, diminishing the amount of the various cytokines expressed.

A 2019 study by Somann *et al.* found that intraperitoneal injection of LPS led to the increase of cytokines, such as IL-10 and TNF-α as soon as 40 and 60 min[412]. Other cytokines, such as IL-6, IL-17F, and GM-CSF were detected around 120 min and expression of these genes leveled off soon after, while the cytokines IFN-γ and IL-22 were elevated until around 180 min[412]. Though not in the top 25, AT111 downregulated genes were enriched for positive regulation of interferon-gamma production (GO:0032729, FDR = 0.0336). It is feasible that these cytokines may contribute to autocrine signaling events in the macrophage thus modulating the inflammatory response[259], which is mitigated by AT111. However, in U937 cells, genes relating to c-type lectin receptors were not enriched, although *CLEC7A* and other CLEC proteins, were still downregulated.

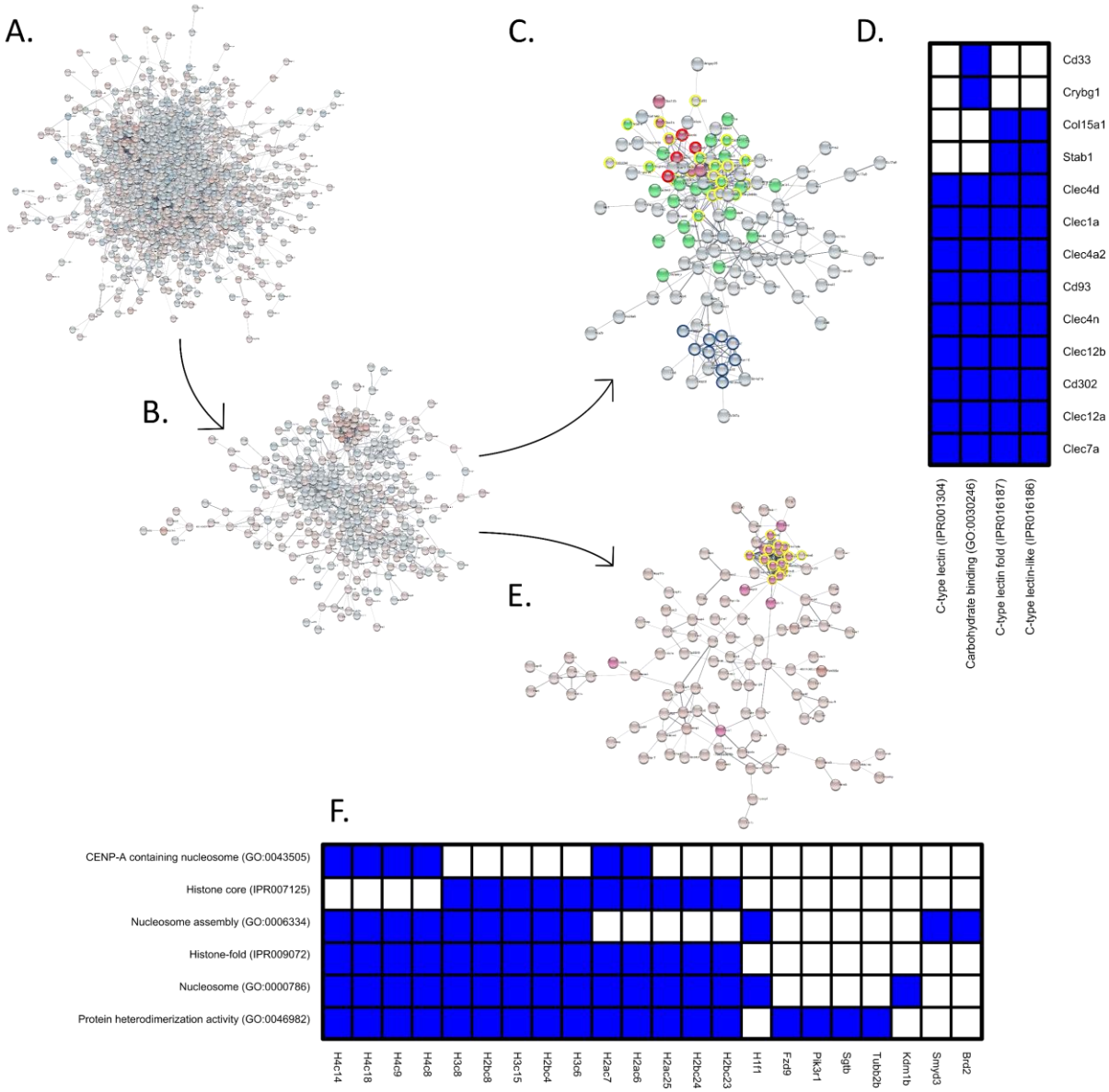

Figure 42. Grouping an annotation of enriched GO/InterPro terms for AT111 DEGs in RAW 264.7 cells. A. STRING cluster map of representative AT111 DEGs compared to the vehicle control in LPS-stimulated RAW 246.7 cells. B. STRING cluster map of AT111 genes not included in the list of LPS DEGs from Figure 40 A. C. Downregulated DEGs from B. Terms associated with functional–annotation cluster 2 - c-type lectin receptors and

carbohydrate binding (D) are shown in purple. Genes from enriched terms relating to the immune system (GO:0006955, GO:0006954, GO:0061760, GO:0045087, GO:0032729, and GO:0002376) that were not part of D. are displayed in green. Red ring: overlapping genes related to the immune system and cluster 2. Yellow ring: local STRING clusters for immune responses determined through STRING functional enrichment using the whole genome as background (CL374, CL376, CL610, CL684, CL202, CL2021, CL2022, CL2099). Blue ring: genes associated with cell division/ cell cycle. E. Upregulated DEGs from B. Terms associated with functional annotation cluster 1 – nucleosome/ histone related genes (F) are shown in purple. Yellow ring: local STRING clusters relating to the nucleosome/chromatin (CL18576, CL18582, CL18583, CL18590, CL18595, CL18599, CL18602, CL18605) using the whole genome as a background. Functional annotation clusters from DAVID (D and F) used a background generated from all measured genes with at least one treatment having an average count greater than 15 (0.5 counts/ million). Genes without an ensemble ID were excluded from STRING analysis, while genes which were not recognized by DAVID were also excluded.

In U937 cells, both the genes upregulated and the downregulated by AT111 only seemed to form distinct groups (Figure 43 B). The top functional annotation cluster from DAVID group genes belonging to GPCRs together (enrichment score: 6.46; Figure 43 D) while the second functional annotation cluster included genes which had immunoglobulin-like folds (enrichment score: 6.31; not shown). The genes related to GPCRs did not group together and were spread throughout the STRING cluster map (Figure 43 C; purple). Genes belonging to immune-related enriched terms (“immune response” [GO:0006955], “defense response to

virus" [GO:0051607], "response to bacterium" [GO:0009617], "innate immune response" [GO:0045087], "positive regulation of tumor necrosis factor production" [GO:0032760], "inflammatory response" [GO:0006954]) were grouped together near the center of the web (Figure 43 C; green). Only 17 genes from these groups overlapped (red ring), the majority of which grouped in the center of the web indicating that these genes, including CCLs, CCRs, and others, are more associated with each other. Genes belonging to the STRING clusters relating to functions of the immune system including chemokine signaling, adaptive immunity, TLR signaling, and TNF receptors (CL15535, CL15536, CL15538, CL16582, CL16584) associated with many of the overlapping nodes at the center of the web as well as indicating a few other proteins not included in either group (Figure 43 C; blue ring). *CCR1*, *CCR3*, *CCR5*, *CCL2*, *CCL7*, *XCR1* belonged to all three groups. Other prominent STRING clusters indicated were related to IFNα/β signaling (CL16994, CL16999, CL17001, CL17003, CL17006, CL17009) and consisted of 26 genes including 19 genes contained in the previously mentioned immune-related functional enrichment terms from DAVID (Figure 43 C; yellow ring). 15 of those genes had murine orthologs of which 12 were downregulated in AT111-treated RAW 264.7 cells. Though the collection of these IFNα/β signaling related genes were not enriched using DAVID in U937 or RAW 264.7 cells their down-regulation may implicate interference of IFN signaling/production as a possible anti-inflammatory mechanism modulated by AT111.

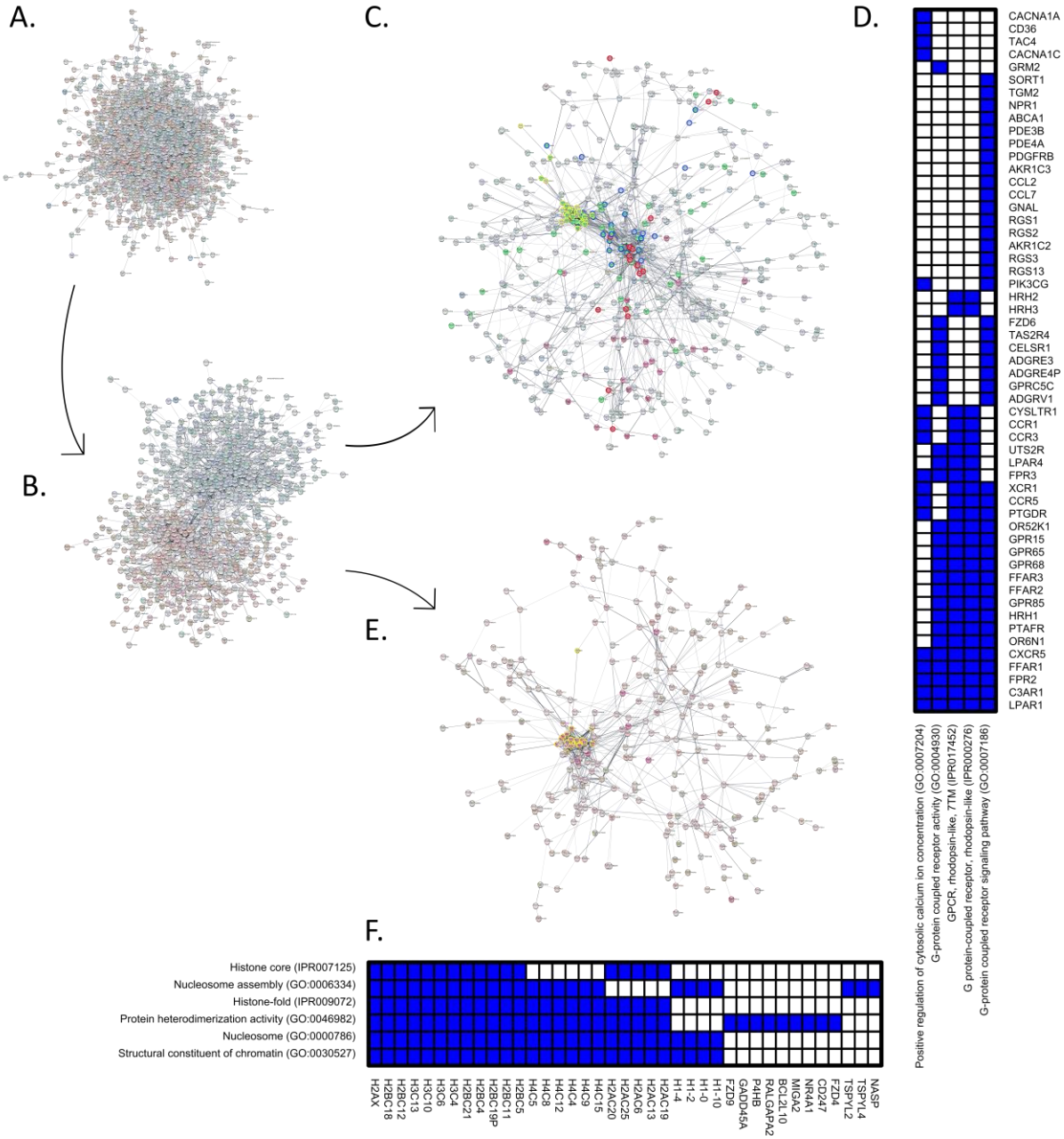
A.
B.
C.
D.
E.
F.
CACNA1A
CD36
TAC4
CACNA1C
GRM2
SORT1
TGM2
NPR1
ABCA1
PDE3B
PDE4A
PDGFRB
AKR1C3
CCL2
CCL7
GNAL
RGS1
RGS2
AKR1C2
RGS3
RGS13
PIK3CG
HRH2
HRH3
FZD6
TAS2R4
CELSR1
ADGRE3
ADGRE4P
GPRC5C
ADGRV1
CYSLTR1
CCR1
CCR3
UTS2R
LPAR4
FPR3
XCR1
CCR5
PTGDR
OR52K1
GPR15
GPR65
GPR68
FFAR3
FFAR2
GPR85
HRH1
PTAFR
OR6N1
CXCR5
FFAR1
FPR2
C3AR1
LPAR1
Positive regulation of cytosolic calcium ion concentration (GO:0007204)
G-protein coupled receptor activity (GO:0004930)
GPCR, rhodopsin-like, 7TM (IPR017452)
G protein-coupled receptor, rhodopsin-like (IPR000276)
G-protein coupled receptor signaling pathway (GO:0007186)
Histone core (IPR007125)
Nucleosome assembly (GO:0006334)
Histone-fold (IPR009072)
Protein heterodimerization activity (GO:0046982)
Nucleosome (GO:0000786)
Structural constituent of chromatin (GO:0030527)
H2AX
H2BC18
H2BC12
H3C13
H3C10
H3C6
H3C4
H2BC21
H2BC4
H2BC19P
H2BC11
H2BC5
H4C5
H4C8
H4C12
H4C4
H4C9
H4C15
H2AC20
H2AC25
H2AC8
H2AC13
H2AC19
H1-4
H1-2
H1-0
H1-10
FZD9
GADD45A
P4HB
RALGAPA2
BCL2L10
MIGA2
NR4A1
CD247
FZD4
TSPYL2
TSPYL4
NASP

Figure 43. Grouping an annotation of enriched GO/InterPro terms for AT111 DEGs in U937 cells. A. STRING cluster map of representative AT111 DEGs compared to the vehicle control in LPS-stimulated PMA-differentiated U937 cells . B. STRING cluster map of AT111 genes not included in the list of LPS DEGs from Figure 40 B. C. Downregulated DEGs from B. Terms associated with functional annotation cluster 1 – G protein-coupled receptors and positive reg. of calcium ion concentration (D) are shown in purple. Genes from immune-related enriched terms (GO:0006955, GO:0051607, GO:0009617, GO:0045087, GO:0032760, and GO:0006954) that were not part of D. are displayed in green. Red ring: overlapping genes related to the immune system and cluster 1. Yellow ring: local STRING clusters for IFNα/β signaling determined through STRING functional enrichment using the whole genome as background (CL16994, CL16999, CL17001, CL17003, C;17006, and CL17009). Blue ring: STRING clusters relating to functions of the immune system including chemokine signaling, adaptive immunity, TLR signaling, and TNF receptors (CL15535, CL15536, CL15538, CL16582, CL16584) not included in other categories. E. Upregulated DEGs from B. Terms associated with functional annotation cluster 1 – nucleosome/histone/chromatin related genes (F) are shown in purple. Yellow ring: local STRING clusters relating to the nucleosome/chromatin (CL4760, CL4763, CL4766, CL4767, and CL4768) using the whole genome as a background. Functional annotation clusters from DAVID (D and F) used a background generated from all measured genes with at least one treatment having an average count greater than 15 (0.5 counts/ million). Genes without an ensemble ID were excluded from STRING analysis, while genes which were not recognized by DAVID were also excluded.

Enrichment for nucleosome/histone related genes was unaffected by the removal of LVC genes. In both cell lines the terms for “histone core” (IPR007125)” “nucleosome assembly" (GO:0006334), “histone-fold” (IPR009072), “nucleosome” (GO:0000786), and “protein heterodimerization activity” (GO:0046982) were included in the functional annotation clusters with the highest enrichment score (Figures 42 F and 43 F). Though not included in the top enriched annotation cluster of both cell lines, the GO terms “CENP-A containing nucleosome” (GO:0043505) and “structural constituent of chromatin” (GO:0030527) were still enriched. STRING annotation clusters relating to chromatin/ the nucleosome overlapped almost completely with the annotations from DAVID (Figures 42 E and 43 E; yellow ring).

In RAW 264.7 cells, only histone deacetylase 6 (*Hdac6*) was missing from the DAVID enrichment. Though STRING annotations describe the role of HDAC6 in the deacetylation of lysine residues on core histones leading to transcriptional repression, it largely remains in the cytoplasm where it functions as a mediator for many functions such as cell motility and inflammation[413]**.** In U937 cells, DNA (cytosine -5-)-methyltransferase (*DNMT3B*) and Msh homeobox 1-like protein (*MSX1*) were not found in DAVID enrichment. DNMT3B and MSX1 both function as transcriptional regulators during development[414,415].

The involvement of histones and the immune system has been heavily studied (reviewed by Li *et al*. in 2022)[416]. The majority of the studies involving histones refer to their extracellular roles, either as damage-associated molecular patterns (DAMPs), anti-microbials, or as a part of the neutrophil extracellular trap (NET) and by extension the macrophage extracellular trap (MET)[416,417]. As DAMPs, extracellular histones can lead to inflammation and

immune cell maturation/recruitment by binding to TLRs, including TLR4, where these factors trigger the production of inflammatory cytokines and chemokines through NF-κB activation[416]. Histones, along with DNA, are a key component of extracellular traps (ETs), which lose their ability to eradicate bacteria without them[418]. Different stimuli trigger ET formation and release for different cells. For example, PMA has been shown to cause NET formation (neutrophils), LPS has been shown to lead to eosinophil ET (EET) formation, and TNF-α has been shown to trigger MET formation in RAW 264.7 macrophages[418-420].

KEGG enrichment analysis of the genes upregulated by AT111 showed enrichment for genes associated with NET formation (hsa04613/mmu04613). Despite this enrichment, MET formation is unlikely to occur in AT111-treated cells. ET formation has been shown to occur in as little as one second depending on the stimulus but has been detected at 30 min and 2 h in response to various stimuli[418-420]. Therefore, METs would have been most likely visible in the brightfield images of the fluorescent imaging experiments (Figure 32) . One study found that the percentage of dead RAW 264.7 cells corresponded to the same percentage of cells which produced METs[421]. The loss in cell viability in RAW 264.7 cells was minimal in AT111-treated cells (Figure 23 B). Additionally, treatment with AT111 reduced the inflammatory response to LPS whereas the histones found in ETs are pro-inflammatory[416].

The enzyme peptidyl arginine deiminase 4 (PAD4/PADI4) coded for by the gene *PADI4* in humans and *Padi4* in mice is responsible for the hyper citrullination of histone H3 leading to the rapid decondensation of chromatin needed for ET formation[422]. The gene for PAD4 was not present among the background data set in either cell line as it did not meet the minimum count threshold. One study by Silva *et al.* described a PAD4-independent mechanism of NET

release in response to *Aspergillus fumigatus* through Src kinase, serine-tyrosine kinase, and Phosphoinositide 3-kinases (PI3K)[423]. In AT111-treated RAW 264.7 cells the gene for PI3K regulatory subunit 1 (PIK3R1) is upregulated ($log_2FC = 1.31$, adj. p-value = $4.23E^{-18}$), but it is still unlikely that AT111 is triggering MET release for the reasons previously described.

Intracellular histones have also been linked to contributing to the innate immune response as well. For example, one study found that human papillomavirus Type 11 and 16 infections were reduced by H2B[424]. However, the focus of studies involving intracellular histones and the immune system involves epigenetic modifications[416,425]. Typically, histone methylation is associated with decreased transcription. As such, demethylation through the function of histone demethylases is thought to increase transcription of various genes. However, opposing roles of histone methylation have been ascribed to inflammation. For example, the histone demethylase lysine demethylase 6B (KDM6B/JMJD3) has been linked to demethylation of histone 3 at lysine 27 (H3K27me3) and has also been linked to inflammation and M2 polarization, though its demethylation activity may be unrelated[426-428]. In RAW 264.7 cells, *Kdm6b* was downregulated ($log_2FC = -1.33$, adj. p-value = $2.94E^{-24}$) while in U937 cells it was unaffected.

Alternatively, H3K4 methylation has been shown to be associated with enhancer regions across many cell types and was associated with STAT1 binding upon IFN-γ stimulation of HeLa cells[429]. This demonstrates that the site of histone modification is also important in determining its role in transcription.

Another important post-translational modification for histones is acetylation. Histone acetylation has long been associated with increased transcription through decondensation of

chromatin[398,403]. In inflammation, the histone acetyltransferase activity of p300 has been linked to the transcriptional activity of NF-κB upon TNF-α stimulation[430]. Conversely, some histone deacetylases (HDACs) have been linked to the transcriptional upregulation of inflammatory genes upon LPS stimulation[431] while inhibitors of HDACs actually decrease their expression[432]. HDACs are separated into IV classes. Class I HDACs include HDAC1, 2, 3, and 8 while class IV is made up of only HDAC11[433]. Class II is subdivided into two subclasses; class IIa which includes HDAC4, 5, 7, 9 and class IIb which includes HDAC6 and 10[433]. Class III HDACs consist of the sirtuin family (SIRT), which may have alternative roles besides deacetylation[433,434]. One study showed that HDAC7 was upregulated in thioglycolate-elicited peritoneal macrophages (inflammatory) as opposed to RAW 264.7 cells and bone marrow-derived macrophages (BMDM/BMM)[435]. As RAW 264.7 cells express low levels of HDAC7 especially following LPS stimulation, they were transfected with plasmids to express an active form of HDAC7 lacking the N-terminal 22 amino acids (HDAC7-u)[435]. They found that expression of this version of HDAC7 increased LPS-stimulated gene expression including transcription of endothelin 1 (*Edn1*), a gene regulated by a hypoxia-inducible factor 1 cis-regulatory site, which was lowered upon treatment with broad spectrum and specific HDAC inhibitors[435]. These effects were lost in RAW 264.7 cells transfected with a plasmid encoding the full-length version of HDAC7[435]. The authors hypothesized that this was due to interactions with C-terminal binding protein 1 a transcriptional repressor, something that could not be done without the 22 amino acids at the N-terminus[435].

In both RAW 264.7 cells and U937 cells, *Edn1*/EDN1 was downregulated (log_2FC= -5.70, adj. p-value = $3.23E^{-77}$- RAW 264.7; log_2FC = -4.0–, adj. p-value = $1.33E^{-192}$ - U937). In

relation to the aforementioned study[435], *Hdac7* transcripts failed to pass the low count cut-off in RAW 264.7 cells. However, expression did occur, and was downregulated, in U937 cells (log_2FC = -1.25, adj. P-value = $1.15E^{-32}$). Other HDACs were up regulated in both cell lines, but not the same HDACs. For example, in RAW 264.7 cells, both *Hdac6* and *Hdac9* were upregulated (log_2FC = 1.73, adj. p-value = $7.86E^{-20}$ and log_2FC = 1.03, adj p-value = $2.13E^{-12}$, respectively), but in U937 cells *HDAC6* was barely changed (log_2FC = 0.34, adj. p-value = 0.047) and *HDAC9* failed to pass the low count cutoff. In U937 cells, *HDAC11* was upregulated (log_2FC = 1.11, adj. p-value = $1.69E^{-5}$) but failed to pass the low count cutoff in RAW 264.7 cells. In U937s, *SIRT2* and *4* were both upregulated (log_2FC = 1.00, adj. p-value = $4.90E^{-23}$ and log_2FC = 1.31, adj. p-value = 0.01) while neither were differently expressed in RAW 264.7 cells. *HDAC5* was not differently expressed in either cell line based on the set cut-offs, however, in RAW 264.7 cells, it led to a log_2FC = 0.896 with an adj. p-value = $9.94E^{-12}$ and a log_2FC = 0.575 with an adj. p-value = $3.05E^{-6}$ in U937 cells.

HDAC6 is linked to tubulin deacetylation and cell migration, as well as the inflammatory response to LPS[436-439]. Inhibition of HDAC6 in various cell types leads to the reduction of some inflammatory response genes, while possibly leading to the increase in others[439,440]. There are also conflicting reports of its role in IL-10 production where some studies say that HDAC inhibition increases IL-10, while others show it is diminished[438,440-442]. Though *Hdac6* is upregulated in RAW 264.7 cells, IL-10 is diminished (Figure 30 C). One study showed that inhibition of HDAC6 in microglial cells stimulated with LPS reduced cytokines IFN-γ, IL-1β, IL-2, IL-5, and IL-10 but did not have an effect on TNF-α and IL-6[440]. However, their study seemed flawed as they saw decreased protein levels of IL-6 and increased

levels of IL-1β in overall protein levels compared to the LPS treatment control but the inverse when cytokine levels were standardized to the LPS control[440]. It is possible the methods were just unclear[440].

Contrary to other studies, Into *et al*. (2010) showed that siRNA knock down of HDAC6 in RAW 264.7 cells led to an increase in *Il6* and *Nos2* and a decrease in *Nfkbiz* and *Tnf* without interfering with downstream IκBα degradation, though other TLR4 signaling pathways were interrupted[443]. Another study by Cheng *et al.* (2014) implicates an association between HDAC6 and HDAC11 in the early regulation of IL-10 transcription[442] thus linking their roles. HDAC11 has also been implicated in having a regulatory role of IL-13 production in $CD4^+$ T cells through interactions with its transcription factor[444]. HDAC11 was also shown to have a role in IFN-α signaling[445]. HDAC11 was shown to mitigate expression the IFNα-induced expression of *Isg15* and *Eif2ak2* (PKR) through diacylation interactions with serine hydroxy methyltransferase 2α[445]. As stated previously, *HDAC11* was up regulated in U937 cells treated with AT111 but was not differentially expressed in RAW 264.7 cells. However, both *Isg15* and *Eif2ak2* were downregulated in RAW 264.7 cells and only *EIF2AK2* was significantly downregulated in U937 cells. In U937 cells, *ISG15* did not meet the criteria as a biologically relevant DEG, but it did have a $\log_2FC = -0.65$ and an adj. p-value = $2.38E^{-6}$.

HDAC9 is also shown to have a role in inflammation through deacetylation of IKKα and β, leading to their activation[446]. As stated earlier, *Hdac9* was up regulated in RAW 264.7 cells, but could not be detected in U937 cells. The up regulation of *Hdac9* in RAW 264.7 cells treated with AT111 is surprising given the observed reduction in pro-inflammatory cytokines and other inflammatory response genes. The SIRT family of deacetylases (Class III HDACs)

have also been linked to inflammation, however this time with a suppressive effect[447]. Inhibition of both SIRT2 and SIRT4 have been shown to increase p65 translocation to the nucleus, while over-expression of SIRT4 inhibited it[448,449]. Both *SIRT2* and *SIRT4* are upregulated in U937 cells but not in RAW 264.7 cells. Given the roles of HDACs in inflammation, it is surprising that their upregulation is associated with AT111. Broad spectrum inhibition of HDACs using trichostatin A (TSA) and suberoylanilide hydroxamic acid (SAHA) has also been shown to have anti-inflammatory activity[432,450,451].

Treatment with both compounds led to reduction in mRNA levels of both *Tnf*, *IKKε*, and *Nos2*, while only SAHA decreased levels of *Il1b* and *Il10*[450]. Both TSA at higher concentrations and SAHA lead to the increase of *Ptgs2* (COX-2) mRNA which was only slightly apparent in protein levels[450]. Conversely, the authors also demonstrated that treatment with both TSA and SAHA increased both levels of p65 and activity of p65 without interfering with IκBα levels nor LPS-induced p65 nuclear translocation[450]. However, upon performing knock outs for the various HDACs, contradictory results were reported indicating that there may be other contributing factors[450]. Another report by Chong *et al.* (2012) found that SAHA does indeed inhibit nuclear p65 localization in LPS stimulated RAW 264.7 cells, however this report demonstrated that localization after 6 h post-treatment[451]. Halili *et al.* (2010) found that treatment with TSA and SAHA led to suppression of LPS-induced *Edn1*, *Ccl7*, and *Il12b* (*Il-12p40*) but amplified others such as *Ptgs2* (COX-2) and *Serpine1*[452]. The HDAC6 specific inhibitor compound 17a at a concentration of 100 μM led to the same anti-inflammatory activity, but did not affect levels of *Ptgs2*[452].

AT111 had a similar effect in both U937 cells and in RAW 264.7 cells which demonstrated inhibition of *Edn1* and *Ccl7* but not *Il12b*. In U937 cells AT111 did not cause the differential expression of either *PTGS2* or *SERPINE1* whereas in RAW 264.7 cells AT111 led to a decrease of *Ptgs2*. Though *Ptgs2* was downregulated on a transcriptional level at 4 h in RAW 264.7 cells (log_2FC = -1.01 adj. p-value = $8.38E^{-14}$), COX-2 protein levels were not affected at 24 h post-LPS (Figure 29). This is similar to what was observed with TNF-α, where *Tnf* mRNA was downregulated at 4 h (log_2FC = -1.03 adj. p-value = $4.02E^{-14}$; $2^{-\Delta\Delta ct}$ = 0.398 ± 0.055 A.U. [Figure 31]) while protein levels of TNF-α were only affected by higher concentrations of AT111 (Figure 30 D).

Williams *et al.* (2013) found that the knockout of HDAC6 increased phosphorylation of both ERK1/2 compared to the wild-type mouse embryonic fibroblasts[436]. They also showed that HDAC6 phosphorylation could occur in an epidermal growth factor receptor-Ras-Raf-MEK-ERK dependent manner, linking HDAC6 activity to ERK1/2, but attributed control of HDAC6 to phosphorylation by ERK1 only[436]. Wu *et al.* (2018) reported that an ERK1/2 was a direct substrate of HDAC6 and that an acetylation mutant of ERK1 impacted its phosphorylation and activity[453]. These together imply dual controlling roles for both HDAC6 and ERK1, and possibly ERK2, though further research is required.

These findings suggest that AT111 may possibly be functioning as an HDAC inhibitor, similarly to an HDAC6 inhibitor. Indeed, cells treated with TSA had similar changes in gene expression as AT111-treated cells. When compared to a list of genes inhibited by TSA in BMDMs it was found that AT111 reduced expression of 68 genes out of the 206 genes detected

using a microarray[432]. This list encompassed both LPS and Pam3CysSerLys4 (Pam_3CSK_4) stimulated genes without discriminating between the two[432].

Pam_3CSK_4 is a synthetic lipopeptide TLR1/2-heterodimer ligand capable of triggering a similar pathway as TLR4, without the secondary MyD88-independent TRIF pathway. Of the genes listed, AT111 DEGs seemed to overlap with specific categories of genes. AT111 downregulated 13 out of 28 listed innate immune receptors, 21 out of 37 cytokines, chemokines, and growth factors, and 9 out 18 genes not categorized. However, AT111 had little effect on genes associated with signal transduction (7 out of 22 genes), transcriptional regulators (3 out of 30 genes), and ubiquitination (2 out of 18 genes).

When compared to a list of genes highly upregulated and highly downregulated by SAHA in unstimulated MC3T3-E1 Subclone 4 murine pre-osteoblasts, there was very little overlap where AT111 led to the upregulation of 17 similar genes out of 127, including *Pkp2*, *Mknk2,* and *Slc9a3r1* (*Nherf2*) and down-regulation of only 1 gene, *Ccnb1* out of the 130 listed[454]. Though the DEGs did not over-lap with SAHA[454], that study was performed on unstimulated cells while this dissertation used LPS-stimulated macrophages, therefore these differences are not surprising. The study using TSA and LPS/ Pam_3CSK_4 stimulated RAW 264.7 cells[432] may be a better comparison.

Based on the similarities of AT111 treatment with the broad-spectrum HDAC inhibitor TSA and similarities to the HDAC6 inhibitor, compound 17a[452], as well as the modulation of ERK2 phosphorylation (Thr202/Tyr204; Figure 33), it is possible that AT111 may be functioning as an HDAC inhibitor, leading to the dysregulation of the immune response, without affecting the signal transduction pathways. However, AT111 may also be influencing

the PTMs required for activation of HDACs[455]. Alternatively, the increase in various histone subunits observed in both AT111 treated RAW 264.7 cells and in U937 cells may be causing the observed dysregulation, as histones compete with RNA polymerases for DNA binding, thus limiting transcription[456]. AT111 may be acting as an HDAC inhibitor, or through increasing transcription of various histones, or both, resulting in the variation observed in both RAW 264.7 cells and U937 cells. However, except for the conserved increase of histone proteins, this is purely speculative based on the literature. In order to make a definitive statement, more research is required.

Examination of the top 30 most significant DEGs (by adj. p-value) in both AT111-treated RAW 264.7 cells and U937 cells compared to the LVC cells, revealed little similarity, but did highlight some key genes which may provide some insight into the potential mechanism for the anti-inflammatory activity of AT111 (Figure 44). In RAW 264.7 cells, AT111 reduced both *Il1a* and *Il1b* as the top and third-most genes by a $\log_2$FC of -6.74 (adj. p-value = 0) and -3.75 (adj. p-value = $7.61E^{-165}$), respectively (Figure 44 B). In U937 cells, of these genes, only *IL1A* is statistically reduced with a $\log_2$FC of -3.44 (adj. p-value = $2.53E^{-40}$). *IL1B* was not changed (adj. p-value = 0.132).

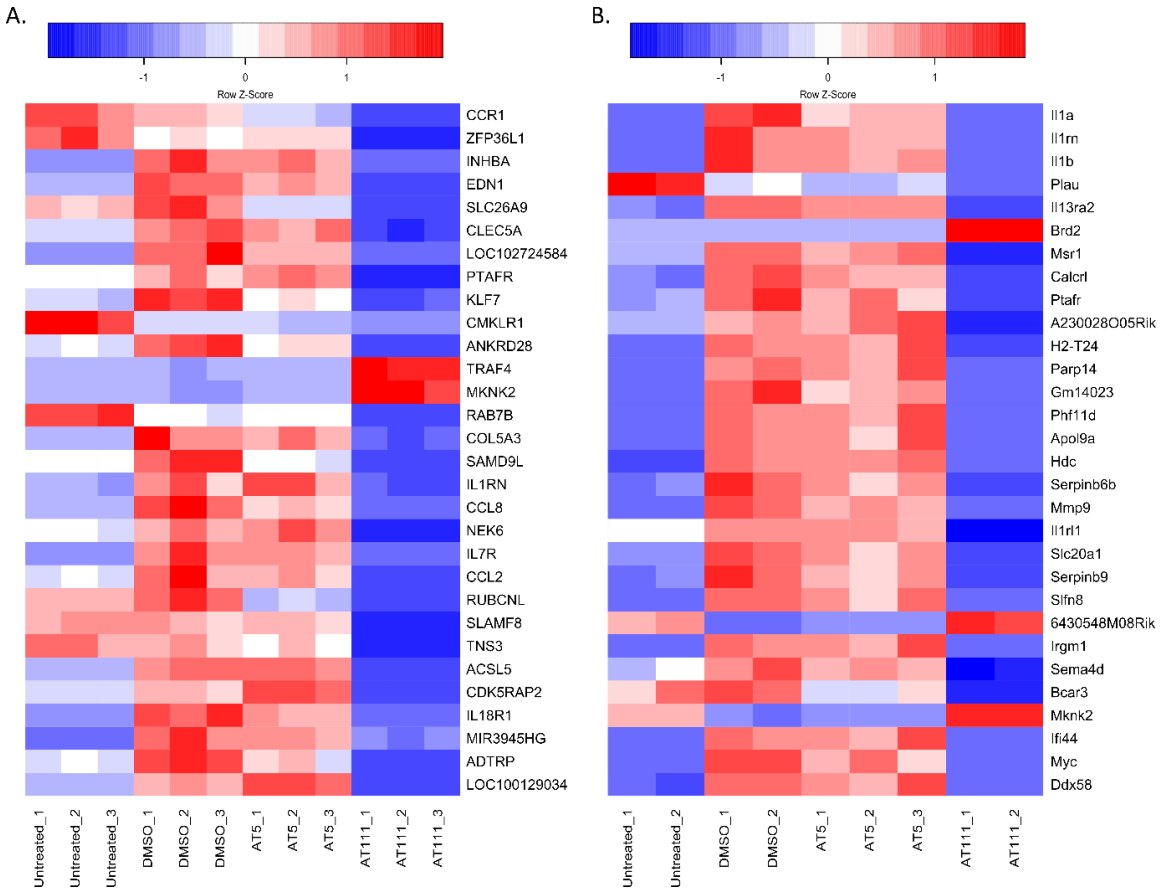

Figure 44. Top 30 DEGs in U937 cells and RAW 264.7 cells. Heatmaps displaying the relative expression levels of the top 30 most significant AT111 DEGs compared to the vehicle control ranked by adj. p-value for both A. U937 cells and B. RAW 264.7 cells. The relative z-score was determined by subtracting the mean standardized count from the individual standardized count for each gene then divided by the standard deviation. Samples with positive z-scores, indicating counts above the average, are in red, while genes with negative z-scores are in blue. Heatmaps were made using the standardized count output file from DESeq2 and created using heatmap2 from the Gplots library in RStudio.

Contrary to the anti-inflammatory properties reported earlier, AT111 downregulates transcripts associated with interleukin-1 receptor antagonist (*IL1RN*/*Il1rn*; IL-1RA), an immunoglobulin protein and known inhibitor of IL-1β (secreted IL-1RA) and IL-1α (intra-cellular IL-1RA) signaling, which is upregulated in the later stages of LPS signaling[457-459] and is a hallmark of M2 polarization. As such, it is not surprising that this cytokine is reduced if AT111 is reducing LPS induced signaling. This, together with the reduction in IL-10, implies that although AT111 interferes with inflammation caused by LPS, it does not do so by influencing the macrophage to polarize from M1 to M2.

In U937 cells, the genes *CCR1*, *ZFP36L1*, *SLC26A9*, *TRAF4*, *MKNK2*, and *RUBCNL* seem to have different expression profiles than the untreated or LPS controls, while in RAW 264.7 cells *Brd2*, *Il1rl1*, *Bcar3*, *Mknk2*, and *Sema4d* are also noteworthy (Figure 44).

CCR1 is a transmembrane G protein-coupled receptor associated with the innate immune response[460]. In mice lacking CCR1, the bacterial clearance following cecal ligation and puncture was diminished as was levels of pro-inflammatory cytokines and chemokines[460]. However, mice lacking CCR1 showed increased levels of nitrite in response to *E. coli*. Additionally, CCR1 null murine macrophages treated with 1 μg/mL LPS had increased levels of chemokines CXCL1, CCL2, CCL3, CCL5, CCL6, CCL22, and CXCL10[460]. In RAW 264.7 cells treated with AT111 compared to the vehicle control, none of these genes were differentially expressed while only *CCL3* was upregulated in U937 cells. Zinc finger protein 36, C3H type-like 1 (Zpf36l1) is a destabilizing mRNA-binding protein that has been shown to have an essential role in osteoarthritis[461] and is downregulated in both cell lines. Knock out of this protein has been linked to increased heat-shock protein 70 (HSP) A1A and HSPA1B[461].

HSPA1A and *HSPA1B* expression levels are both upregulated in AT111-treated LPS-stimulated U937 cells compared to the vehicle control but are not modulated in RAW 264.7 cells. Solute carrier family 26 member 9 (Slc26a9) is a calcium transporter which has been hypothesized as an alternative therapeutic target to treating cystic fibrosis[462-464]. Activation of this protein have been linked to airway inflammation through IL-13, and mutations of this gene have been implicated in asthma[465].

The gene *Slc26a9* is downregulated in both cell lines, while ORAI calcium release-activated calcium modulator 1 (*ORAI1*) is upregulated in both, potentially implicating a role for AT111 in calcium signaling modulation, but there is little study of Slc26a9 in macrophages and the role of ORAI1 in macrophages is not well understood[466]. Bromodomain containing 2 (BRD2) is a member of the bromodomains and extra terminal domain family involved in interpreting acetylation PTMs of histone 4 and has been primarily described for its role in chromatin remodeling and the cell cycle[467,468]. Although BRD2 has also been linked to inflammation, potentially through transcriptional regulation of the p50 (*Nfkb1*) subunit[469,470], gene expression is highly upregulated in RAW 264.7 cells and unchanged in U937s. It would follow that since there is an upregulation of *Brd2* in RAW 264.7 cells, there would be increased inflammation, which is not apparent.

TRAF4 is a unique member of the TRAF family in that it cannot bind to most TNFRs nor activate NF-κB in OX40 (another TNFR) signaling[471,472]. TRAF4 has also been shown to have a regulatory role in the TLR4-LPS signal transduction pathway through interactions with TRAF6 and TRIF/TICAM1[473]. However, this role of TRAF4 remains controversial and poorly understood. A 2022 study by Chen *et al.* into the role of TRAF4 in teleosts showed that TRAF4

enhances, not represses, TRIF and TRAF6 signaling[474]. Das *et al.* found that TRAF4 worked together with Atox1 as a part of an inflammatory response to TNF-α[475]. In 2012, Marinis *et al.* demonstrated that TRAF is phosphorylated S426 by IKKα through association of nucleotide binding oligomerization domain containing 2 (NOD2) leading to the down-regulation of NOD2-induced TNF-α and CXCL2 (MIP2A)[476]. Two studies using the same miRNA (miR-4443) to inhibit TRAF4 revealed contradictory roles for TRAF4 in different types of inflammatory systems[477,478]. These alternative functions for TRAF4-related immune responses may be due to the intricate nature of cell signaling pathways, where even cell-type and model system may influence the observed outcomes.

AT111 downregulated *Irf7* and *Ifnb1* in RAW 264.7 cells, though it did not in U937. IFN-α gene expression was not detected in either cell line. Typically, type 1 IFNs are associated with viral infections, but IFN-β has been shown to be produced after LPS stimulation in RAW 264.7 cells while IFN-α has not[479,480]. Additionally IFN-β signaling has been shown to have a role in LPS-induced iNOS production[480] This suggests that in RAW264.7 cells, AT111 may be inhibiting TRIF signaling, while it is not in U937 cells.

It is possible that AT111 is interrupting AP-1 signaling as opposed to other mechanisms. Shi *et al.* (2017) postulated that the protein malignant fibrous histiocytoma amplified sequence 1 (MFHAS1) may inhibit AP-1 mediated inflammation through stimulation of the Ras-Raf-ERK signaling pathway leading to cytoplasmic translocation of the of C subunit of protein phosphatase 2 and subsequently decreasing c-Jun dephosphorylation[481]. The authors report that over expression of MFHAS1 led to decreased expression of both Il-6 and Il-8 in an NF-κB independent manner[481]. *Mfhas1* is upregulated in RAW 264.7 cells (log_2FC = 1.077001575,

adj. p-value = $2.11E^{-09}$) but is unchanged in U937s. This gene is not upregulated in LVC cells, however, the authors show that though LPS does induce MFHAS1, it happens 12 h post-LPS treatment[481]. Though this may not be the direct mechanism of the anti-inflammatory activity of AT111, it does demonstrate that AT111 may potentially be acting on the activity of AP-1.

The Ras-Raf-ERK signaling pathway tends to be initiated through receptor tyrosine kinase and GPCRs. However, the activation pathway taken can lead to the cytoplasmic or nuclear localization of ERK1/2[482,483]. This signaling occurs usually through a Ras-Raf-MEK signaling cascade, which has been heavily reviewed[482,484-486]. GPCR and GPCR signaling related terms are enriched in the downregulated genes of both U937 cells and RAW 264.7 cells (Figure 41). Ras proteins are also regulated by guanine nucleotide exchange-factors (GEFs)[486]. Ras proteins are also inhibited by GTPase-activating proteins (GAPs) which work alongside GEFs to regulate Ras signaling[486]. Gene expression for GAPs disabled adapter protein 2 interacting protein (*DAB2IP*) and sprouty protein with EVH-1 domain (*SPRED*) 1 are downregulated in U937 cells while *Spred3* is downregulated in RAW 264.7 cells. Genes encoding various other proteins involved in the Ras-Raf-ERK signaling pathway, including receptor tyrosine kinases, are dysregulated in both cell lines. For example the genes for MAPK phosphatases Dual specificity phosphatase (DUSP) 6 and 16, which dephosphorylate ERK1/2, are downregulated in the AT111-treated U937 cells compared to the vehicle control, while *DUSP2* is upregulated. *DUSP16* and *DUSP5* levels are downregulated in the AT111-treated RAW 264.7 cells[487]. DUSP5 and 6 only regulate ERK1/2, DUSP2 regulates ERK1/2, JNK1/2, and p38, and DUSP16 regulates JNK1/2 and possibly p38[487]. DUSPs function through their phosphatase activity but can also bind to their respective proteins and keep them in the

cytoplasm or nucleus, thus regulating their activity[487]. This dysregulation, coupled with the downregulation of DUSP5 and 6, may be linked to the increased levels of ERK2 phosphorylation (Thr202/Tyr204; Figure 44).

ERK2 is thought to be functionally similar to ERK1 and subsequently grouped together in most research. A study by Frémin *et al.* (2015) discussing the redundancy of ERK1/2, found that ERK2 knock down mice possessed developmental issues and even embryonic mortality whereas ERK1 knock out mice did not[488]. The defects observed in ERK2 knock out mice were rescued by transgenic ERK1 expression leading the authors to describe a redundant role for the ERK proteins[488]. It is widely accepted that ERK1/2 have redundant functions and that the apparent changes in effect, or lack thereof, is due to a reduction in total ERK1/2, or p-ERK1/2, not unique function[288]. The Bernstein group showed that ERK2, but not ERK1, forms complexes to c-Jun[489,490], a subunit of AP-1, which has been corroborated by Guedea *et al.* examining the role of ERK signaling in the hippocampus during fear extinction[491]. Both groups postulated that ERK2 binding to c-Jun could limit its association with AP-1, however no research has been able to support that claim[489,491]. Another group explored ERK2-DNA binding activity and proposed that ERK2 may have alternative phosphorylation events which lead to differential activity[492]. However, most studies on ERK signaling in inflammation report on the influence of ERK1/2 as a whole[273]. Though ERK2 has been postulated to bind to AP-1, it has been shown to be indispensable to TNF-α-induced NF-κB activity through phosphorylation of poly(ADP-ribose) polymerase-1[493]. Another group linked *H. influenzae* CXCL2 production in ear fibrocytes to the ERK2 c-Jun/AP-1 pathway where CXCL2 expression was not dependent

of NF-κB, but AP-1[494]. Another study reported that ERK2, but not ERK1, aided in LPS-induced expression CSF3, potentially through chromatin remodeling[495].

As stated previously, ERK1/2 interacts with many different proteins including MAPKAPKs, RSKs/MSKs (including *Rps6ka5* [*MSK1*] which is upregulated in both cell lines) and MNKs (*MKNK1*/2) modulating different cellular functions based on spatial/temporal restraints and presence of appropriate scaffolds[274,482]. In both cell lines only *MKNK2*/*Mknk2* was found in the top 30 lists (Figure 44). Though phosphorylation of many of these proteins is linked to both p38 and ERK1/2, MNK2 has been linked to ERK1/2 directly, not p38[274,289]. MNK2 activation leads to the phosphorylation of eukaryotic translation initiation factor 4E (eIF4E), an initiator of 5'-cap dependent translation[290]. MNK2 modulation of eIF4E has been implicated to promote the anti-inflammatory phenotype in tumor-associated macrophages[291]. Suppression of MNK2 led to a pro-inflammatory polarized state[291]. Increases in MNK2 activity is linked to cancer tumorigenesis and poor prognosis[496,497]. Increased levels of TRAF4 have also been associated with cancer[471]. Additionally, expression of replication dependent histones is upregulated during the G1 and S-phases of the cell cycle[498]. It is possible that AT111 is promoting an oncogenic phenotype in these LPS-induced macrophages triggering the rapid cycling of the cell cycle and thus an apparent increase in histone mRNA. However, mRNA for the proteins responsible for forming the histone locus body (a nuclear body responsible for histones production), nor the proteins activating its formation were differentially expressed in either cell line. Treatment with AT111 did not influence cell viability indicating that either a stall, or a rapid progression of the cell cycle is unlikely.

Upon exposure to pathogens, macrophages may become inflamed leading to the release of multiple pro-inflammatory mediators[46-50,241]. Usually, these inflammatory proteins are necessary to allow for pathogen clearance, however their over-production can lead to detrimental diseases including RA and IBD[52,243,246,248-250]. As such there is a search for small molecules that may inhibit an over-active inflammatory response. Both 1,2,3-triazoles and aurones have been previously shown to have anti-inflammatory properties, therefore it was hypothesized that these novel aurone-derived 1,2,3-triazoles may share those same qualities. Here we show that AT111, and to a much lesser extent, AT5 was able to mitigate the LPS-induced inflammatory response. Both AT5 and AT111 were able to reduce LPS stimulated levels of nitrite and inflammatory-cytokines in a dose-dependent manner, with AT111 doing so on a protein and mRNA level. This observed anti-inflammatory activity of AT111 and AT5 did not seem to be through inhibition of TLR4 signaling, nor did either AT interfere with the initial phosphorylation and nuclear translocation of p65. AT111 did not reduce expression of p65 nor Ikaros, both involved in the positive feedback mechanism of NF-κB and linked to its sustained presence in the nucleus[362]. Neither AT111 or AT5 lowered mCherry production under the control of the *Nos2* promoter containing κB cis-regulatory sites implying that it did not interfere with the transcriptional activity of NF-κB. The increased levels of fluorescence detected in the *Nos2*-reporter cells may be explained by the fluorescent properties of the ATs which both fluoresce when excited by a 555 nm laser. AT111 also appeared to augment ERK2 phosphorylation (Thr202/Tyr204), but not ERK1, though it could be because ERK1 had much less total protein than ERK2, making changes in p-ERK1 more difficult to detect. RNA sequencing and functional enrichment analysis in both RAW 264.7 cells and U937 cells

revealed that indeed AT111 decreased genes associated with various inflammatory responses, GPCRs, and c-type lectins while increasing the levels of histones and histone/nucleosome related proteins, however the specific genes modulated varied greatly. While treatment with AT111 downregulated *Irf7* and *Ifnb1* in RAW 264.7 cells it did not in U937 cells suggesting that in RAW264.7 cells, AT111 may be inhibiting TRIF signaling, while it is not in U937 cells. However, IRF7 signaling through TLR4 tends to not occur unless under specific conditions[499]. MKNK2 is a known substrate of ERK1/2, and which can promote an anti-inflammatory, albeit oncogenic, phenotype and is upregulated in the top 30 DEGs in both cell lines. AT111-treated cells also revealed dysregulation of mRNA for proteins associated with Ras-Raf-ERK signaling indicating a potential role where the increased phosphorylation of ERK2, possibly due to decreased DUSP activity, leads to modulation of AP-1 and subsequent gene activation. However, more research is required before any determination can be made.

Though the exact mechanism of action for AT111 and AT5 remains unclear, it is apparent that AT111 reduces the LPS-induced inflammatory response in macrophages, and that it may be occurring possibly through chromatin remodeling, ERK2 activation of MKNK2, dysregulation of TRIF signaling (RAW 264.7 cells only), or aberrant Ras-Raf-ERK-AP-1 signaling. Results of this study indicate that ATs show promise as a platform for future studies.

Chapter V

Overall Conclusions

This study examined the uses of novel small molecules termed "aurone-derived 1,2,3-triazoles" (ATs) due their creation stemming from the addition of a 1,2,3-triazole moiety onto an existing aurone system leading to a salicyl-substituted 1,2,3-triazole with a variable, usually aromatic, side chain. Since both aurones and 1,2,3-triazole-containing compounds have been shown to have many bioactivities and fluorescent properties, it was thought that these molecules may possess similar attributes. There is always the need for various fluorescent molecules, especially ones which are easily customizable, and have large Stokes shifts. Currently, there is a need for new anti-inflammatory compounds that act in a manner differently than current available NSAIDs or steroids, either as reducers of cytokine production or cytokine signaling.

In this dissertation, it was described that ATs have the potential as a scaffold to be modified into compounds that can be fluorescent or anti-inflammatory. Of the 47 ATs screened, two were eventually selected as a model for each application. AT5 was shown to have fluorescent properties, which were relatively unique as it had increased fluorescence in protic solutions with a large Stokes shift. AT111 was shown to have a dose-dependent effect on the LPS-induced inflammatory response in macrophages. Inversely, AT111 displayed minimal fluorescence with increased emissions in more polar-aprotic solvents. The excitation and emissions spectra of AT111 differed depending on the solvent. This was attributed to excited state intramolecular proton transfer, which may have caused keto-enol tautomerization on the salicylic group of AT111. Though this may have been occurring with AT5, this effect was

overshadowed by the much larger effect of protic solvents. Biologically, AT5 acted in a manner different from AT111. Initially, it was observed that AT5 was able to reduce levels of excreted nitrite and cytokines. This effect was lost with variability in timing, batch, and cells. Though substantially weaker in the lower passage cells, AT5 still had an effect on nitrite secretion into the supernatant. When examined for other anti-inflammatory effects, even using RNA sequencing, AT5 demonstrated minimal activity.

For their ascribed purpose, both AT111 and AT5 seemed to provide evidence that ATs can be modified to act as either fluorescent or anti-inflammatory compounds. AT5 fluoresced when excited by a 405 nm laser. This was shown to occur in a dose-dependent manner, as well. AT5 was also shown to have increased fluorescence in aqueous solutions with neutral pH, such as PBS or cell culture medium. This AT was shown to fluoresce brighter in SDS, an anionic detergent in a salt solution, and in PBS indicating that ionic interactions may contribute to fluorescence in an aqueous solution. Contrary to the observed increased intensity in protic environments, fluorescence of AT5 was quenched at lower pH. Though this was not discussed in the published manuscript contained in chapter II, it may indicate the need for AT5 to act as both a hydrogen bond acceptor and as a hydrogen bond donor. This is supported by the slight increase, and red-shift, of fluorescence in more polar solutions and in the presence of phosphates (PBS) and sulfates (SDS). AT5 also fluoresced in cells, both live and fixed, indicating the potential for ATs as fluorescent probes *in vitro*. Due to all these findings, it is indicated that ATs can be used as fluorophores, providing a novel unique scaffold, having a large Stokes shift, which may be customized to have different fluorescent properties.

AT111, though weakly fluorescent, showed greater anti-inflammatory activity than AT5. Cells treated with AT111 exhibited decreased transcription, expression, and/or secretion of pro-inflammatory mediators, such as cytokines, chemokines, enzymes, and RNS induced by LPS. Typically, when discussing inflammation caused by the addition of LPS, NF-κB and p38 MAPK are the focus of the study. In contrast, AT111 did not seem to interfere with the initial, Myd88-dependent LPS-TLR4 signaling pathway. AT111 did not mitigate phosphorylation of both p65 (Ser536), p38 (Thr180/ Tyr182), nor JNK (Thr183/Tyr185), but did increase phosphorylation of ERK2 (Thr202/ Tyr204). This increase was thought to drive activation of MNK2, a protein whose transcripts were increased upon treatment with AT111. AT111 also did not interfere with the initial nuclear localization of p65 and increased NF-κB-driven mCherry-PEST expression from a *Nos2* promoter. This is contrary to the observation that LPS-induced endogenous *Nos2* transcription was reduced in RAW 264.7 cells treated with AT111. Since the *Nos2*-reporter cell line only contains the core *Nos2* promoter region it may be lacking other cis-regulatory sites that may be necessary to recreate this effect. RNA sequencing data which showed that in both human and murine macrophage-like cells treatment with AT111 increased transcription of genes related to nucleosome assembly, while decreasing levels of *KDM6B*, a histone demethylase. This implies that AT111 may be limiting overall transcription through the competition of histones. However, other studies such as ChIPseq may be useful in corroborating this hypothesis. This is supported by the differential profiles of dysregulated transcripts between RAW 264.7 cells and U937 cells, though there were similar overall changes, the individual transcripts that were differentially expressed were quite different in the two species. However, this could also be attributed to differences in cell types.

Though the idea that AT111 caused the dysregulation of genes relating to histone expression may be a viable explanation, AT111 also caused both up and downregulation of genes related to Ras-Raf signaling, and the altered expression of various cell surface receptors. This implies that though AT111 is not interfering with the initial LPS-TLR4 signaling pathway, it may be limiting autocrine signaling, thus mitigating the overall inflammatory response. Finally, RNA sequencing showed *TRAF4* and *MKNK2* in were upregulated in both LPS-stimulated U937 and RAW 264.7 cells treated with AT111 compared to the vehicle control. As both TRAF4 and MKNK2 have been implicated in lowering the inflammatory response/ phenotype in various cells and conditions, it is possible that these proteins may be the link between the observed phenotypes in RAW 264.7 cells and in U937 cells. Though AT111 was shown to decrease the inflammatory phenotype in LPS-stimulated macrophages, many of the genes with increased transcripts were related to oncogenesis. This is not unexpected as cancer cells often exhibit a more proliferative anti-inflammatory phenotype, thus mitigating inflammation-induced apoptosis. Though the exact mechanism of bioactivity remains elusive, AT111 provides evidence that the core AT scaffold may be modified to have anti-inflammatory activities, laying the groundwork for future synthesis and exploration of more potent compounds.

This dissertation described the potential for the core salicyl-substituted AT scaffold to be used as a backbone to develop both fluorophores and anti-inflammatory drugs. Though each AT required a relatively high dosage to exhibit these properties, these studies provide strong evidence for the potential use of these compounds.

APPENDICES

Appendix I

Supplementary Data for Chapter II

Originally published in RSC advances[1]

Figure S1. NMR spectra for AT2 and AT5

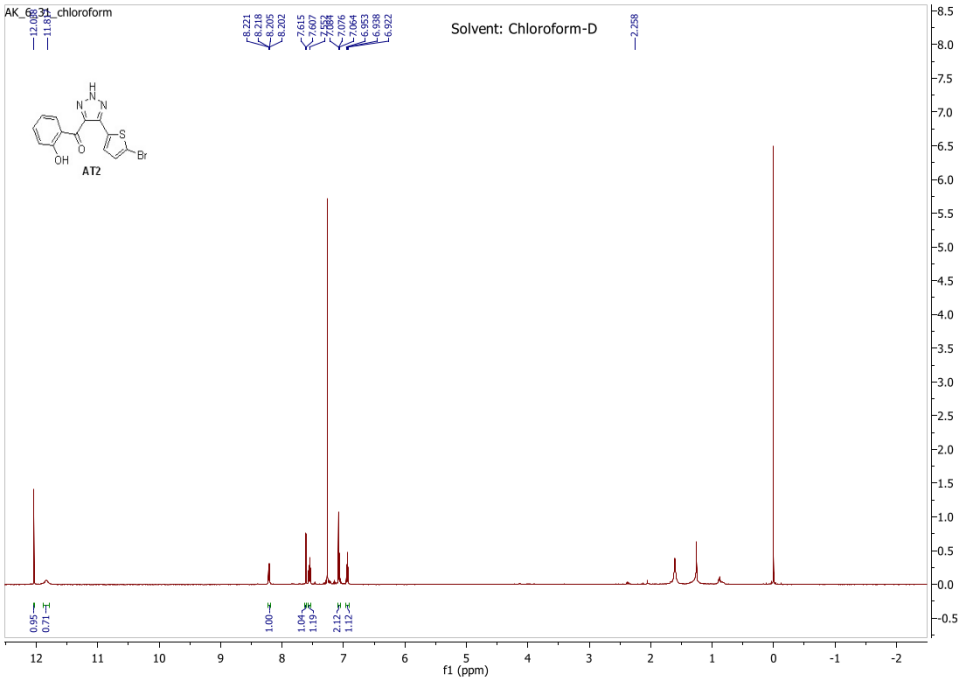

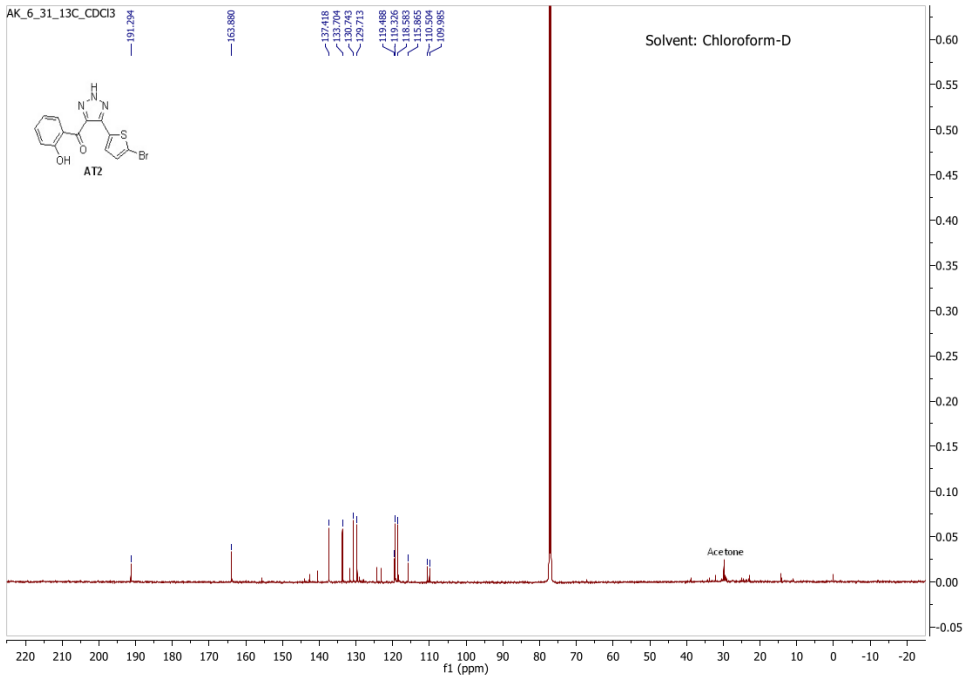

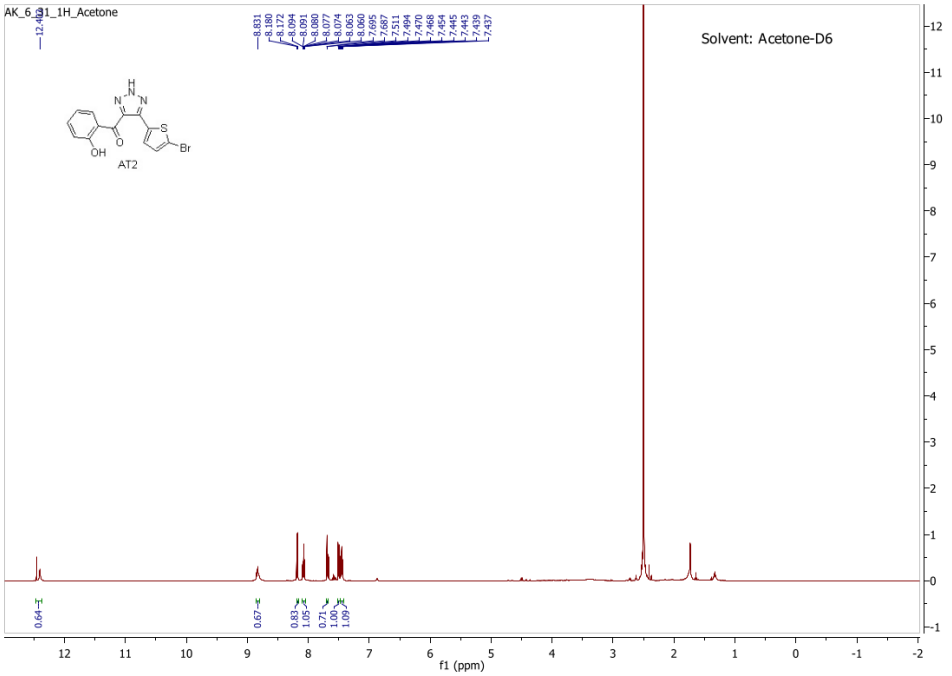
AK_6_31_1H_Acetone
Solvent: Acetone-D6
AT2
f1 (ppm)

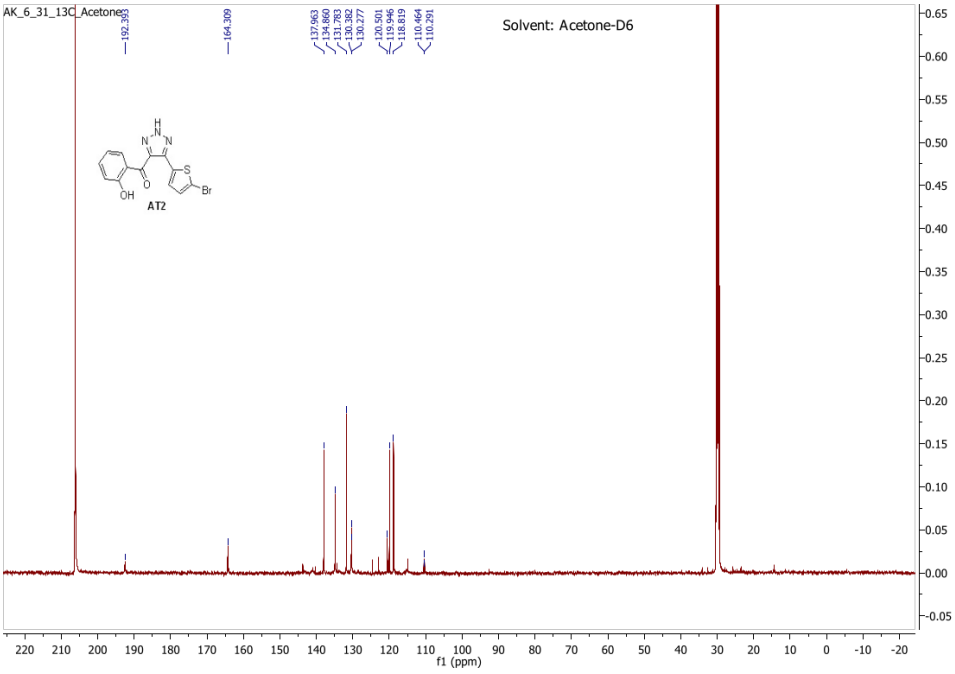
AK_6_31_13C_Acetone
Solvent: Acetone-D6
AT2
f1 (ppm)

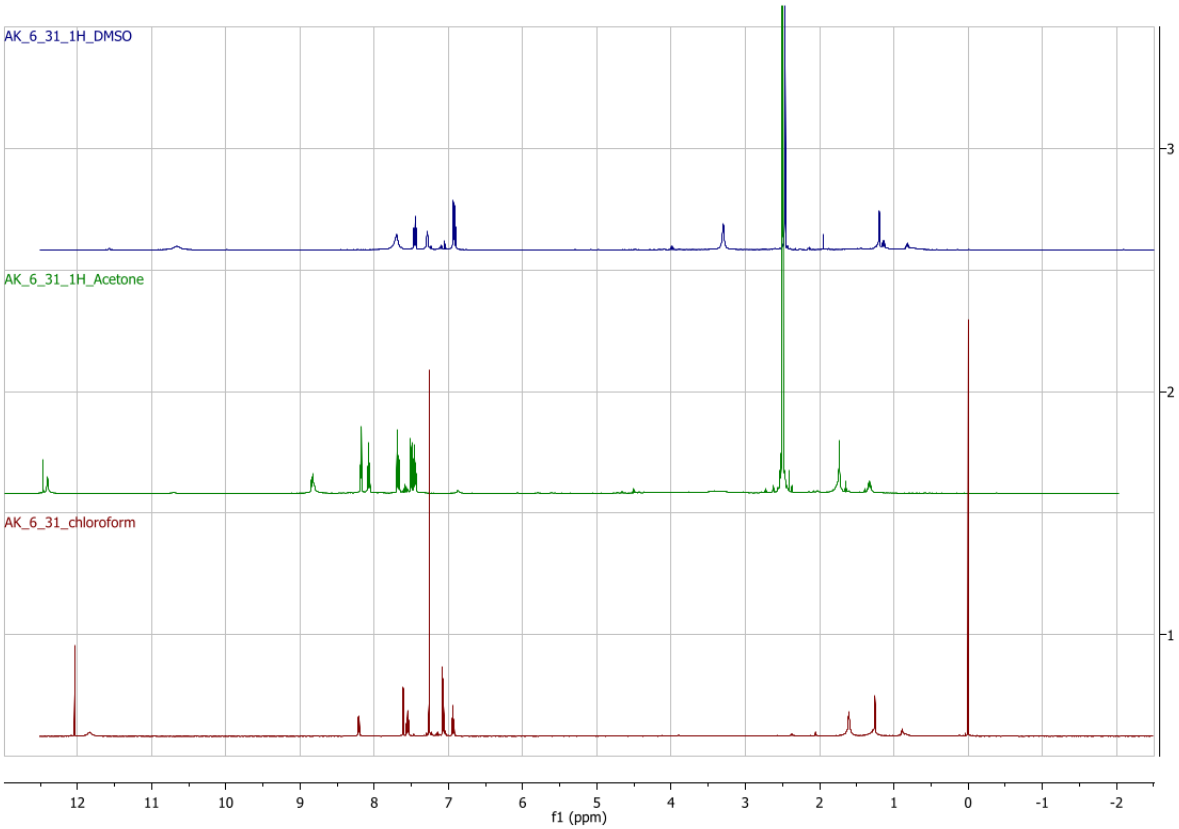
AK_6_31_1H_DMSO
AK_6_31_1H_Acetone
AK_6_31_chloroform
3
2
1
12
11
10
9
8
7
6
5
4
3
2
1
0
-1
-2
f1 (ppm)

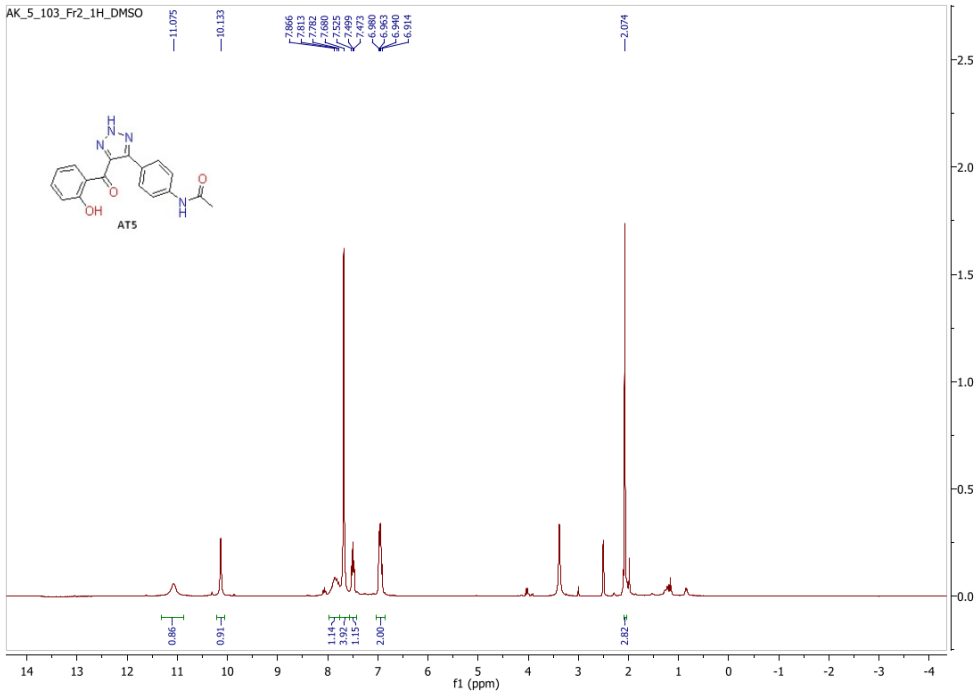
AK_5_103_Fr2_1H_DMSO
11.075
10.133
7.866
7.813
7.782
7.680
7.525
7.499
7.473
6.980
6.963
6.940
6.914
2.074
AT5
0.86
0.91
1.14
3.92
1.15
2.00
2.82
f1 (ppm)

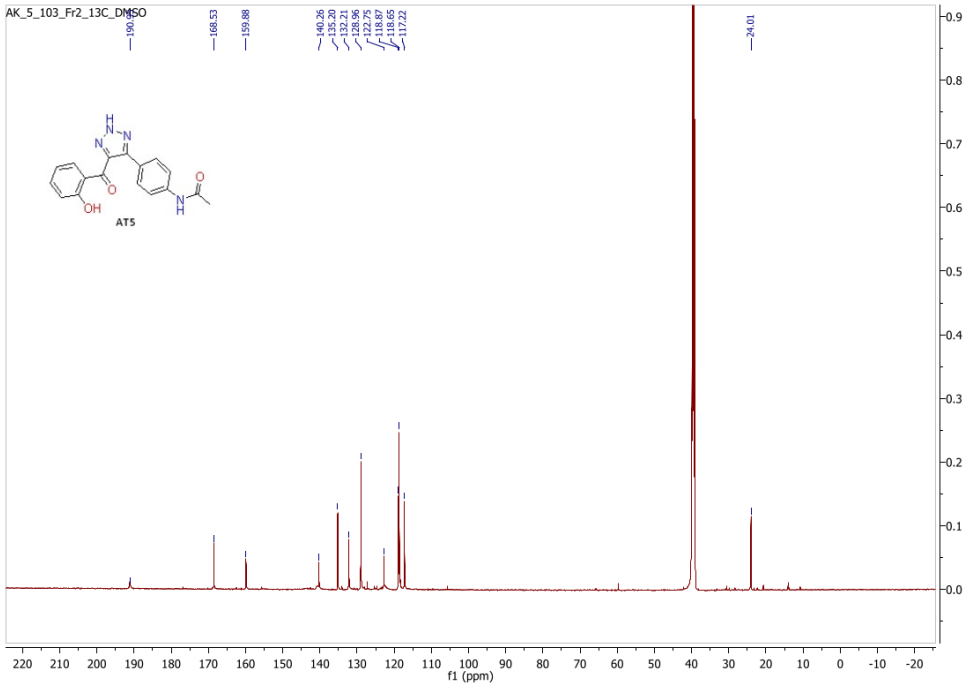
AK_5_103_Fr2_13C_DMSO
190.63
168.53
159.88
140.26
135.20
132.21
129.96
122.75
118.87
118.65
117.22
24.01
AT5
f1 (ppm)

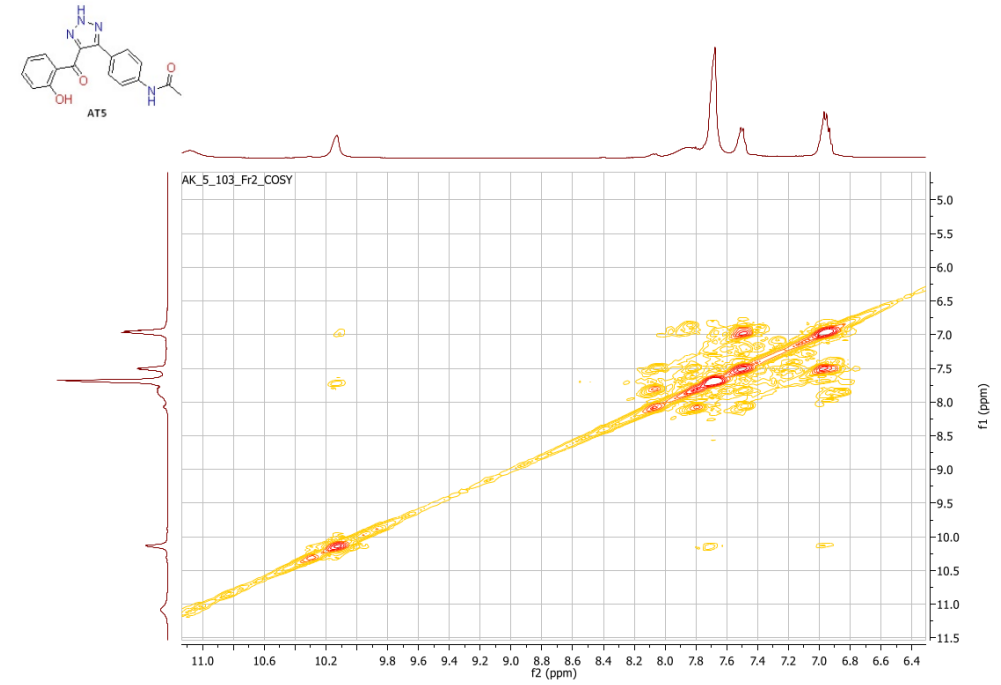
AT5
AK_5_103_Fr2_COSY
f1 (ppm)
f2 (ppm)

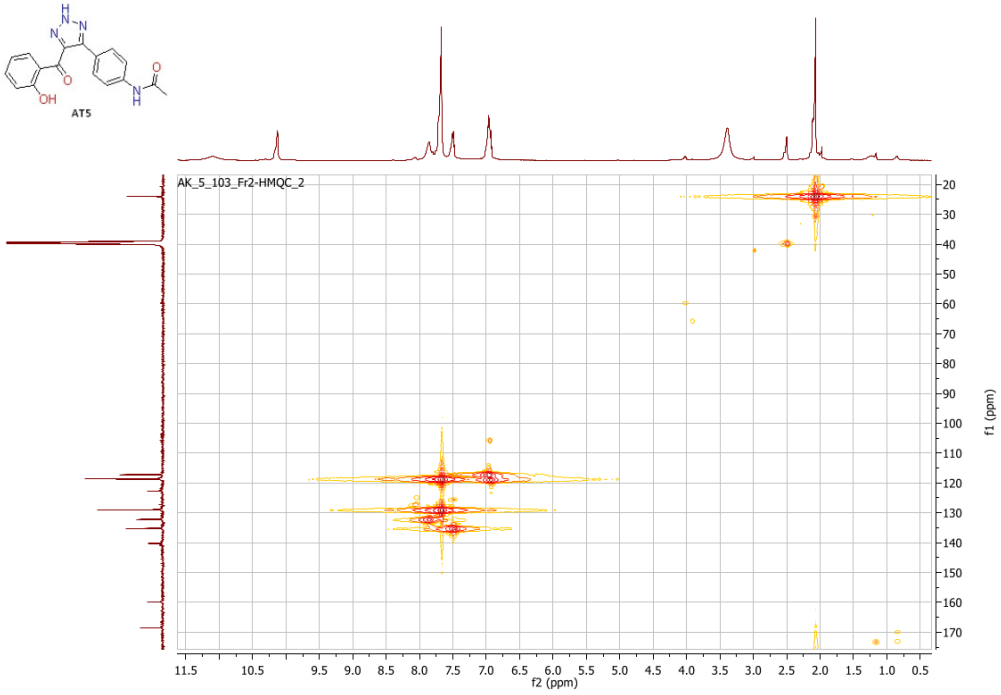
AT5
AK_5_103_Fr2-HMQC_2
f1 (ppm)
f2 (ppm)

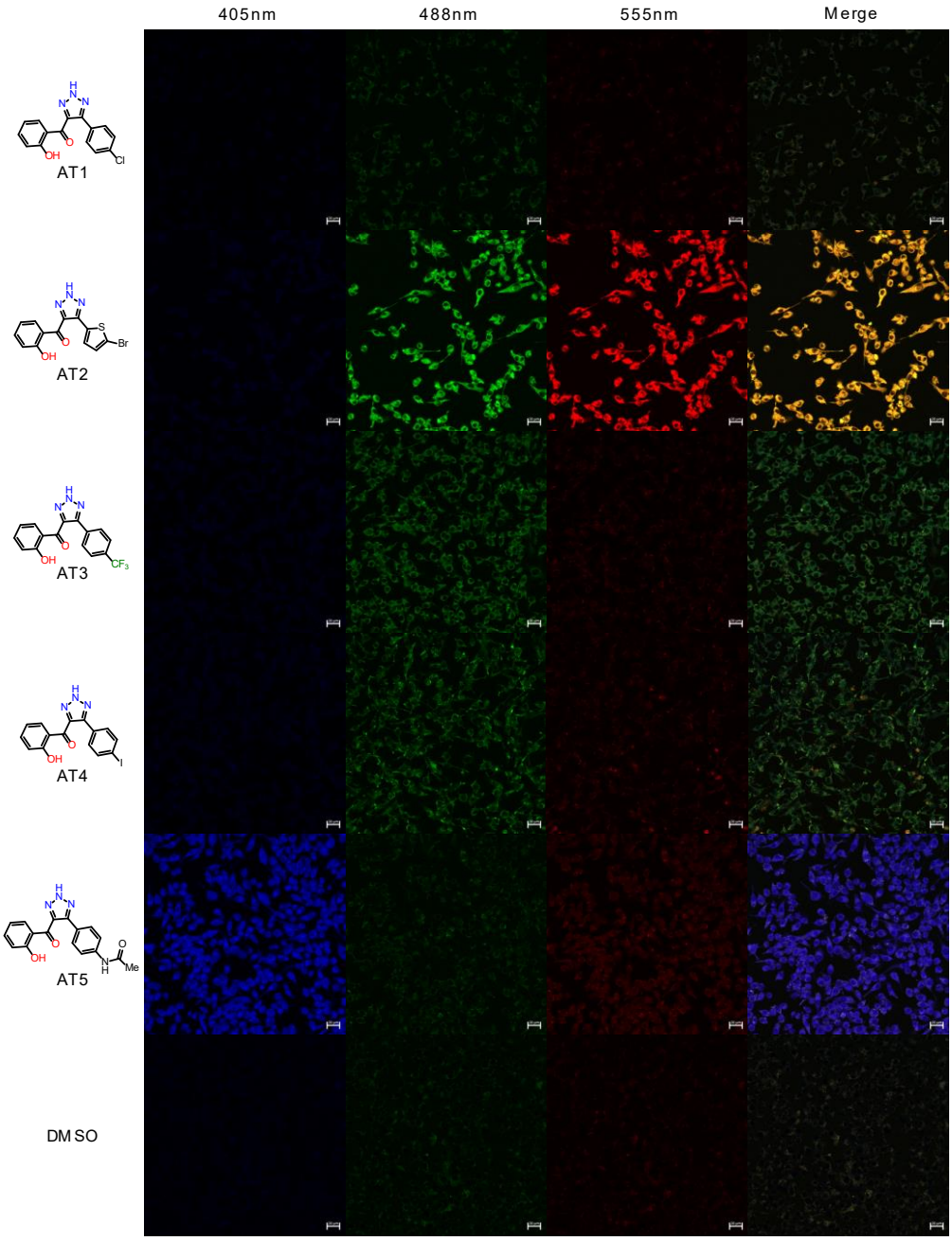

Figure S2. Full set of structures and images for Figure 2. Brightness across all images was adjusted equally post analysis. Scale bars are 20 μm.

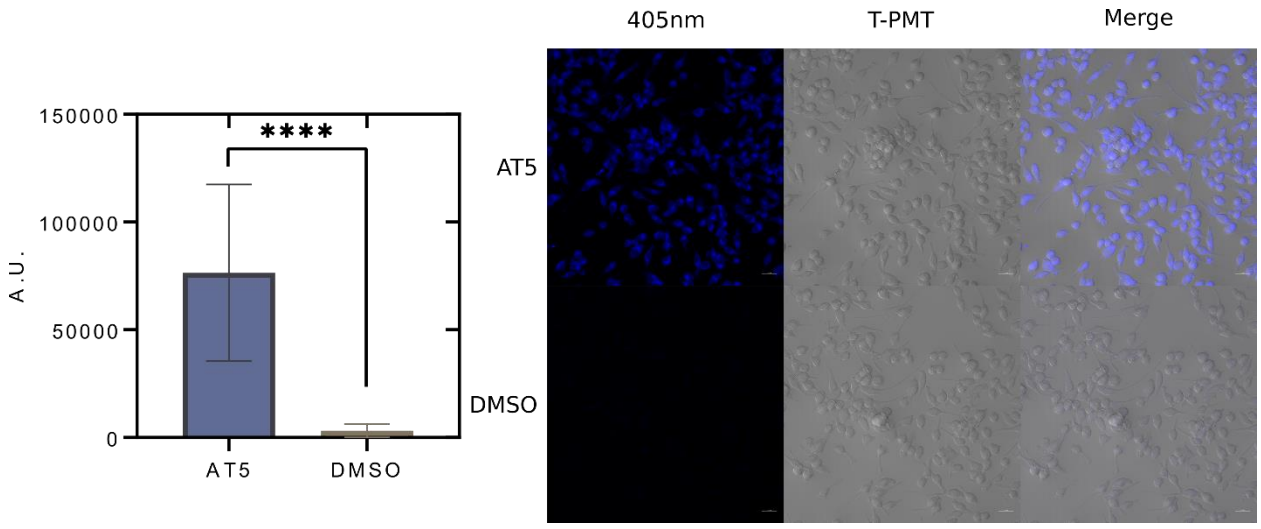

Figure S3. Fluorescent signal of AT5 in fixed RAW 264.7 cells/unit area (pixel). Data is shown as the mean ± SD, *n = 300* cells across three, independent replicates. ****p<0.0001 using a two-tailed t-test with a Welch's correction. Values where the fluorescence intensity of the cell was less than the background (negative values) were set to zero. Brightness across all images was adjusted equally post analysis.

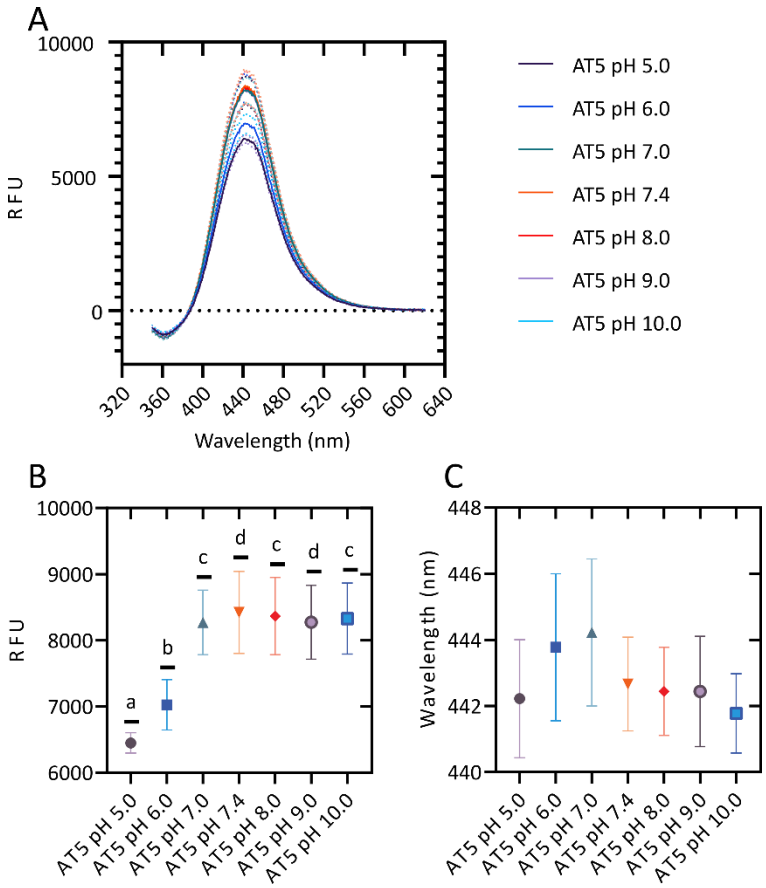

Figure S4. Effect of pH on emission of AT5. **A.** Emissions spectra of 100 µM **AT5** in PBS at various pH. **B.** Peak emissions ± SD of 100 µM **AT5** in PBS at various pH. **C.** Peak emission wavelengths of 100 µM **AT5** in PBS at various pH. Each value was measured using the CLARIOstar microplate reader in triplicate for three, independent replicates (*n = 9*). Statistical analysis was done using a Brown-Forsythe and Welch ANOVA; a-b, $p<0.05$; a-c/d, $p\leq0.0001$; b-c, $p< 0.0010$; b-d, $p< 0.0014$; c-d, $p> 0.9999$.

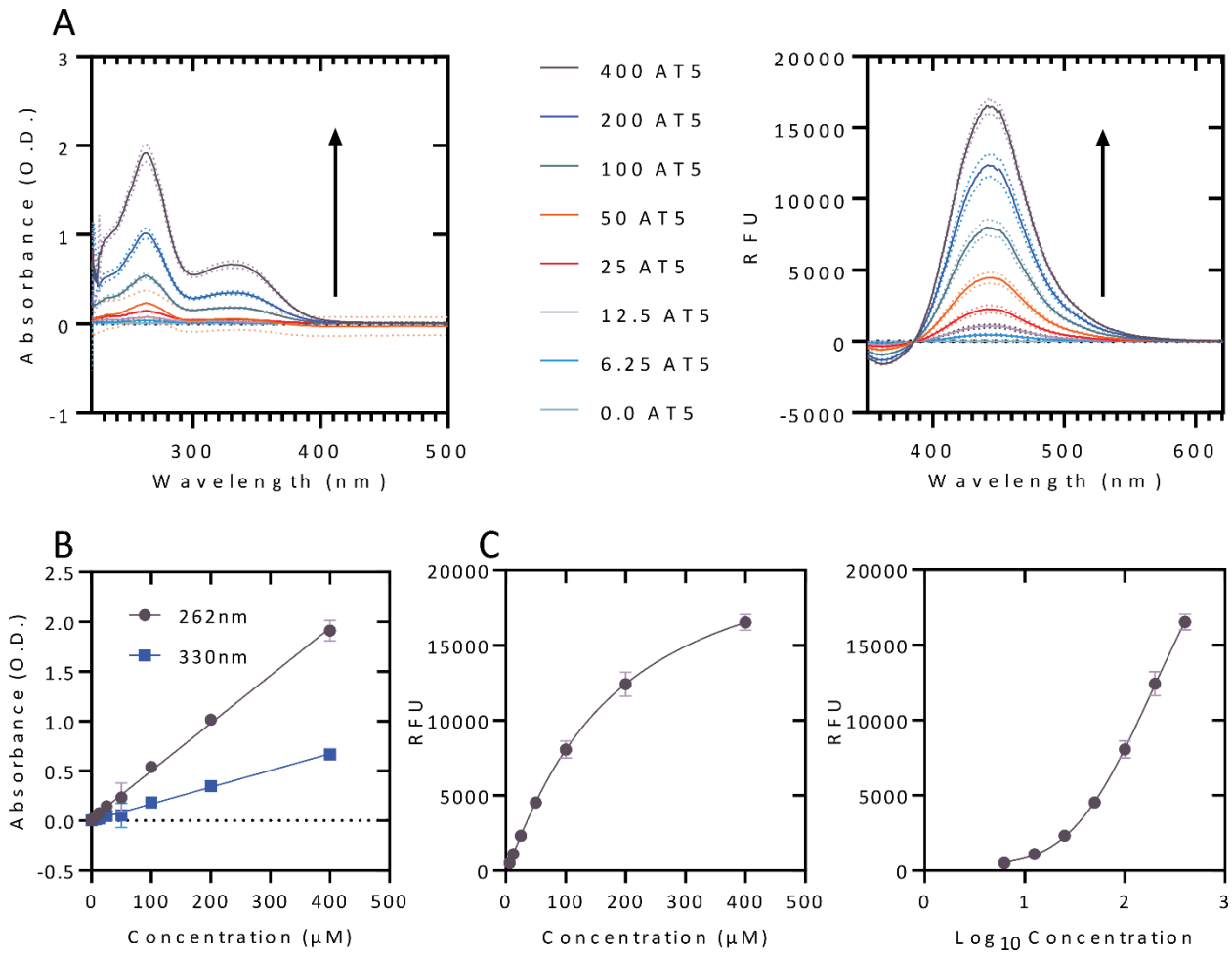

Figure S5. Absorbance and emission spectra for AT5 at varying concentrations in PBS. **A.** Absorbance (left) and emissions (right) spectra of increasing concentrations (arrow) of **AT5** in µM**.** Absorbance at wavelengths above 500 nm not shown. **B**. Absorbance at 262 nm and 330 nm for increasing concentrations of **AT5** including a linear regression analysis for each (r^2_{262nm} = 0.988 and r^2_{330nm} = 0.958). **C.** Peak emissions for increasing concentrations (left) and the $\log_{10}$ of each concentration (right) of **AT5**. Peak emissions for 0.0 µM could not be determined due to lack of signal. Each value was measured using the CLARIOstar microplate reader in triplicate for three, independent replicates ($n = 9$).

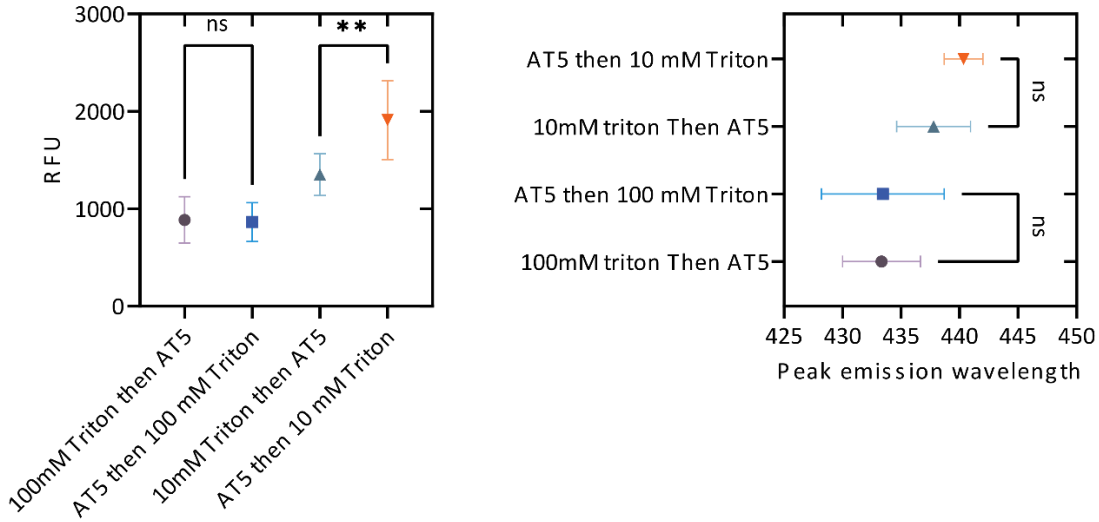

Figure S6. Order of mixing of AT5 in Triton X-100. **AT5** was added to PBS either 30min before or 30min after the addition of Triton X-100. The solutions were then mixed and pipetted in triplicate into UV 96-well plates. Peak fluorescent intensity and peak emission wavelength for each is represented as the mean ± SD. Statistical analysis performed is a Brown-Forsythe and Welch ANOVA, $n = 9$ wells across three, independent replicates. **$p<0.01$.

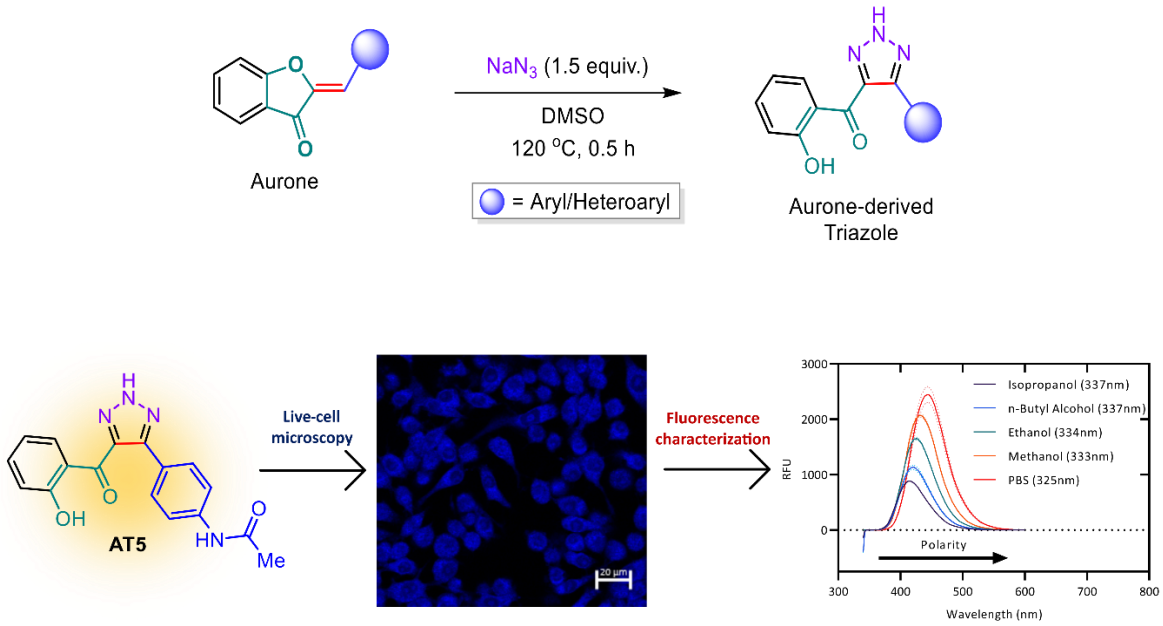

Figure S7. Graphical abstract submitted with Chapter II[1].

Extra methodology for confocal microscopy experiments. The power for all lasers was set to 6.5 %. All images were taken using a Zeiss Plan-Apochromat 20x/0.8 m27 objective. Quantification of signal per pixel (signal/ unit area; arbitrary unit, A.U.) was measured by acquiring the signal for each cell using the entire cell as a region of interest. The signal for the whole cell was then divided by the area to account for the variation in size of each cell. The Brightness mentioned in the text refers to adjustments in white point for each image.

Table S1: Full Table I (Chapter II). "Stokes shift and peak emissions of AT5 in various solvents". Emission spectra for **AT5** in various solvents was measured and blank corrected using 0.1 % (v/v) DMSO as a vehicle background. Peak emissions and peak emission wavelengths were determined as *n = 3* independent replicates for the indicated excitation wavelength. Stokes shift was determined as the difference between the excitation wavelength and the peak emissions wavelength, *n = 3* *Low solubility. **Negative values for one replicate led to only using an *n = 2*. [+]Aqueous solvents not statistically different due to high variability. [0]Polarity data not known for PBS. [1]Polarity based on the relative normalized $E_T(30)$ [E_T^N] polarity[216].

Solvent (excitation)	**Relative polarity[1]**	**Stokes shift (nm)**	**Std dev.**	**Peak emission (RFU)**	**Std dev**
APROTIC					
Cyclohexane (331nm)	0.006	75.53	22.41	6.07	3.68
Toluene (325nm)	0.099	75.33	2.22	11.54	1.71
Ethyl Acetate (296nm)	0.228	94.53	8.48	15.27	4.20
Chloroform (340nm)	0.259	67.73	1.75	25.33	0.86
Dichloromethane (323nm)*	0.309	80.13	2.86	17.71	1.40
Acetone (325nm)**	0.355	88.60	0.80	9.43	1.33
Dimethylformamide (304nm)	0.386	117.93	1.57	18.09	4.09
DMSO (307nm)	0.444	116.07	6.05	20.74	3.71
PROTIC					
Isopropanol (337nm)	0.546	77.07	0.57	889.07	10.96
n-Butyl Alcohol (337nm)	0.586	82.93	1.24	1135.33	57.48
Ethanol (334nm)	0.654	92.07	0.19	1660.33	26.04
Methanol (333nm)	0.762	98.07	0.25	2072.67	36.75
Water (330nm)*[+]	1.000	110.93	1.39	1349.03	337.84
PBS (325nm)[+]	--	118.27	0.52	2451.00	204.25

Appendix II

Supplementary Data for Chapter III

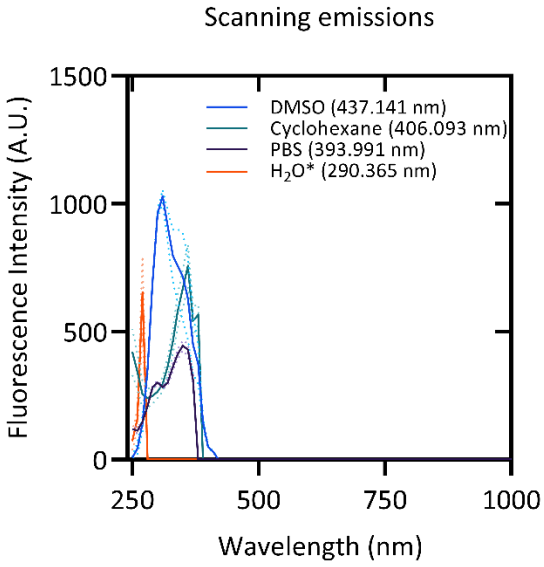

Figure S1. Overlap of scanning emissions spectra for AT111 in various solvents. In cyclohexane, emulsions of AT111 in DMSO were formed.

Appendix III

Supplementary Data for Chapter IV

Table S1. Calculated solubility/ permeability of AT5 and AT111 compared to known limits[293,294]. Calculations were determined based on structure using the Molinspiration Property Calculation Service[292]. MiLogP is the Molinspiration calculation for lipophilicity.

	Limit	AT5	AT111
Molecular weight	<500 g/mol	332.32 g/mol	355.35 g/mol
Hydrogen donors	<5	3	2
Hydrogen acceptors	<10	7	8
Calculated lipophilicity (MLogP)	<4.15	2.31 (MiLogP)	2.72 (MiLogP)
Rotational bonds	<10	4	6
PSA	<140 **Å²**	107.97 **Å²**	106.58 **Å²**

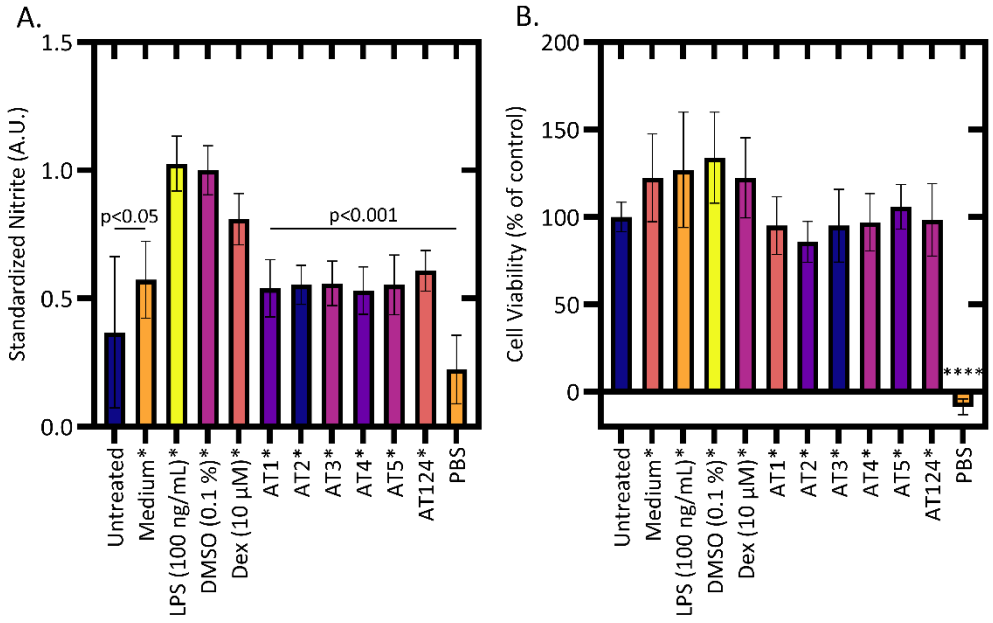

Figure S1. Relative levels of nitrite and cell viability from RAW 264.7 cells. Cells were pretreated with ATs or controls for 12 h, then cotreated with 100 ng/mL LPS for an additional 12 h*. Relative levels of both nitrite (A.) and cell viability (B.) were determined. Data is displayed as the mean ratio to the positive (LPS) control (A.) or untreated control (B.) ± S.D. Data was collected in triplicate wells across two independent biological replicates for an n = 6. Statistical analysis was done using a Brown-Forsythe and Welch ANOVA with a Dunnett T3 correction for multiple comparisons for each replicate compared to the vehicle (0.1 % [v/v] DMSO*) control (A.) or untreated control (B.). For p-values with indicated maxima, all significance was below that value to varying degrees. ****p< 0.0001.

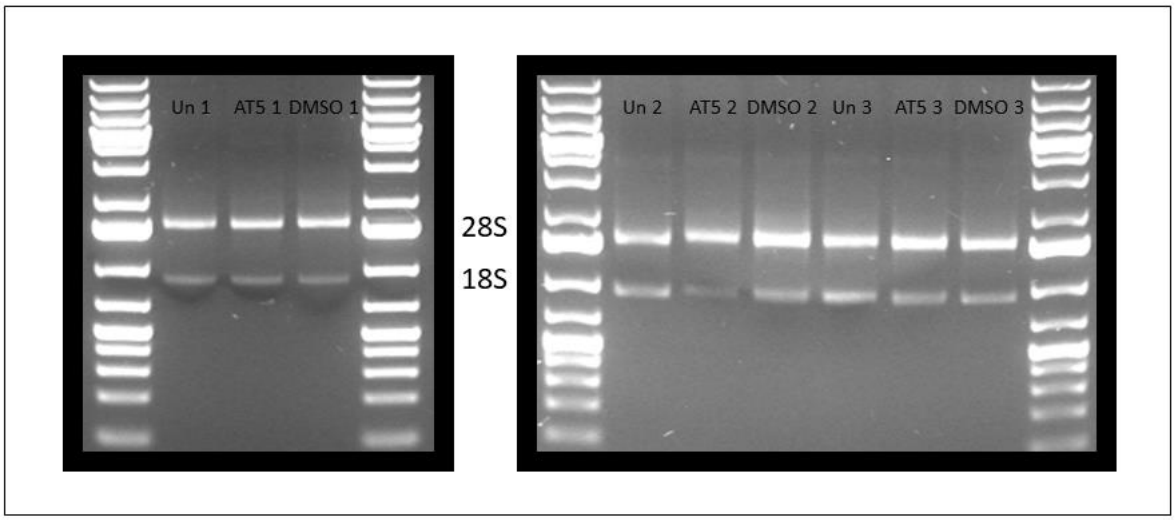

Figure S2. RNA quality from RAW 264.7 cells cotreated with AT5 or various controls for 18 h. RNA was extracted and examined for quality and degradation using a 1 % (w/v) agarose gel in 1x tris-acetate-EDTA (TAE) buffer containing a final concentration of 1 % (v/v) Clorox® bleach. Degradation was determined through examination of the quality of both the 28S and 18S ribosomal RNA. 5S ribosomal RNA was not visible at the indicated concentration.

A.

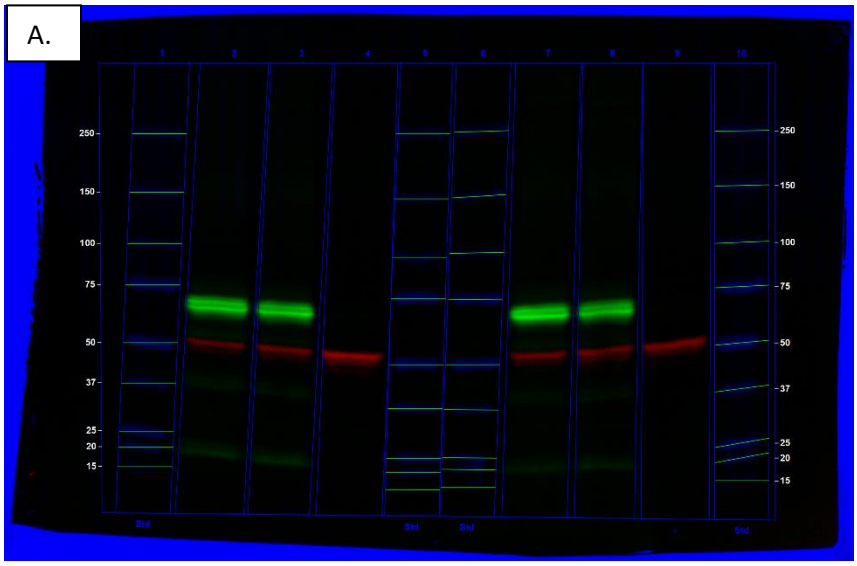
1
2
3
4
5
6
7
8
9
10
250
150
100
75
50
37
25
20
15
Std

B.

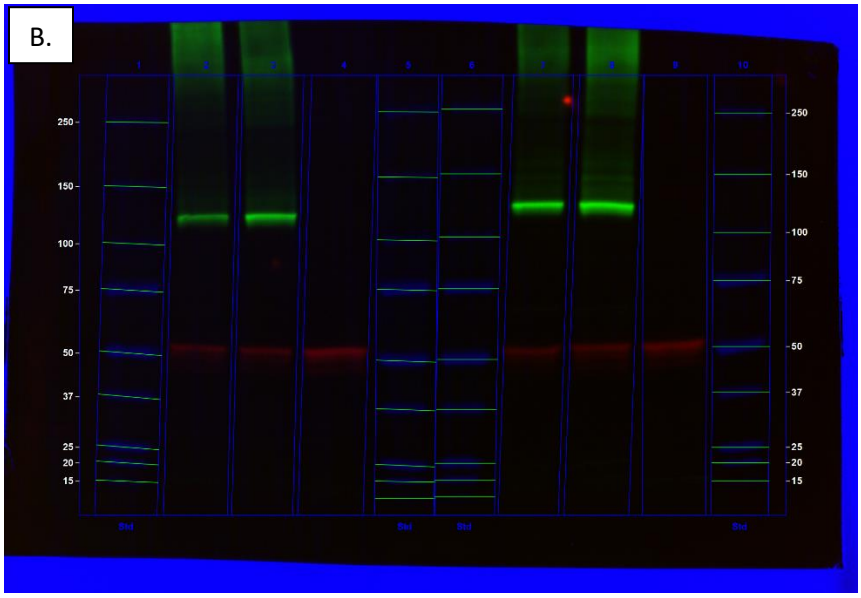
1
2
3
4
5
6
7
8
9
10
250
150
100
75
50
37
25
20
15
Std

Figure S3. Full blots showing preliminary analysis of COX-2 and iNOS. RAW 264.7 cells were cotreated with 100 ng/mL LPS and various controls for 24 h. Proteins were then harvested and equivalent amounts of 15 μg of protein were loaded into each lane. Gels were transferred to low-fluorescent PVDF membrane and proteins were examined using murine COX-2 (A.) and iNOS (B.) specific antibodies, probed for with Bio-Rad StarBright Blue 520 goat anti-rabbit secondary antibody (Green). β-tubulin hFAB rhodamine was used as a loading control (Red). Two biological replicates were run for each blot (lanes 1-5; replicate 1, lanes 6-10; replicate 2). Lanes 2 and 7 represent the AT111 + LPS samples, lanes 3 and 8 represent the DMSO + LPS samples, and lanes 4 and 9 represent the untreated samples. Lanes 1, 5, 6, 10 contained the ladders. Brightness and darkness levels were adjusted equally for visualization and visual background signal reduction, gamma values remained at 1.

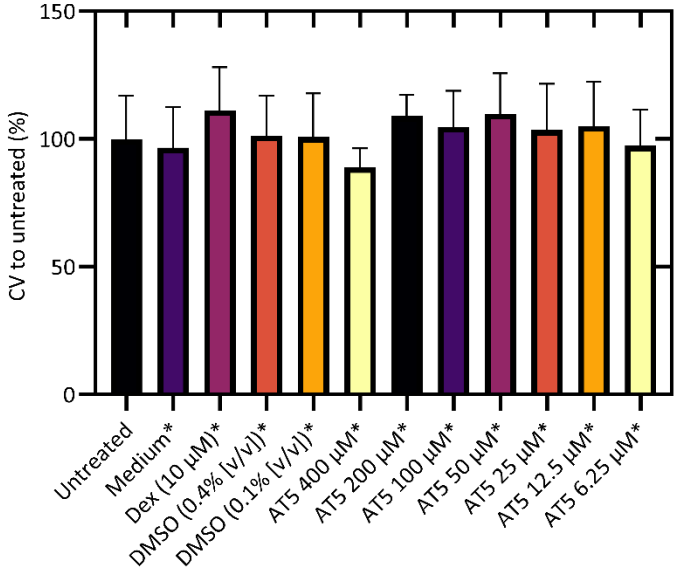

Figure S4. Cell viability of RAW 264.7 cells 24 h cotreated. Cells were cotreated with various concentrations of AT5 or various controls and 100 ng/mL LPS* for 24 h. Data is displayed as the mean percent cell viability compared to the average untreated control for each biological replicate ± S.D The experiment was performed in triplicate for five independent biological replicates, n = 15. Statistical significance was determined using a one-way ANOVA with a Dunnett's multiple comparisons test compared to the untreated control. Figure corresponds with Figure 21.

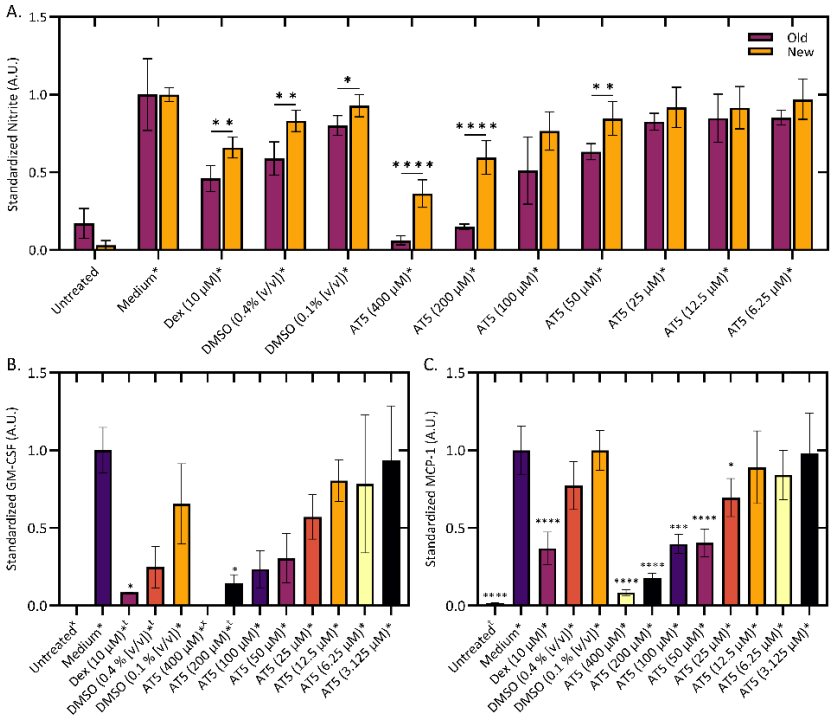

Figure S5. Comparison between old and new samples for levels of nitrite and inflammatory markers. Supernatants from RAW 264.7 cells cotreated with AT5, or various controls, and 100 ng/mL LPS for 24 h, shown in Figure 21, were utilized. A. Relative levels of nitrite from the first two biological replicates using the previous RAW 264.7 cells (old; n = 6) and the subsequent three biological replicates with the newly purchased RAW 264.7 cells (new; n = 9). B. Relative levels of GM-CSF and C. Relative levels of MCP-1 for the first two biological replicates, n = 6. Data was standardized to the positive (medium*) control for each biological replicate. Treatment* = cotreated with 100 ng/mL LPS. [t]Some values were below the limit of detection and excluded. [x]All values were below the limit of detection and could not be analyzed. Statistical analysis for A. was performed using unpaired t-test with a Welch correction, *p was performed using a Brown-Forsythe and Welch ANOVA with a Dunnett T3 correction for multiple comparisons. *p<0.05, **p<0.01, ***p<0.001, ****p<0.0001.

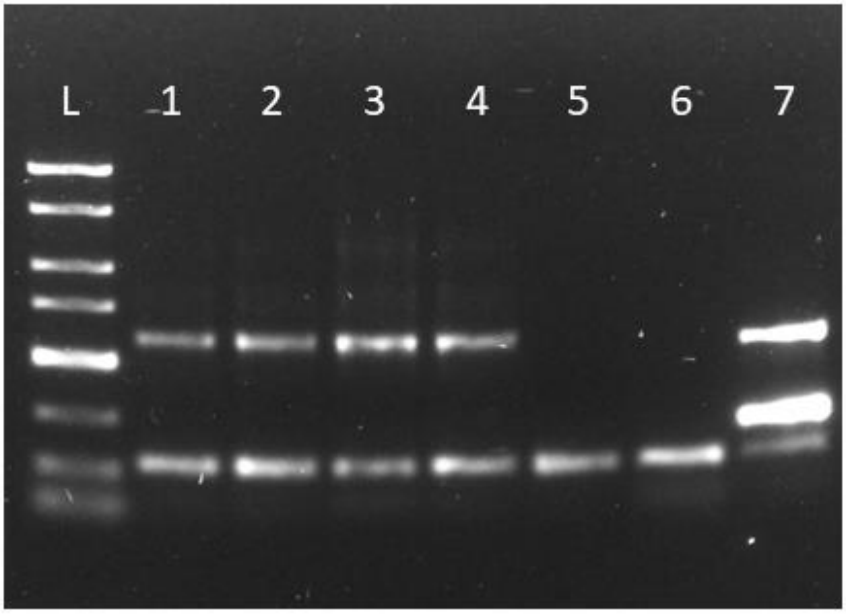

Figure S6. Mycoplasma detection of RAW 264.7 cells. DNA from RAW cells was extracted via boiling and mycoplasma detection was determined using the Myco-Sniff™ mycoplasma PCR detection kit (093050201). Various amounts of cells, 1 mL, 1.5 mL, and 2.5 mL were isolated from a T-25 tissue culture flask and lysed for DNA. PCR products from the kit using standardized amounts of DNA were run on a 1% agarose gel with SYBR safe for 45min at 100v. Lanes contain: L; ladder, 1; 1mL RAW cell PCR product (no loading dye), 2; 1mL RAW cell PCR product (with loading dye; LD), 3; 1.5mL RAW cell product LD, 4; 2.5mL RAW cell PCR product, 5; No template PBS, 6; No template nuclease free water, 7; positive control.

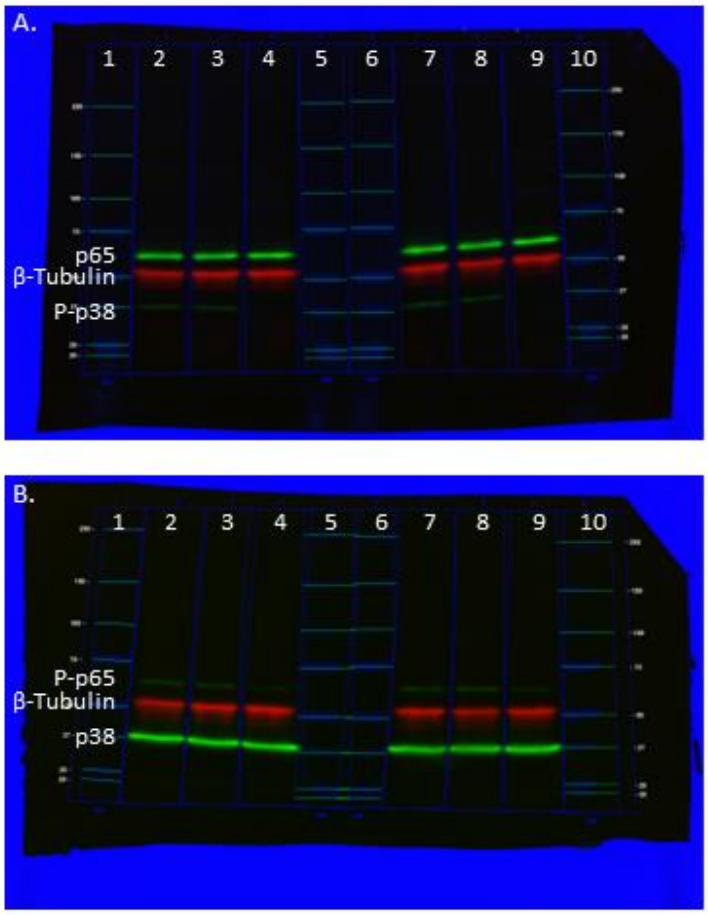

Figure S7. Full western blots for Figure 22. A. Western blots for p65 and p-p38 and B. p-p65 and p38. Lanes 1-5 are biological replicate 1 and lanes 6-10 are biological replicate 2. Lanes 2 and 7 are AT111+LPS, lanes 3 and 8 are LPS+DMSO and lanes 4 and 9 are untreated. Lanes 1, 5, 6, 10 are ladders. Brightness and darkness levels were adjusted equally for visualization and visual background signal reduction, gamma values remained at 1.

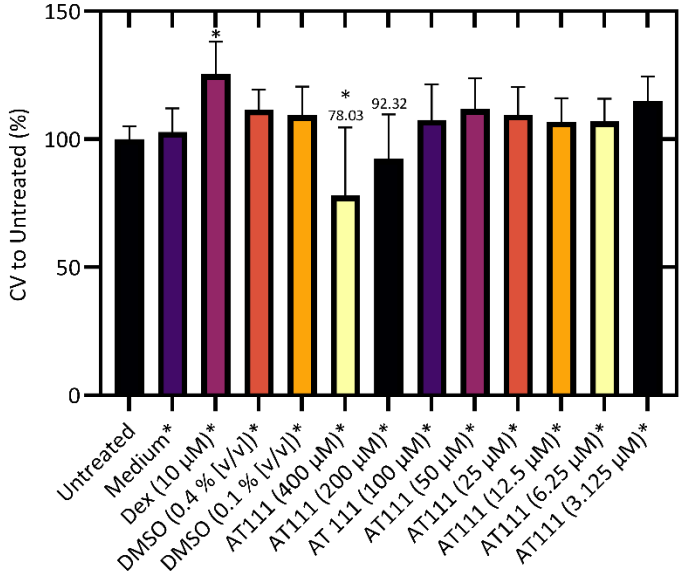

Figure S8. Cell viability of RAW 264.7 cells cotreated for 24 h with various concentrations of AT111. Cells were cotreated with AT111 or various controls and 100 ng/mL LPS*. Cell viability for Figure 24. Each data point is represented as the mean ratio of the untreated control performed in triplicate for four independent biological replicates, n = 12. Statistical significance was determined using a Brown-Forsythe and Welch ANOVA with a Dunnett T3 multiple comparisons test compared to the untreated control. *$p<0.05$.

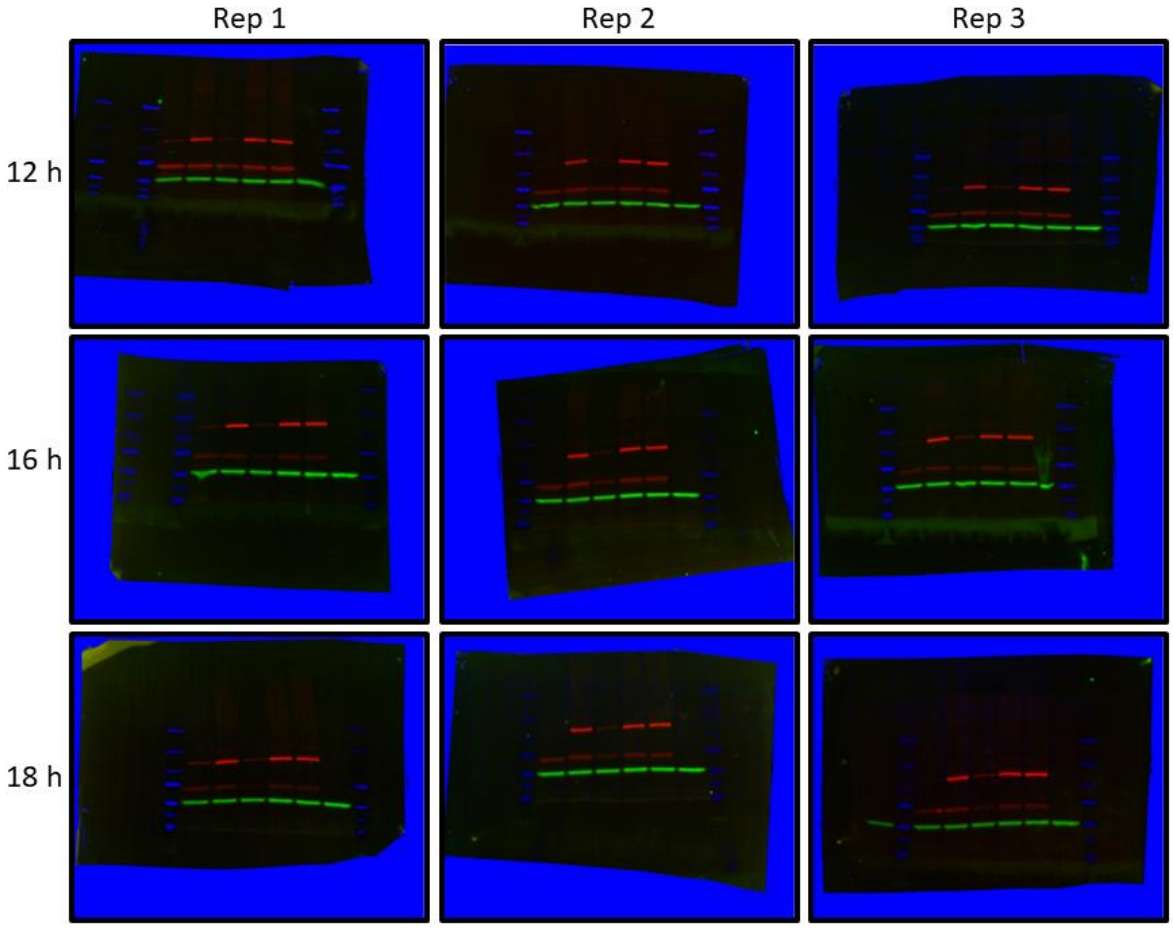

Figure S9. Full blots from Figure 26. Samples **right to left**: ladder, untreated, medium*, DMSO (0.1% v/v)*, 10 µM dexamethasone*, 100 µM AT5, 100 µM AT111, ladder, other wells not pertaining to this experiment. Proteins top to bottom: iNOS, COX-2, and β-tubulin. Brightness and darkness levels were adjusted equally for visualization and visual background signal reduction, gamma values remained at 1.

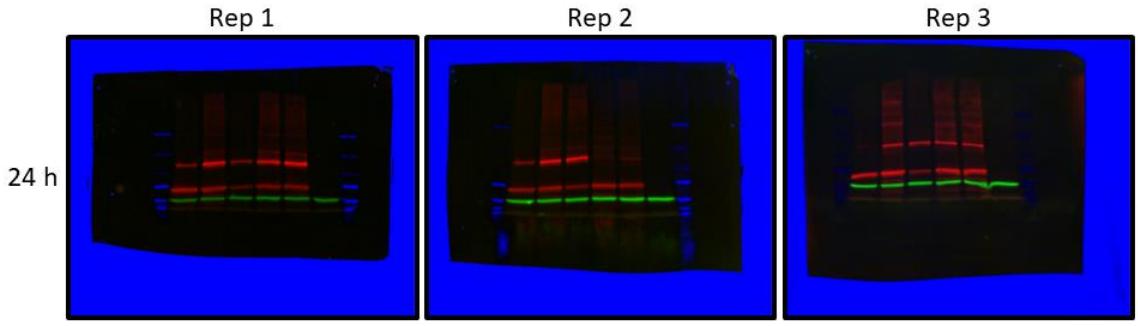

Figure S10. Full iNOS western blots for RAW 264.7 cells. Full western blots of proteins isolated from RAW 264.7 cells pretreated with 100 μM ATs or various controls for 24 h then cotreated for an additional 24 h. Samples **right to left**: ladder, untreated, medium*, DMSO (0.1% v/v)*, 10 μM dexamethasone*, 100 μM AT5, 100 μM AT111, ladder. Proteins top to bottom: iNOS, COX-2, and β-tubulin. Brightness and darkness levels were adjusted equally for visualization and visual background signal reduction, gamma values remained at 1.

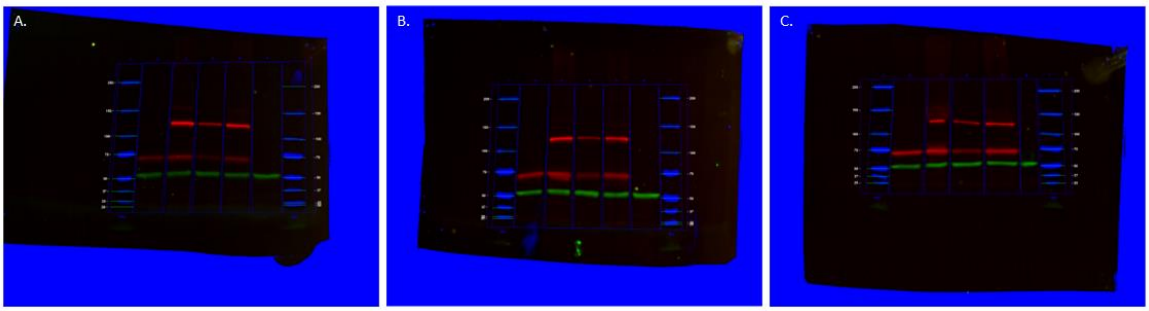

Figure S11. Full iNOS and COX-2 blots from Figure 29. A. Replicate 1, used in Figure 29. B. Replicate 2. C. Replicate 3. Samples for each replicate listed as **right to left**: Untreated, 0.1 % (v/v) DMSO*, 10 μM dexamethasone*, 100 μM AT5*, 100 μM AT111*. Cells were pretreated with the listed compounds for 4 h then *cotreated with 100 ng/mL LPS for an additional 24 h or not. Listed proteins from **top to bottom**: iNOS, COX-2, β-tubulin. Brightness and darkness levels were adjusted equally for visualization and visual background signal reduction, gamma values remained at 1.

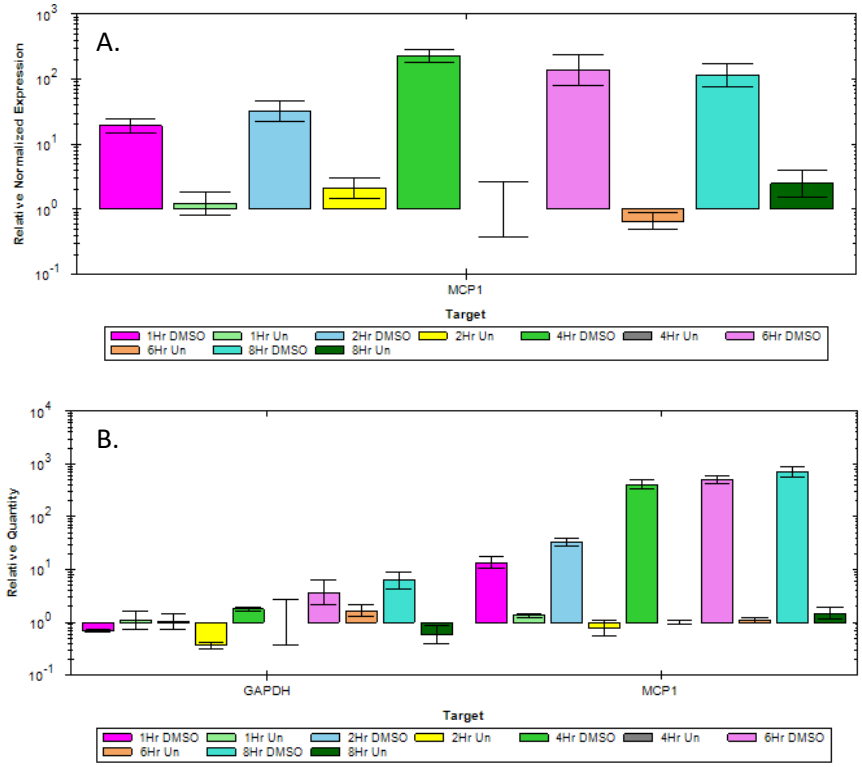

Figure S12. Determining mRNA treatment timepoints. RAW 264.7 cells were pretreated with either 0.1 % (v/v) DMSO for 4 h then cotreated with 1 µg/mL LPS for the indicated time points or untreated for 4 h with the medium then refreshed for the indicated time points. mRNA was converted to cDNA and MCP-1 (*Ccl2*) was measured using the aforementioned primers as described in the methods. GAPDH was used as a loading control/ standardization. A. Relative levels of amplified cDNA for MCP-1 for all time points were standardized to their corresponding GAPDH control, then compared to changes in relative expression of standardized MCP-1 with the 4 h untreated levels using the ΔΔCt method in the Bio-Rad CFX Maestro 2.3 software v. 5.3.022. 1030 (2021). B. ΔCt comparison showing variable GAPDH levels which were minimally amplified, and had erratic melt curves, this experiment. MCP-1 expression was mostly equal for 4, 6, and 8 h time points.

A.

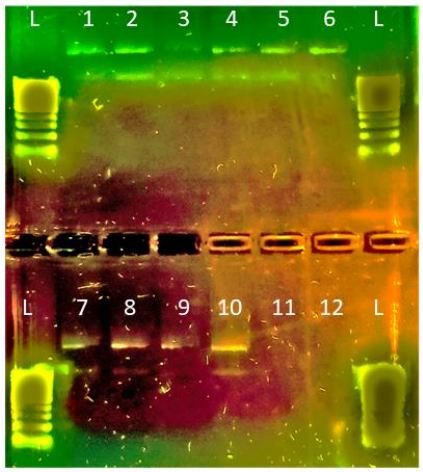

B.

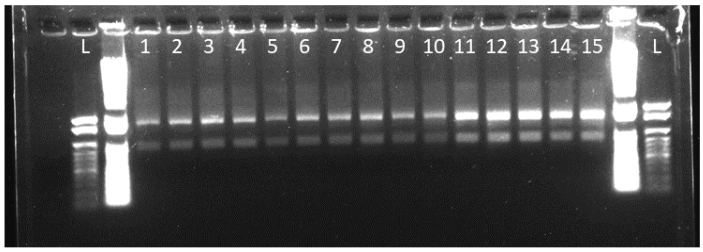

Figure S13. RNA quality for qRT-PCR. Quality of RNA extracted for A. the time-course experiment (Figure S12) and B. the inflammatory response genes qRTPCR experiment (Figure 31). Quality was determined using a 1 % Agarose TAE gel containing 1 % (v/v) Clorox® bleach as described earlier. A. All samples were pretreated with medium or 0.1 % (v/v) DMSO for 4 h, then cotreated with 1 µg/mL LPS or remained untreated for 1 h (lanes 1 and 2), 2 h (3 and 4), 4 h (5 and 6), 6 h (7 and 8), and 8 h (9 and 10). Lanes 11 and 12 are no-template controls. B. Samples were pretreated with medium (lanes 1, 6, and 11), 0.1 % (v/v) DMSO (lanes 2, 7, and 12), 10 µM dexamethasone (lanes 3, 8, and 13), 100 µM AT5 (lanes 4, 9, and 14), and AT111 (lanes 5, 10, and 15) for 4 h then cotreated with 1 µg/mL LPS for an additional 4 h. Lanes 1-5 indicate replicate 1, 6-10 replicate 2, and 11-15 replicate 3. Top band depicts the 28S rRNA and the lower band is the 18S rRNA.

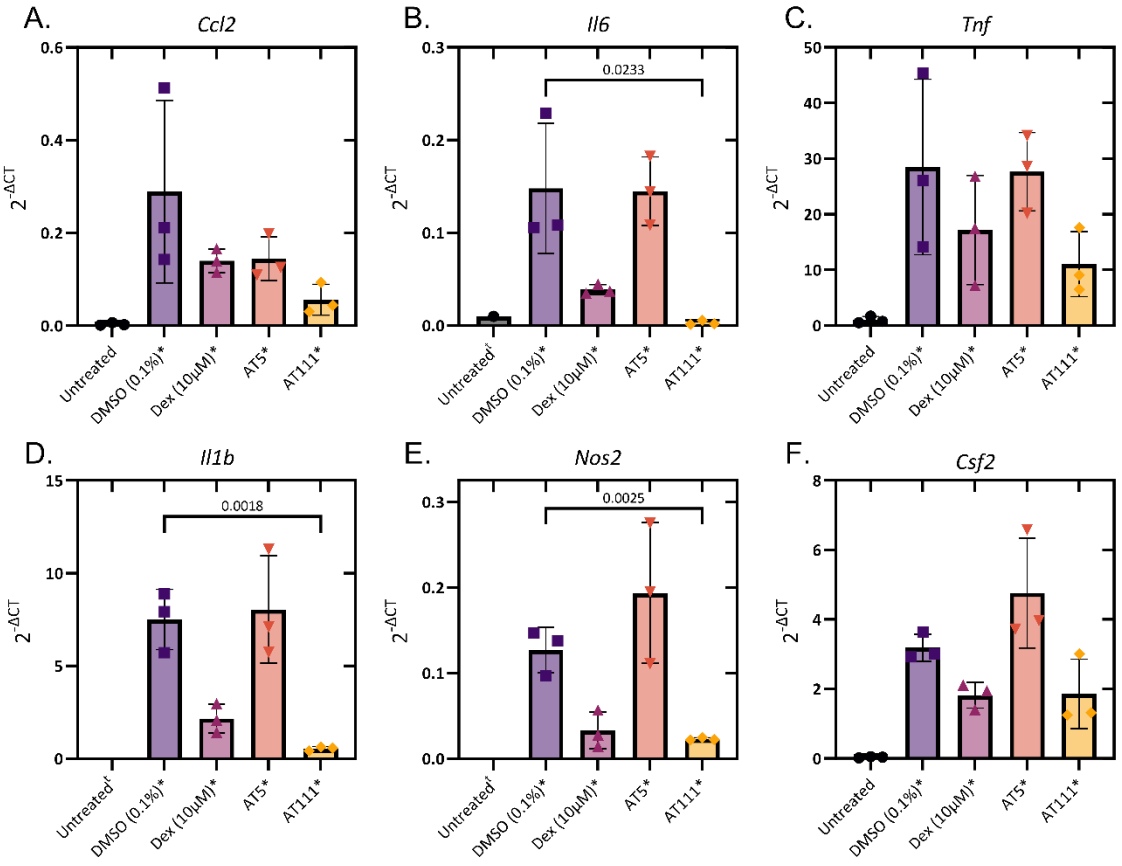

Figure S14. Delta CT method analysis of qRT-PCR experiment from Figure 31. The ΔCT for each indicated gene was determined as the average amplification cycle for two technical replicates standardized to the average amplification cycle for GAPDH for that sample. The data shown is the average $2^{-\Delta CT}$ ± S.D. for three biological replicates. One technical replicate of one biological replicate of the DMSO* control for *Csf2* was excluded for minimal amplification. Cells were treated for 4 h with 100 μM ATs or controls at the indicated concentrations, then *cotreated with 1 μg/mL LPS for an additional 4 h. Statistical analysis was done using an unpaired two-tailed t-test comparing AT111 to the DMSO* control. Significant p-values are displayed on each graph, n = 3.

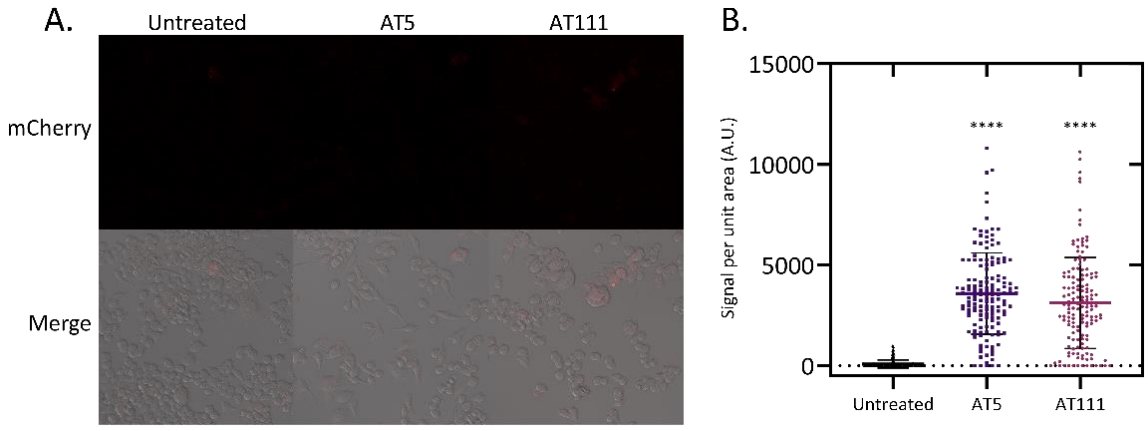

Figure S15. *Nos2* reporter background fluorescence. A. Representative photos displaying the fluorescence for cells treated with 100 µM AT5 and AT111 (without LPS – with 0.1 % DMSO as a co-solvent) for 4 h, then treated again for an additional 24 h, compared to the untreated control from Figure 32. B. Quantification of A. Each datum point represents the background-subtracted mean signal/ unit area for one cell. Negative values, where the fluorescence within the cell was lower than the background, were set to zero. Outliers from each sample were detected using the ROUT method with a Q = 1 % using GraphPad Prism version 10.0.0-10.0.1 then removed, n = 114 (untreated), 150 (AT5), and 148 (AT111) cells. Significance was determined using a Kruskal-Wallis with a Dunn's correction compared to the untreated control. ****$p<0.0001$.

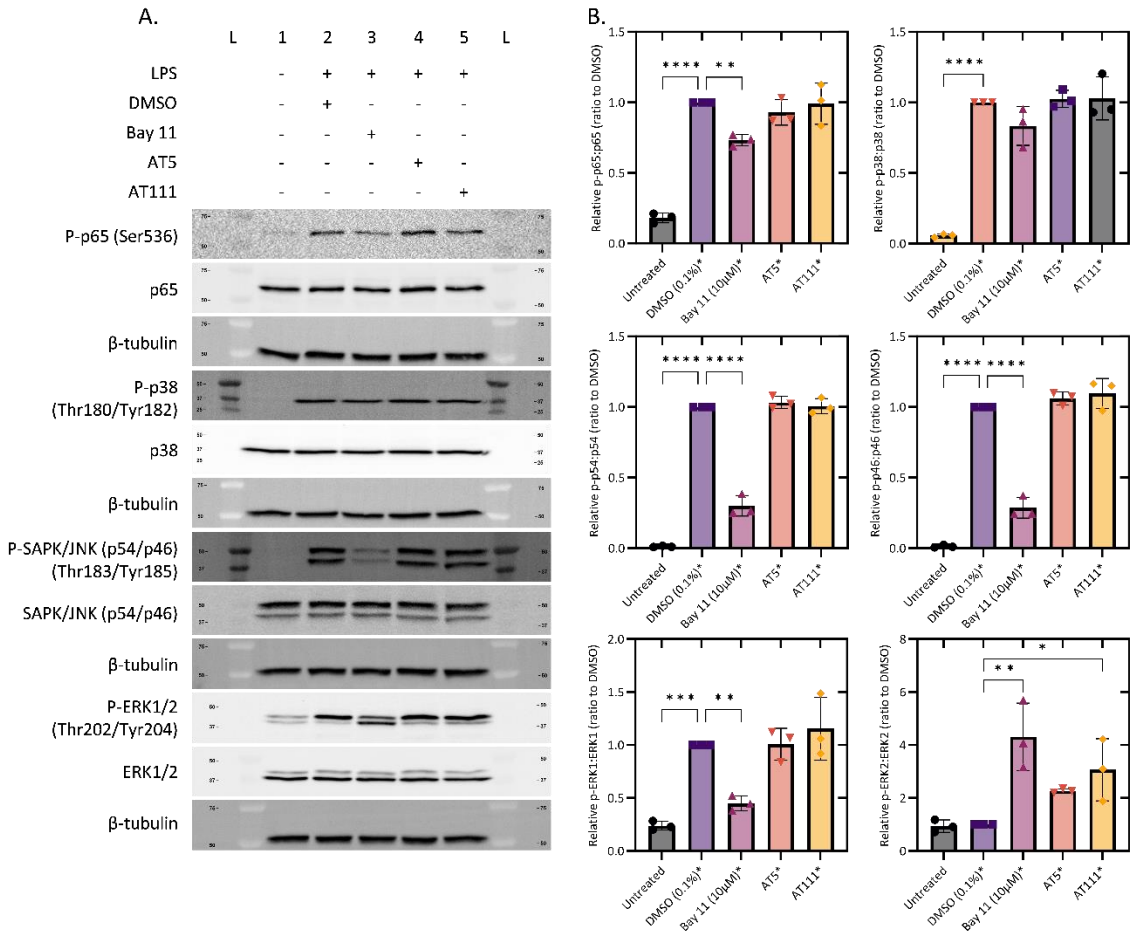

Figure S16. Aberrant ERK2 blots. Alternative cell lysates depicting the effect of AT5 and AT111 on aspects of the initial, MyD88-dependent, TLR4 signal transduction pathway with errant p-ERK2 (Thr202/Tyr204). As stated before, RAW 264.7 cells were treated with 100 μM AT111, 100 μM AT5, or the indicated controls for 4 h. The cells were then cotreated with 100 ng/mL LPS for an additional 15 min. 10 μg of total protein were loaded into each lane and detected as described in the methods. A. Representative blot depicting the indicated proteins, and their respective β-tubulin from each blot from the same cell lysates. Blot was inverted and the brightness auto-adjusted post analysis for visualization. B. Densitometric analysis of A. for each indicated protein. Data was normalized first to the level of β-tubulin, then the ratio of

phosphorylated:total protein for each indicated protein was determined. The resultant ratio is then standardized to the vehicle (DMSO) control for each of three biological replicates. Statistical analysis was done using an ordinary one-way ANOVA with a Dunnet's correction, n = 3 biological replicates. *p<0.05, **p<0.01, ***p<0.001, ****p<0.0001. Full blots for all replicates are shown in Appendix III; Figure S18.

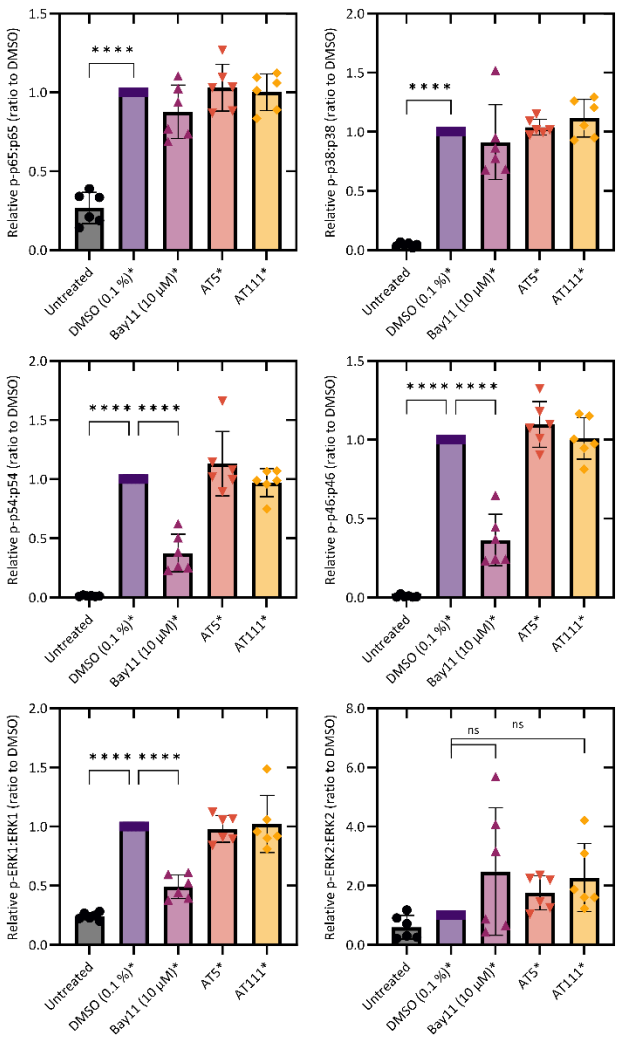

Figure S17. Combined quantifications for both Figure 33 and Appendix III; Figure S16. Statistical analysis was done using an ordinary one-way ANOVA with a Dunnet's correction, n = 6 biological replicates. ****p<0.0001.

P-p65(Ser536) – Blue, p65 – Red, β-tubulin – Green

Fig 33

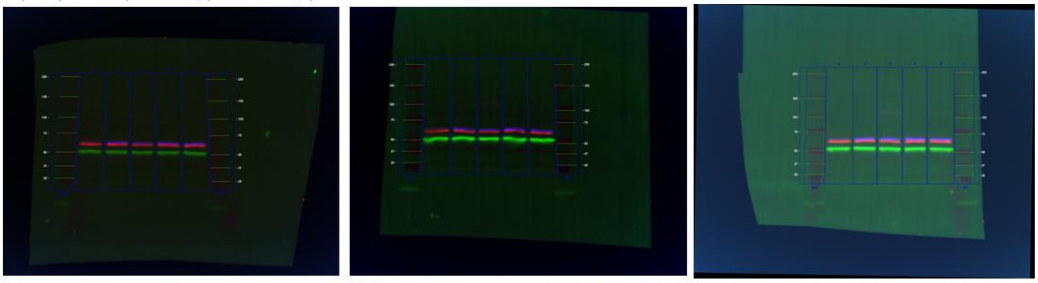

Fig S16

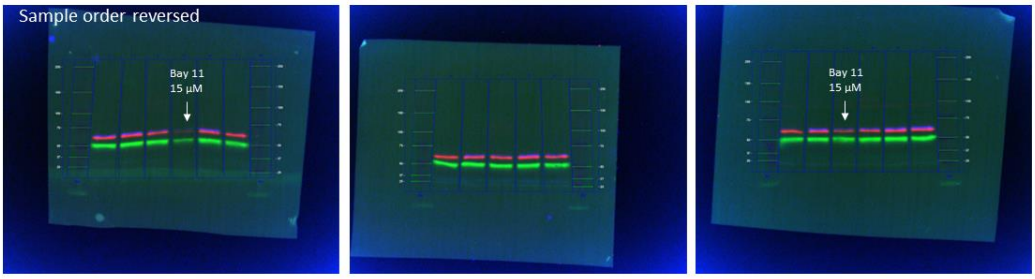

P-p38(Thr180/Tyr182) – Red, p38 – Blue, β-tubulin – Green

Fig 33

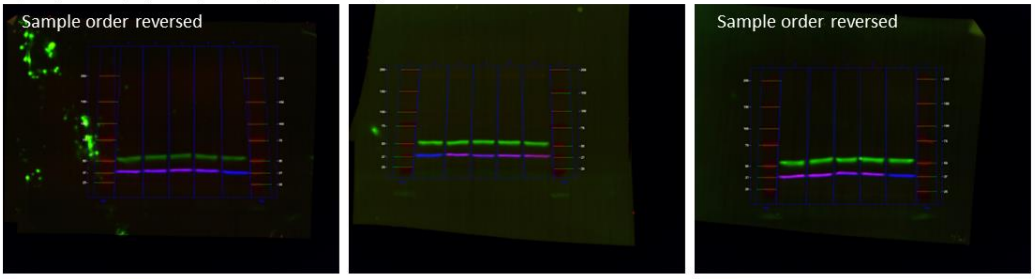

Fig S16

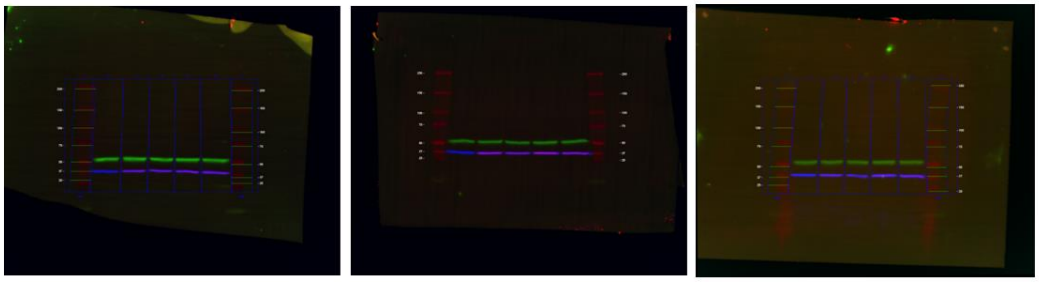

P-SAPK/JNK(Thr183/Tyr185) – Red, SAPK/JNK – Blue, β-tubulin – Green

Fig 33

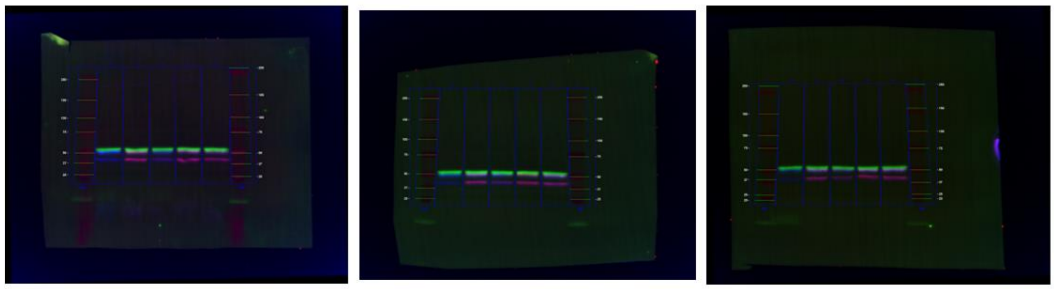

Fig S16

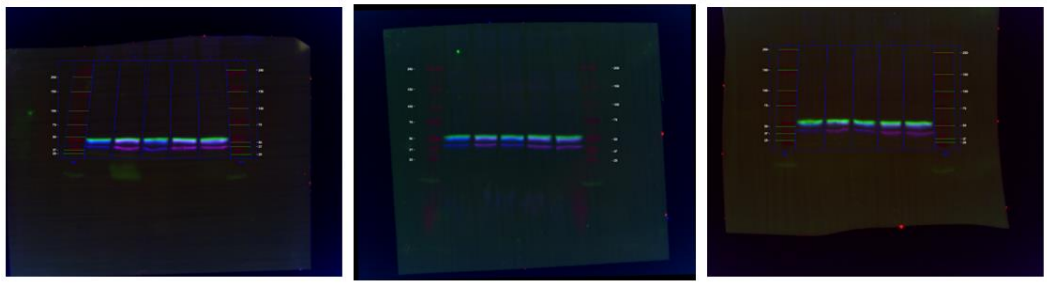

P-ERK1/2(Thr202/Tyr204) – Blue, ERK1/2 – Red, β-tubulin – Green

Fig 33

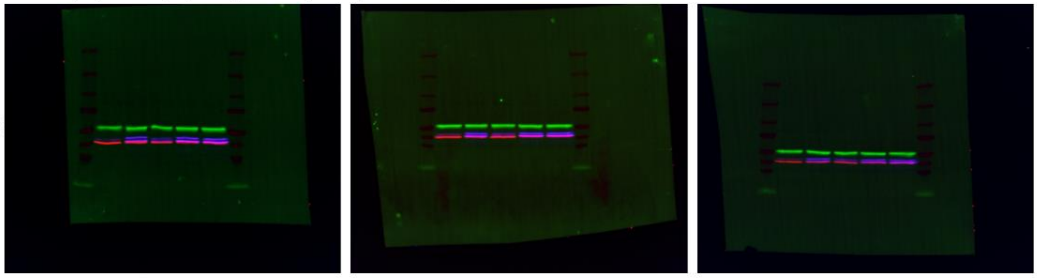

Fig S16

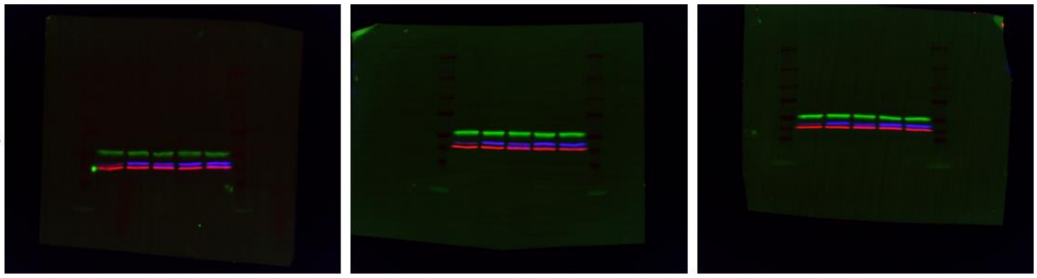

Figure S18. Full blots from both Figure 33 and Appendix III; Figure S16. Certain channels may be difficult to see unless isolated. For all samples order of lysates from **left to right;** Untreated, 0.1 % (v/v) DMSO*, 10 μM Bay 11-7082, 100 μM AT5, and 100 μM AT111 unless otherwise indicated. Brightness and darkness levels were adjusted equally for all pixels on each individual channel to remove background for visualization only. The gamma score was not modified (= 1).

Appendix IV

RNA Sequencing Quality Control

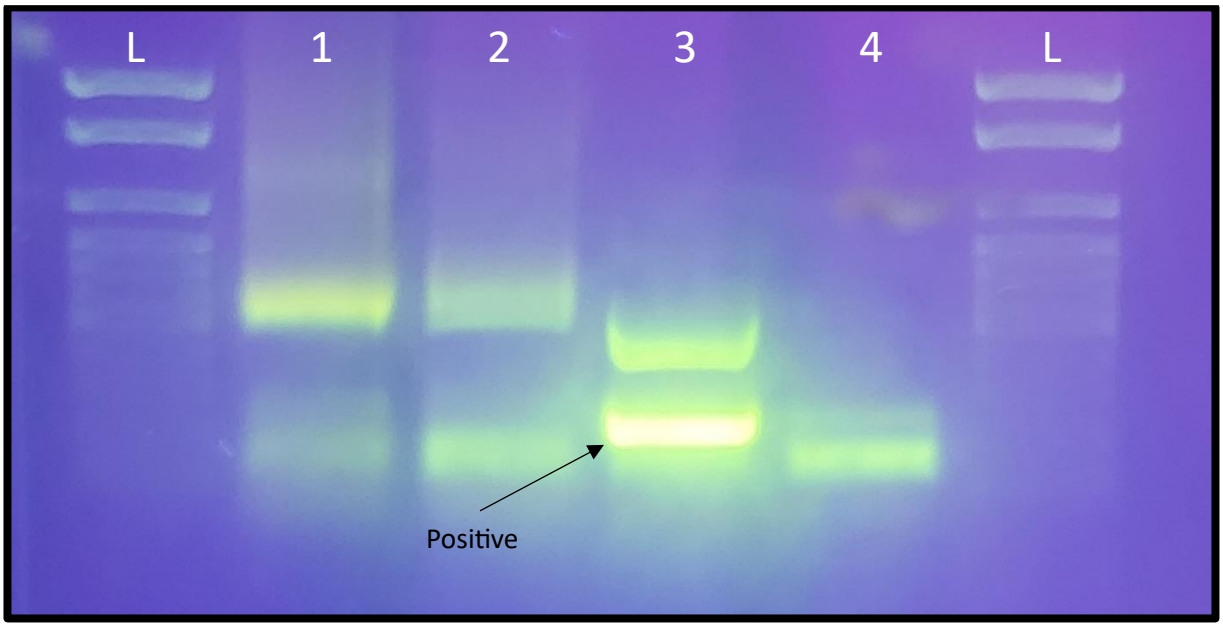

Figure S1. Mycoplasma detection of U937 cells and RAW 264.7 cells. DNA from each cell line was extracted via boiling and mycoplasma detection was determined using the Myco-Sniff™ mycoplasma PCR detection kit (093050201). PCR products were run on a 1% agarose gel with SYBR safe for 45min at 100v. Lanes contain: L; ladder, 1; U937 cell PCR product, 2; RAW 264.7 cell PCR product, 3; positive control, 4; no template nuclease-free water control.

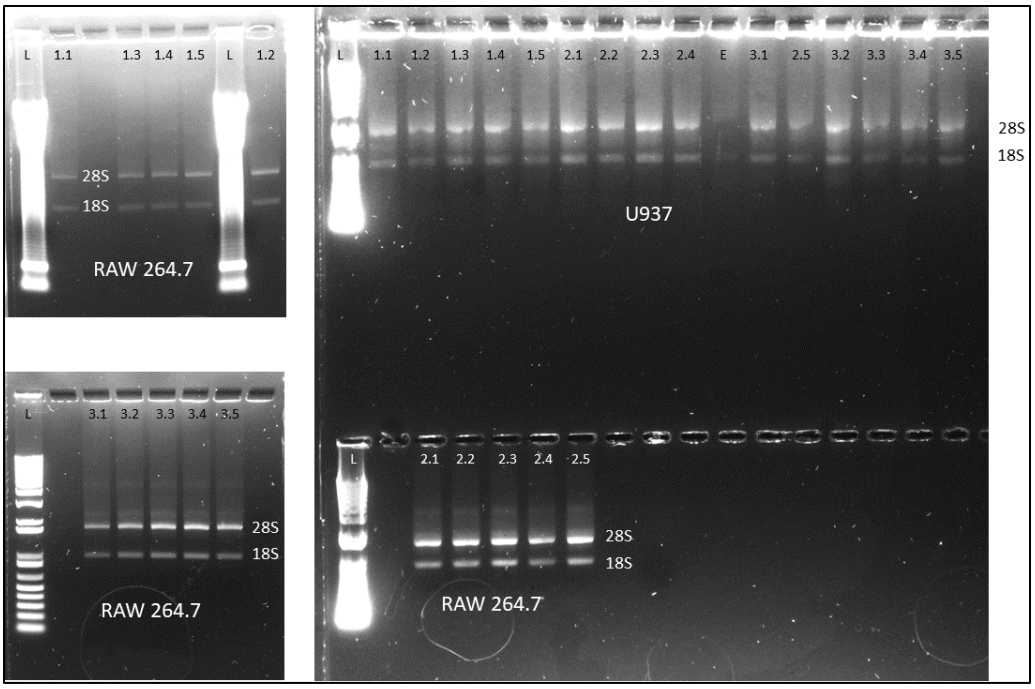

Figure S2. Quality of RNA extracted for RNA sequencing for both RAW 264.7 cells and PMA-differentiated U937 cells for RNA sequencing. Quality was determined using a 1 % Agarose TAE gel containing 1 % (v/v) Clorox© bleach as described earlier. Labels are depicted as replicate number and treatment (R#.treatment). R#.1 is the untreated sample. R#.2 is the 0.1% (v/v) DMSO* sample. R#.3 is the 10 µM dexamethasone* sample. R#.4 is the 100 µM AT5* sample. R#.5 is the 100 µM AT111* sample. *4 h pretreatment then 4 h cotreatment with 1 µg/mL LPS. Medium for the untreated sample was refreshed at the 4 h mark. RNA was extracted using the simplyRNA LEV kit as described in the methods. The top band depicts the 28S rRNA and the lower band is the 18S rRNA.

U937 cells.

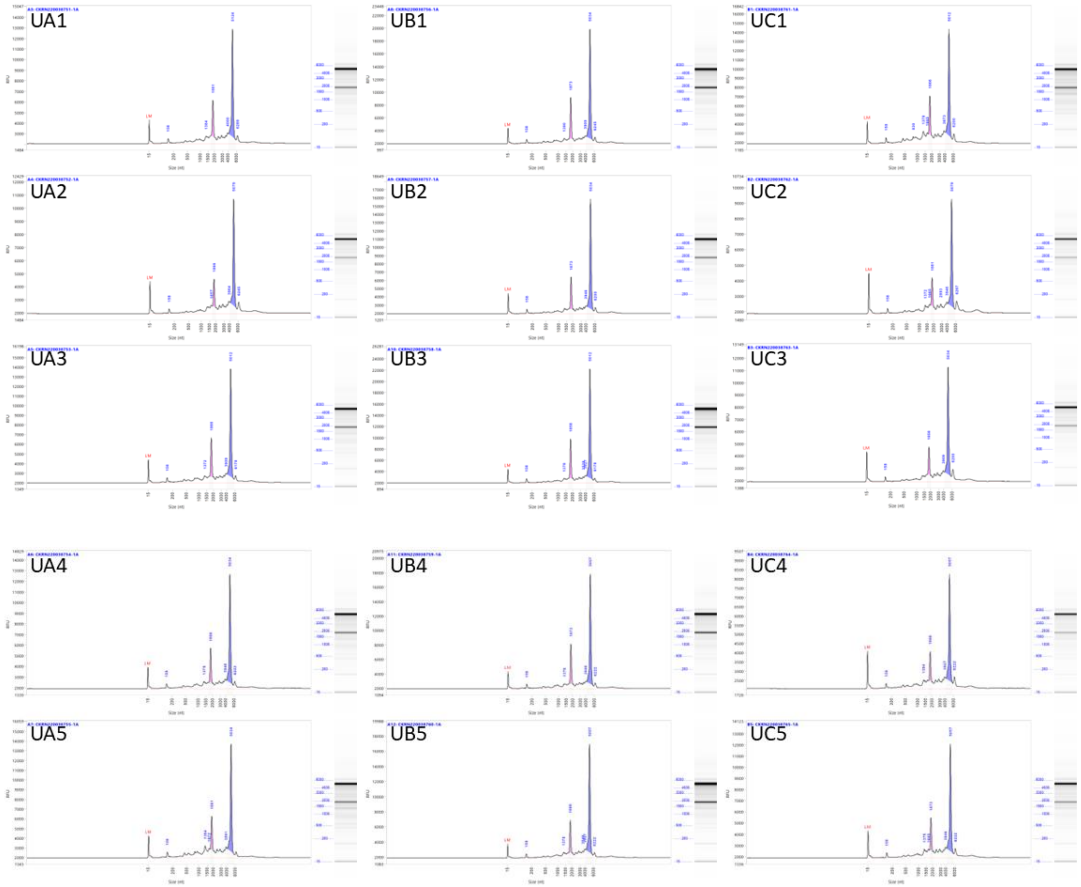

RAW 264.7 cells

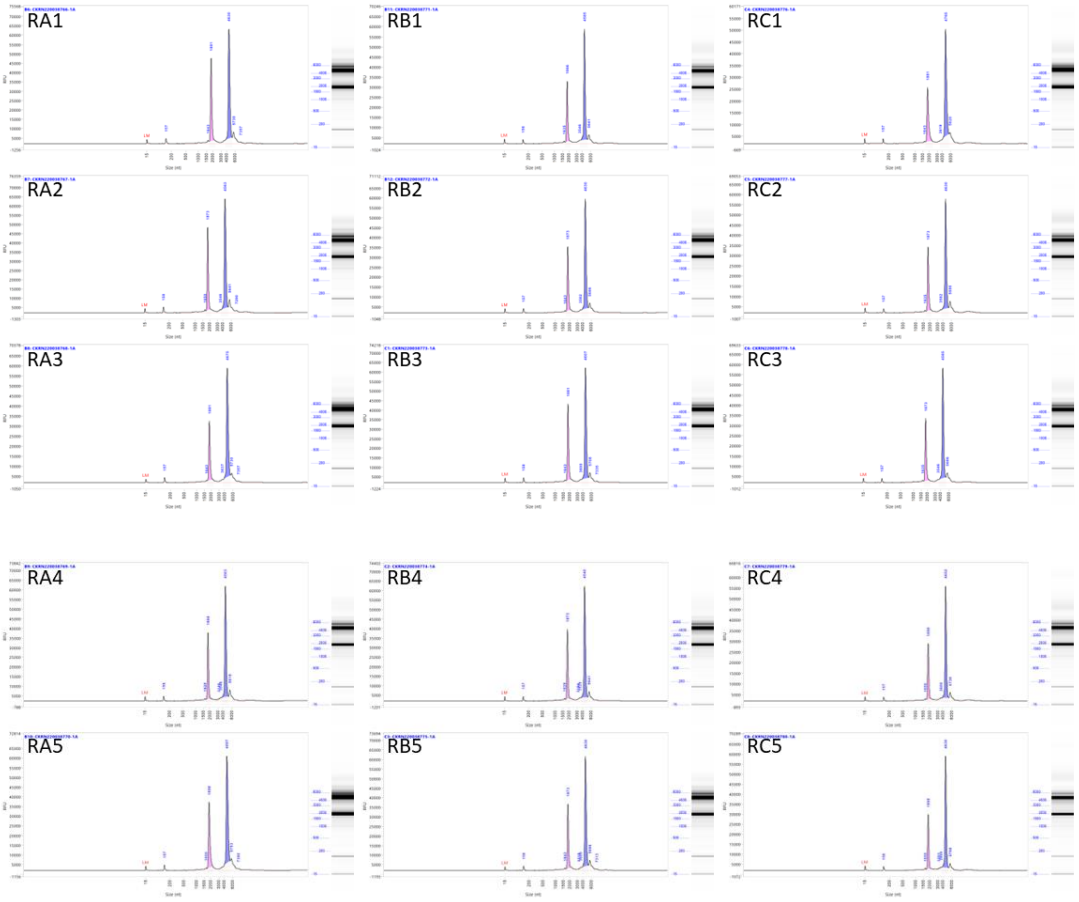

Figure S3. Initial QC analysis sent by Novogene. It includes bioanalyzer data for sample QC prior to sequencing. R = RAW 264.7 cells and U = U937 cells. A, B, and C refer to biological replicates 1, 2, and 3. Individual numbers 1-5 refer to the various treatments. 1 = untreated, 2 = 0.1 % (v/v) DMSO*, 3 = 10 μM dexamethasone*, 4 = 100 μM AT5*, 5 = 100 μM AT111*. For example, UA1 means "U937 biological replicate 1 untreated." *Pretreated for 4 h with reagent listed then cotreated for 4 additional hours with 1 μg/mL LPS. Untreated samples were treated with medium for 4 h then the medium was refreshed prior to the remaining 4 h. RNA was extracted as previously described and quantified prior to sending to Novogene using a nanodrop.

Table S1. Quality control analysis table determined by Novogene as described in Figure S3 (Appendix IV). RNA integrity number (RIN) is on a scale from 1 – 10 where 1 is totally degraded and 10 is the highest quality[500].

No.	Sample Name	Nucleic Acid ID	Concentration (ng/μL)	Volume (μl)	Total amount (μg)	RIN	Sample QC Results
1	UA1	CKRN220038751-1A	96.73	31	3.00	8.8	Pass
2	UA2	CKRN220038752-1A	70.42	33	2.32	9.1	Pass
3	UA3	CKRN220038753-1A	98.58	29	2.86	8.5	Pass
4	UA4	CKRN220038754-1A	100.29	32	3.21	8.7	Pass
5	UA5	CKRN220038755-1A	112.58	30	3.38	7.9	Pass
6	UB1	CKRN220038756-1A	128.91	30	3.87	9	Pass
7	UB2	CKRN220038757-1A	89.39	29	2.59	9.3	Pass
8	UB3	CKRN220038758-1A	131.95	30	3.96	9.4	Pass
9	UB4	CKRN220038759-1A	112.65	32	3.60	9.1	Pass
10	UB5	CKRN220038760-1A	134.93	31	4.18	9.4	Pass
11	UC1	CKRN220038761-1A	125.54	31	3.89	8	Pass
12	UC2	CKRN220038762-1A	59.27	31	1.84	9	Pass
13	UC3	CKRN220038763-1A	72.00	29	2.09	9.4	Pass
14	UC4	CKRN220038764-1A	65.12	33	2.15	8.6	Pass
15	UC5	CKRN220038765-1A	83.64	32	2.68	8.8	Pass
16	RA1	CKRN220038766-1A	454.66	30	13.64	10	Pass
17	RA2	CKRN220038767-1A	459.29	30	13.78	10	Pass
18	RA3	CKRN220038768-1A	471.90	31	14.63	10	Pass
19	RA4	CKRN220038769-1A	341.65	31	10.59	10	Pass
20	RA5	CKRN220038770-1A	455.74	31	14.13	10	Pass
21	RB1	CKRN220038771-1A	341.12	30	10.23	10	Pass
22	RB2	CKRN220038772-1A	396.53	30	11.90	10	Pass
23	RB3	CKRN220038773-1A	396.61	28	11.11	10	Pass

24	RB4	CKRN220038774-1A	362.44	31	11.24	10	Pass
25	RB5	CKRN220038775-1A	417.69	31	12.95	10	Pass
26	RC1	CKRN220038776-1A	375.39	31	11.64	10	Pass
27	RC2	CKRN220038777-1A	339.08	27	9.16	10	Pass
28	RC3	CKRN220038778-1A	376.46	29	10.92	10	Pass
29	RC4	CKRN220038779-1A	337.32	32	10.79	10	Pass
30	RC5	CKRN220038780-1A	287.04	29	8.32	10	Pass

Table S2. Quality control analysis post sequencing from Novogene as described in Figure S3 (Appendix IV). Headers are described by Novogene as follows: Sample. Raw reads are the total amount of paired end (PE) reads of raw data, equal to the amount of read 1 and read 2. Raw data: number of raw reads times 150 (sequence length) in G. Effective: percent showing the number of clean reads divided by the number of raw reads. Error is the base error rate (%). Q20 and Q30 values are the base count of Phred value > 20 or 30 (Q_{phred}) / Total base count. Q_{phred} is the base quality value for a given error rate (e) where $Q_{phred} = -10\log_{10}(e)$. GC: G and C bases / total bases.

Sample	Raw reads	Raw data	Effective(%)	Error(%)	Q20(%)	Q30(%)	GC(%)
RA3	81761406	12.3	98.29	0.03	97.94	94.22	49.81
RA4	78606582	11.8	98.12	0.02	97.96	94.28	48.61
RA5	89484958	13.4	98.56	0.02	98.04	94.41	49.68
RB2	88434930	13.3	98.51	0.03	97.92	94.17	49.56
RB3	90846584	13.6	98.62	0.03	97.90	94.07	49.41
RB4	74595348	11.2	98.38	0.02	98.00	94.38	49.14
RB5	85995876	12.9	97.60	0.02	98.05	94.46	49.71
RC1	80582796	12.1	98.08	0.02	98.08	94.55	49.53
RC3	77725466	11.7	98.23	0.02	98.03	94.42	49.24
RC4	82221716	12.3	98.12	0.02	97.99	94.31	48.75
RC5	68861826	10.3	98.44	0.02	98.14	94.70	49.39
UA2	97461628	14.6	97.45	0.03	97.85	94.07	49.32
UA3	91877910	13.8	97.90	0.03	97.73	93.81	49.86
UA4	115256538	17.3	98.32	0.03	97.89	94.17	49.49
UA5	88172208	13.2	96.26	0.02	98.06	94.52	50.14
UB1	88963490	13.3	98.56	0.03	97.92	94.26	49.89
UB2	81622062	12.2	97.78	0.02	98.00	94.31	48.04
UB3	83636830	12.5	96.35	0.03	97.89	94.16	49.53
UB4	96990878	14.5	96.80	0.03	97.88	93.93	50.21
UB5	98994824	14.8	98.53	0.03	97.84	94.03	50.61
UC1	92328008	13.8	98.45	0.03	97.91	94.23	50.42
UC2	75597274	11.3	97.65	0.03	97.89	94.14	47.94
UC3	108952392	16.3	97.97	0.03	97.85	94.11	50.48
UC4	93998216	14.1	98.05	0.02	97.93	94.30	49.67
UC5	90490134	13.6	97.58	0.03	97.85	94.10	49.98
RA1	83774984	12.6	98.07	0.03	97.91	94.11	48.99
RA2	74419054	11.2	98.13	0.02	98.02	94.37	49.54
RB1	82153206	12.3	98.85	0.03	97.34	92.57	49.58
RC2	101458222	15.2	96.43	0.03	97.53	92.98	47.98
UA1	109765414	16.5	98.12	0.03	97.10	92.17	50.47

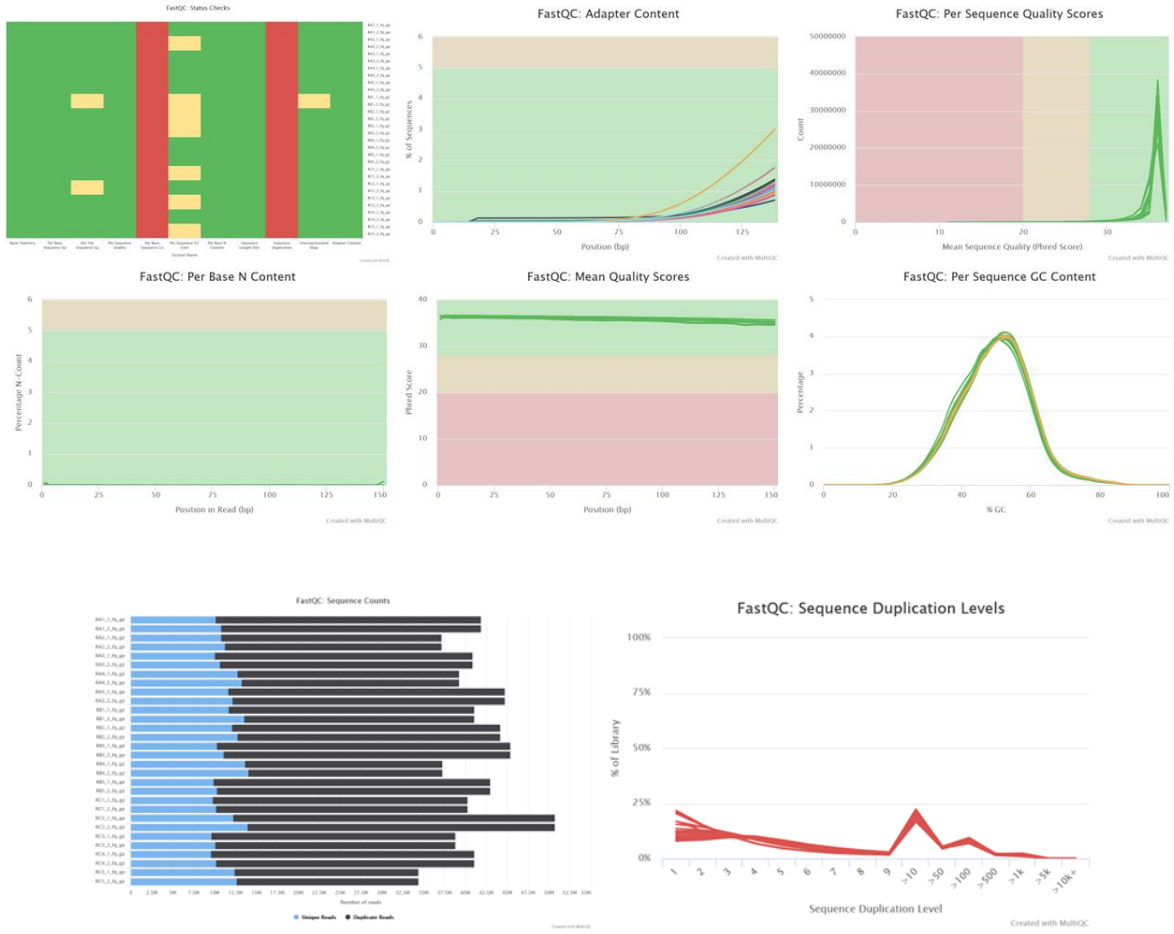

Figure S4. MultiQC analysis on raw data for RAW 264.7 cells. RAW 264.7 RNA sequencing MultiQC analysis output analyzing the FastQC output files for each treatment both fwd and rev. Labels are described in Figure S3 (Appendix IV).

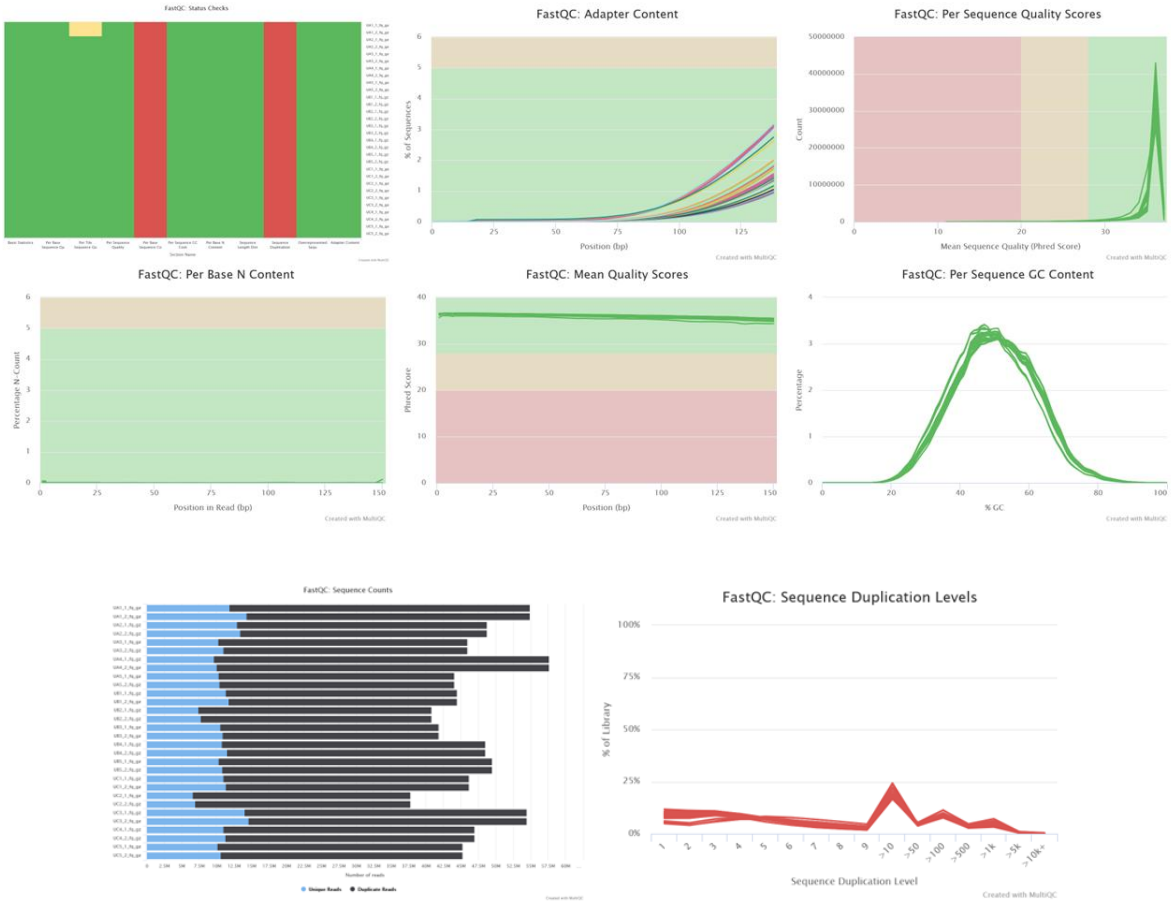

Figure S5. MultiQC analysis on raw data for U937 cells. U937 RNA sequencing MultiQC analysis output analyzing the FastQC output files for each raw fasta file for treatment both fwd and rev. Labels are described in Figure S3 (Appendix IV).

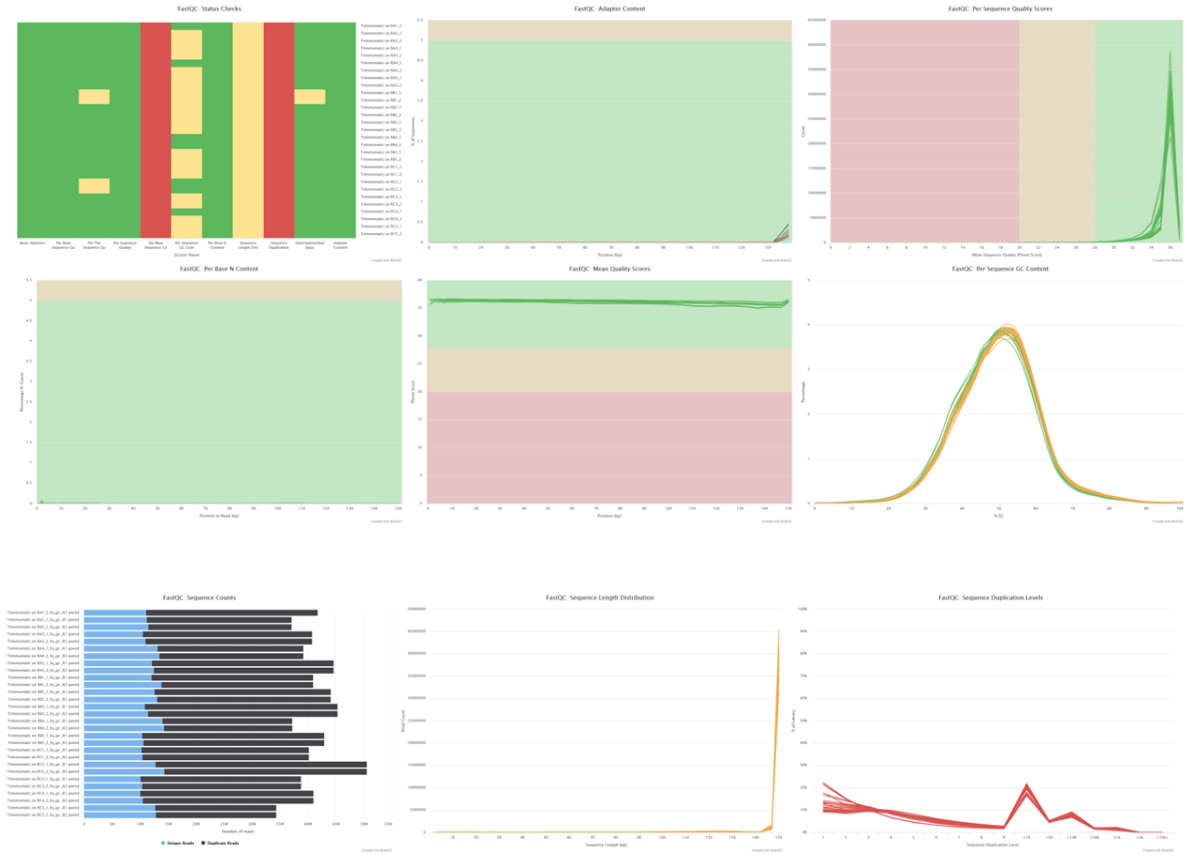

Figure S6. MultiQC analysis on the trimmed reads for RAW 264.7 cells. RAW 264.7 RNA sequencing MultiQC analysis output analyzing the FastQC output files for each Trimmomatic output file for treatment both fwd and rev. This is the quality control step for the trimmed reads. Labels are described in Figure S3 (Appendix IV).

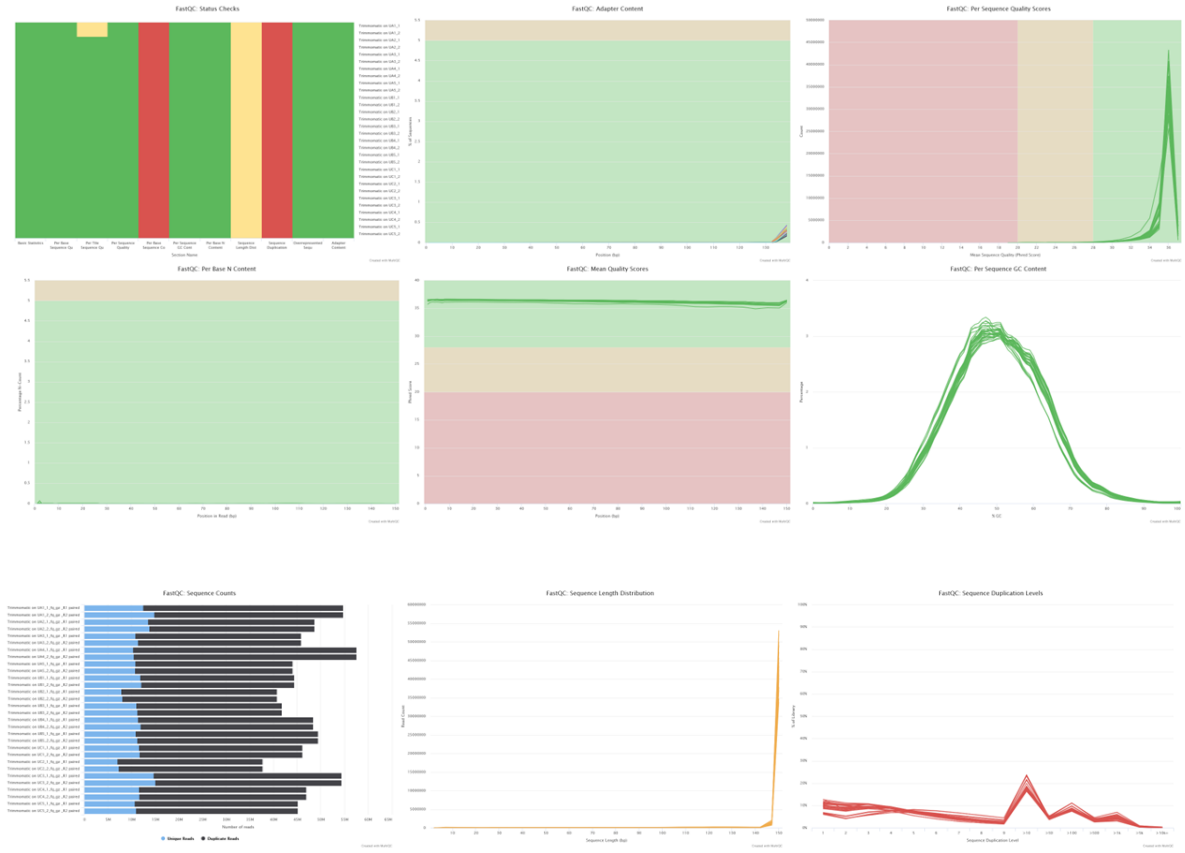

Figure S7. MultiQC analysis on the trimmed reads for U937 cells. U937 RNA sequencing MultiQC analysis output analyzing the FastQC output files for each Trimmomatic output file for treatment both fwd and rev. This is the quality control step for the trimmed reads. Labels are described in Figure S3 (Appendix IV).

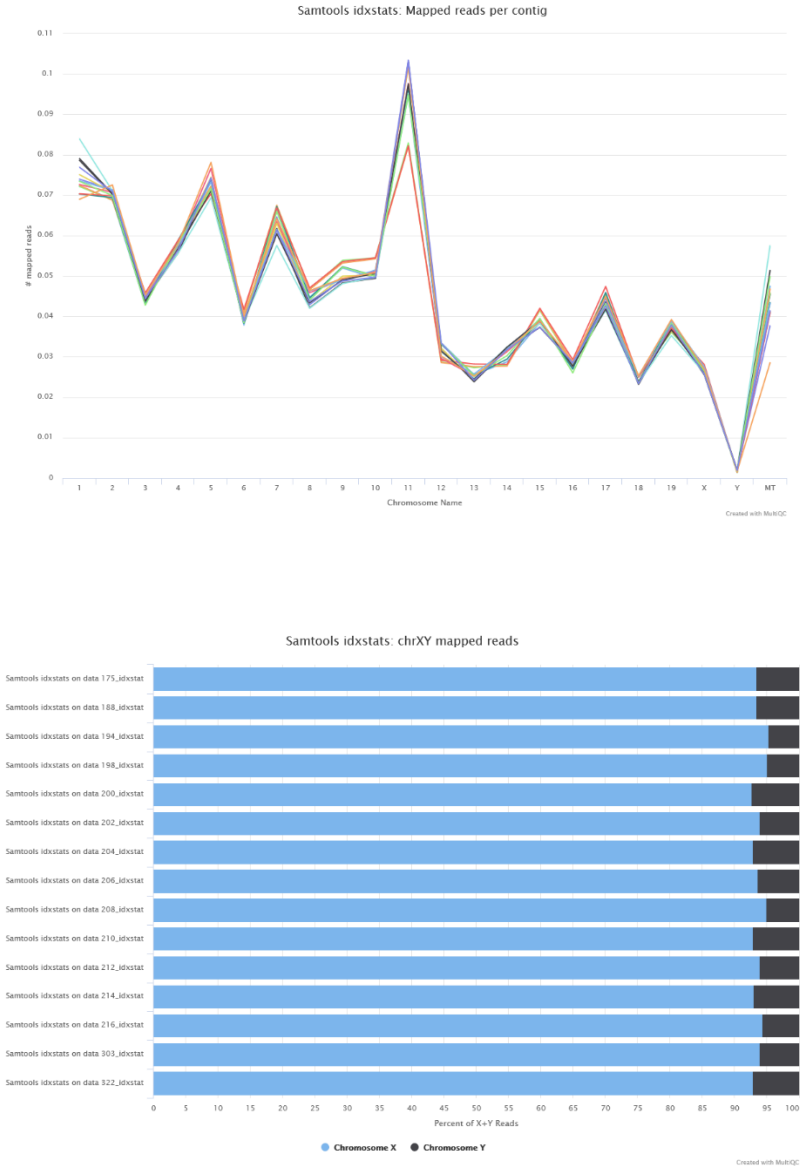

Figure S8. Chromosomal distribution of transcripts for RAW 264.7 cells. RAW 264.7 RNA sequencing MultiQC analysis output analyzing chromosomal distribution of the assembled transcripts (StringTie) aligned to the murine genome (HISAT2) using the Samtools output files for each treatment. This is the quality control step for both transcript assembly and genome alignment. Labels are described in Figure S3 (Appendix IV).

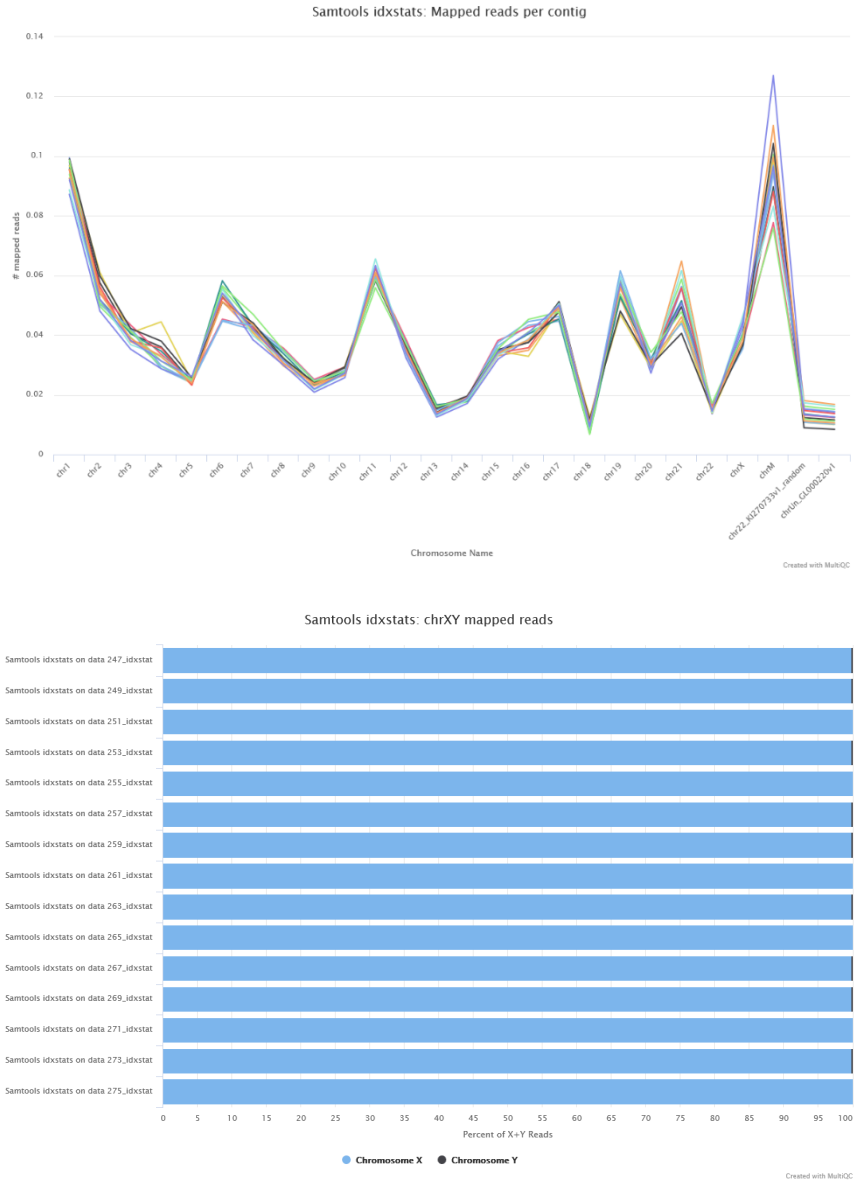

Figure S9. Chromosomal distribution of transcripts for U937 cells. U937 RNA sequencing MultiQC analysis output analyzing chromosomal distribution of the assembled transcripts (StringTie) aligned to the murine genome (HISAT2) using the Samtools output files for each treatment. This is the quality control step for both transcript assembly and genome alignment. Labels are described in Figure S3 (Appendix IV).

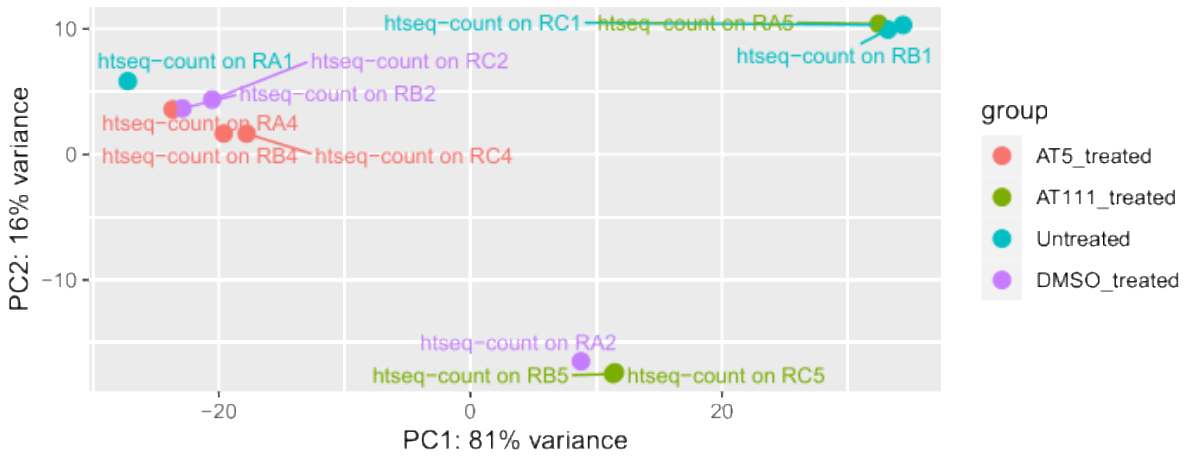

Figure S10. Full PCA analysis of RNA sequencing replicates for RAW 264.7 cells. PCA analysis was done using the DEseq2 tool on the use galaxy server as described in the methods. Naming conventions are described in Figure S3 (Appendix IV).

References

1 Bryant, D. L., Kafle, A., Handy, S. T., Farone, A. L. & Miller, J. M. Aurone-derived 1,2,3-triazoles as potential fluorescence molecules in vitro. *RSC Advances* **12**, 22639-22649, doi:10.1039/D2RA02578G (2022).

2 Uivarosi, V., Munteanu, A.-C. & Nițulescu, G. M. in *Studies in Natural Products Chemistry* Vol. 60 (ed Rahman Atta ur) Ch. 2, 29-84 (Elsevier, 2019).

3 Panche, A. N., Diwan, A. D. & Chandra, S. R. Flavonoids: an overview. *Journal of Nutritional Science* **5**, e47, doi:10.1017/jns.2016.41 (2016).

4 Cushnie, T. P. & Lamb, A. J. Antimicrobial activity of flavonoids. *Int J Antimicrob Agents* **26**, 343-356, doi:10.1016/j.ijantimicag.2005.09.002 (2005).

5 Abotaleb, M. *et al.* Flavonoids in Cancer and Apoptosis. *Cancers* **11**, doi:10.3390/cancers11010028 (2019).

6 Ferrándiz, M. L. & Alcaraz, M. J. Anti-inflammatory activity and inhibition of arachidonic acid metabolism by flavonoids. *Agents and Actions* **32**, 283-288, doi:10.1007/BF01980887 (1991).

7 Kang, S. R. *et al.* Anti-inflammatory effect of flavonoids isolated from Korea Citrus aurantium L. on lipopolysaccharide-induced mouse macrophage RAW 264.7 cells by blocking of nuclear factor-kappa B (NF-κB) and mitogen-activated protein kinase (MAPK) signalling pathways. *Food Chemistry* **129**, 1721-1728, doi:https://doi.org/10.1016/j.foodchem.2011.06.039 (2011).

8 Serafini, M., Peluso, I. & Raguzzini, A. Flavonoids as anti-inflammatory agents. *Proceedings of the Nutrition Society* **69**, 273-278, doi:10.1017/S002966511000162X (2010).

9 Zaragozá, C., Villaescusa, L., Monserrat, J., Zaragozá, F. & Álvarez-Mon, M. Potential Therapeutic Anti-Inflammatory and Immunomodulatory Effects of Dihydroflavones, Flavones, and Flavonols. *Molecules* **25**, doi:10.3390/molecules25041017 (2020).

10 Pietta, P.-G. Flavonoids as Antioxidants. *Journal of Natural Products* **63**, 1035-1042, doi:10.1021/np9904509 (2000).

11 Jiang, W. *et al.* Quercetin suppresses NLRP3 inflammasome activation and attenuates histopathology in a rat model of spinal cord injury. *Spinal Cord* **54**, 592-596, doi:10.1038/sc.2015.227 (2016).

12 Domiciano, T. P. *et al.* Quercetin Inhibits Inflammasome Activation by Interfering with ASC Oligomerization and Prevents Interleukin-1 Mediated Mouse Vasculitis. *Sci Rep* **7**, 41539-41539, doi:10.1038/srep41539 (2017).

13 David, A. V. A., Arulmoli, R. & Parasuraman, S. Overviews of biological importance of quercetin: A bioactive flavonoid. *Pharmacognosy reviews* **10**, 84 (2016).

14 Zhang, X., Wang, G., Gurley, E. C. & Zhou, H. Flavonoid Apigenin Inhibits Lipopolysaccharide-Induced Inflammatory Response through Multiple Mechanisms in Macrophages. *PLoS One* **9**, e107072, doi:10.1371/journal.pone.0107072 (2014).

15 Nicholas, C. *et al.* Apigenin Blocks Lipopolysaccharide-Induced Lethality In Vivo and Proinflammatory Cytokines Expression by Inactivating NF-κB through the Suppression of p65 Phosphorylation. *The Journal of Immunology* **179**, 7121-7127, doi:10.4049/jimmunol.179.10.7121 (2007).

16 Madunić, J., Madunić, I. V., Gajski, G., Popić, J. & Garaj-Vrhovac, V. Apigenin: A dietary flavonoid with diverse anticancer properties. *Cancer Letters* **413**, 11-22, doi:https://doi.org/10.1016/j.canlet.2017.10.041 (2018).

17 DeRango-Adem, E. F. & Blay, J. Does Oral Apigenin Have Real Potential for a Therapeutic Effect in the Context of Human Gastrointestinal and Other Cancers? *Frontiers in Pharmacology* **12**, doi:10.3389/fphar.2021.681477 (2021).

18 Kashyap, P., Shikha, D., Thakur, M. & Aneja, A. Functionality of apigenin as a potent antioxidant with emphasis on bioavailability, metabolism, action mechanism and in vitro and in vivo studies: A review. *Journal of Food Biochemistry* **46**, e13950, doi:https://doi.org/10.1111/jfbc.13950 (2022).

19 Khandelwal, N. *et al.* Antiviral activity of Apigenin against buffalopox: Novel mechanistic insights and drug-resistance considerations. *Antiviral Research* **181**, 104870, doi:https://doi.org/10.1016/j.antiviral.2020.104870 (2020).

20 Qian, S. *et al.* Apigenin Restricts FMDV Infection and Inhibits Viral IRES Driven Translational Activity. *Viruses* **7**, 1613-1626 (2015).

21 Morimoto, Y., Baba, T., Sasaki, T. & Hiramatsu, K. Apigenin as an anti-quinolone-resistance antibiotic. *Int J Antimicrob Agents* **46**, 666-673, doi:https://doi.org/10.1016/j.ijantimicag.2015.09.006 (2015).

22 McDonald, L. *et al.* Fluorescent flavonoids for endoplasmic reticulum cell imaging. *Journal of Materials Chemistry B* **4**, 7902-7908, doi:10.1039/C6TB02456D (2016).

23 Klymchenko, A. S., Duportail, G., Mély, Y. & Demchenko, A. P. Ultrasensitive two-color fluorescence probes for dipole potential in phospholipid membranes. *Proceedings of the National Academy of Sciences* **100**, 11219-11224, doi:doi:10.1073/pnas.1934603100 (2003).

24 Mazziotti, I., Petrarolo, G. & La Motta, C. Aurones: A Golden Resource for Active Compounds. *Molecules (Basel, Switzerland)* **27**, 2, doi:10.3390/molecules27010002 (2021).

25 Zwergel, C. *et al.* Aurones: Interesting Natural and Synthetic Compounds with Emerging Biological Potential. *Natural Product Communications* **7**, doi:10.1177/1934578x1200700322 (2012).

26 Sui, G. *et al.* Recent advances on synthesis and biological activities of aurones. *Bioorganic & Medicinal Chemistry* **29**, 115895, doi:https://doi.org/10.1016/j.bmc.2020.115895 (2021).

27 Asen, S., Norris, K. H. & Stewart, R. N. Copigmentation of aurone and flavone from petals of Antirrhinum majus. *Phytochemistry* **11**, 2739-2741, doi:https://doi.org/10.1016/S0031-9422(00)86505-X (1972).

28 Harborne, J. B. Comparative biochemistry of the flavonoids-VI.: Flavonoid patterns in the bignoniaceae and the gesneriaceae. *Phytochemistry* **6**, 1643-1651, doi:https://doi.org/10.1016/S0031-9422(00)82897-6 (1967).

29 Harborne, J. B. & Smith, D. M. Anthochlors and other flavonoids as honey guides in the compositae. *Biochemical Systematics and Ecology* **6**, 287-291, doi:https://doi.org/10.1016/0305-1978(78)90047-9 (1978).

30 Alsayari, A. *et al.* Aurone: A biologically attractive scaffold as anticancer agent. *European Journal of Medicinal Chemistry* **166**, 417-431, doi:https://doi.org/10.1016/j.ejmech.2019.01.078 (2019).

31 Cheng, H. *et al.* Design, synthesis and discovery of 5-hydroxyaurone derivatives as growth inhibitors against HUVEC and some cancer cell lines. *European Journal of Medicinal Chemistry* **45**, 5950-5957, doi:https://doi.org/10.1016/j.ejmech.2010.09.061 (2010).

32 Alsaif, G. *et al.* Evaluation of Fourteen Aurone Derivatives as Potential Anti-Cancer Agents. *Current Pharmaceutical Biotechnology* **18**, 384-390, doi:http://dx.doi.org/10.2174/1389201018666170502112303 (2017).

33 Sim, H.-M., Wu, C.-P., Ambudkar, S. V. & Go, M.-L. In vitro and in vivo modulation of ABCG2 by functionalized aurones and structurally related analogs. *Biochemical pharmacology* **82**, 1562-1571, doi:10.1016/j.bcp.2011.08.002 (2011).

34 Sim, H. M., Loh, K. Y., Yeo, W. K., Lee, C. Y. & Go, M. L. Aurones as Modulators of ABCG2 and ABCB1: Synthesis and Structure–Activity Relationships. *ChemMedChem* **6**, 713-724, doi:https://doi.org/10.1002/cmdc.201000520 (2011).

35 Sim, H.-M., Lee, C.-Y., Ee, P. L. R. & Go, M.-L. Dimethoxyaurones: Potent inhibitors of ABCG2 (breast cancer resistance protein). *European Journal of Pharmaceutical Sciences* **35**, 293-306, doi:https://doi.org/10.1016/j.ejps.2008.07.008 (2008).

36 Boumendjel, A. *et al.* 4-Hydroxy-6-methoxyaurones with High-Affinity Binding to Cytosolic Domain of P-Glycoprotein. *Chemical and Pharmaceutical Bulletin* **50**, 854-856, doi:10.1248/cpb.50.854 (2002).

37 Bandgar, B. P. *et al.* Synthesis and biological evaluation of a novel series of 2,2-bisaminomethylated aurone analogues as anti-inflammatory and antimicrobial agents. *European Journal of Medicinal Chemistry* **45**, 3223-3227, doi:https://doi.org/10.1016/j.ejmech.2010.03.045 (2010).

38 Olleik, H. *et al.* Aurone derivatives as promising antibacterial agents against resistant Gram-positive pathogens. *European Journal of Medicinal Chemistry* **165**, 133-141, doi:https://doi.org/10.1016/j.ejmech.2019.01.022 (2019).

39 Alqahtani, F. M. *et al.* Chemogenomic profiling to understand the antifungal action of a bioactive aurone compound. *PLoS One* **14**, e0226068, doi:10.1371/journal.pone.0226068 (2019).

40 Sutton, C. L., Taylor, Z. E., Farone, M. B. & Handy, S. T. Antifungal activity of substituted aurones. *Bioorganic & Medicinal Chemistry Letters* **27**, 901-903, doi:https://doi.org/10.1016/j.bmcl.2017.01.012 (2017).

41 Haudecoeur, R. *et al.* Discovery of Naturally Occurring Aurones That Are Potent Allosteric Inhibitors of Hepatitis C Virus RNA-Dependent RNA Polymerase. *Journal of Medicinal Chemistry* **54**, 5395-5402, doi:10.1021/jm200242p (2011).

42 Meguellati, A. *et al.* B-ring modified aurones as promising allosteric inhibitors of hepatitis C virus RNA-dependent RNA polymerase. *European Journal of Medicinal Chemistry* **80**, 579-592, doi:https://doi.org/10.1016/j.ejmech.2014.04.005 (2014).

43 Malbari, K. D. *et al.* Structure-aided drug development of potential neuraminidase inhibitors against pandemic H1N1 exploring alternate binding mechanism. *Molecular Diversity* **23**, 927-951, doi:10.1007/s11030-019-09919-6 (2019).

44 McAuley, J. L., Gilbertson, B. P., Trifkovic, S., Brown, L. E. & McKimm-Breschkin, J. L. Influenza Virus Neuraminidase Structure and Functions. *Front Microbiol* **10**, 39, doi:10.3389/fmicb.2019.00039 (2019).

45 Chintakrindi, A. S., Gohil, D. J., Chowdhary, A. S. & Kanyalkar, M. A. Design, synthesis and biological evaluation of substituted flavones and aurones as potential anti-influenza agents. *Bioorganic & Medicinal Chemistry* **28**, 115191, doi:https://doi.org/10.1016/j.bmc.2019.115191 (2020).

46 More, G. K. & Makola, R. T. In-vitro analysis of free radical scavenging activities and suppression of LPS-induced ROS production in macrophage cells by Solanum sisymbriifolium extracts. *Sci Rep* **10**, 6493, doi:10.1038/s41598-020-63491-w (2020).
47 Arango Duque, G. & Descoteaux, A. Macrophage Cytokines: Involvement in Immunity and Infectious Diseases. *Frontiers in Immunology* **5**, doi:10.3389/fimmu.2014.00491 (2014).
48 Turvey, S. E. & Broide, D. H. Innate immunity. *J Allergy Clin Immunol* **125**, S24-S32, doi:10.1016/j.jaci.2009.07.016 (2010).
49 Agard, M., Asakrah, S. & Morici, L. PGE2 suppression of innate immunity during mucosal bacterial infection. *Frontiers in Cellular and Infection Microbiology* **3**, doi:10.3389/fcimb.2013.00045 (2013).
50 Ricciotti, E. & FitzGerald, G. A. Prostaglandins and Inflammation. *Arteriosclerosis, Thrombosis, and Vascular Biology* **31**, 986-1000, doi:doi:10.1161/ATVBAHA.110.207449 (2011).
51 Firestein, G. S. & McInnes, I. B. Immunopathogenesis of Rheumatoid Arthritis. *Immunity* **46**, 183-196, doi:https://doi.org/10.1016/j.immuni.2017.02.006 (2017).
52 Neurath, M. F. Targeting immune cell circuits and trafficking in inflammatory bowel disease. *Nature Immunology* **20**, 970-979, doi:10.1038/s41590-019-0415-0 (2019).
53 Ramamoorthy, S. & Cidlowski, J. A. Corticosteroids: Mechanisms of Action in Health and Disease. *Rheum Dis Clin North Am* **42**, 15-31, vii, doi:10.1016/j.rdc.2015.08.002 (2016).
54 Hardy, R. S., Raza, K. & Cooper, M. S. Therapeutic glucocorticoids: mechanisms of actions in rheumatic diseases. *Nature Reviews Rheumatology* **16**, 133-144, doi:10.1038/s41584-020-0371-y (2020).
55 Barnes, P. J. Mechanisms and resistance in glucocorticoid control of inflammation. *The Journal of Steroid Biochemistry and Molecular Biology* **120**, 76-85, doi:https://doi.org/10.1016/j.jsbmb.2010.02.018 (2010).
56 De Bosscher, K. *et al.* Glucocorticoids repress NF-κB-driven genes by disturbing the interaction of p65 with the basal transcription machinery, irrespective of coactivator levels in the cell. *Proceedings of the National Academy of Sciences* **97**, 3919-3924, doi:doi:10.1073/pnas.97.8.3919 (2000).
57 Nelson, G. *et al.* NF-κB signalling is inhibited by glucocorticoid receptor and STAT6 via distinct mechanisms. *Journal of Cell Science* **116**, 2495-2503, doi:10.1242/jcs.00461 (2003).
58 Quatrini, L. & Ugolini, S. New insights into the cell- and tissue-specificity of glucocorticoid actions. *Cellular & Molecular Immunology* **18**, 269-278, doi:10.1038/s41423-020-00526-2 (2021).
59 Widén, C., Gustafsson, J.-Å. & Wikström, A.-C. Cytosolic glucocorticoid receptor interaction with nuclear factor-kappaB proteins in rat liver cells. *Biochemical Journal* **373**, 211-220, doi:10.1042/bj20030175 (2003).
60 Schäcke, H., Döcke, W.-D. & Asadullah, K. Mechanisms involved in the side effects of glucocorticoids. *Pharmacology & Therapeutics* **96**, 23-43, doi:https://doi.org/10.1016/S0163-7258(02)00297-8 (2002).
61 Vane, J. R. & Botting, R. M. Anti-inflammatory drugs and their mechanism of action. *Inflammation Research* **47**, 78-87, doi:10.1007/s000110050284 (1998).
62 Park, J. Y., Pillinger, M. H. & Abramson, S. B. Prostaglandin E2 synthesis and secretion: The role of PGE2 synthases. *Clinical Immunology* **119**, 229-240, doi:https://doi.org/10.1016/j.clim.2006.01.016 (2006).

63 Liu, X., Moon, S. H., Jenkins, C. M., Sims, H. F. & Gross, R. W. Cyclooxygenase-2 Mediated Oxidation of 2-Arachidonoyl-Lysophospholipids Identifies Unknown Lipid Signaling Pathways. *Cell Chem Biol* **23**, 1217-1227, doi:10.1016/j.chembiol.2016.08.009 (2016).

64 Tsuge, K., Inazumi, T., Shimamoto, A. & Sugimoto, Y. Molecular mechanisms underlying prostaglandin E2-exacerbated inflammation and immune diseases. *International Immunology* **31**, 597-606, doi:10.1093/intimm/dxz021 (2019).

65 Domingo, C., Palomares, O., Sandham, D. A., Erpenbeck, V. J. & Altman, P. The prostaglandin D2 receptor 2 pathway in asthma: a key player in airway inflammation. *Respiratory Research* **19**, 189, doi:10.1186/s12931-018-0893-x (2018).

66 Echizen, K., Hirose, O., Maeda, Y. & Oshima, M. Inflammation in gastric cancer: Interplay of the COX-2/prostaglandin E2 and Toll-like receptor/MyD88 pathways. *Cancer Science* **107**, 391-397, doi:https://doi.org/10.1111/cas.12901 (2016).

67 Jiang, J. & Dingledine, R. Prostaglandin receptor EP2 in the crosshairs of anti-inflammation, anti-cancer, and neuroprotection. *Trends in Pharmacological Sciences* **34**, 413-423, doi:https://doi.org/10.1016/j.tips.2013.05.003 (2013).

68 Kawahara, K., Hohjoh, H., Inazumi, T., Tsuchiya, S. & Sugimoto, Y. Prostaglandin E2-induced inflammation: Relevance of prostaglandin E receptors. *Biochimica et Biophysica Acta (BBA) - Molecular and Cell Biology of Lipids* **1851**, 414-421, doi:https://doi.org/10.1016/j.bbalip.2014.07.008 (2015).

69 Bindu, S., Mazumder, S. & Bandyopadhyay, U. Non-steroidal anti-inflammatory drugs (NSAIDs) and organ damage: A current perspective. *Biochemical Pharmacology* **180**, 114147, doi:https://doi.org/10.1016/j.bcp.2020.114147 (2020).

70 Fosslien, E. Adverse effects of nonsteroidal anti-inflammatory drugs on the gastrointestinal system. *Ann Clin Lab Sci* **28**, 67-81 (1998).

71 Moon, J. E., Kim, D.-M. & Kim, J. Y. Anti-inflammatory effect of Rhus verniciflua stokes extract in the murine macrophage cell line, Raw264.7. *Journal of the Korean Society for Applied Biological Chemistry* **58**, 481-486, doi:10.1007/s13765-015-0065-3 (2015).

72 Park, H. S. *et al.* Suppression of LPS-induced NF-κB activity in macrophages by the synthetic aurone, (Z)-2-((5-(hydroxymethyl) furan-2-yl) methylene) benzofuran-3(2H)-one. *International Immunopharmacology* **43**, 116-128, doi:https://doi.org/10.1016/j.intimp.2016.12.004 (2017).

73 Liu, T., Zhang, L., Joo, D. & Sun, S.-C. NF-κB signaling in inflammation. *Signal Transduction and Targeted Therapy* **2**, 17023, doi:10.1038/sigtrans.2017.23 (2017).

74 Wang, Z., Bae, E. J. & Han, Y. T. Synthesis and anti-inflammatory activities of novel dihydropyranoaurone derivatives. *Archives of Pharmacal Research* **40**, 695-703, doi:10.1007/s12272-017-0910-5 (2017).

75 Kim, H.-G. *et al.* Aurones and Flavonols from Coreopsis lanceolata L. Flowers and Their Anti-Oxidant, Pro-Inflammatory Inhibition Effects, and Recovery Effects on Alloxan-Induced Pancreatic Islets in Zebrafish. *Molecules* **26**, 6098 (2021).

76 Shanker, N., Dilek, O., Mukherjee, K., McGee, D. W. & Bane, S. L. Aurones: small molecule visible range fluorescent probes suitable for biomacromolecules. *J Fluoresc* **21**, 2173-2184, doi:10.1007/s10895-011-0919-y (2011).

77 Espinosa-Bustos, C. *et al.* Fluorescence properties of aurone derivatives: an experimental and theoretical study with some preliminary biological applications. *Photochemical & Photobiological Sciences* **16**, 1268-1276, doi:10.1039/C7PP00078B (2017).

78 Xue, Y. *et al.* Electronic structure and spectral properties of aurones as visible range fluorescent probes: a DFT/TDDFT study. *RSC Advances* **6**, 7002-7010, doi:10.1039/C5RA25733F (2016).
79 Ono, M. *et al.* Aurones serve as probes of β-amyloid plaques in Alzheimer's disease. *Biochemical and Biophysical Research Communications* **361**, 116-121, doi:https://doi.org/10.1016/j.bbrc.2007.06.162 (2007).
80 Reichardt, C. Solvatochromic Dyes as Solvent Polarity Indicators. *Chemical Reviews* **94**, 2319-2358, doi:10.1021/cr00032a005 (1994).
81 Muñoz-Becerra, K., Villegas-Escobar, N., Zúñiga-Loyola, C., Cortés-Arriagada, D. & Toro-Labbé, A. Substituent effects on the photophysical properties of amino-aurone-derivatives. *Molecular Physics* **117**, 1451-1458, doi:10.1080/00268976.2018.1559372 (2019).
82 Chen, H. *et al.* Three hydroxy aurone compounds as chemosensors for cyanide anions. *Spectrochimica Acta Part A: Molecular and Biomolecular Spectroscopy* **116**, 389-393, doi:https://doi.org/10.1016/j.saa.2013.07.041 (2013).
83 Chen, H. *et al.* Two new fluorescence turn-on chemosensors for cyanide based on dipyridylamine and aurone moiety. *Sensors and Actuators B: Chemical* **199**, 115-120, doi:https://doi.org/10.1016/j.snb.2014.03.106 (2014).
84 Xu, Y. *et al.* Synthesis and cyanide anion recognition of a new displacement fluorescence chemosensor based on two-branched aurone. *Fibers and Polymers* **17**, 181-185, doi:10.1007/s12221-016-5774-7 (2016).
85 Zhang, M. *et al.* An Aurone-derived Low-molecular-weight Fluorescence Probe for the Detection of Hg2+ in Aqueous Solution and Living Cells. *Journal of Heterocyclic Chemistry* **55**, 1130-1135, doi:https://doi.org/10.1002/jhet.3143 (2018).
86 Kafle, A., Bhattarai, S., Miller, J. M. & Handy, S. T. Hydrogen sulfide sensing using an aurone-based fluorescent probe. *RSC Advances* **10**, 45180-45188, doi:10.1039/D0RA08802A (2020).
87 Tomé, S. M., Soengas, R. G., Badía-Laíño, R. & Silva, A. M. S. Novel aurone-type compounds with an extended π-system: Synthesis and optical properties. *Dyes and Pigments* **205**, 110569, doi:https://doi.org/10.1016/j.dyepig.2022.110569 (2022).
88 Berdnikova, D. V., Steup, S., Bolte, M. & Suta, M. Design of Aurone-Based Dual-State Emissive (DSE) Fluorophores. *Chemistry – A European Journal* **29**, e202300356, doi:https://doi.org/10.1002/chem.202300356 (2023).
89 Belmonte-Vázquez, J. L., Amador-Sánchez, Y. A., Rodríguez-Cortés, L. A. & Rodríguez-Molina, B. Dual-State Emission (DSE) in Organic Fluorophores: Design and Applications. *Chemistry of Materials* **33**, 7160-7184, doi:10.1021/acs.chemmater.1c02460 (2021).
90 Bozorov, K., Zhao, J. & Aisa, H. A. 1,2,3-Triazole-containing hybrids as leads in medicinal chemistry: A recent overview. *Bioorganic & Medicinal Chemistry* **27**, 3511-3531, doi:https://doi.org/10.1016/j.bmc.2019.07.005 (2019).
91 Lal, K. & Yadav, P. Recent Advancements in 1,4-Disubstituted 1H-1,2,3-Triazoles as Potential Anticancer Agents. *Anti-Cancer Agents in Medicinal Chemistry* **18**, 21-37, doi:http://dx.doi.org/10.2174/1871520616666160811113531 (2018).
92 Kharb, R., Sharma, P. C. & Yar, M. S. Pharmacological significance of triazole scaffold. *Journal of Enzyme Inhibition and Medicinal Chemistry* **26**, 1-21, doi:10.3109/14756360903524304 (2011).
93 Rani, A. *et al.* CuAAC-ensembled 1,2,3-triazole-linked isosteres as pharmacophores in drug discovery: review. *RSC Advances* **10**, 5610-5635, doi:10.1039/C9RA09510A (2020).

94 Agalave, S. G., Maujan, S. R. & Pore, V. S. Click Chemistry: 1,2,3-Triazoles as Pharmacophores. *Chemistry – An Asian Journal* **6**, 2696-2718, doi:https://doi.org/10.1002/asia.201100432 (2011).

95 Li, W.-T., Wu, W.-H., Tang, C.-H., Tai, R. & Chen, S.-T. One-Pot Tandem Copper-Catalyzed Library Synthesis of 1-Thiazolyl-1,2,3-triazoles as Anticancer Agents. *ACS Combinatorial Science* **13**, 72-78, doi:10.1021/co1000234 (2011).

96 Kumbhare, R. M. *et al.* Synthesis and anticancer evaluation of novel triazole linked N-(pyrimidin-2-yl)benzo[d]thiazol-2-amine derivatives as inhibitors of cell survival proteins and inducers of apoptosis in MCF-7 breast cancer cells. *Bioorganic & Medicinal Chemistry Letters* **25**, 654-658, doi:https://doi.org/10.1016/j.bmcl.2014.11.083 (2015).

97 Yu, J.-L. *et al.* Synthesis and antitumor activity of novel 2',3'-dideoxy-2',3'-diethanethionucleosides bearing 1,2,3-triazole residues. *Bioorganic & Medicinal Chemistry Letters* **20**, 240-243, doi:https://doi.org/10.1016/j.bmcl.2009.10.127 (2010).

98 Ding, Y. *et al.* Copper(I) oxide nanoparticles catalyzed click chemistry based synthesis of melampomagnolide B-triazole conjugates and their anti-cancer activities. *European Journal of Medicinal Chemistry* **156**, 216-229, doi:https://doi.org/10.1016/j.ejmech.2018.06.058 (2018).

99 Reddy, V. G. *et al.* 4β-amidotriazole linked podophyllotoxin congeners: DNA topoisomerase-IIα inhibition and potential anticancer agents for prostate cancer. *European Journal of Medicinal Chemistry* **144**, 595-611, doi:https://doi.org/10.1016/j.ejmech.2017.12.050 (2018).

100 Valdomir, G. *et al.* Oxa/thiazole-tetrahydropyran triazole-linked hybrids with selective antiproliferative activity against human tumour cells. *New Journal of Chemistry* **42**, 13784-13789, doi:10.1039/C8NJ02388C (2018).

101 Abe, T. *et al.* Key role of CD36 in Toll-like receptor 2 signaling in cerebral ischemia. *Stroke* **41**, 898-904, doi:10.1161/STROKEAHA.109.572552 (2010).

102 Mishra, R. K., Potteti, H. R., Tamatam, C. R., Elangovan, I. & Reddy, S. P. c-Jun Is Required for Nuclear Factor-κB-Dependent, LPS-Stimulated Fos-Related Antigen-1 Transcription in Alveolar Macrophages. *Am J Respir Cell Mol Biol* **55**, 667-674, doi:10.1165/rcmb.2016-0028OC (2016).

103 Kant, R. *et al.* Synthesis of newer 1,2,3-triazole linked chalcone and flavone hybrid compounds and evaluation of their antimicrobial and cytotoxic activities. *European Journal of Medicinal Chemistry* **113**, 34-49, doi:https://doi.org/10.1016/j.ejmech.2016.02.041 (2016).

104 Aly, M. R. E. S., Saad, H. A. & Mohamed, M. A. M. Click reaction based synthesis, antimicrobial, and cytotoxic activities of new 1,2,3-triazoles. *Bioorganic & Medicinal Chemistry Letters* **25**, 2824-2830, doi:https://doi.org/10.1016/j.bmcl.2015.04.096 (2015).

105 Ruddarraju, R. R. *et al.* Design, synthesis, anticancer, antimicrobial activities and molecular docking studies of theophylline containing acetylenes and theophylline containing 1,2,3-triazoles with variant nucleoside derivatives. *European Journal of Medicinal Chemistry* **123**, 379-396, doi:https://doi.org/10.1016/j.ejmech.2016.07.024 (2016).

106 Jadhav, R. P., Raundal, H. N., Patil, A. A. & Bobade, V. D. Synthesis and biological evaluation of a series of 1,4-disubstituted 1,2,3-triazole derivatives as possible antimicrobial agents. *Journal of Saudi Chemical Society* **21**, 152-159, doi:https://doi.org/10.1016/j.jscs.2015.03.003 (2017).

107 Singh, H., Sindhu, J., Khurana, J. M., Sharma, C. & Aneja, K. R. Ultrasound promoted one pot synthesis of novel fluorescent triazolyl spirocyclic oxindoles using DBU based task specific ionic liquids and their antimicrobial activity. *European Journal of Medicinal Chemistry* **77**, 145-154, doi:https://doi.org/10.1016/j.ejmech.2014.03.016 (2014).

108 Garudachari, B., Isloor, A. M., Satyanarayana, M. N., Fun, H.-K. & Hegde, G. Click chemistry approach: Regioselective one-pot synthesis of some new 8-trifluoromethylquinoline based 1,2,3-triazoles as potent antimicrobial agents. *European Journal of Medicinal Chemistry* **74**, 324-332, doi:https://doi.org/10.1016/j.ejmech.2014.01.008 (2014).

109 Kushwaha, K., Kaushik, N., Lata & Jain, S. C. Design and synthesis of novel 2H-chromen-2-one derivatives bearing 1,2,3-triazole moiety as lead antimicrobials. *Bioorganic & Medicinal Chemistry Letters* **24**, 1795-1801, doi:https://doi.org/10.1016/j.bmcl.2014.02.027 (2014).

110 Nagender, P. *et al.* Synthesis, cytotoxicity, antimicrobial and anti-biofilm activities of novel pyrazolo[3,4-b]pyridine and pyrimidine functionalized 1,2,3-triazole derivatives. *Bioorganic & Medicinal Chemistry Letters* **24**, 2905-2908, doi:https://doi.org/10.1016/j.bmcl.2014.04.084 (2014).

111 Shaikh, M. H. *et al.* Synthesis, biological evaluation and molecular docking of novel coumarin incorporated triazoles as antitubercular, antioxidant and antimicrobial agents. *Medicinal Chemistry Research* **25**, 790-804, doi:10.1007/s00044-016-1519-9 (2016).

112 Tahghighi, A. *et al.* Synthesis and anti-leishmanial activity of 5-(5-nitrofuran-2-yl)-1,3,4-thiadiazol-2-amines containing N-[(1-benzyl-1H-1,2,3-triazol-4-yl)methyl] moieties. *European Journal of Medicinal Chemistry* **50**, 124-128, doi:https://doi.org/10.1016/j.ejmech.2012.01.046 (2012).

113 Gontijo, V. S. *et al.* Leishmanicidal, antiproteolytic, and mutagenic evaluation of alkyltriazoles and alkylphosphocholines. *European Journal of Medicinal Chemistry* **101**, 24-33, doi:https://doi.org/10.1016/j.ejmech.2015.06.005 (2015).

114 Patil, V. *et al.* Antimalarial and antileishmanial activities of histone deacetylase inhibitors with triazole-linked cap group. *Bioorganic & Medicinal Chemistry* **18**, 415-425, doi:https://doi.org/10.1016/j.bmc.2009.10.042 (2010).

115 Guimarães, T. T. *et al.* Potent naphthoquinones against antimony-sensitive and -resistant Leishmania parasites: Synthesis of novel α- and nor-α-lapachone-based 1,2,3-triazoles by copper-catalyzed azide–alkyne cycloaddition. *European Journal of Medicinal Chemistry* **63**, 523-530, doi:https://doi.org/10.1016/j.ejmech.2013.02.038 (2013).

116 Liu, Y. *et al.* Design, synthesis, and biological evaluation of new 1,2,3-triazolo-2′-deoxy-2′-fluoro- 4′-azido nucleoside derivatives as potent anti-HBV agents. *European Journal of Medicinal Chemistry* **143**, 137-149, doi:https://doi.org/10.1016/j.ejmech.2017.11.028 (2018).

117 Karypidou, K. *et al.* Synthesis, biological evaluation and molecular modeling of a novel series of fused 1,2,3-triazoles as potential anti-coronavirus agents. *Bioorganic & Medicinal Chemistry Letters* **28**, 3472-3476, doi:https://doi.org/10.1016/j.bmcl.2018.09.019 (2018).

118 Yan, L. *et al.* Synthesis of pentacyclic iminosugars with constrained butterfly-like conformation and their HIV-RT inhibitory activity. *Bioorganic & Medicinal Chemistry Letters* **28**, 425-428, doi:https://doi.org/10.1016/j.bmcl.2017.12.025 (2018).

119 Liu, M. *et al.* Design, synthesis, and structure-activity relationships of novel imidazo[4,5-c]pyridine derivatives as potent non-nucleoside inhibitors of hepatitis C virus NS5B. *Bioorganic & Medicinal Chemistry* **26**, 2621-2631, doi:https://doi.org/10.1016/j.bmc.2018.04.029 (2018).

120 Kaoukabi, H. *et al.* Dihydropyrimidinone/1,2,3-triazole hybrid molecules: Synthesis and anti-varicella-zoster virus (VZV) evaluation. *European Journal of Medicinal Chemistry* **155**, 772-781, doi:https://doi.org/10.1016/j.ejmech.2018.06.028 (2018).

121 Tian, Y. *et al.* Targeting the entrance channel of NNIBP: Discovery of diarylnicotinamide 1,4-disubstituted 1,2,3-triazoles as novel HIV-1 NNRTIs with high potency against wild-type and E138K mutant virus. *European Journal of Medicinal Chemistry* **151**, 339-350, doi:https://doi.org/10.1016/j.ejmech.2018.03.059 (2018).

122 Hammouda, M. B. *et al.* Design, synthesis, biological evaluation and in silico studies of novel 1,2,3-triazole linked benzoxazine-2,4-dione conjugates as potent antimicrobial, antioxidant and anti-inflammatory agents. *Arabian Journal of Chemistry* **15**, 104226, doi:https://doi.org/10.1016/j.arabjc.2022.104226 (2022).

123 Zheng, J. *et al.* Radezolid Is More Effective Than Linezolid Against Planktonic Cells and Inhibits Enterococcus faecalis Biofilm Formation. *Frontiers in Microbiology* **11**, doi:10.3389/fmicb.2020.00196 (2020).

124 Blackwell, C. C., Freimer, E. H. & Tuke, G. C. In vitro evaluation of the new oral cephalosporin cefatrizine: comparison with other cephalosporins. *Antimicrob Agents Chemother* **10**, 288-292, doi:10.1128/aac.10.2.288 (1976).

125 Schoonover, L. L., Occhipinti, D. J., Rodvold, K. A. & Danziger, L. H. Piperacillin/tazobactam: a new beta-lactam/beta-lactamase inhibitor combination. *Ann Pharmacother* **29**, 501-514, doi:10.1177/106002809502900510 (1995).

126 Wuest, F., Tang, X., Kniess, T., Pietzsch, J. & Suresh, M. Synthesis and cyclooxygenase inhibition of various (aryl-1,2,3-triazole-1-yl)-methanesulfonylphenyl derivatives. *Bioorganic & Medicinal Chemistry* **17**, 1146-1151, doi:https://doi.org/10.1016/j.bmc.2008.12.032 (2009).

127 Dewitt, D. L. & Meade, E. A. Serum and Glucocorticoid Regulation of Gene Transcription and Expression of the Prostaglandin H Synthase-1 and Prostaglandin H Synthase-2 Isozymes. *Archives of Biochemistry and Biophysics* **306**, 94-102, doi:https://doi.org/10.1006/abbi.1993.1485 (1993).

128 Smith, W. L., Garavito, R. M. & DeWitt, D. L. Prostaglandin Endoperoxide H Synthases (Cyclooxygenases)-1 and -2. *Journal of Biological Chemistry* **271**, 33157-33160, doi:10.1074/jbc.271.52.33157 (1996).

129 Moussa, G. *et al.* Novel click modifiable thioquinazolinones as anti-inflammatory agents: Design, synthesis, biological evaluation and docking study. *European Journal of Medicinal Chemistry* **144**, 635-650, doi:https://doi.org/10.1016/j.ejmech.2017.12.065 (2018).

130 Zhang, C., Li, N. & Niu, F. Baicalein triazole prevents respiratory tract infection by RSV through suppression of oxidative damage. *Microbial Pathogenesis* **131**, 227-233, doi:https://doi.org/10.1016/j.micpath.2019.03.026 (2019).

131 Kim, T. W. *et al.* Synthesis and biological evaluation of phenyl-1H-1,2,3-triazole derivatives as anti-inflammatory agents. *Bioorganic Chemistry* **59**, 1-11, doi:https://doi.org/10.1016/j.bioorg.2015.01.003 (2015).

132 Angajala, K. K. *et al.* Synthesis, anti-inflammatory, bactericidal activities and docking studies of novel 1,2,3-triazoles derived from ibuprofen using click chemistry. *SpringerPlus* **5**, 423, doi:10.1186/s40064-016-2052-5 (2016).

133 Assis, S. P., da Silva, M. T., de Oliveira, R. N. & Lima, V. L. Synthesis and anti-inflammatory activity of new alkyl-substituted phthalimide 1H-1,2,3-triazole derivatives. *ScientificWorldJournal* **2012**, 925925, doi:10.1100/2012/925925 (2012).

134 Naaz, F. *et al.* 1,2,3-triazole tethered Indole-3-glyoxamide derivatives as multiple inhibitors of 5-LOX, COX-2 & tubulin: Their anti-proliferative & anti-inflammatory activity. *Bioorganic Chemistry* **81**, 1-20, doi:https://doi.org/10.1016/j.bioorg.2018.07.029 (2018).

135 Yan, W. *et al.* N-2-Aryl-1,2,3-triazoles: A Novel Class of UV/Blue-Light-Emitting Fluorophores with Tunable Optical Properties. *Chemistry – A European Journal* **17**, 5011-5018, doi:https://doi.org/10.1002/chem.201002937 (2011).
136 Zhang, Y., Ye, X., Petersen, J. L., Li, M. & Shi, X. Synthesis and Characterization of Bis-N-2-Aryl Triazole as a Fluorophore. *The Journal of Organic Chemistry* **80**, 3664-3669, doi:10.1021/acs.joc.5b00006 (2015).
137 Zhang, Y.-C., Jin, R., Li, L.-Y., Chen, Z. & Fu, L.-M. Study on the Fluorescent Activity of N^2-Indolyl-1,2,3-triazole. *Molecules (Basel, Switzerland)* **22**, 1380, doi:10.3390/molecules22091380 (2017).
138 Berlier, J. E. *et al.* Quantitative Comparison of Long-wavelength Alexa Fluor Dyes to Cy Dyes: Fluorescence of the Dyes and Their Bioconjugates. *Journal of Histochemistry & Cytochemistry* **51**, 1699-1712, doi:10.1177/002215540305101214 (2003).
139 Huang, R. *et al.* Synthesis, characterization, and biological studies of emissive rhenium–glutamine conjugates. *JBIC Journal of Biological Inorganic Chemistry* **18**, 831-844, doi:10.1007/s00775-013-1023-3 (2013).
140 Szafrański, P. W., Kasza, P., Kępczyński, M. & Cegła, M. T. Fluorescent 1,2,3-triazole derivative of 3'-deoxy-3-azidothymidine: synthesis and absorption/emission spectra. *Heterocyclic Communications* **21**, 263-267, doi:doi:10.1515/hc-2015-0195 (2015).
141 Ngororabanga, J. M. V., Okerio, J. & Mama, N. Synthesis of Fluorescent Poly(coumarin-triazoles) via a CuAAC 'click' reaction. *South African Journal of Chemistry* **70**, 89-93 (2017).
142 Meisner, Q. J. *et al.* Fluorescence of Hydroxyphenyl-Substituted "Click" Triazoles. *The Journal of Physical Chemistry A* **122**, 2956-2973, doi:10.1021/acs.jpca.8b00577 (2018).
143 Ghasemi, Z., Mirzaie, A., Arabzadeh, R., Fathi, Z. & Abolghassemi Fakhree, A. Synthesis and optical properties of novel 1,2,3-triazole derivatives possessing highly substituted imidazoles. *Journal of Chemical Research* **43**, 262-267, doi:10.1177/1747519819861004 (2019).
144 Reddivari, C. K. R. *et al.* Design, Synthesis, Biological Evaluation and Molecular Docking Studies of 1,4-Disubstituted 1,2,3-Triazoles: PEG-400:H2O Mediated Click Reaction of Fluorescent Organic Probes under Ultrasonic Irradiation. *Polycyclic Aromatic Compounds* **42**, 3953-3974, doi:10.1080/10406638.2021.1878246 (2022).
145 Govdi, A. I. *et al.* 4,5-Bis(arylethynyl)-1,2,3-triazoles—A New Class of Fluorescent Labels: Synthesis and Applications. *Molecules* **27**, 3191 (2022).
146 Ghosh, D. *et al.* A simple and effective 1,2,3-triazole based "turn-on" fluorescence sensor for the detection of anions. *New Journal of Chemistry* **39**, 295-303, doi:10.1039/C4NJ01411A (2015).
147 Lai, Q. *et al.* Triazole-imidazole (TA-IM) derivatives as ultrafast fluorescent probes for selective Ag+ detection. *Organic & Biomolecular Chemistry* **16**, 7801-7805, doi:10.1039/C8OB02482K (2018).
148 Debia, N. P. *et al.* Synthesis of Amino Acid-Derived 1,2,3-Triazoles: Development of a Nontrivial Fluorescent Sensor in Solution for the Enantioselective Sensing of a Carbohydrate and Bovine Serum Albumin Interaction. *The Journal of Organic Chemistry* **83**, 1348-1357, doi:10.1021/acs.joc.7b02852 (2018).
149 Ding, G. *et al.* The specific binding of a new 1,2,3-triazole to three blood proteins and it's appended rhodamine complex for selective detection of Hg2+. *Spectrochimica Acta Part A: Molecular and Biomolecular Spectroscopy* **228**, 117728, doi:https://doi.org/10.1016/j.saa.2019.117728 (2020).

150 He, W. *et al.* A new 1,2,3-triazole and its rhodamine B derivatives as a fluorescence probe for mercury ions. *Analytical Biochemistry* **598**, 113690, doi:https://doi.org/10.1016/j.ab.2020.113690 (2020).
151 Zhengfeng, X. *et al.* A Novel 2-Phenyl-1,2,3-Triazole Derived Fluorescent Probe for Recyclable Detection of Al3+ in Aqueous Medium and Its Application. *Russian Journal of Bioorganic Chemistry* **46**, 627-641, doi:10.1134/S1068162020040214 (2020).
152 Wu, C. *et al.* A 1,2,3-triazole-based Chiral Fluorescence Sensor for the Sensitive Recognition of Ferric Ion. *IOP Conference Series: Earth and Environmental Science* **772**, 012059, doi:10.1088/1755-1315/772/1/012059 (2021).
153 Ji, P. *et al.* A novel fluorescent molecule based on 1,2,3-triazole for determination of palladium (II) and hydrazine hydrate in aqueous system. *Spectrochimica Acta Part A: Molecular and Biomolecular Spectroscopy* **293**, 122492, doi:https://doi.org/10.1016/j.saa.2023.122492 (2023).
154 Liu, H. *et al.* A Indole-Trizole-Rhodamine Triad as Ratiometric Fluorescent Probe for Nanomolar-Concentration Level Hg2+ Sensing with High Selectivity. *J Fluoresc* **25**, 1259-1266, doi:10.1007/s10895-015-1614-1 (2015).
155 Pereira, D., Pinto, M., Correia-da-Silva, M. & Cidade, H. Recent Advances in Bioactive Flavonoid Hybrids Linked by 1,2,3-Triazole Ring Obtained by Click Chemistry. *Molecules* **27**, 230 (2022).
156 Podolski-Renić, A. *et al.* Ferrocene–cinchona hybrids with triazolyl-chalcone linkers act as pro-oxidants and sensitize human cancer cell lines to paclitaxel. *Metallomics* **9**, 1132-1141, doi:10.1039/c7mt00183e (2017).
157 Jernei, T. *et al.* Synthesis, Structure and In Vitro Cytotoxic Activity of Novel Cinchona—Chalcone Hybrids with 1,4-Disubstituted- and 1,5-Disubstituted 1,2,3-Triazole Linkers. *Molecules* **24**, 4077 (2019).
158 Yan, W., Xiangyu, C., Ya, L., Yu, W. & Feng, X. An orally antitumor chalcone hybrid inhibited HepG2 cells growth and migration as the tubulin binding agent. *Investigational New Drugs* **37**, 784-790, doi:10.1007/s10637-019-00737-z (2019).
159 Manna, T., Pal, K., Jana, K. & Misra, A. K. Anti-cancer potential of novel glycosylated 1,4-substituted triazolylchalcone derivatives. *Bioorganic & Medicinal Chemistry Letters* **29**, 126615, doi:https://doi.org/10.1016/j.bmcl.2019.08.019 (2019).
160 Djemoui, A. *et al.* A step-by-step synthesis of triazole-benzimidazole-chalcone hybrids: Anticancer activity in human cells+. *Journal of Molecular Structure* **1204**, 127487, doi:https://doi.org/10.1016/j.molstruc.2019.127487 (2020).
161 Gurrapu, N. *et al.* Synthesis, biological evaluation and molecular docking studies of novel 1,2,3-triazole tethered chalcone hybrids as potential anticancer agents. *Journal of Molecular Structure* **1217**, 128356, doi:https://doi.org/10.1016/j.molstruc.2020.128356 (2020).
162 Wong, I. L. K. *et al.* Discovery of Novel Flavonoid Dimers To Reverse Multidrug Resistance Protein 1 (MRP1, ABCC1) Mediated Drug Resistance in Cancers Using a High Throughput Platform with “Click Chemistry”. *Journal of Medicinal Chemistry* **61**, 9931-9951, doi:10.1021/acs.jmedchem.8b00834 (2018).
163 Zhu, X. *et al.* Triazole Bridged Flavonoid Dimers as Potent, Nontoxic, and Highly Selective Breast Cancer Resistance Protein (BCRP/ABCG2) Inhibitors. *Journal of Medicinal Chemistry* **62**, 8578-8608, doi:10.1021/acs.jmedchem.9b00963 (2019).

164 Znati, M., Horchani, M., Latapie, L., Ben Jannet, H. & Bouajila, J. New 1,2,3-triazole linked flavonoid conjugates: Microwave-assisted synthesis, cytotoxic activity and molecular docking studies. *Journal of Molecular Structure* **1246**, 131216, doi:https://doi.org/10.1016/j.molstruc.2021.131216 (2021).

165 Fan, Z.-F. *et al.* Design, Synthesis and Molecular Docking Analysis of Flavonoid Derivatives as Potential Telomerase Inhibitors. *Molecules* **24**, 3180 (2019).

166 Rao, Y. J., Sowjanya, T., Thirupathi, G., Murthy, N. Y. S. & Kotapalli, S. S. Synthesis and biological evaluation of novel flavone/triazole/benzimidazole hybrids and flavone/isoxazole-annulated heterocycles as antiproliferative and antimycobacterial agents. *Molecular Diversity* **22**, 803-814, doi:10.1007/s11030-018-9833-4 (2018).

167 Wang, G.-q., Yan, L.-l. & Wang, Q.-a. Synthesis and antiproliferative activity of flavonoid triazolyl glycosides. *Heterocyclic Communications* **24**, 119-124, doi:doi:10.1515/hc-2017-0241 (2018).

168 Gupta, N. *et al.* Synthesis and biological evaluation of novel bavachinin analogs as anticancer agents. *European Journal of Medicinal Chemistry* **145**, 511-523, doi:https://doi.org/10.1016/j.ejmech.2018.01.006 (2018).

169 Latif, A. D. *et al.* Protoflavone-Chalcone Hybrids Exhibit Enhanced Antitumor Action through Modulating Redox Balance, Depolarizing the Mitochondrial Membrane, and Inhibiting ATR-Dependent Signaling. *Antioxidants* **9**, 519 (2020).

170 Sharma, B. *et al.* Design, synthesis, and anti-proliferative evaluation of 1H-1,2,3-triazole grafted tetrahydro-β-carboline-chalcone/ferrocenylchalcone conjugates in estrogen responsive and triple negative breast cancer cells. *New Journal of Chemistry* **44**, 11137-11147, doi:10.1039/D0NJ00879F (2020).

171 Raghavender, M., Kumar, A. K., Sunitha, V., Vishnu, T. & Jalapathi, P. Synthesis and Cytotoxicity of Chalcone Based 1,2,3-Triazole Derivatives. *Russian Journal of General Chemistry* **90**, 697-702, doi:10.1134/S1070363220040210 (2020).

172 Nagaraju, R. *et al.* Synthesis and Anticancer Activity of a Novel Series of Tetrazolo[1,5-a]quinoline Based 1,2,3-Triazole Derivatives. *Russian Journal of General Chemistry* **90**, 314-318, doi:10.1134/S1070363220020255 (2020).

173 Aneja, B. *et al.* N-Substituted 1,2,3-Triazolyl-Appended Indole-Chalcone Hybrids as Potential DNA Intercalators Endowed with Antioxidant and Anticancer Properties. *ChemistrySelect* **3**, 2638-2645, doi:https://doi.org/10.1002/slct.201702913 (2018).

174 Mistry, B., Patel, R. V. & Keum, Y.-S. Access to the substituted benzyl-1,2,3-triazolyl hesperetin derivatives expressing antioxidant and anticancer effects. *Arabian Journal of Chemistry* **10**, 157-166, doi:https://doi.org/10.1016/j.arabjc.2015.10.004 (2017).

175 Kiran, K. *et al.* Design, Synthesis, and Biological Activity of New Bis-1,2,3-triazole Derivatives Bearing Thiophene-Chalcone Moiety. *Russian Journal of General Chemistry* **89**, 1859-1866, doi:10.1134/S1070363219090214 (2019).

176 Singh, G. *et al.* A strategic approach to the synthesis of ferrocene appended chalcone linked triazole allied organosilatranes: Antibacterial, antifungal, antiparasitic and antioxidant studies. *Bioorganic & Medicinal Chemistry* **27**, 188-195, doi:https://doi.org/10.1016/j.bmc.2018.11.038 (2019).

177 Nagaraja, M., Kalluraya, B., Asma, Shreekanth, T. K. & Kumar, M. S. Synthesis of chalcone precursor via Cu(I) catalyzed 1,3-dipolar reaction of functionalized acetylene and pyrazole embedded dipole. *Journal of Heterocyclic Chemistry* **57**, 3642-3652, doi:https://doi.org/10.1002/jhet.4083 (2020).

178 Ngameni, B. *et al.* Synthesis and structural characterization of novel O-substituted phenolic and chalcone derivatives with antioxidant activity. *Journal of Chemical Research* **45**, 159-165, doi:10.1177/1747519820932789 (2021).

179 Línzembold, I. *et al.* Study on the Synthesis, Antioxidant Properties, and Self-Assembly of Carotenoid–Flavonoid Conjugates. *Molecules* **25**, 636 (2020).

180 Yadav, P. *et al.* Synthesis, crystal structure and antimicrobial potential of some fluorinated chalcone-1,2,3-triazole conjugates. *European Journal of Medicinal Chemistry* **155**, 263-274, doi:https://doi.org/10.1016/j.ejmech.2018.05.055 (2018).

181 Pujari, V. K. *et al.* Microwave Assisted Synthesis and Antimicrobial Activity of (E)-1-{2/3/4-[(1-Aryl-1H-1,2,3-triazol-4-yl)methoxy]phenyl}-3-(2-morpholinoquinolin-3-yl)prop-2-en-1-ones. *Russian Journal of General Chemistry* **88**, 1502-1507, doi:10.1134/S1070363218070241 (2018).

182 Sunitha, V., Kumar, A. K., Jalapathi, P. & Lincoln, C. A. Synthesis and Antimicrobial Activity of Bis-1,2,3-triazole Based Chalcones. *Russian Journal of General Chemistry* **90**, 154-159, doi:10.1134/S1070363220010247 (2020).

183 Yadav, P., Lal, K. & Kumar, A. Antimicrobial Screening, in Silico Studies and QSAR of Chalcone-based 1,4-disubstituted 1,2,3-triazole Hybrids. *Drug Res (Stuttg)* **71**, 149-156, doi:10.1055/a-1296-7751 (2020).

184 Yerrabelly, J. R. & Mallepaka, P. Facile Synthesis of Novel Isoflavone/1,2,3-Triazole HybridHeterocycles as Potential Antimicrobial Agents. *Russian Journal of General Chemistry* **90**, 911-916, doi:10.1134/S1070363220050266 (2020).

185 Lal, K., Yadav, P., Kumar, A., Kumar, A. & Paul, A. K. Design, synthesis, characterization, antimicrobial evaluation and molecular modeling studies of some dehydroacetic acid-chalcone-1,2,3-triazole hybrids. *Bioorganic Chemistry* **77**, 236-244, doi:https://doi.org/10.1016/j.bioorg.2018.01.016 (2018).

186 Zhang, H. *et al.* Flavonoid-triazolyl hybrids as potential anti-hepatitis C virus agents: Synthesis and biological evaluation. *European Journal of Medicinal Chemistry* **218**, 113395, doi:https://doi.org/10.1016/j.ejmech.2021.113395 (2021).

187 Bhowmik, S. *et al.* Synthesis of new chrysin derivatives with substantial antibiofilm activity. *Molecular Diversity* **26**, 137-156, doi:10.1007/s11030-020-10162-7 (2022).

188 Singh, G. *et al.* Designing of chalcone functionalized 1,2,3-triazole allied bis-organosilanes as potent antioxidants and optical sensor for recognition of Sn2+ and Hg2+ ions. *Journal of Organometallic Chemistry* **953**, 122049, doi:https://doi.org/10.1016/j.jorganchem.2021.122049 (2021).

189 Boshra, A. N., Abdu-Allah, H. H. M., Mohammed, A. F. & Hayallah, A. M. Click chemistry synthesis, biological evaluation and docking study of some novel 2'-hydroxychalcone-triazole hybrids as potent anti-inflammatory agents. *Bioorganic Chemistry* **95**, 103505, doi:https://doi.org/10.1016/j.bioorg.2019.103505 (2020).

190 Menghereş, G., Olajide, O. & Hemming, K. The synthesis and anti-inflammatory evaluation of 1,2,3-triazole linked isoflavone benzodiazepine hybrids. *ARKIVOC* **2020**, 306-321, doi:10.24820/ark.5550190.p011.396 (2020).

191 Zheng, Y. *et al.* Design and synthesis of 7-O-1,2,3-triazole hesperetin derivatives to relieve inflammation of acute liver injury in mice. *European Journal of Medicinal Chemistry* **213**, 113162, doi:https://doi.org/10.1016/j.ejmech.2021.113162 (2021).
192 Saroha, B. *et al.* Novel 1,2,3-triazole-aurone hybrids as cathepsin B inhibitors: One-pot synthesis, anti-proliferative, and drug modeling studies. *European Journal of Medicinal Chemistry Reports* **5**, 100056, doi:https://doi.org/10.1016/j.ejmcr.2022.100056 (2022).
193 Saroha, B. *et al.* Ultrasound assisted a one pot multicomponent and greener synthesis of 1,2,3-triazole incorporated aurone hybrids: Cathepsin B inhibition, anti-cancer activity against AGS cell line, and in-silico docking evaluation. *Current Research in Green and Sustainable Chemistry* **5**, 100295, doi:https://doi.org/10.1016/j.crgsc.2022.100295 (2022).
194 Kafle, A., Bhattarai, S. & Handy, S. T. An Unusual Triazole Synthesis from Aurones. *Synthesis* **52**, 2337-2346 (2020).
195 Shin, S. Y., Shin, M. C., Shin, J.-S., Lee, K.-T. & Lee, Y. S. Synthesis of aurones and their inhibitory effects on nitric oxide and PGE2 productions in LPS-induced RAW 264.7 cells. *Bioorganic & Medicinal Chemistry Letters* **21**, 4520-4523, doi:https://doi.org/10.1016/j.bmcl.2011.05.117 (2011).
196 Song, M.-Y. *et al.* Sulfuretin attenuates allergic airway inflammation in mice. *Biochemical and Biophysical Research Communications* **400**, 83-88, doi:https://doi.org/10.1016/j.bbrc.2010.08.014 (2010).
197 Kayser, O., Kiderlen, A. F. & Brun, R. In Vitro Activity of Aurones against Plasmodium falciparum Strains K1 and NF54. *Planta Med* **67**, 718-721 (2001).
198 Václavíková, R. *et al.* The effect of flavonoid derivatives on doxorubicin transport and metabolism. *Bioorganic & Medicinal Chemistry* **16**, 2034-2042, doi:https://doi.org/10.1016/j.bmc.2007.10.093 (2008).
199 Lawrence, N. J., Rennison, D., McGown, A. T. & Hadfield, J. A. The total synthesis of an aurone isolated from Uvaria hamiltonii: aurones and flavones as anticancer agents. *Bioorganic & Medicinal Chemistry Letters* **13**, 3759-3763, doi:https://doi.org/10.1016/j.bmcl.2003.07.003 (2003).
200 Geissman, T. A. & Harborne, J. B. Anthochlor Pigments. X. Aureusin and Cernuoside. *Journal of the American Chemical Society* **77**, 4622-4624, doi:10.1021/ja01622a054 (1955).
201 Varma, R. S. & Varma, M. Alumina-mediated condensation. A simple synthesis of aurones. *Tetrahedron Letters* **33**, 5937-5940, doi:https://doi.org/10.1016/S0040-4039(00)61093-6 (1992).
202 Qi, X., Li, R. & Wu, X.-F. Selective palladium-catalyzed carbonylative synthesis of aurones with formic acid as the CO source. *RSC Advances* **6**, 62810-62813, doi:10.1039/C6RA13615J (2016).
203 Jong, T.-T. & Leu, S.-J. Intramolecular cyclisation catalysed by silver(I) ion; a convenient synthesis of aurones. *Journal of the Chemical Society, Perkin Transactions 1*, 423-424, doi:10.1039/P19900000423 (1990).
204 Harkat, H., Blanc, A., Weibel, J.-M. & Pale, P. Versatile and Expeditious Synthesis of Aurones via AuI-Catalyzed Cyclization. *The Journal of Organic Chemistry* **73**, 1620-1623, doi:10.1021/jo702197b (2008).
205 Hawkins, I. & Handy, S. T. Synthesis of aurones under neutral conditions using a deep eutectic solvent. *Tetrahedron* **69**, 9200-9204, doi:https://doi.org/10.1016/j.tet.2013.08.060 (2013).
206 Gottlieb, H. E., Kotlyar, V. & Nudelman, A. NMR chemical shifts of common laboratory solvents as trace impurities. *Journal of Organic Chemistry* **62**, 7512-7515 (1997).

207 Schindelin, J. *et al.* Fiji: an open-source platform for biological-image analysis. *Nat Methods* **9**, 676-682, doi:10.1038/nmeth.2019 (2012).

208 Li, W., Zhang, M., Zhang, J. & Han, Y. Self-assembly of cetyl trimethylammonium bromide in ethanol-water mixtures. *Frontiers of Chemistry in China* **1**, 438-442, doi:10.1007/s11458-006-0069-y (2006).

209 Moroi, Y., Motomura, K. & Matuura, R. The critical micelle concentration of sodium dodecyl sulfate-bivalent metal dodecyl sulfate mixtures in aqueous solutions. *Journal of Colloid and Interface Science* **46**, 111-117, doi:https://doi.org/10.1016/0021-9797(74)90030-7 (1974).

210 Hammouda, B. Temperature Effect on the Nanostructure of SDS Micelles in Water. *J Res Natl Inst Stand Technol* **118**, 151-167, doi:10.6028/jres.118.008 (2013).

211 Kalyanasundaram, K. & Thomas, J. K. Environmental effects on vibronic band intensities in pyrene monomer fluorescence and their application in studies of micellar systems. *Journal of the American Chemical Society* **99**, 2039-2044, doi:10.1021/ja00449a004 (1977).

212 Hait, S. K. & Moulik, S. P. Determination of critical micelle concentration (CMC) of nonionic surfactants by donor-acceptor interaction with Iodine and correlation of CMC with hydrophile-lipophile balance and other parameters of the surfactants. *Journal of Surfactants and Detergents* **4**, 303-309, doi:https://doi.org/10.1007/s11743-001-0184-2 (2001).

213 Koley, D. & Bard, A. J. Triton X-100 concentration effects on membrane permeability of a single HeLa cell by scanning electrochemical microscopy (SECM). *Proceedings of the National Academy of Sciences* **107**, 16783-16787, doi:10.1073/pnas.1011614107 (2010).

214 Tiller, G. E., Mueller, T. J., Dockter, M. E. & Struve, W. G. Hydrogenation of Triton X-100 eliminates its fluorescence and ultraviolet light absorption while preserving its detergent properties. *Analytical Biochemistry* **141**, 262-266, doi:https://doi.org/10.1016/0003-2697(84)90455-X (1984).

215 Patist, A., Bhagwat, S. S., Penfield, K. W., Aikens, P. & Shah, D. O. On the measurement of critical micelle concentrations of pure and technical-grade nonionic surfactants. *Journal of Surfactants and Detergents* **3**, 53-58, doi:10.1007/s11743-000-0113-4 (2000).

216 Reichardt, C. & Welton, T. in *Solvents and Solvent Effects in Organic Chemistry* (eds Christian Reichardt & Thomas Welton) 425-508, 549-586 (2010).

217 Kamlet, M. J., Abboud, J. L. & Taft, R. W. The solvatochromic comparison method. 6. The .pi.* scale of solvent polarities. *Journal of the American Chemical Society* **99**, 6027-6038, doi:10.1021/ja00460a031 (1977).

218 Marcus, Y. *The Properties of Solvents*. Vol. 4 142-144 (John Wiley & Sons Ltd, 1998).

219 Tian, H. *et al.* Micelle-induced multiple performance improvement of fluorescent probes for H2S detection. *Analytica Chimica Acta* **768**, 136-142, doi:https://doi.org/10.1016/j.aca.2013.01.030 (2013).

220 Tai, D. & Liu, J. A simple and sensitive turn-on fluorescence probe for detection of cetyltrimethylammonium bromide in aqueous samples. *Luminescence* **30**, 358-361, doi:https://doi.org/10.1002/bio.2739 (2015).

221 Garavito, R. M. & Ferguson-Miller, S. Detergents as Tools in Membrane Biochemistry *. *Journal of Biological Chemistry* **276**, 32403-32406, doi:10.1074/jbc.R100031200 (2001).

222 Seddon, A. M., Curnow, P. & Booth, P. J. Membrane proteins, lipids and detergents: not just a soap opera. *Biochimica et Biophysica Acta (BBA) - Biomembranes* **1666**, 105-117, doi:https://doi.org/10.1016/j.bbamem.2004.04.011 (2004).

223 Nnyigide, O. S., Lee, S.-G. & Hyun, K. In Silico Characterization of the Binding Modes of Surfactants with Bovine Serum Albumin. *Sci Rep* **9**, 10643, doi:10.1038/s41598-019-47135-2 (2019).

224 Javadian, S. *et al.* Self-Assembled CTAB Nanostructures in Aqueous/Ionic Liquid Systems: Effects of Hydrogen Bonding. *Industrial & Engineering Chemistry Research* **52**, 4517-4526, doi:10.1021/ie302411t (2013).

225 Li, H. *et al.* Conformational change due to intramolecular hydrophobic interaction leads to large blue-shifted emission from single molecular cage solutions. *Chemical Communications* **55**, 330-333, doi:10.1039/C8CC09038F (2019).

226 Baraldi, I., Brancolini, G., Momicchioli, F., Ponterini, G. & Vanossi, D. Solvent influence on absorption and fluorescence spectra of merocyanine dyes: a theoretical and experimental study. *Chemical Physics* **288**, 309-325, doi:https://doi.org/10.1016/S0301-0104(03)00046-6 (2003).

227 Joshi, H. C. & Antonov, L. Excited-State Intramolecular Proton Transfer: A Short Introductory Review. *Molecules* **26**, 1475 (2021).

228 Yi, P. G., Liang, Y. H. & Cao, C. Z. Intramolecular proton or hydrogen-atom transfer in the ground- and excited-states of 2-hydroxybenzophenone: A theoretical study. *Chemical Physics* **315**, 297-302, doi:https://doi.org/10.1016/j.chemphys.2005.04.046 (2005).

229 Maheshwari, S. *et al.* Ground and Excited State Intramolecular Proton Transfer in Salicylic Acid: an Ab Initio Electronic Structure Investigation. *The Journal of Physical Chemistry A* **103**, 6257-6262, doi:10.1021/jp9911999 (1999).

230 Joshi, H. C., Mishra, H. & Tripathi, H. B. Photophysics and photochemistry of salicylic acid revisited. *Journal of Photochemistry and Photobiology A: Chemistry* **105**, 15-20, doi:https://doi.org/10.1016/S1010-6030(96)04565-0 (1997).

231 Tang, Z., Wei, H. & Zhou, P. Effects of solvents on the excited state intramolecular proton transfer and hydrogen bond mechanisms of alizarin and its isomers. *Journal of Molecular Liquids* **301**, 112415, doi:https://doi.org/10.1016/j.molliq.2019.112415 (2020).

232 Qin, T. *et al.* Solvatofluorochromic flavonoid dyes with enlarged transition dipole moments enable the ratiometric detection of methanol in commercial biodiesel with improved sensitivities. *Journal of Materials Chemistry C* **8**, 16808-16814, doi:10.1039/D0TC04542J (2020).

233 Klymchenko, A. S. & Demchenko, A. P. Multiparametric probing of intermolecular interactions with fluorescent dye exhibiting excited state intramolecular proton transfer. *Physical Chemistry Chemical Physics* **5**, 461-468, doi:10.1039/B210352D (2003).

234 Chen, Y., Yang, Y., Zhao, Y., Liu, S. & Li, Y. Effect of solvent environment on excited state intramolecular proton transfer in 2-(4-(dimethylamino)phenyl)-3-hydroxy-6,7-dimethoxy-4h-chromen-4-one. *Physical Chemistry Chemical Physics* **21**, 17711-17719, doi:10.1039/C9CP03752G (2019).

235 Joshi, H. C., Tripathi, H. B., Pant, T. C. & Pant, D. D. Hydrogen-bonding effect on the dual emission of salicylic acid. *Chemical Physics Letters* **173**, 83-86, doi:https://doi.org/10.1016/0009-2614(90)85307-X (1990).

236 Kenfack, C. A., Klymchenko, A. S., Duportail, G., Burger, A. & Mély, Y. Ab initio study of the solvent H-bonding effect on ESIPT reaction and electronic transitions of 3-hydroxychromone derivatives. *Physical Chemistry Chemical Physics* **14**, 8910-8918, doi:10.1039/C2CP40869D (2012).

237 Peng, Y., Ye, Y., Xiu, X. & Sun, S. Mechanism of Excited-State Intramolecular Proton Transfer for 1,2-Dihydroxyanthraquinone: Effect of Water on the ESIPT. *The Journal of Physical Chemistry A* **121**, 5625-5634, doi:10.1021/acs.jpca.7b03877 (2017).
238 Seo, J., Kim, S. & Park, S. Y. Strong Solvatochromic Fluorescence from the Intramolecular Charge-Transfer State Created by Excited-State Intramolecular Proton Transfer. *Journal of the American Chemical Society* **126**, 11154-11155, doi:10.1021/ja047815i (2004).
239 Zhou, P., Hoffmann, M. R., Han, K. & He, G. New Insights into the Dual Fluorescence of Methyl Salicylate: Effects of Intermolecular Hydrogen Bonding and Solvation. *The Journal of Physical Chemistry B* **119**, 2125-2131, doi:10.1021/jp501881j (2015).
240 Sandros, K. Hydrogen Bonding Effects on the Fluorescence of Methyl Salicylate. *Acta Chemica Scandinavica* **30a**, 761-763, doi:10.3891/acta.chem.scand.30a-0761 (1976).
241 Gough, P. & Myles, I. A. Tumor Necrosis Factor Receptors: Pleiotropic Signaling Complexes and Their Differential Effects. *Frontiers in Immunology* **11**, doi:10.3389/fimmu.2020.585880 (2020).
242 Parameswaran, N. & Patial, S. Tumor necrosis factor-α signaling in macrophages. *Crit Rev Eukaryot Gene Expr* **20**, 87-103, doi:10.1615/critreveukargeneexpr.v20.i2.10 (2010).
243 Dinarello, C. Biologic basis for interleukin-1 in disease. *Blood* **87**, 2095-2147, doi:10.1182/blood.V87.6.2095.bloodjournal8762095 (1996).
244 Mantovani, A., Allavena, P., Sica, A. & Balkwill, F. Cancer-related inflammation. *Nature* **454**, 436-444, doi:10.1038/nature07205 (2008).
245 Dinarello, C. A. Immunological and Inflammatory Functions of the Interleukin-1 Family. *Annual Review of Immunology* **27**, 519-550, doi:10.1146/annurev.immunol.021908.132612 (2009).
246 Tanaka, T., Narazaki, M. & Kishimoto, T. IL-6 in inflammation, immunity, and disease. *Cold Spring Harb Perspect Biol* **6**, a016295, doi:10.1101/cshperspect.a016295 (2014).
247 Tesmer, L. A., Lundy, S. K., Sarkar, S. & Fox, D. A. Th17 cells in human disease. *Immunol Rev* **223**, 87-113, doi:10.1111/j.1600-065X.2008.00628.x (2008).
248 Deshmane, S. L., Kremlev, S., Amini, S. & Sawaya, B. E. Monocyte chemoattractant protein-1 (MCP-1): an overview. *J Interferon Cytokine Res* **29**, 313-326, doi:10.1089/jir.2008.0027 (2009).
249 Vasanthi, P., Nalini, G. & Rajasekhar, G. Role of tumor necrosis factor-alpha in rheumatoid arthritis: a review. *APLAR Journal of Rheumatology* **10**, 270-274, doi:https://doi.org/10.1111/j.1479-8077.2007.00305.x (2007).
250 MacDermott, R. P. Chemokines in the Inflammatory Bowel Diseases. *Journal of Clinical Immunology* **19**, 266-272, doi:10.1023/A:1020583306627 (1999).
251 Li, D. & Wu, M. Pattern recognition receptors in health and diseases. *Signal Transduction and Targeted Therapy* **6**, 291, doi:10.1038/s41392-021-00687-0 (2021).
252 Lu, Y.-C., Yeh, W.-C. & Ohashi, P. S. LPS/TLR4 signal transduction pathway. *Cytokine* **42**, 145-151, doi:https://doi.org/10.1016/j.cyto.2008.01.006 (2008).
253 Sul, O.-J. & Ra, S. W. Quercetin Prevents LPS-Induced Oxidative Stress and Inflammation by Modulating NOX2/ROS/NF-kB in Lung Epithelial Cells. *Molecules* **26**, 6949 (2021).
254 Hsu, H.-Y. & Wen, M.-H. Lipopolysaccharide-mediated Reactive Oxygen Species and Signal Transduction in the Regulation of Interleukin-1 Gene Expression. *Journal of Biological Chemistry* **277**, 22131-22139, doi:10.1074/jbc.M111883200 (2002).

255 Uematsu, S., Matsumoto, M., Takeda, K. & Akira, S. Lipopolysaccharide-Dependent Prostaglandin E2 Production Is Regulated by the Glutathione-Dependent Prostaglandin E2 Synthase Gene Induced by the Toll-Like Receptor 4/MyD88/NF-IL6 Pathway1. *The Journal of Immunology* **168**, 5811-5816, doi:10.4049/jimmunol.168.11.5811 (2002).
256 Rossol, M. *et al.* LPS-induced Cytokine Production in Human Monocytes and Macrophages. **31**, 379-446, doi:10.1615/CritRevImmunol.v31.i5.20 (2011).
257 Li, X., Jiang, S. & Tapping, R. I. Toll-like receptor signaling in cell proliferation and survival. *Cytokine* **49**, 1-9, doi:10.1016/j.cyto.2009.08.010 (2010).
258 Guha, M. & Mackman, N. LPS induction of gene expression in human monocytes. *Cellular Signalling* **13**, 85-94, doi:https://doi.org/10.1016/S0898-6568(00)00149-2 (2001).
259 Dorrington, M. G. & Fraser, I. D. C. NF-κB Signaling in Macrophages: Dynamics, Crosstalk, and Signal Integration. *Frontiers in Immunology* **10**, doi:10.3389/fimmu.2019.00705 (2019).
260 Hayden, M. S. & Ghosh, S. Signaling to NF-κB. *Genes & Development* **18**, 2195-2224, doi:10.1101/gad.1228704 (2004).
261 West, A. P., Koblansky, A. A. & Ghosh, S. Recognition and Signaling by Toll-Like Receptors. *Annual Review of Cell and Developmental Biology* **22**, 409-437, doi:10.1146/annurev.cellbio.21.122303.115827 (2006).
262 Gay, N. J. & Keith, F. J. Drosophila Toll and IL-1 receptor. *Nature* **351**, 355-356, doi:10.1038/351355b0 (1991).
263 Seemann, S., Zohles, F. & Lupp, A. Comprehensive comparison of three different animal models for systemic inflammation. *Journal of Biomedical Science* **24**, 60, doi:10.1186/s12929-017-0370-8 (2017).
264 Kawai, T. & Akira, S. Signaling to NF-κB by Toll-like receptors. *Trends in Molecular Medicine* **13**, 460-469, doi:10.1016/j.molmed.2007.09.002 (2007).
265 Kumar, H., Kawai, T. & Akira, S. Toll-like receptors and innate immunity. *Biochemical and Biophysical Research Communications* **388**, 621-625, doi:https://doi.org/10.1016/j.bbrc.2009.08.062 (2009).
266 Oeckinghaus, A., Hayden, M. S. & Ghosh, S. Crosstalk in NF-κB signaling pathways. *Nature Immunology* **12**, 695-708, doi:10.1038/ni.2065 (2011).
267 Christian, F., Smith, E. L. & Carmody, R. J. The Regulation of NF-κB Subunits by Phosphorylation. *Cells* **5**, 12, doi:10.3390/cells5010012 (2016).
268 Ullah, M. O., Sweet, M. J., Mansell, A., Kellie, S. & Kobe, B. TRIF-dependent TLR signaling, its functions in host defense and inflammation, and its potential as a therapeutic target. *Journal of Leukocyte Biology* **100**, 27-45, doi:https://doi.org/10.1189/jlb.2RI1115-531R (2016).
269 Festjens, N., Vanden Berghe, T., Cornelis, S. & Vandenabeele, P. RIP1, a kinase on the crossroads of a cell's decision to live or die. *Cell Death & Differentiation* **14**, 400-410, doi:10.1038/sj.cdd.4402085 (2007).
270 Kawai, T. *et al.* Lipopolysaccharide Stimulates the MyD88-Independent Pathway and Results in Activation of IFN-Regulatory Factor 3 and the Expression of a Subset of Lipopolysaccharide-Inducible Genes. *The Journal of Immunology* **167**, 5887-5894, doi:10.4049/jimmunol.167.10.5887 (2001).
271 Sin, W. X. *et al.* IRF-7 Mediates Type I IFN Responses in Endotoxin-Challenged Mice. *Front Immunol* **11**, 640, doi:10.3389/fimmu.2020.00640 (2020).
272 Karin, M. The Regulation of AP-1 Activity by Mitogen-activated Protein Kinases. *Journal of Biological Chemistry* **270**, 16483-16486, doi:10.1074/jbc.270.28.16483 (1995).

273 Lucas, R. M., Luo, L. & Stow, J. L. ERK1/2 in immune signalling. *Biochem Soc Trans* **50**, 1341-1352, doi:10.1042/bst20220271 (2022).
274 Yoon, S. & Seger, R. The extracellular signal-regulated kinase: Multiple substrates regulate diverse cellular functions. *Growth Factors* **24**, 21-44, doi:10.1080/02699050500284218 (2006).
275 Kang, Y. J. *et al.* Macrophage Deletion of p38α Partially Impairs Lipopolysaccharide-Induced Cellular Activation1. *The Journal of Immunology* **180**, 5075-5082, doi:10.4049/jimmunol.180.7.5075 (2008).
276 Han, J., Wu, J. & Silke, J. An overview of mammalian p38 mitogen-activated protein kinases, central regulators of cell stress and receptor signaling [version 1; peer review: 2 approved]. *F1000Research* **9**, doi:10.12688/f1000research.22092.1 (2020).
277 Neuder, L. E., Keener, J. M., Eckert, R. E., Trujillo, J. C. & Jones, S. L. Role of p38 MAPK in LPS induced pro-inflammatory cytokine and chemokine gene expression in equine leukocytes. *Vet Immunol Immunopathol* **129**, 192-199, doi:10.1016/j.vetimm.2008.11.006 (2009).
278 Yu, T. *et al.* The Regulatory Role of Activating Transcription Factor 2 in Inflammation. *Mediators Inflamm* **2014**, 950472, doi:10.1155/2014/950472 (2014).
279 Reimold, A. M., Kim, J., Finberg, R. & Glimcher, L. H. Decreased immediate inflammatory gene induction in activating transcription factor-2 mutant mice. *International Immunology* **13**, 241-248, doi:10.1093/intimm/13.2.241 (2001).
280 Glushkova, O. V. *et al.* Inhibitors of TLR-4, NF-κB, and SAPK/JNK signaling reduce the toxic effect of lipopolysaccharide on RAW 264.7 cells. *Journal of Immunotoxicology* **10**, 133-140, doi:10.3109/1547691X.2012.700652 (2013).
281 Swantek, J. L., Cobb, M. H. & Geppert, T. D. Jun N-Terminal Kinase/Stress-Activated Protein Kinase (JNK/SAPK) Is Required for Lipopolysaccharide Stimulation of Tumor Necrosis Factor Alpha (TNF-α) Translation: Glucocorticoids Inhibit TNF-α Translation by Blocking JNK/SAPK. *Molecular and Cellular Biology* **17**, 6274-6282, doi:10.1128/MCB.17.11.6274 (1997).
282 Risco, A. *et al.* p38γ and p38δ kinases regulate the Toll-like receptor 4 (TLR4)-induced cytokine production by controlling ERK1/2 protein kinase pathway activation. *Proceedings of the National Academy of Sciences* **109**, 11200-11205, doi:doi:10.1073/pnas.1207290109 (2012).
283 Saraiva, M. & O'Garra, A. The regulation of IL-10 production by immune cells. *Nature Reviews Immunology* **10**, 170-181, doi:10.1038/nri2711 (2010).
284 Banerjee, A., Gugasyan, R., McMahon, M. & Gerondakis, S. Diverse Toll-like receptors utilize Tpl2 to activate extracellular signal-regulated kinase (ERK) in hemopoietic cells. *Proceedings of the National Academy of Sciences* **103**, 3274-3279, doi:doi:10.1073/pnas.0511113103 (2006).
285 Dumitru, C. D. *et al.* TNF-α; Induction by LPS Is Regulated Posttranscriptionally via a Tpl2/ERK-Dependent Pathway. *Cell* **103**, 1071-1083, doi:10.1016/S0092-8674(00)00210-5 (2000).
286 Shi, L., Kishore, R., McMullen, M. R. & Nagy, L. E. Lipopolysaccharide stimulation of ERK1/2 increases TNF-α production via Egr-1. *American Journal of Physiology-Cell Physiology* **282**, C1205-C1211, doi:10.1152/ajpcell.00511.2001 (2002).
287 Cargnello, M. & Roux, P. P. Activation and Function of the MAPKs and Their Substrates, the MAPK-Activated Protein Kinases. *Microbiology and Molecular Biology Reviews* **75**, 50-83, doi:doi:10.1128/mmbr.00031-10 (2011).

288 Buscà, R., Pouysségur, J. & Lenormand, P. ERK1 and ERK2 Map Kinases: Specific Roles or Functional Redundancy? *Frontiers in Cell and Developmental Biology* **4**, doi:10.3389/fcell.2016.00053 (2016).
289 Waskiewicz, A. J., Flynn, A., Proud, C. G. & Cooper, J. A. Mitogen-activated protein kinases activate the serine/threonine kinases Mnk1 and Mnk2. *EMBO J* **16**, 1909-1920, doi:https://doi.org/10.1093/emboj/16.8.1909 (1997).
290 Scheper, G. C., Morrice, N. A., Kleijn, M. & Proud, C. G. The mitogen-activated protein kinase signal-integrating kinase Mnk2 is a eukaryotic initiation factor 4E kinase with high levels of basal activity in mammalian cells. *Mol Cell Biol* **21**, 743-754, doi:10.1128/mcb.21.3.743-754.2001 (2001).
291 Bartish, M. *et al.* MNK2 governs the macrophage antiinflammatory phenotype. *Proceedings of the National Academy of Sciences* **117**, 27556-27565, doi:doi:10.1073/pnas.1920377117 (2020).
292 *Molinspiration Cheminformatics free web services*, <https://www.molinspiration.com> (
293 Lipinski, C. A., Lombardo, F., Dominy, B. W. & Feeney, P. J. Experimental and computational approaches to estimate solubility and permeability in drug discovery and development settings1PII of original article: S0169-409X(96)00423-1. The article was originally published in Advanced Drug Delivery Reviews 23 (1997) 3–25.1. *Advanced Drug Delivery Reviews* **46**, 3-26, doi:https://doi.org/10.1016/S0169-409X(00)00129-0 (2001).
294 Veber, D. F. *et al.* Molecular Properties That Influence the Oral Bioavailability of Drug Candidates. *Journal of Medicinal Chemistry* **45**, 2615-2623, doi:10.1021/jm020017n (2002).
295 Yang, N. J. & Hinner, M. J. Getting across the cell membrane: an overview for small molecules, peptides, and proteins. *Methods Mol Biol* **1266**, 29-53, doi:10.1007/978-1-4939-2272-7_3 (2015).
296 Ghosh, R. *et al.* Panax quinquefolius (North American ginseng) cell suspension culture as a source of bioactive polysaccharides: Immunostimulatory activity and characterization of a neutral polysaccharide AGC1. *International Journal of Biological Macromolecules* **139**, 221-232, doi:https://doi.org/10.1016/j.ijbiomac.2019.07.215 (2019).
297 Aranda, P. S., LaJoie, D. M. & Jorcyk, C. L. Bleach gel: a simple agarose gel for analyzing RNA quality. *Electrophoresis* **33**, 366-369, doi:10.1002/elps.201100335 (2012).
298 Ko, W.-K. *et al.* Anti-inflammatory effects of ursodeoxycholic acid by lipopolysaccharide-stimulated inflammatory responses in RAW 264.7 macrophages. *PLoS One* **12**, e0180673, doi:10.1371/journal.pone.0180673 (2017).
299 Endale, M. *et al.* Quercetin disrupts tyrosine-phosphorylated phosphatidylinositol 3-kinase and myeloid differentiation factor-88 association, and inhibits MAPK/AP-1 and IKK/NF-κB-induced inflammatory mediators production in RAW 264.7 cells. *Immunobiology* **218**, 1452-1467, doi:https://doi.org/10.1016/j.imbio.2013.04.019 (2013).
300 Wang, X. *et al.* Lipopolysaccharide and palmitic acid synergistically induced MCP-1 production via MAPK-meditated TLR4 signaling pathway in RAW264.7 cells. *Lipids in Health and Disease* **18**, 71, doi:10.1186/s12944-019-1017-4 (2019).
301 Kim, J.-B. *et al.* Inhibition of LPS-Induced iNOS, COX-2 and Cytokines Expression by Poncirin through the NF-κB Inactivation in RAW 264.7 Macrophage Cells. *Biological and Pharmaceutical Bulletin* **30**, 2345-2351, doi:10.1248/bpb.30.2345 (2007).

302 The Galaxy Community. The Galaxy platform for accessible, reproducible and collaborative biomedical analyses: 2022 update. *Nucleic Acids Res* **50**, W345-W351, doi:10.1093/nar/gkac247 (2022).
303 Andrews, S. *FastQC A Quality Contro tool for High Throughput Sequence Data*.
304 Ewels, P., Magnusson, M., Lundin, S. & Käller, M. MultiQC: summarize analysis results for multiple tools and samples in a single report. *Bioinformatics* **32**, 3047-3048, doi:10.1093/bioinformatics/btw354 (2016).
305 Bolger, A. M., Lohse, M. & Usadel, B. Trimmomatic: a flexible trimmer for Illumina sequence data. *Bioinformatics* **30**, 2114-2120, doi:10.1093/bioinformatics/btu170 (2014).
306 Kim, D., Langmead, B. & Salzberg, S. L. HISAT: a fast spliced aligner with low memory requirements. *Nat Methods* **12**, 357-360, doi:10.1038/nmeth.3317 (2015).
307 Li, H. Improving SNP discovery by base alignment quality. *Bioinformatics* **27**, 1157-1158, doi:10.1093/bioinformatics/btr076 (2011).
308 Li, H. A statistical framework for SNP calling, mutation discovery, association mapping and population genetical parameter estimation from sequencing data. *Bioinformatics* **27**, 2987-2993, doi:10.1093/bioinformatics/btr509 (2011).
309 Li, H. *et al.* The Sequence Alignment/Map format and SAMtools. *Bioinformatics* **25**, 2078-2079, doi:10.1093/bioinformatics/btp352 (2009).
310 Pertea, M. *et al.* StringTie enables improved reconstruction of a transcriptome from RNA-seq reads. *Nature Biotechnology* **33**, 290-295, doi:10.1038/nbt.3122 (2015).
311 Kovaka, S. *et al.* Transcriptome assembly from long-read RNA-seq alignments with StringTie2. *Genome Biology* **20**, 278, doi:10.1186/s13059-019-1910-1 (2019).
312 Anders, S., Pyl, P. T. & Huber, W. HTSeq—a Python framework to work with high-throughput sequencing data. *Bioinformatics* **31**, 166-169, doi:10.1093/bioinformatics/btu638 (2014).
313 Love, M. I., Huber, W. & Anders, S. Moderated estimation of fold change and dispersion for RNA-seq data with DESeq2. *Genome Biology* **15**, 550, doi:10.1186/s13059-014-0550-8 (2014).
314 Huang da, W., Sherman, B. T. & Lempicki, R. A. Systematic and integrative analysis of large gene lists using DAVID bioinformatics resources. *Nat Protoc* **4**, 44-57, doi:10.1038/nprot.2008.211 (2009).
315 Huang da, W., Sherman, B. T. & Lempicki, R. A. Bioinformatics enrichment tools: paths toward the comprehensive functional analysis of large gene lists. *Nucleic Acids Res* **37**, 1-13, doi:10.1093/nar/gkn923 (2009).
316 Sherman, B. T. *et al.* DAVID: a web server for functional enrichment analysis and functional annotation of gene lists (2021 update). *Nucleic Acids Res* **50**, W216-w221, doi:10.1093/nar/gkac194 (2022).
317 Wijesooriya, K., Jadaan, S. A., Perera, K. L., Kaur, T. & Ziemann, M. Urgent need for consistent standards in functional enrichment analysis. *PLOS Computational Biology* **18**, e1009935, doi:10.1371/journal.pcbi.1009935 (2022).
318 Stelzer, G. *et al.* The GeneCards Suite: From Gene Data Mining to Disease Genome Sequence Analyses. *Current Protocols in Bioinformatics* **54**, 1.30.31-31.30.33, doi:https://doi.org/10.1002/cpbi.5 (2016).
319 Safran, M. *et al.* in *Practical Guide to Life Science Databases* (eds Imad Abugessaisa & Takeya Kasukawa) 27-56 (Springer Nature Singapore, 2021).
320 Blake, J. A. *et al.* Mouse Genome Database (MGD): Knowledgebase for mouse-human comparative biology. *Nucleic Acids Res* **49**, D981-d987, doi:10.1093/nar/gkaa1083 (2021).

321 Baldarelli, R. M. *et al.* The mouse Gene Expression Database (GXD): 2021 update. *Nucleic Acids Res* **49**, D924-d931, doi:10.1093/nar/gkaa914 (2021).
322 Krupke, D. M. *et al.* The Mouse Tumor Biology Database: A Comprehensive Resource for Mouse Models of Human Cancer. *Cancer Research* **77**, e67-e70, doi:10.1158/0008-5472.Can-17-0584 (2017).
323 Benjamini, Y. & Hochberg, Y. On the Adaptive Control of the False Discovery Rate in Multiple Testing With Independent Statistics. *Journal of Educational and Behavioral Statistics* **25**, 60-83, doi:10.3102/10769986025001060 (2000).
324 Ge, S. X., Jung, D. & Yao, R. ShinyGO: a graphical gene-set enrichment tool for animals and plants. *Bioinformatics* **36**, 2628-2629, doi:10.1093/bioinformatics/btz931 (2019).
325 Kanehisa, M., Furumichi, M., Sato, Y., Ishiguro-Watanabe, M. & Tanabe, M. KEGG: integrating viruses and cellular organisms. *Nucleic Acids Res* **49**, D545-D551, doi:10.1093/nar/gkaa970 (2020).
326 Luo, W. & Brouwer, C. Pathview: an R/Bioconductor package for pathway-based data integration and visualization. *Bioinformatics* **29**, 1830-1831, doi:10.1093/bioinformatics/btt285 (2013).
327 Oliveros, J. C. *Venny. An interactive tool for comparing lists with Venn's diagrams.*, <https://bioinfogp.cnb.csic.es/tools/venny/index.html> (2007-2015).
328 gplots: Various R Programming Tools for Plotting Data v. 3.1.3 (2022).
329 Wickham, H. *ggplot2: Elegant Graphics for Data Analysis*. (Springer-Verlag New York, 2016).
330 R: A Language and Environment for Statistical Computing (R Foundation for Statistical Computing, 2022).
331 RStudio: Integrated Development Environment for R v. 2022.12.0.353 (Posit Software, PBC, 2022).
332 Szklarczyk, D. *et al.* STRING v11: protein-protein association networks with increased coverage, supporting functional discovery in genome-wide experimental datasets. *Nucleic Acids Res* **47**, D607-d613, doi:10.1093/nar/gky1131 (2019).
333 Shannon, P. *et al.* Cytoscape: A Software Environment for Integrated Models of Biomolecular Interaction Networks. *Genome Research* **13**, 2498-2504, doi:10.1101/gr.1239303 (2003).
334 Lundberg, J. O., Weitzberg, E. & Gladwin, M. T. The nitrate–nitrite–nitric oxide pathway in physiology and therapeutics. *Nature Reviews Drug Discovery* **7**, 156-167, doi:10.1038/nrd2466 (2008).
335 Elisia, I. *et al.* DMSO Represses Inflammatory Cytokine Production from Human Blood Cells and Reduces Autoimmune Arthritis. *PLoS One* **11**, e0152538-e0152538, doi:10.1371/journal.pone.0152538 (2016).
336 Liu, Y., Su, W.-W., Wang, S. & Li, P.-B. Naringin inhibits chemokine production in an LPS-induced RAW 264.7 macrophage cell line. *Mol Med Rep* **6**, 1343-1350, doi:10.3892/mmr.2012.1072 (2012).
337 Cao, Y. *et al.* Punicalagin Prevents Inflammation in LPS-Induced RAW264.7 Macrophages by Inhibiting FoxO3a/Autophagy Signaling Pathway. *Nutrients* **11**, doi:10.3390/nu11112794 (2019).
338 Makita, N., Hizukuri, Y., Yamashiro, K., Murakawa, M. & Hayashi, Y. IL-10 enhances the phenotype of M2 macrophages induced by IL-4 and confers the ability to increase eosinophil migration. *Int Immunol* **27**, 131-141, doi:10.1093/intimm/dxu090 (2015).

339 Netea, M. G. *et al.* Differential requirement for the activation of the inflammasome for processing and release of IL-1β in monocytes and macrophages. *Blood* **113**, 2324-2335, doi:10.1182/blood-2008-03-146720 (2009).
340 Pelegrin, P., Barroso-Gutierrez, C. & Surprenant, A. P2X7 Receptor Differentially Couples to Distinct Release Pathways for IL-1β in Mouse Macrophage. *The Journal of Immunology* **180**, 7147-7157, doi:10.4049/jimmunol.180.11.7147 (2008).
341 Das, A. *et al.* Dual RNA Sequencing Reveals the Expression of Unique Transcriptomic Signatures in Lipopolysaccharide-Induced BV-2 Microglial Cells. *PLoS One* **10**, e0121117, doi:10.1371/journal.pone.0121117 (2015).
342 Xie, Y., Sun, M., Xia, Y. & Shu, R. An RNA-seq screen of P. gingivalis LPS treated human gingival fibroblasts. *Archives of Oral Biology* **88**, 77-84, doi:https://doi.org/10.1016/j.archoralbio.2018.01.002 (2018).
343 Hald, A., Rønø, B., Lund, L. R. & Egerod, K. L. LPS counter regulates RNA expression of extracellular proteases and their inhibitors in murine macrophages. *Mediators Inflamm* **2012**, 157894, doi:10.1155/2012/157894 (2012).
344 Sharif, O., Bolshakov, V. N., Raines, S., Newham, P. & Perkins, N. D. Transcriptional profiling of the LPS induced NF-κB response in macrophages. *BMC Immunology* **8**, 1, doi:10.1186/1471-2172-8-1 (2007).
345 de Vries, S. *et al.* P23 Acts as Functional RBP in the Macrophage Inflammation Response. *Frontiers in Molecular Biosciences* **8**, doi:10.3389/fmolb.2021.625608 (2021).
346 Liu, C. *et al.* An integrated network pharmacology and RNA-Seq approach for exploring the preventive effect of Lonicerae japonicae flos on LPS-induced acute lung injury. *Journal of Ethnopharmacology* **264**, 113364, doi:https://doi.org/10.1016/j.jep.2020.113364 (2021).
347 Ye, S. *et al.* Chlojaponilactone B Attenuates Lipopolysaccharide-Induced Inflammatory Responses by Suppressing TLR4-Mediated ROS Generation and NF-κB Signaling Pathway. *Molecules* **24**, 3731 (2019).
348 Marletta, M. A., Yoon, P. S., Iyengar, R., Leaf, C. D. & Wishnok, J. S. Macrophage oxidation of L-arginine to nitrite and nitrate: nitric oxide is an intermediate. *Biochemistry* **27**, 8706-8711 (1988).
349 Hla, T. & Neilson, K. Human cyclooxygenase-2 cDNA. *Proceedings of the National Academy of Sciences* **89**, 7384-7388, doi:doi:10.1073/pnas.89.16.7384 (1992).
350 Simon, L. S. Role and regulation of cyclooxygenase-2 during inflammation. *The American Journal of Medicine* **106**, 37S-42S, doi:https://doi.org/10.1016/S0002-9343(99)00115-1 (1999).
351 Han, J. *et al.* Quality prediction of cell substrate using gene expression profiling. *Genomics* **87**, 552-559, doi:https://doi.org/10.1016/j.ygeno.2005.11.017 (2006).
352 Chacko, J. V. & Eliceiri, K. W. Autofluorescence lifetime imaging of cellular metabolism: Sensitivity toward cell density, pH, intracellular, and intercellular heterogeneity. *Cytometry A* **95**, 56-69, doi:10.1002/cyto.a.23603 (2019).
353 Merdanovic, M. *et al.* Activation by substoichiometric inhibition. *Proc Natl Acad Sci U S A* **117**, 1414-1418, doi:10.1073/pnas.1918721117 (2020).
354 de Waal Malefyt, R., Abrams, J., Bennett, B., Figdor, C. G. & de Vries, J. E. Interleukin 10(IL-10) inhibits cytokine synthesis by human monocytes: an autoregulatory role of IL-10 produced by monocytes. *Journal of Experimental Medicine* **174**, 1209-1220, doi:10.1084/jem.174.5.1209 (1991).

355 Lee, J., Rhee, M. H., Kim, E. & Cho, J. Y. BAY 11-7082 Is a Broad-Spectrum Inhibitor with Anti-Inflammatory Activity against Multiple Targets. *Mediators Inflamm* **2012**, 416036, doi:10.1155/2012/416036 (2012).

356 Relic, B. *et al.* BAY 11-7085 induces glucocorticoid receptor activation and autophagy that collaborate with apoptosis to induce human synovial fibroblast cell death. *Oncotarget* **7** (2016).

357 Relic, B. *et al.* Peroxisome Proliferator-activated Receptor-γ1 Is Dephosphorylated and Degraded during BAY 11-7085-induced Synovial Fibroblast Apoptosis *. *Journal of Biological Chemistry* **281**, 22597-22604, doi:10.1074/jbc.M512807200 (2006).

358 Relić, B. *et al.* 15-Deoxy-$\Delta^{12,14}$-prostaglandin J2 Inhibits Bay 11-7085-induced Sustained Extracellular Signal-regulated Kinase Phosphorylation and Apoptosis in Human Articular Chondrocytes and Synovial Fibroblasts *. *Journal of Biological Chemistry* **279**, 22399-22403, doi:10.1074/jbc.M314118200 (2004).

359 Weinstein, S. L., Sanghera, J. S., Lemke, K., DeFranco, A. L. & Pelech, S. L. Bacterial lipopolysaccharide induces tyrosine phosphorylation and activation of mitogen-activated protein kinases in macrophages. *Journal of Biological Chemistry* **267**, 14955-14962, doi:https://doi.org/10.1016/S0021-9258(18)42133-3 (1992).

360 van der Bruggen, T., Nijenhuis, S., van Raaij, E., Verhoef, J. & van Asbeck, B. S. Lipopolysaccharide-induced tumor necrosis factor alpha production by human monocytes involves the raf-1/MEK1-MEK2/ERK1-ERK2 pathway. *Infect Immun* **67**, 3824-3829, doi:10.1128/iai.67.8.3824-3829.1999 (1999).

361 Nelson, D. E. *et al.* Oscillations in NF-κB Signaling Control the Dynamics of Gene Expression. *Science* **306**, 704-708, doi:10.1126/science.1099962 (2004).

362 Sung, M.-H. *et al.* Switching of the relative dominance between feedback mechanisms in lipopolysaccharide-induced NF-κB signaling. *Science signaling* **7**, ra6-ra6, doi:10.1126/scisignal.2004764 (2014).

363 Hayes, J. B. *et al.* Modulation of Macrophage Inflammatory Nuclear Factor κB (NF-κB) Signaling by Intracellular Cryptococcus neoformans. *J Biol Chem* **291**, 15614-15627, doi:10.1074/jbc.M116.738187 (2016).

364 Ashall, L. *et al.* Pulsatile Stimulation Determines Timing and Specificity of NF-κB-Dependent Transcription. *Science* **324**, 242-246, doi:doi:10.1126/science.1164860 (2009).

365 Smith, E. L. *et al.* The regulation of sequence specific NF-κB DNA binding and transcription by IKKβ phosphorylation of NF-κB p50 at serine 80. *Nucleic Acids Res* **47**, 11151-11163, doi:10.1093/nar/gkz873 (2019).

366 Yu, Y., Wan, Y. & Huang, C. The biological functions of NF-kappaB1 (p50) and its potential as an anti-cancer target. *Curr Cancer Drug Targets* **9**, 566-571, doi:10.2174/156800909788486759 (2009).

367 Pedrinaci, S., Ruiz-Cabello, F., Gomez, O., Collado, A. & Garrido, F. Protein kinase C-mediated regulation of the expression of CD14 and CD11 /CD18 in U937 cells. *International Journal of Cancer* **45**, 294-298, doi:https://doi.org/10.1002/ijc.2910450215 (1990).

368 García, A. *et al.* Differential effect on U937 cell differentiation by targeting transcriptional factors implicated in tissue- or stage-specific induced integrin expression. *Experimental Hematology* **27**, 353-364, doi:https://doi.org/10.1016/S0301-472X(98)00038-1 (1999).

369 Yang, L., Dai, F., Tang, L., Le, Y. & Yao, W. Macrophage differentiation induced by PMA is mediated by activation of RhoA/ROCK signaling. *J Toxicol Sci* **42**, 763-771, doi:10.2131/jts.42.763 (2017).
370 Gatto, F. *et al.* PMA-Induced THP-1 Macrophage Differentiation is Not Impaired by Citrate-Coated Platinum Nanoparticles. *Nanomaterials (Basel)* **7**, doi:10.3390/nano7100332 (2017).
371 Lund, M. E., To, J., O'Brien, B. A. & Donnelly, S. The choice of phorbol 12-myristate 13-acetate differentiation protocol influences the response of THP-1 macrophages to a pro-inflammatory stimulus. *Journal of Immunological Methods* **430**, 64-70, doi:https://doi.org/10.1016/j.jim.2016.01.012 (2016).
372 Chanput, W., Mes, J. J. & Wichers, H. J. THP-1 cell line: An in vitro cell model for immune modulation approach. *International Immunopharmacology* **23**, 37-45, doi:https://doi.org/10.1016/j.intimp.2014.08.002 (2014).
373 Nascimento, C. R., Rodrigues Fernandes, N. A., Gonzalez Maldonado, L. A. & Rossa Junior, C. Comparison of monocytic cell lines U937 and THP-1 as macrophage models for in vitro studies. *Biochem Biophys Rep* **32**, 101383, doi:10.1016/j.bbrep.2022.101383 (2022).
374 Song, M.-g. *et al.* NRF2 Signaling Negatively Regulates Phorbol-12-Myristate-13-Acetate (PMA)-Induced Differentiation of Human Monocytic U937 Cells into Pro-Inflammatory Macrophages. *PLoS One* **10**, e0134235, doi:10.1371/journal.pone.0134235 (2015).
375 Daigneault, M., Preston, J. A., Marriott, H. M., Whyte, M. K. B. & Dockrell, D. H. The Identification of Markers of Macrophage Differentiation in PMA-Stimulated THP-1 Cells and Monocyte-Derived Macrophages. *PLoS One* **5**, e8668, doi:10.1371/journal.pone.0008668 (2010).
376 Baxter, E. W. *et al.* Standardized protocols for differentiation of THP-1 cells to macrophages with distinct M(IFNγ+LPS), M(IL-4) and M(IL-10) phenotypes. *Journal of Immunological Methods* **478**, 112721, doi:https://doi.org/10.1016/j.jim.2019.112721 (2020).
377 Giambelluca, S., Ochs, M. & Lopez-Rodriguez, E. Resting time after phorbol 12-myristate 13-acetate in THP-1 derived macrophages provides a non-biased model for the study of NLRP3 inflammasome. *Front Immunol* **13**, 958098, doi:10.3389/fimmu.2022.958098 (2022).
378 Schneemann, M. *et al.* Nitric Oxide Synthase Is Not a Constituent of the Antimicrobial Armature of Human Mononuclear Phagocytes. *The Journal of Infectious Diseases* **167**, 1358-1363, doi:10.1093/infdis/167.6.1358 (1993).
379 Schneemann, M. & Schoeden, G. Macrophage biology and immunology: man is not a mouse. *Journal of Leukocyte Biology* **81**, 579-579, doi:10.1189/jlb.1106702 (2007).
380 Azenabor, A. A., Kennedy, P. & York, J. Free intracellular Ca2+ regulates bacterial lipopolysaccharide induction of iNOS in human macrophages. *Immunobiology* **214**, 143-152, doi:https://doi.org/10.1016/j.imbio.2008.06.001 (2009).
381 Jung, J. Y. *et al.* The intracellular environment of human macrophages that produce nitric oxide promotes growth of mycobacteria. *Infect Immun* **81**, 3198-3209, doi:10.1128/iai.00611-13 (2013).
382 van Straaten, J. F. *et al.* Macrophages in lung tissue from patients with pulmonary emphysema express both inducible and endothelial nitric oxide synthase. *Mod Pathol* **11**, 648-655 (1998).
383 Connelly, L., Jacobs, A. T., Palacios-Callender, M., Moncada, S. & Hobbs, A. J. Macrophage Endothelial Nitric-oxide Synthase Autoregulates Cellular Activation and Pro-inflammatory Protein Expression *. *Journal of Biological Chemistry* **278**, 26480-26487, doi:10.1074/jbc.M302238200 (2003).

384 Rosenbaum, D. M., Rasmussen, S. G. F. & Kobilka, B. K. The structure and function of G-protein-coupled receptors. *Nature* **459**, 356-363, doi:10.1038/nature08144 (2009).
385 Agrawal, V. *et al.* Platelet-activating factor: a role in preterm delivery and an essential interaction with Toll-like receptor signaling in mice. *Biol Reprod* **91**, 119, doi:10.1095/biolreprod.113.116012 (2014).
386 Ban, J. Y., Kim, B. S., Kim, S. C., Kim, D. H. & Chung, J.-H. Microarray Analysis of Gene Expression Profiles in Response to Treatment with Melatonin in Lipopolysaccharide Activated RAW 264.7 Cells. *kjpp* **15**, 23-29, doi:10.4196/kjpp.2011.15.1.23 (2011).
387 Orecchioni, M., Matsunami, H. & Ley, K. Olfactory receptors in macrophages and inflammation. *Front Immunol* **13**, 1029244, doi:10.3389/fimmu.2022.1029244 (2022).
388 Holloman, B. L. *et al.* Characterization of Chemotaxis-Associated Gene Dysregulation in Myeloid Cell Populations in the Lungs during Lipopolysaccharide-Mediated Acute Lung Injury. *The Journal of Immunology* **210**, 2016-2028, doi:10.4049/jimmunol.2200822 (2023).
389 Akhabir, L. & Sandford, A. Genetics of interleukin 1 receptor-like 1 in immune and inflammatory diseases. *Curr Genomics* **11**, 591-606, doi:10.2174/138920210793360907 (2010).
390 Breschi, A., Gingeras, T. R. & Guigó, R. Comparative transcriptomics in human and mouse. *Nat Rev Genet* **18**, 425-440, doi:10.1038/nrg.2017.19 (2017).
391 Chamberlain, L. M., Godek, M. L., Gonzalez-Juarrero, M. & Grainger, D. W. Phenotypic non-equivalence of murine (monocyte-) macrophage cells in biomaterial and inflammatory models. *Journal of Biomedical Materials Research Part A* **88A**, 858-871, doi:https://doi.org/10.1002/jbm.a.31930 (2009).
392 Martire, S. & Banaszynski, L. A. The roles of histone variants in fine-tuning chromatin organization and function. *Nature Reviews Molecular Cell Biology* **21**, 522-541, doi:10.1038/s41580-020-0262-8 (2020).
393 Mariño-Ramírez, L., Kann, M. G., Shoemaker, B. A. & Landsman, D. Histone structure and nucleosome stability. *Expert Rev Proteomics* **2**, 719-729, doi:10.1586/14789450.2.5.719 (2005).
394 Fyodorov, D. V., Zhou, B.-R., Skoultchi, A. I. & Bai, Y. Emerging roles of linker histones in regulating chromatin structure and function. *Nature Reviews Molecular Cell Biology* **19**, 192-206, doi:10.1038/nrm.2017.94 (2018).
395 Robinson, P. J. J. & Rhodes, D. Structure of the '30nm' chromatin fibre: A key role for the linker histone. *Current Opinion in Structural Biology* **16**, 336-343, doi:https://doi.org/10.1016/j.sbi.2006.05.007 (2006).
396 Luger, K., Dechassa, M. L. & Tremethick, D. J. New insights into nucleosome and chromatin structure: an ordered state or a disordered affair? *Nat Rev Mol Cell Biol* **13**, 436-447, doi:10.1038/nrm3382 (2012).
397 McGhee, J. D. & Felsenfeld, G. Nucleosome structure. *Annual review of biochemistry* **49**, 1115-1156 (1980).
398 Millán-Zambrano, G., Burton, A., Bannister, A. J. & Schneider, R. Histone post-translational modifications — cause and consequence of genome function. *Nature Reviews Genetics* **23**, 563-580, doi:10.1038/s41576-022-00468-7 (2022).
399 Venkatesh, S. & Workman, J. L. Histone exchange, chromatin structure and the regulation of transcription. *Nature Reviews Molecular Cell Biology* **16**, 178-189, doi:10.1038/nrm3941 (2015).

400 Shvedunova, M. & Akhtar, A. Modulation of cellular processes by histone and non-histone protein acetylation. *Nature Reviews Molecular Cell Biology* **23**, 329-349, doi:10.1038/s41580-021-00441-y (2022).
401 Greer, E. L. & Shi, Y. Histone methylation: a dynamic mark in health, disease and inheritance. *Nature Reviews Genetics* **13**, 343-357, doi:10.1038/nrg3173 (2012).
402 Wasylyk, B. & Chambon, P. Transcription by Eukaryotic RNA Polymerases A and B of Chromatin Assembled in vitro. *European Journal of Biochemistry* **98**, 317-327, doi:https://doi.org/10.1111/j.1432-1033.1979.tb13191.x (1979).
403 Bannister, A. J., Schneider, R. & Kouzarides, T. Histone Methylation: Dynamic or Static? *Cell* **109**, 801-806, doi:10.1016/S0092-8674(02)00798-5 (2002).
404 Nurminskaya, M. V. & Belkin, A. M. Cellular functions of tissue transglutaminase. *Int Rev Cell Mol Biol* **294**, 1-97, doi:10.1016/b978-0-12-394305-7.00001-x (2012).
405 Tatsukawa, H., Furutani, Y., Hitomi, K. & Kojima, S. Transglutaminase 2 has opposing roles in the regulation of cellular functions as well as cell growth and death. *Cell Death & Disease* **7**, e2244-e2244, doi:10.1038/cddis.2016.150 (2016).
406 Occhigrossi, L. *et al.* Transglutaminase 2 Regulates Innate Immunity by Modulating the STING/TBK1/IRF3 Axis. *J Immunol* **206**, 2420-2429, doi:10.4049/jimmunol.2001122 (2021).
407 Brown, G. D., Willment, J. A. & Whitehead, L. C-type lectins in immunity and homeostasis. *Nature Reviews Immunology* **18**, 374-389, doi:10.1038/s41577-018-0004-8 (2018).
408 Graham, L. M. *et al.* The C-type lectin receptor CLECSF8 (CLEC4D) is expressed by myeloid cells and triggers cellular activation through Syk kinase. *J Biol Chem* **287**, 25964-25974, doi:10.1074/jbc.M112.384164 (2012).
409 Jeon, J.-W. *et al.* Soluble CD93 Induces Differentiation of Monocytes and Enhances TLR Responses. *The Journal of Immunology* **185**, 4921-4927, doi:10.4049/jimmunol.0904011 (2010).
410 Drouin, M. *et al.* CLEC-1 is a death sensor that limits antigen cross-presentation by dendritic cells and represents a target for cancer immunotherapy. *Science Advances* **8**, eabo7621, doi:doi:10.1126/sciadv.abo7621 (2022).
411 Hollmén, M., Figueiredo, C. R. & Jalkanen, S. New tools to prevent cancer growth and spread: a 'Clever' approach. *British Journal of Cancer* **123**, 501-509, doi:10.1038/s41416-020-0953-0 (2020).
412 Somann, J. P. *et al.* Characterization of plasma cytokine response to intraperitoneally administered LPS & subdiaphragmatic branch vagus nerve stimulation in rat model. *PLoS One* **14**, e0214317, doi:10.1371/journal.pone.0214317 (2019).
413 Li, Y., Shin, D. & Kwon, S. H. Histone deacetylase 6 plays a role as a distinct regulator of diverse cellular processes. *FEBS J* **280**, 775-793, doi:https://doi.org/10.1111/febs.12079 (2013).
414 Gagliardi, M., Strazzullo, M. & Matarazzo, M. R. DNMT3B Functions: Novel Insights From Human Disease. *Frontiers in Cell and Developmental Biology* **6**, doi:10.3389/fcell.2018.00140 (2018).
415 Bendall, A. J. & Abate-Shen, C. Roles for Msx and Dlx homeoproteins in vertebrate development. *Gene* **247**, 17-31, doi:https://doi.org/10.1016/S0378-1119(00)00081-0 (2000).
416 Li, X. *et al.* Histones: The critical players in innate immunity. *Frontiers in Immunology* **13**, doi:10.3389/fimmu.2022.1030610 (2022).

417 Weng, W., Hu, Z. & Pan, Y. Macrophage Extracellular Traps: Current Opinions and the State of Research regarding Various Diseases. *J Immunol Res* **2022**, 7050807, doi:10.1155/2022/7050807 (2022).
418 Brinkmann, V. *et al.* Neutrophil Extracellular Traps Kill Bacteria. *Science* **303**, 1532-1535, doi:doi:10.1126/science.1092385 (2004).
419 Yousefi, S. *et al.* Catapult-like release of mitochondrial DNA by eosinophils contributes to antibacterial defense. *Nature Medicine* **14**, 949-953, doi:10.1038/nm.1855 (2008).
420 Mohanan, S., Horibata, S., McElwee, J., Dannenberg, A. & Coonrod, S. Identification of Macrophage Extracellular Trap-Like Structures in Mammary Gland Adipose Tissue: A Preliminary Study. *Frontiers in Immunology* **4**, doi:10.3389/fimmu.2013.00067 (2013).
421 Chow, O. A. *et al.* Statins Enhance Formation of Phagocyte Extracellular Traps. *Cell Host & Microbe* **8**, 445-454, doi:https://doi.org/10.1016/j.chom.2010.10.005 (2010).
422 Leshner, M. *et al.* PAD4 mediated histone hypercitrullination induces heterochromatin decondensation and chromatin unfolding to form neutrophil extracellular trap-like structures. *Frontiers in Immunology* **3**, doi:10.3389/fimmu.2012.00307 (2012).
423 Silva, J. C. *et al.* Mac-1 triggers neutrophil DNA extracellular trap formation to Aspergillus fumigatus independently of PAD4 histone citrullination. *Journal of Leukocyte Biology* **107**, 69-83, doi:10.1002/jlb.4a0119-009rr (2019).
424 Kobiyama, K. *et al.* Extrachromosomal Histone H2B Mediates Innate Antiviral Immune Responses Induced by Intracellular Double-Stranded DNA. *Journal of Virology* **84**, 822-832, doi:doi:10.1128/jvi.01339-09 (2010).
425 Mehta, S. & Jeffrey, K. L. Beyond receptors and signaling: epigenetic factors in the regulation of innate immunity. *Immunology & Cell Biology* **93**, 233-244, doi:https://doi.org/10.1038/icb.2014.101 (2015).
426 De Santa, F. *et al.* Jmjd3 contributes to the control of gene expression in LPS-activated macrophages. *EMBO J* **28**, 3341-3352, doi:10.1038/emboj.2009.271 (2009).
427 Satoh, T. *et al.* The Jmjd3-Irf4 axis regulates M2 macrophage polarization and host responses against helminth infection. *Nat Immunol* **11**, 936-944, doi:10.1038/ni.1920 (2010).
428 De Santa, F. *et al.* The Histone H3 Lysine-27 Demethylase Jmjd3 Links Inflammation to Inhibition of Polycomb-Mediated Gene Silencing. *Cell* **130**, 1083-1094, doi:10.1016/j.cell.2007.08.019 (2007).
429 Heintzman, N. D. *et al.* Histone modifications at human enhancers reflect global cell-type-specific gene expression. *Nature* **459**, 108-112, doi:10.1038/nature07829 (2009).
430 Berghe, W. V., De Bosscher, K., Boone, E., Plaisance, S. & Haegeman, G. The Nuclear Factor-κB Engages CBP/p300 and Histone Acetyltransferase Activity for Transcriptional Activation of the Interleukin-6 Gene Promoter *. *Journal of Biological Chemistry* **274**, 32091-32098, doi:10.1074/jbc.274.45.32091 (1999).
431 Das Gupta, K. *et al.* Class IIa Histone Deacetylases Drive Toll-like Receptor-Inducible Glycolysis and Macrophage Inflammatory Responses via Pyruvate Kinase M2. *Cell Rep* **30**, 2712-2728.e2718, doi:10.1016/j.celrep.2020.02.007 (2020).
432 Roger, T. *et al.* Histone deacetylase inhibitors impair innate immune responses to Toll-like receptor agonists and to infection. *Blood* **117**, 1205-1217, doi:10.1182/blood-2010-05-284711 (2011).

433 Park, S.-Y. & Kim, J.-S. A short guide to histone deacetylases including recent progress on class II enzymes. *Experimental & Molecular Medicine* **52**, 204-212, doi:10.1038/s12276-020-0382-4 (2020).
434 Frye, R. A. Characterization of Five Human cDNAs with Homology to the Yeast SIR2 Gene: Sir2-like Proteins (Sirtuins) Metabolize NAD and May Have Protein ADP-Ribosyltransferase Activity. *Biochemical and Biophysical Research Communications* **260**, 273-279, doi:https://doi.org/10.1006/bbrc.1999.0897 (1999).
435 Shakespear, M. R. *et al.* Histone Deacetylase 7 Promotes Toll-like Receptor 4-dependent Proinflammatory Gene Expression in Macrophages*. *Journal of Biological Chemistry* **288**, 25362-25374, doi:10.1074/jbc.M113.496281 (2013).
436 Williams, K. A. *et al.* Extracellular Signal-regulated Kinase (ERK) Phosphorylates Histone Deacetylase 6 (HDAC6) at Serine 1035 to Stimulate Cell Migration *. *Journal of Biological Chemistry* **288**, 33156-33170, doi:10.1074/jbc.M113.472506 (2013).
437 Hubbert, C. *et al.* HDAC6 is a microtubule-associated deacetylase. *Nature* **417**, 455-458, doi:10.1038/417455a (2002).
438 Wang, B. *et al.* Microtubule acetylation amplifies p38 kinase signalling and anti-inflammatory IL-10 production. *Nat Commun* **5**, 3479, doi:10.1038/ncomms4479 (2014).
439 Ran, J. & Zhou, J. Targeted inhibition of histone deacetylase 6 in inflammatory diseases. *Thorac Cancer* **10**, 405-412, doi:10.1111/1759-7714.12974 (2019).
440 Liu, G. *et al.* Design, synthesis, and anti-inflammatory activity characterization of novel brain-permeable HDAC6 inhibitors. *Eur J Med Chem* **254**, 115327, doi:10.1016/j.ejmech.2023.115327 (2023).
441 Cheng, F. *et al.* A Novel Role for Histone Deacetylase 6 in the Regulation of the Tolerogenic STAT3/IL-10 Pathway in APCs. *The Journal of Immunology* **193**, 2850-2862, doi:10.4049/jimmunol.1302778 (2014).
442 Cheng, F. *et al.* Divergent roles of histone deacetylase 6 (HDAC6) and histone deacetylase 11 (HDAC11) on the transcriptional regulation of IL10 in antigen presenting cells. *Mol Immunol* **60**, 44-53, doi:https://doi.org/10.1016/j.molimm.2014.02.019 (2014).
443 Into, T., Inomata, M., Niida, S., Murakami, Y. & Shibata, K. Regulation of MyD88 aggregation and the MyD88-dependent signaling pathway by sequestosome 1 and histone deacetylase 6. *J Biol Chem* **285**, 35759-35769, doi:10.1074/jbc.M110.126904 (2010).
444 Yuan, L. *et al.* HDAC11 regulates interleukin-13 expression in CD4+ T cells in the heart. *Journal of Molecular and Cellular Cardiology* **122**, 1-10, doi:https://doi.org/10.1016/j.yjmcc.2018.07.253 (2018).
445 Cao, J. *et al.* HDAC11 regulates type I interferon signaling through defatty-acylation of SHMT2. *Proceedings of the National Academy of Sciences* **116**, 5487-5492, doi:doi:10.1073/pnas.1815365116 (2019).
446 Asare, Y. *et al.* Histone Deacetylase 9 Activates IKK to Regulate Atherosclerotic Plaque Vulnerability. *Circulation Research* **127**, 811-823, doi:doi:10.1161/CIRCRESAHA.120.316743 (2020).
447 Pan, Z., Dong, H., Huang, N. & Fang, J. Oxidative stress and inflammation regulation of sirtuins: New insights into common oral diseases. *Front Physiol* **13**, 953078, doi:10.3389/fphys.2022.953078 (2022).

448 Yuan, F. *et al.* SIRT2 inhibition exacerbates neuroinflammation and blood–brain barrier disruption in experimental traumatic brain injury by enhancing NF-κB p65 acetylation and activation. *Journal of Neurochemistry* **136**, 581-593, doi:https://doi.org/10.1111/jnc.13423 (2016).
449 Tao, Y. *et al.* SIRT4 Suppresses Inflammatory Responses in Human Umbilical Vein Endothelial Cells. *Cardiovascular Toxicology* **15**, 217-223, doi:10.1007/s12012-014-9287-6 (2015).
450 Weiss, U. *et al.* Inhibition of HDAC Enzymes Contributes to Differential Expression of Pro-Inflammatory Proteins in the TLR-4 Signaling Cascade. *Int J Mol Sci* **21**, 8943 (2020).
451 Chong, W. *et al.* Histone deacetylase inhibitor suberoylanilide hydroxamic acid attenuates Toll-like receptor 4 signaling in lipopolysaccharide-stimulated mouse macrophages. *Journal of Surgical Research* **178**, 851-859, doi:https://doi.org/10.1016/j.jss.2012.07.023 (2012).
452 Halili, M. A. *et al.* Differential effects of selective HDAC inhibitors on macrophage inflammatory responses to the Toll-like receptor 4 agonist LPS. *Journal of Leukocyte Biology* **87**, 1103-1114, doi:10.1189/jlb.0509363 (2010).
453 Wu, J. Y. *et al.* Histone deacetylase 6 (HDAC6) deacetylates extracellular signal-regulated kinase 1 (ERK1) and thereby stimulates ERK1 activity. *J Biol Chem* **293**, 1976-1993, doi:10.1074/jbc.M117.795955 (2018).
454 Dudakovic, A. *et al.* Histone deacetylase inhibition promotes osteoblast maturation by altering the histone H4 epigenome and reduces Akt phosphorylation. *J Biol Chem* **288**, 28783-28791, doi:10.1074/jbc.M113.489732 (2013).
455 Bahl, S. & Seto, E. Regulation of histone deacetylase activities and functions by phosphorylation and its physiological relevance. *Cell Mol Life Sci* **78**, 427-445, doi:10.1007/s00018-020-03599-4 (2021).
456 Joseph, S. R. *et al.* Competition between histone and transcription factor binding regulates the onset of transcription in zebrafish embryos. *Elife* **6**, doi:10.7554/eLife.23326 (2017).
457 Ding, Y., Yi, J., Wang, J. & Sun, Z. Interleukin-1 receptor antagonist: a promising cytokine against human squamous cell carcinomas. *Heliyon* **9**, e14960, doi:https://doi.org/10.1016/j.heliyon.2023.e14960 (2023).
458 Dinarello, C. A. & Thompson, R. C. Blocking IL-1: interleukin 1 receptor antagonist in vivo and in vitro. *Immunology Today* **12**, 404-410, doi:https://doi.org/10.1016/0167-5699(91)90142-G (1991).
459 Andersson, J., Björk, L., Dinarello, C. A., Towbin, H. & Andersson, U. Lipopolysaccharide induces human interleukin-1 receptor antagonist and interleukin-1 production in the same cell. *European Journal of Immunology* **22**, 2617-2623, doi:https://doi.org/10.1002/eji.1830221022 (1992).
460 Ness, T. L. *et al.* CCR1 and CC Chemokine Ligand 5 Interactions Exacerbate Innate Immune Responses during Sepsis1. *The Journal of Immunology* **173**, 6938-6948, doi:10.4049/jimmunol.173.11.6938 (2004).
461 Son, Y.-O., Kim, H.-E., Choi, W.-S., Chun, C.-H. & Chun, J.-S. RNA-binding protein ZFP36L1 regulates osteoarthritis by modulating members of the heat shock protein 70 family. *Nature Communications* **10**, 77, doi:10.1038/s41467-018-08035-7 (2019).
462 Gong, J. *et al.* Genetic evidence supports the development of SLC26A9 targeting therapies for the treatment of lung disease. *npj Genomic Medicine* **7**, 28, doi:10.1038/s41525-022-00299-9 (2022).

463 Balázs, A. & Mall, M. A. Role of the SLC26A9 Chloride Channel as Disease Modifier and Potential Therapeutic Target in Cystic Fibrosis. *Front Pharmacol* **9**, 1112, doi:10.3389/fphar.2018.01112 (2018).
464 Gorrieri, G., Zara, F. & Scudieri, P. SLC26A9 as a Potential Modifier and Therapeutic Target in Cystic Fibrosis Lung Disease. *Biomolecules* **12**, doi:10.3390/biom12020202 (2022).
465 Anagnostopoulou, P. *et al.* SLC26A9-mediated chloride secretion prevents mucus obstruction in airway inflammation. *J Clin Invest* **122**, 3629-3634, doi:10.1172/jci60429 (2012).
466 Clemens, R. A. & Lowell, C. A. CRAC channel regulation of innate immune cells in health and disease. *Cell Calcium* **78**, 56-65, doi:10.1016/j.ceca.2019.01.003 (2019).
467 Ali, H. A. *et al.* A Comprehensive Review of BET Protein Biochemistry, Physiology, and Pathological Roles. *Frontiers in Pharmacology* **13**, doi:10.3389/fphar.2022.818891 (2022).
468 Denis, G. V. *et al.* Identification of Transcription Complexes that Contain the Double Bromodomain Protein Brd2 and Chromatin Remodeling Machines. *Journal of Proteome Research* **5**, 502-511, doi:10.1021/pr050430u (2006).
469 Gallagher, S. J. *et al.* Control of NF-kB activity in human melanoma by bromodomain and extra-terminal protein inhibitor I-BET151. *Pigment Cell & Melanoma Research* **27**, 1126-1137, doi:https://doi.org/10.1111/pcmr.12282 (2014).
470 Belkina, A. C., Nikolajczyk, B. S. & Denis, G. V. BET protein function is required for inflammation: Brd2 genetic disruption and BET inhibitor JQ1 impair mouse macrophage inflammatory responses. *J Immunol* **190**, 3670-3678, doi:10.4049/jimmunol.1202838 (2013).
471 Rousseau, A., Rio, M.-C. & Alpy, F. TRAF4, at the Crossroad between Morphogenesis and Cancer. *Cancers* **3**, 2734-2749 (2011).
472 Kawamata, S., Hori, T., Imura, A., Takaori-Kondo, A. & Uchiyama, T. Activation of OX40 Signal Transduction Pathways Leads to Tumor Necrosis Factor Receptor-associated Factor (TRAF) 2- and TRAF5-mediated NF-κB Activation *. *Journal of Biological Chemistry* **273**, 5808-5814, doi:10.1074/jbc.273.10.5808 (1998).
473 Takeshita, F. *et al.* TRAF4 acts as a silencer in TLR-mediated signaling through the association with TRAF6 and TRIF. *European Journal of Immunology* **35**, 2477-2485, doi:https://doi.org/10.1002/eji.200526151 (2005).
474 Chen, Y. *et al.* Novel Findings in Teleost TRAF4, a Protein Acts as an Enhancer in TRIF and TRAF6 Mediated Antiviral and Inflammatory Signaling. *Front Immunol* **13**, 944528, doi:10.3389/fimmu.2022.944528 (2022).
475 Das, A., Sudhahar, V., Ushio-Fukai, M. & Fukai, T. Novel interaction of antioxidant-1 with TRAF4: role in inflammatory responses in endothelial cells. *American Journal of Physiology-Cell Physiology* **317**, C1161-C1171, doi:10.1152/ajpcell.00264.2019 (2019).
476 Marinis, J. M. *et al.* IκB Kinase α Phosphorylation of TRAF4 Downregulates Innate Immune Signaling. *Molecular and Cellular Biology* **32**, 2479-2489, doi:10.1128/MCB.00106-12 (2012).
477 Li, S. *et al.* MicroRNA-4443 regulates monocyte activation by targeting tumor necrosis factor receptor associated factor 4 in stroke-induced immunosuppression. *European Journal of Neurology* **27**, 1625-1637, doi:https://doi.org/10.1111/ene.14282 (2020).
478 Qi, Y. *et al.* MicroRNA-4443 Causes CD4+ T Cells Dysfunction by Targeting TNFR-Associated Factor 4 in Graves' Disease. *Frontiers in Immunology* **8**, doi:10.3389/fimmu.2017.01440 (2017).

479 Jiang, W. & Pisetsky, D. S. The Role of IFN-α and Nitric Oxide in the Release of HMGB1 by RAW 264.7 Cells Stimulated with Polyinosinic-Polycytidylic Acid or Lipopolysaccharide1. *The Journal of Immunology* **177**, 3337-3343, doi:10.4049/jimmunol.177.5.3337 (2006).
480 Jacobs, A. T. & Ignarro, L. J. Lipopolysaccharide-induced expression of interferon-beta mediates the timing of inducible nitric-oxide synthase induction in RAW 264.7 macrophages. *J Biol Chem* **276**, 47950-47957, doi:10.1074/jbc.M106639200 (2001).
481 Shi, Q. *et al.* MFHAS1 suppresses TLR4 signaling pathway via induction of PP2A C subunit cytoplasm translocation and inhibition of c-Jun dephosphorylation at Thr239. *Mol Immunol* **88**, 79-88, doi:https://doi.org/10.1016/j.molimm.2017.06.017 (2017).
482 Eishingdrelo, H. & Kongsamut, S. Minireview: Targeting GPCR Activated ERK Pathways for Drug Discovery. *Curr Chem Genom Transl Med* **7**, 9-15, doi:10.2174/2213988501307010009 (2013).
483 Roux, P. P. & Blenis, J. ERK and p38 MAPK-activated protein kinases: a family of protein kinases with diverse biological functions. *Microbiol Mol Biol Rev* **68**, 320-344, doi:10.1128/mmbr.68.2.320-344.2004 (2004).
484 Roskoski, R. MEK1/2 dual-specificity protein kinases: Structure and regulation. *Biochemical and Biophysical Research Communications* **417**, 5-10, doi:https://doi.org/10.1016/j.bbrc.2011.11.145 (2012).
485 Matallanas, D. *et al.* Raf family kinases: old dogs have learned new tricks. *Genes Cancer* **2**, 232-260, doi:10.1177/1947601911407323 (2011).
486 Simanshu, D. K., Nissley, D. V. & McCormick, F. RAS Proteins and Their Regulators in Human Disease. *Cell* **170**, 17-33, doi:10.1016/j.cell.2017.06.009 (2017).
487 Chen, H. F., Chuang, H. C. & Tan, T. H. Regulation of Dual-Specificity Phosphatase (DUSP) Ubiquitination and Protein Stability. *Int J Mol Sci* **20**, doi:10.3390/ijms20112668 (2019).
488 Frémin, C., Saba-El-Leil, Marc K., Lévesque, K., Ang, S.-L. & Meloche, S. Functional Redundancy of ERK1 and ERK2 MAP Kinases during Development. *Cell Reports* **12**, 913-921, doi:10.1016/j.celrep.2015.07.011 (2015).
489 Bernstein, L. R., Ferris, D. K., Colburn, N. H. & Sobel, M. E. A family of mitogen-activated protein kinase-related proteins interacts in vivo with activator protein-1 transcription factor. *Journal of Biological Chemistry* **269**, 9401-9404, doi:https://doi.org/10.1016/S0021-9258(17)36892-8 (1994).
490 Kumar, N. V. & Bernstein, L. R. Ten ERK-related Proteins in Three Distinct Classes Associate with AP-1 Proteins and/or AP-1 DNA *. *Journal of Biological Chemistry* **276**, 32362-32372, doi:10.1074/jbc.M103677200 (2001).
491 Guedea, A. L. *et al.* ERK-associated changes of AP-1 proteins during fear extinction. *Mol Cell Neurosci* **47**, 137-144, doi:10.1016/j.mcn.2011.03.009 (2011).
492 McReynolds, A. C. *et al.* Phosphorylation or Mutation of the ERK2 Activation Loop Alters Oligonucleotide Binding. *Biochemistry* **55**, 1909-1917, doi:10.1021/acs.biochem.6b00096 (2016).
493 Vuong, B. *et al.* NF-κB transcriptional activation by TNFα requires phospholipase C, extracellular signal-regulated kinase 2 and poly(ADP-ribose) polymerase-1. *Journal of Neuroinflammation* **12**, 229, doi:10.1186/s12974-015-0448-8 (2015).
494 Oh, S., Woo, J.-I., Lim, D. J. & Moon, S. K. ERK2-Dependent Activation of c-Jun Is Required for Nontypeable Haemophilus influenzae-Induced CXCL2 Upregulation in Inner Ear Fibrocytes. *The Journal of Immunology* **188**, 3496-3505, doi:10.4049/jimmunol.1103182 (2012).

495 Chang, S.-F. *et al.* LPS-Induced G-CSF Expression in Macrophages Is Mediated by ERK2, but Not ERK1. *PLoS One* **10**, e0129685, doi:10.1371/journal.pone.0129685 (2015).
496 Guo, Z. *et al.* MAP kinase-interacting serine/threonine kinase 2 promotes proliferation, metastasis, and predicts poor prognosis in non-small cell lung cancer. *Sci Rep* **7**, 10612, doi:10.1038/s41598-017-10397-9 (2017).
497 Hay, N. Mnk earmarks eIF4E for cancer therapy. *Proceedings of the National Academy of Sciences* **107**, 13975-13976, doi:doi:10.1073/pnas.1008908107 (2010).
498 Armstrong, C. & Spencer, S. L. Replication-dependent histone biosynthesis is coupled to cell-cycle commitment. *Proceedings of the National Academy of Sciences* **118**, e2100178118, doi:doi:10.1073/pnas.2100178118 (2021).
499 Ning, S., Pagano, J. S. & Barber, G. N. IRF7: activation, regulation, modification and function. *Genes & Immunity* **12**, 399-414, doi:10.1038/gene.2011.21 (2011).
500 Schroeder, A. *et al.* The RIN: an RNA integrity number for assigning integrity values to RNA measurements. *BMC Molecular Biology* **7**, 3, doi:10.1186/1471-2199-7-3 (2006).